

STUDIES OF THE EFFECTS OF HIGH VOLTAGE ON THE
PERFORMANCE AND IMPEDANCE OF LITHIUM-ION BATTERIES

by

Kathlyne Nelson

Submitted in partial fulfilment of the requirements
for the degree of Doctor of Philosophy

at

Dalhousie University
Halifax, Nova Scotia
September 2017

© Copyright by Kathlyne Nelson, 2017

To Patrick,

TABLE OF CONTENTS

LIST OF TABLES	vii
LIST OF FIGURES	viii
ABSTRACT.....	xvii
LIST OF ABBREVIATIONS AND SYMBOLS USED.....	xviii
ACKNOWLEDGEMENTS.....	xxi
CHAPTER 1. INTRODUCTION	1
1.1 MOTIVATION.....	1
1.2 LITHIUM-ION BATTERIES.....	3
1.2.1 POSITIVE ELECTRODE	4
1.2.2 NEGATIVE ELECTRODE.....	6
1.2.3 SEPARATOR.....	7
1.2.4 ELECTROLYTE SYSTEMS	7
1.2.5 ELECTROLYTE ADDITIVES	10
1.3 THESIS OUTLINE.....	12
CHAPTER 2. SOLID ELECTROLYTE INTERPHASES AND THE ROLE OF ELECTROLYTE ADDITIVES	15
2.1 SEI AT THE NEGATIVE ELECTRODE.....	15
2.2 SEI AT THE POSITIVE ELECTRODE	20

2.3	EFFECT OF ELECTROLYTE ADDITIVES ON THE SOLID ELECTROLYTE INTERPHASES.....	24
2.4	ROCK SALT SURFACE LAYER ON NMC POSITIVE ELECTRODES.....	26
CHAPTER 3.	EXPERIMENTAL METHODS.....	29
3.1	POUCH CELLS AND CELL CHEMISTRIES	29
3.2	LITHIUM ION CELL CYCLING EXPERIMENTS	30
3.3	GAS VOLUME MEASUREMENTS.....	34
3.4	ELECTROCHEMICAL IMPEDANCE SPECTROSCOPY	35
3.5	AUTOMATIC EIS AND CYCLING	47
3.6	SYMMETRIC CELLS.....	52
3.7	EQUIVALENT CIRCUIT MODELS FROM LITERATURE.....	53
CHAPTER 4.	EFFECTS OF UPPER CUTOFF POTENTIAL AND SURFACE COATING ON THE IMPEDANCE OF NMC/GRAPHITE POUCH CELLS.....	56
4.1	EXPERIMENTAL.....	57
4.2	RESULTS	58
4.3	CONCLUSION.....	72
CHAPTER 5.	A COMPARISON OF NMC/GRAPHITE POUCH CELLS AND COMMERCIALY AVAILABLE LCO CELLS TESTED TO HIGH POTENTIAL....	74
5.1	EXPERIMENTAL.....	76
5.2	RESULTS	77

5.3	CONCLUSION.....	87
CHAPTER 6. EFFECTS OF VARIOUS CELL COMPONENTS ON THE IMPEDANCE OF NMC/GRAPHITE POUCH CELLS		
		88
6.1	EXPERIMENTAL.....	90
6.2	CHARGE-HOLD-DISCHARGE CYCLING AT 20°C.....	92
6.2.1	EXPERIMENTAL.....	92
6.2.2	RESULTS	94
6.3	LONG-TERM CYCLING AT 40°C.....	110
6.3.1	EXPERIMENTAL.....	110
6.3.2	RESULTS	112
6.4	CONCLUSIONS.....	124
CHAPTER 7. EFFECTS OF VARIOUS ELECTRODE CHEMISTRIES AND ELECTROLYTES ON THE IMPEDANCE OF NMC/GRAPHITE POUCH CELLS .		
		126
7.1	EXPERIMENTAL.....	126
7.2	RESULTS	128
7.2.1	CELLS WITH ARTIFICIAL GRAPHITE.....	128
7.2.2	CELLS WITH NATURAL GRAPHITE	143
7.2.3	SELECTED FITTING RESULTS.....	157
7.3	CONCLUSION.....	176
CHAPTER 8. REVERSIBLE AND IRREVERSIBLE IMPEDANCE GROWTH..		
		177
8.1	CHARACTERIZATION	178

8.2	LITERATURE REVIEW	186
8.3	CONCLUSION.....	194
CHAPTER 9. IMPEDANCE OF SYMMETRIC CELLS AFTER FULL CELL STORAGE AT 60°C		
		196
9.1	EXPERIMENTAL.....	196
9.2	RESULTS: CONTROL AND VC CELLS.....	198
9.3	RESULTS: PES222 CELLS	208
9.4	CONCLUSION.....	216
CHAPTER 10. CONCLUSIONS.....		
		218
10.1	CONCLUSIONS.....	218
10.2	FUTURE WORK.....	222
REFERENCES		230
APPENDIX A.....		243

LIST OF TABLES

Table 3.1 Circuit elements and their calculated impedance. Adapted from Nelson. ¹³	37
Table 3.2 Simplified equivalent circuit models for Li-ion electrodes and Li-ion cells, and their calculated impedance. Adapted from Nelson. ¹³	46
Table 3.3 List of equivalent circuit models from literature used to fit impedance spectra of Li-ion cells.	53
Table 6.1 Information about the Al ₂ O ₃ content in the PP and PET separator obtained after 900°C heating for 2 hours.	91
Table 7.1 Cell chemistry and name of the cells presented in this work.....	127
Table 8.1 Characterization of impedance growth in Li-ion cells.....	183
Table 9.1 The drop in voltage during open circuit voltage storage at 60°C for the control cells with initial voltage of 4.2 V.	198
Table 9.2 The drop in voltage during open circuit voltage storage at 60°C for the 2% VC cells with initial voltage of 4.2 V.	201
Table 9.3 The drop in voltage during open circuit voltage storage at 60°C for the PES222 cells with initial voltage of 4.2 and 4.4 V	210
Table 0.1 Cell details for some of the lithium-ion pouch cells presented in this thesis..	243

LIST OF FIGURES

Figure 1.1 A voltage-capacity curve for NMC622 vs Li/Li^+	2
Figure 1.2 Schematic of a Li-ion cell.....	4
Figure 1.3 The chemical structures of commonly used salts for electrolytes in Li-ion cells.....	8
Figure 1.4 The chemical structures of commonly used electrolyte solvents.....	10
Figure 1.5 The chemical structures of the electrolyte additives discussed previously.....	12
Figure 3.1 Photograph of a) an NMC442/graphite wound pouch cell from LiFUN Technologies and b) a clamped pouch cell.....	30
Figure 3.2 The charge-hold-discharge method used in much of the work presented in this thesis.....	32
Figure 3.3 The discharge capacity for cells containing 2% PES + 1% MMDS + 1% TTSPi undergoing cycling tests according to continuous charge-discharge cycling or charge-hold-discharge cycling.....	33
Figure 3.4 The current-voltage Lissajous figures for impedance measurements of a Li-ion cell using an applied a) 1 mV AC potential, b) 10 mV AC potential, and c) 20 mV AC potential shown for selected frequencies.....	36
Figure 3.5 An a) imaginary Bode, b) real Bode, and c) Nyquist representation of the impedance spectrum for an RC circuit in series with a resistor.....	39
Figure 3.6 Example of Nyquist plot for a cell exhibiting a) a single-peak impedance spectrum and b) a two-peak impedance spectrum.....	40
Figure 3.7 Example of the contribution of the equipment to the measured impedance, obtained by measuring EIS of a short circuit using the four-wire system.....	41
Figure 3.8 Example of an imaginary Bode plot for a cell exhibiting a) a single-peak feature and b) a two-peak feature. Example of a real bode plot for a cell exhibiting c) a single-peak feature and d) a two-peak feature.....	42
Figure 3.9 a) Discrete transmission line model circuit of the positive electrode used to interpret impedance spectra	43

Figure 3.10 a) Imaginary Bode, b) real Bode, and c) Nyquist representations of the impedance spectra for a circuit consisting of a CPE in parallel with a resistor.....	45
Figure 3.11 Impedance spectra of a Li-ion cell undergoing charge-hold-discharge cycling.....	49
Figure 3.12 The discharge capacity for cells containing 2% PES + 1% MMDS + 1% TTSPi undergoing cycling tests and FRA measurements according to continuous charge-discharge cycling or charge-hold-discharge cycling as a function of a) time and b) cycle number. The combination of charge transfer resistance (both positive and negative electrodes) and resistance due to motion of ions through the SEI layers.....	51
Figure 4.1 The discharge capacity of a) LaPO ₄ -coated and b) uncoated NMC442/graphite pouch cells undergoing charge-hold-discharge cycling tests.....	59
Figure 4.2 The impedance spectra as measured by the FRA for the coated cell at a) cycle 26, b) cycle 50 and, c) cycle 74 and for the uncoated cell at d) cycle 26, e) cycle 50, and f) cycle 74, both with an upper cutoff of 4.4 V.	61
Figure 4.3 The impedance spectra as measured by the FRA for the coated cell at a) cycle 26, b) cycle 50 and, c) cycle 74 and for the uncoated cell at d) cycle 26, e) cycle 50, and f) cycle 74, both with an upper cutoff of 4.475 V.	62
Figure 4.4 The impedance spectra measured at 10. ± 0.1°C for the a) coated positive symmetric cell, b) uncoated positive symmetric cell, c) coated negative symmetric cell, and d) uncoated negative symmetric cell.....	64
Figure 4.5 a) A transmission line model of the positive electrode used to interpret impedance spectra with the current collector at the left and the separator at the right. b) A Nyquist plot showing how the impedance spectrum changes	66
Figure 4.6 The combination of charge transfer resistance (both positive and negative electrodes) and resistance due to motion of ions through the SEI layers (both positive and negative electrodes), R _{ct} , as a function of voltage.....	68
Figure 4.7 The values of R _{ct} (c and d) and the changes in R _e (or R _i or a combination of R _e and R _i) (a and b) extracted from the impedance spectra of LaPO ₄ -coated cells (red) and from the uncoated cells (black) at 3.4 V (circles) and at 4.4 V (crosses) for cells cycled to 4.4 V (a and c) and to 4.475 V (b and d).....	69
Figure 4.8 The difference between the average charge and discharge voltage, ΔV, as a function of cycle number	70

Figure 4.9 The volume of gas produced in a) coated and b) uncoated cells.....	71
Figure 5.1. The fractional discharge capacity of the LCO and NMC cells undergoing charge-hold-discharge cycling.....	78
Figure 5.2 The combination of charge transfer resistance (both positive and negative electrodes) and resistance due to motion of ions through the SEI layers	79
Figure 5.3 The impedance spectra for the LCO cell cycled to 4.2 V measured at a) 3.9 V and d) 4.2 V. The impedance spectra for the LCO cell cycled to 4.4 V measured at b) 3.9 V and e) 4.4 V. The impedance spectra for the NMC cell cycled to 4.4 V measured at c) 3.9 V and f) 4.4 V.....	80
Figure 5.4 The differential voltage analysis (dV/dQ vs. Q) for the LCO cells aligned at the bottom of discharge	82
Figure 5.5 The voltage (vs. Li/Li ⁺) as a function of the fraction of available Li for LCO and graphite.	82
Figure 5.6 The differential voltage analysis for the LCO cells aligned at the top of charge.....	84
Figure 5.7 The voltage (vs. Li/Li ⁺) as a function of the fraction of available Li for LCO and graphite.	84
Figure 5.8 The measured and calculated differential voltage analysis for the NMC cell.	86
Figure 6.1 The equivalent circuit model used to fit measured spectra.	92
Figure 6.2 The charge-hold-discharge method used in the work presented in this section.	93
Figure 6.3 The discharge capacity as a function of cycle number for the 4.4 V cells containing a) PP and b) PET, for the 4.45 V cells containing c) PP and d) PET, and for the 4.5 V cells containing e) PP and f) PET as the separator material.....	95
Figure 6.4 The impedance spectra measured at 3.8 V and 20°C every 15 cycles for the cells cycled to 4.4 V.....	97
Figure 6.5 The impedance spectra measured at 3.8 V and 20°C every 15 cycles for the cells cycled to 4.45 V.....	98

Figure 6.6 The impedance spectra measured at 3.8 V and 20°C every 15 cycles for the cells cycled to 4.5 V.....	99
Figure 6.7 Selected impedance spectra and the corresponding fit for a 4.4 V cell containing PP, CB and CC-Al	100
Figure 6.8 Impedance spectra for a full 4.4 V pouch cell containing PP, CB and CC-Al and the resulting symmetric coin cell impedance spectra.....	101
Figure 6.9 Parameters for the resistances a) R_1 , b) R_{ohmic} , c) R_2 , and d) R_3 obtained from fitting the impedance spectra of cells containing CB using an equivalent circuit model.	103
Figure 6.10 Parameters for the resistances a) R_1 , b) R_{ohmic} , c) R_2 , and d) R_3 obtained from fitting the impedance spectra of cells containing CNT using an equivalent circuit model.	103
Figure 6.11 Parameters for the resistance, R_1 , obtained from fitting the impedance spectra of cells containing a) CB and b) CNT using an equivalent circuit model compared to the entire widths of the impedance spectra along the real axis, R_{ct} , for the cells containing c) CB and d) CNT.....	105
Figure 6.12 Parameters for the effective capacitance a) C_1 , b) C_2 , and c) C_3 obtained from fitting the impedance spectra of cells containing CB using an equivalent circuit model.	107
Figure 6.13 Parameters for the effective capacitance a) C_1 , b) C_2 , and c) C_3 obtained from fitting the impedance spectra of cells containing CNT using an equivalent circuit model.	108
Figure 6.14 The volume of gas evolved after a) 135 cycles for the cells cycled to 4.4 V and b) after 70 cycles for the cells cycled to 4.45 and 4.5 V.....	109
Figure 6.15 The experimental protocol over 20 hours a) near the beginning of cycling, b) near the end of cycling for a cell with little capacity fade, and c) near the end of cycling for a cell with severe capacity fade.....	111
Figure 6.16 The experimental protocol over 3 hours a) near the beginning of cycling, b) near the end of cycling for a cell with little capacity fade, and c) near the end of cycling for a cell with severe capacity fade.....	111

Figure 6.17 The normalized fractional discharge capacity as a function of cycle number for the PES222 cells containing a) PP and c) PET, and for the EC-free cells containing b) PP and d) PET as the separator material.	112
Figure 6.18 The impedance spectra measured at 3.8 V and 20°C for the cells filled with PES222 electrolyte.	113
Figure 6.19 The impedance spectra measured at 3.8 V and 20°C for the cells filled with EC-free electrolyte.	114
Figure 6.20 Selected impedance spectra and the corresponding fit for the cell containing EC-free electrolyte, PP, CB and CC-Al.	115
Figure 6.21 Parameters for the resistances a) R_1 , b) R_{ohmic} , c) R_2 , and d) R_3 obtained from fitting the impedance spectra of cells containing CB using an equivalent circuit model.	116
Figure 6.22 Parameters for the resistances a) R_1 , b) R_{ohmic} , c) R_2 , and d) R_3 obtained from fitting the impedance spectra of cells containing CNT using an equivalent circuit model.	117
Figure 6.23 Parameters for the resistance R_1 obtained from fitting the impedance spectra of cells containing a) CB and b) CNT using an equivalent circuit model for the first 300 cycles.	118
Figure 6.24 Parameters for the effective capacitance a) C_1 , b) C_2 , and c) C_3 obtained from fitting the impedance spectra of cells containing CB using an equivalent circuit model.	120
Figure 6.25 Parameters for the effective capacitance a) C_1 , b) C_2 , and c) C_3 obtained from fitting the impedance spectra of cells containing CB using an equivalent circuit model.	121
Figure 6.26 The volume of gas evolved after 90 and 600 cycles.	122
Figure 6.27 Parameters for the resistance R_1 obtained from fitting the impedance spectra of PES222 cells plotted as a function of time	123
Figure 7.1 The discharge capacity as a function of cycle number for Rock/AG cells containing 1M LiPF ₆ EC:EMC and a) 2% VC or b) 2% FEC.	129

Figure 7.2 The impedance spectra as measured by the 4-wire FRA for the Rock/AG cells containing 2% VC with an upper cutoff potential of 4.2 V	130
Figure 7.3 The impedance spectra measured at a) 3.8 V and b) 4.4 V for the Rock/AG cells containing 2% VC with an upper cutoff potential of 4.4 V. Spectra shown were measured during cycle 2, 44, and 86. The spectra measured during cycle 2 and 86 have also been scaled (as indicated in the legend) and plotted for comparison.....	132
Figure 7.4 The combination of charge transfer resistance (both positive and negative electrodes) and resistance due to motion of ions through the SEI layers (both positive and negative electrodes), R_{ct} , as a function of voltage measured every 6 cycles for the Rock/AG cells containing 2% VC or 2% FEC.	134
Figure 7.5 The values of R_{ct} , as a function of cycle number, extracted from the impedance spectra of Rock/AG cells filled with a) 2% VC, b) 2% FEC, and c) EC:EMC:DMC:FEC.....	135
Figure 7.6 The values of the high frequency intercept, as a function of cycle number, extracted from the impedance spectra of Rock/AG cells filled with a) 2% VC, b) 2% FEC, and c) EC:EMC:DMC:FEC	136
Figure 7.7 The high frequency intercept as a function of potential for the charge and discharge segments of cycles 8 and 80 for the Rock/AG cell containing VC cycled to a) 4.1 V, b) 4.2 V, c) 4.3 V, and d) 4.4 V.	137
Figure 7.8 The actual and calculated change in ΔV (obtained using equations 7.1 and 7.2) during the C/5 and C/2.5 cycles for the Rock/AG cells containing 2% VC (top panels) and 2% FEC (bottom panels).	140
Figure 7.9 The actual and calculated change in ΔV (obtained using equations 7.1 and 7.2) during the C/5 and C/2.5 cycles for the Rock/AG cells containing EC:EMC:DMC:FEC.....	140
Figure 7.10 The discharge capacity as a function of time for Rock/AG cells that underwent charge-hold-discharge cycling and charge-discharge cycling	141
Figure 7.11 ΔV as a function of time for Rock/AG cells that underwent charge-hold-discharge cycling and charge-discharge cycling	142
Figure 7.12 The discharge capacity as a function of cycle number for cells cycled to 4.1 V containing a) PES211 or b) VC211, cells cycled to 4.2 V containing c)	

PES211 or d) VC211, and cells cycled to 4.3 or 4.4 V containing e) PES211 or f) VC211.....	144
Figure 7.13 The impedance spectra as measured by the 4-wire FRA for the 622A cells cycled to 4.3 V	145
Figure 7.14 The impedance spectra as measured by the 4-wire FRA for the Rock/NG cells containing PES211	147
Figure 7.15 The values of R_{ct} , as a function of cycle number, extracted from the impedance spectra of (a,d) 622A, (b,e) 622B, and (c,f) Rock/NG cells.....	149
Figure 7.16 The values of the high frequency intercept, as a function of cycle number, extracted from the impedance spectra of (a,d) 622A, (b,e) 622B, and (c,f) Rock/NG cells.....	150
Figure 7.17 The actual and calculated change in ΔV (obtained using equations 7.1 and 7.2) during the C/5 and C/2.5 cycles for the 622A cells.....	152
Figure 7.18 The actual and calculated change in ΔV (obtained using equations 7.1 and 7.2) during the C/5 and C/2.5 cycles for the 622B cells.....	153
Figure 7.19 The actual and calculated change in ΔV (obtained using equations 7.1 and 7.2) during the C/5 and C/2.5 cycles for the Rock/NG cells	154
Figure 7.20 The discharge capacity as a function of time for 622A (a,d), 622B (b,e), and Rock/NG (c,f) cells that underwent charge-hold-discharge cycling and charge-discharge cycling	155
Figure 7.21 ΔV as a function of time for 622A (a,d), 622B (b,e), and Rock/NG (c,f) cells that did charge-hold-discharge cycling and charge-discharge cycling	157
Figure 7.22 The equivalent circuit model used to fit measured spectra.	158
Figure 7.23 Parameters for the resistances (a,b), critical frequencies (c,d), and CPE exponents (e,f) obtained from fitting the impedance spectra using an equivalent circuit model for Rock/AG cells.....	160
Figure 7.24 Parameters for the resistances (a,b), critical frequencies (c,d), and CPE exponents (e,f) obtained from fitting the impedance spectra using an equivalent circuit model for 622A cells containing PES211	164

Figure 7.25 Parameters for the resistances (a,b), critical frequencies (c,d), and CPE exponents (e,f) obtained from fitting the impedance spectra using an equivalent circuit model for 622A cells containing VC211	165
Figure 7.26 Parameters for the resistances (a,b), critical frequencies (c,d), and CPE exponents (e,f) obtained from fitting the impedance spectra using an equivalent circuit model for 622B cells containing PES211	168
Figure 7.27 Parameters for the resistances (a,b), critical frequencies (c,d), and CPE exponents (e,f) obtained from fitting the impedance spectra using an equivalent circuit model for 622B cells containing VC211	169
Figure 7.28 Parameters for the resistances (a,b), critical frequencies (c,d), and CPE exponents (e,f) obtained from fitting the impedance spectra using an equivalent circuit model for Rock/NG cells containing PES211	172
Figure 7.29 The combination of charge transfer resistance (both positive and negative electrodes) and resistance due to motion of ions through the SEI layers (both positive and negative electrodes), R_{ct} , as a function of voltage measured every 6 cycles for the Rock/AG cells containing 2% VC cycled to a) 4.2 V and c) 4.4 V. The parameter, R_1 , obtained from fitting using an equivalent circuit model for the Rock/AG cells containing 2% VC cycled to b) 4.2 V and d) 4.4 V.	174
Figure 7.30 a) The values of the high frequency intercept, as a function of cycle number, extracted from the impedance spectra of Rock/AG cells containing 2% VC cycled to 4.2 or 4.3 V. b) The parameter, R_{ohmic} , obtained from fitting using an equivalent circuit model for the Rock/AG cells containing 2% VC	175
Figure 8.1 R_{ct} plotted as a function of voltage for selected cycles for a) an uncoated NMC442 cell with EC:EMC based electrolyte to 4.4 V, b) a coated NMC442 cell with EC:EMC based electrolyte to 4.45 V, and c) an uncoated NMC442 cell with FEC:TFEC based electrolyte to 4.5 V.	180
Figure 9.1 The equivalent circuit model used to fit measured spectra.	198
Figure 9.2 The Nyquist representation (top panels), imaginary Bode representation (middle panels), and real Bode representation (bottom panels) for the impedance of positive and negative symmetric cells made from the control pouch cells at 4.2 V, after storage at 60°C.	200
Figure 9.3 The impedance spectra measured at 4.2 V and 20°C for the control pouch cells after storage at 60°C and 4.2 V.	201

Figure 9.4 The Nyquist representation (top panels), imaginary Bode representation (middle panels), and real Bode representation (bottom panels) for the impedance of positive and negative symmetric cells made from the 2% VC pouch cells at 4.2 V, after storage at 60°C.	203
Figure 9.5 The impedance spectra measured at 4.2 V and 20°C for the 2% VC pouch cells after storage at 60°C and 4.2 V.	204
Figure 9.6 Selected impedance spectra and the corresponding fit for the control cells measured after 0 and 21 days in storage at 60°C and 4.2 V	205
Figure 9.7 Parameters for the resistances a) R_1 , b) R_2 , and c) R_3 obtained from fitting, using an equivalent circuit model, the positive and negative symmetric cell impedance spectra from the control cells as a function of storage time at 60°C. Similarly, parameters for the resistances d) R_1 , e) R_2 , and f) R_3 from the 2% VC cells.	207
Figure 9.8 The sum of the resistances R_1 , R_2 , and R_3 , obtained from fitting using an equivalent circuit model, for the positive and negative symmetric cell impedance spectra from the a) 2% VC cells and b) control cells as a function of storage time at 60°C.	207
Figure 9.9 The Nyquist representation (top panels), imaginary Bode representation (middle panels), and real Bode representation (bottom panels) for the impedance of positive and negative symmetric cells made from the PES222 pouch cells at 4.2 V, after storage at 60°C.	209
Figure 9.10 The Nyquist (top panels), imaginary Bode (middle panels), and real Bode (bottom panels) representation for the impedance of positive and negative symmetric cells made from the first batch of PES222 pouch cells at 4.4 V, after storage at 60°C.....	211
Figure 9.11 The Nyquist (top panels), imaginary Bode (middle panels), and real Bode (bottom panels) representation for the impedance of positive and negative symmetric cells made from the second batch of PES222 pouch cells at 4.4 V, after storage at 60°C.....	212
Figure 9.12 The sum of the resistances R_1 , R_2 , and R_3 , obtained from fitting using an equivalent circuit model, for the positive and negative symmetric cell impedance spectra from the PES222 cells	215
Figure 9.13 The sum of the total resistances (shown in Figure 9.12b and Figure 9.12c) of the positive and negative symmetric cells as a function of storage time	216

ABSTRACT

Lithium-ion batteries play an important role in the transition away from non-renewable sources of energy. Technologies such as electric vehicles and grid energy storage require longer-lasting batteries with higher energy density and lower cost. Although increasing the upper cutoff potential of lithium-ion batteries would lead to higher capacity and higher energy density, achieving long-lasting high potential operation in lithium-ion cells is difficult.

Impedance growth is one obstacle to high potential $\text{Li}[\text{Ni}_{1-x-y}\text{Mn}_x\text{Co}_y]\text{O}_2$ lithium ion cells and is a large contributor to capacity fade and cell failure at high potential. Electrochemical impedance spectroscopy measurements are quick and non-destructive to the cell and can illuminate the processes occurring in lithium ion cells as a function of time, cycle number, and potential. The importance of performing these measurements during cycling, particularly during experiments that are representative of real-life lithium ion cell use, is demonstrated. The fitting of impedance spectra using equivalent circuit models is required to quantitatively study the processes occurring in lithium ion cells at various potentials. The effects of extended periods of time at high potential will be investigated. Furthermore, the effects that various cell components, electrode coatings, electrolyte solvents, and electrolyte additives have on lithium ion cells will be probed.

LIST OF ABBREVIATIONS AND SYMBOLS USED

AC	alternating current
AFM	atomic force microscopy
AG	artificial graphite
Al	aluminum foil
BMF	polypropylene blown microfiber
CB	carbon black
CC-Al	carbon-coated Al foil
CCCV	constant current constant voltage
CEI	cathode-electrolyte interphase
CMC	carboxymethyl cellulose
CNT	carbon nanotubes
CPE	constant phase elements
DEC	diethyl carbonate
DMC	dimethyl carbonate
DOL	1,3-dioxolane
DTD	1,3,2-dioxathiolane-2,2-dioxide
EC	ethylene carbonate
EDX	energy dispersive X-ray spectroscopy
EELS	electron energy loss spectroscopy
EIS	electrochemical impedance spectroscopy
EMC	ethyl methyl carbonate
FEC	fluoroethylene carbonate
FRA	frequency response analyzer
GC-MS	gas chromatography-mass spectrometry
HFI	high frequency intercept
LCO	LiCoO_2
LEDC	lithium ethylene dicarbonate
LiBF_4	lithium tetrafluoroborate
LiFSI	lithium bis(fluorosulfonyl)imide
LiPF_6	lithium hexafluorophosphate
LiTFSI	lithium bis(trifluoromethylsulfonyl)imide
LMC	lithium methyl carbonate
MMDS	methylene methane disulfonate
NCA	$\text{Li}[\text{Ni}_x\text{Co}_y\text{Al}_{1-x-y}]\text{O}_2$
NG	natural graphite
NMC	$\text{Li}[\text{Ni}_{1-x-y}\text{Mn}_x\text{Co}_y]\text{O}_2$
NMC111	$\text{Li}[\text{Ni}_{0.33}\text{Mn}_{0.33}\text{Co}_{0.33}]\text{O}_2$

NMC442	Li[Ni _{0.4} Mn _{0.4} Co _{0.2}]O ₂
NMC532	Li[Ni _{0.5} Mn _{0.3} Co _{0.2}]O ₂
NMC622	Li[Ni _{0.6} Mn _{0.2} Co _{0.2}]O ₂
NMC811	Li[Ni _{0.8} Mn _{0.1} Co _{0.1}]O ₂
NMR	nuclear magnetic resonance spectroscopy
PC	propylene carbonate
PES	prop-1-ene-1,3-sultone
PES211	1M LiPF ₆ in EC:EMC:PES:DTD:TTSPi 29:67:2:1:1
PES222	1M LiPF ₆ in EC:EMC:PES:DTD:TTSPi 28:66:2:2:2
PET	polyethylene terephthalate
PP	polypropylene
PPF	pyridine phosphorus pentafluoride
PVDF	polyvinylidene fluoride
RC	parallel resistor and capacitor circuit
R _{ct}	combination of charge transfer resistances (both positive and negative electrodes) and the resistance due to the motion of ions through the SEI layers (both positive and negative electrodes)
SBR	styrene-butadiene rubber
SEI	solid electrolyte interphase
SEM	scanning electron microscopy
STEM	scanning transmission electron microscopy
TAP	triallyl phosphate
TEM	transmission electron microscopy
TFEC	bis (2,2,2-trifluoroethyl) carbonate
TG-DTA/MS	thermogravimetric-differential thermal analysis with mass spectrometry
TOC	top of charge
TTSP	tris(-trimethyl-silyl)-phosphate
TTSPi	tris(-trimethyl-silyl)-phosphite
VC	vinylene carbonate
VC211	1M LiPF ₆ in EC:EMC:VC:MMDS:TTSPi 29:67:2:1:1
XAS	X-ray absorption spectroscopy
XPS	X-ray photoemission spectroscopy
TOF-SIMS	time-of-flight secondary-ion mass spectrometry
C	capacitance, further denoted by subscript
f	frequency
i	imaginary unit, $\sqrt{-1}$
L	inductance, further denoted by subscript

m	mass
ρ	density
R	Resistance, further denoted by subscript
t	time
V	cell voltage, further denoted by subscript
v	volume
W	Warburg diffusion, further denoted by subscript
ω	angular frequency, further denoted by subscript
Z	impedance, further denoted by subscript

ACKNOWLEDGEMENTS

I would like to thank the NSERC CREATE DREAMS program, Nova Scotia Graduate Scholarship, Walter C. Sumner Fellowship, and NSERC PGS D, along with 3M and Tesla Motors for their partial funding of this work.

I would like to thank my supervisor, Dr. Jeff Dahn, to whom I am grateful to have had the opportunity to learn from his wealth of experience. His support, enthusiasm, and motivation has been invaluable during the past five years. I would like to thank my current and former committee members, Dr. Mark Obrovac, Dr. Ian Hill, and Dr. Jesse Maassen, for their guidance. I would like to thank Tanya Timmins, Heather Ann Jennex and the rest of the departmental staff for their help.

I would like to thank all the members of the Dahn lab, both past and present, that I have interacted with for their support, encouragement, and teamwork. I thank Robbie Sanderson for his patience and expertise, and for answering my countless questions. I am particularly thankful for Rebecca Tingley and Samuel Buteau whose hard work has been showcased in this thesis.

Lastly, I am eternally grateful for my friends and family. I thank my parents for their everlasting love, encouragement, and support, and for being such admirable role models for me in all aspects of their life. I thank my siblings for being incredible people, and for their companionship and silliness. I thank Patrick for his love and support, and for keeping me fed and happy throughout the writing of this thesis.

CHAPTER 1. INTRODUCTION

1.1 MOTIVATION

Lithium-ion (Li-ion) batteries are used in phones, laptop computers, medical devices and, more recently, electric vehicles and grid energy storage. Li-ion batteries play an important role in the transition away from non-renewable sources of energy. Although the lifetime and cost of Li-ion batteries is adequate for short-term-use electronics, technologies such as electric vehicles and grid energy storage require longer-lasting and cheaper batteries with higher energy density. By improving the energy density of Li-ion cells, fewer cells would be needed to provide similar energy and lifetime thereby dramatically reducing the overall cost.

In 2016 in Canada, Nissan sold 1375 Leafs (fully electric vehicles), 1.13% of the total vehicle sales for the year.¹ In 2016 in Canada, Chevrolet sold 3469 Volts (plug-in hybrid vehicles), making up 2.29% of the total vehicle sales for the year.² The extremely low percentage of electric vehicles sold compared to gasoline powered vehicles made by the same company is evidence that consumers are reluctant to purchase electric vehicles. While high cost remains the predominant factor dissuading consumers, other factors include low driving range from a single charge and inconvenient battery charging.³ However, lower cost fully electric vehicles will likely win over consumers. For example, the Tesla Model 3, a fully electric vehicle retailed at \$35,000 USD before rebates, had 325,000 reservations within one week of being announced.⁴ Improving the energy density

of Li-ion cells could help lower the cost and improve the driving range of electric vehicles.

Figure 1.1 shows the voltage-capacity curve for a typical Li-ion positive electrode material, $\text{Li}[\text{Ni}_{0.6}\text{Mn}_{0.2}\text{Co}_{0.2}]\text{O}_2$ (NMC622) vs. Li/Li^+ . Commercial Li-ion cells containing NMC622 are often used up to potentials of 4.2-4.4 V, indicated by the blue line labelled 'current'. The advantage of increasing the upper cutoff potential, indicated by the blue line labelled 'ideal', is the subsequent increase in cell capacity, and thus energy density.

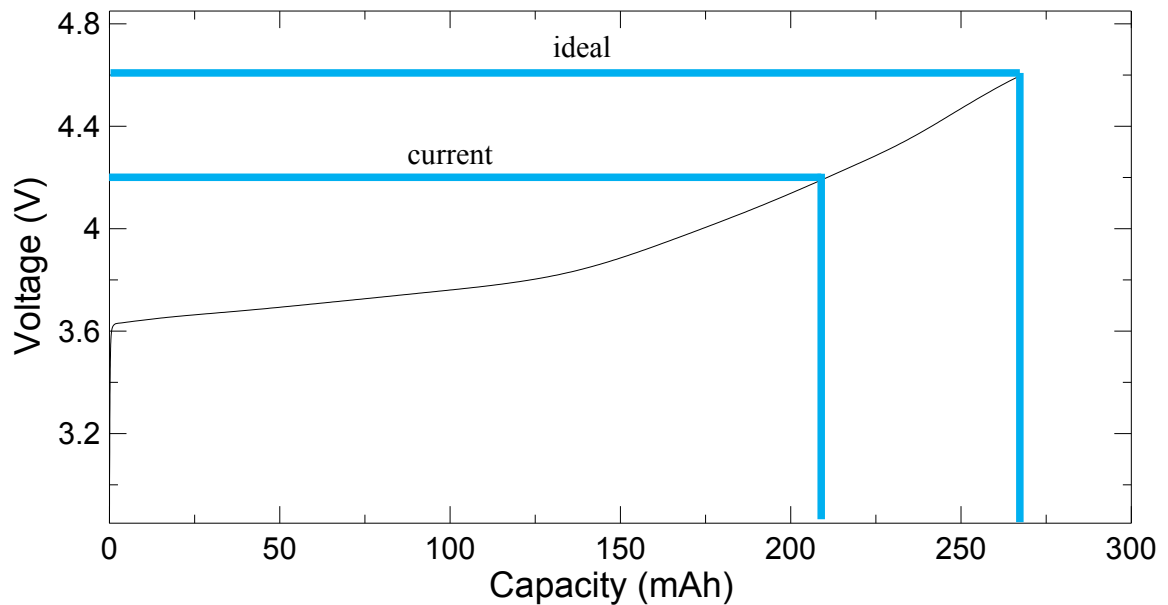


Figure 1.1 A voltage-capacity curve for NMC622 vs Li/Li^+ . The 'current' line indicates the potential to which commercial Li-ion cells are used. The 'ideal' line indicates the increase in capacity that would result from an increase in potential.

Unfortunately, achieving long-lasting high potential operation in Li-ion cells is difficult. Although increasing the working potential of the positive electrode would provide a significant increase in specific capacity, doing so comes with several problems not

limited to, but including, gas evolution,^{5,6} electrolyte dry-out, increased parasitic reactions,⁷ thick layers on the electrodes,^{8,9} thin layers on the electrodes that are unable to effectively protect the active material,⁸ severe capacity fade,¹⁰ and roll-over cell failure.¹¹ Increasing the potential of Li-ion cells is an important and difficult hurdle for the battery community to overcome, but will yield significant improvements and advantages if successful.

1.2 LITHIUM-ION BATTERIES

Li-ion batteries work via intercalation, a process in which Li ions are inserted into or removed from the interstitial space of the positive and negative electrodes in a reversible manner. Figure 1.2 shows a simplified schematic of a Li-ion cell in a discharged state, consisting of a positive and negative electrode separated by an electronically insulating porous membrane. In Figure 1.2 the negative electrode is graphite and the positive electrode is a lithiated transition metal oxide. These are both layered materials, allowing the Li-ions to be reversibly inserted or removed from the interstitial space between the atomic layers in the active material, without causing a significant change in the structure of the host material.¹² Typical layered positive electrodes include LiCoO_2 (LCO), in which the entire transition metal layer is made up of cobalt, or $\text{Li}[\text{Ni}_{1-x-y}\text{Mn}_x\text{Co}_y]\text{O}_2$ (NMC) in which the transition metal layer is made up of nickel, manganese, and cobalt. The arrows in Figure 1.2 indicate the flow of the electrons and ions when a current is applied to the cell during charge. Lithium ions de-intercalate into the electrolyte from the positive electrode and intercalate into the negative electrode during charge and electrons

travel from the positive electrode to the negative electrode through an external circuit. The reverse occurs during discharge as the thermodynamically favoured reactions occur.

A liquid electrolyte, typically a lithium salt dissolved in one or more organic solvents, soaks the separator and wets the electrodes to achieve good ionic conductivity.

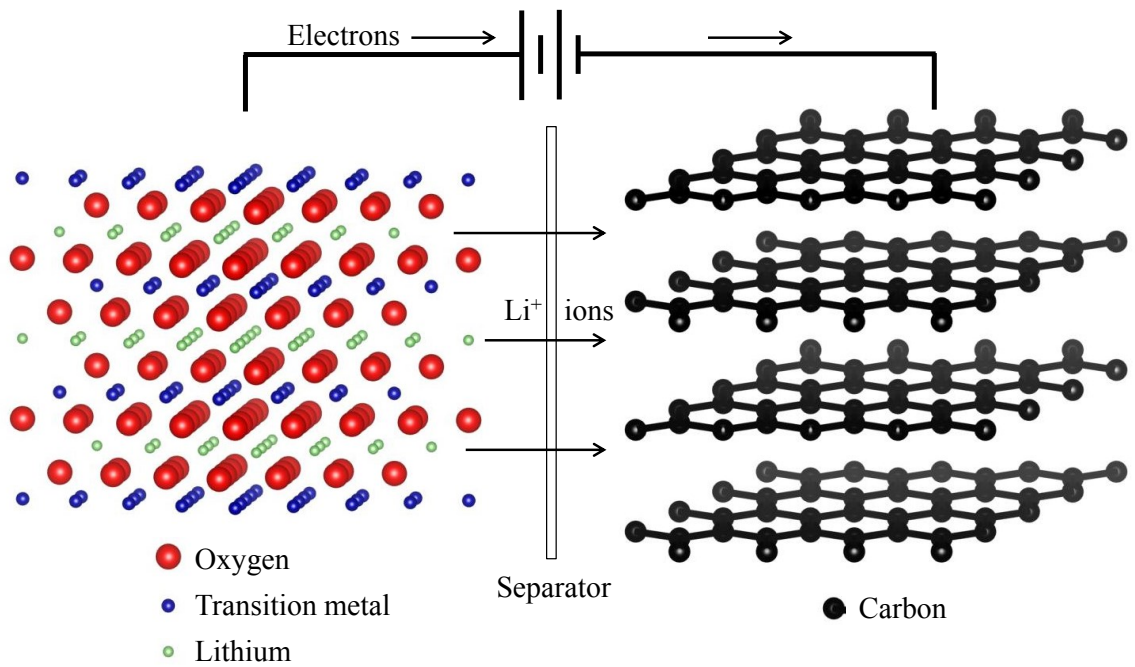


Figure 1.2 Schematic of a Li-ion cell with a graphite negative electrode (right) and a lithium transition metal oxide positive electrode (left). The arrow indicates the direction of the flow of electrons and Li⁺ ions during charge. Adapted, with permission, from K. Nelson, M.Sc thesis.¹³

1.2.1 POSITIVE ELECTRODE

The positive electrode active material is typically blended with a conductive additive, such as carbon black, and a polymeric binder, such as polyvinylidene fluoride (PVDF). This ensures good electronic conductivity, good adhesion to the current collector, and

good mechanical strength. Thin aluminum foil is used as the current collector for the positive electrode due to its low cost and electrochemical stability.

LCO, a layered structure, has good electrochemical performance and is widely used in consumer electronic devices. Cobalt is an expensive material (\$39.70 USD/kg, average over last 12 months)¹⁴ and thus increases the cost of the cell. Substituting nickel (\$9.90 USD/kg, average over last 12 months)¹⁵ and manganese (\$3.97 USD/kg, average over last 12 months)¹⁶ for cobalt in LCO reduces the cost of the material and imparts improved performance and safety, enhances the ability to achieve higher potential, and thus higher energy density.¹⁷ $\text{Li}[\text{Ni}_x\text{Mn}_x\text{Co}_{1-2x}]\text{O}_2$ was first proposed by Lu et al.¹⁸ Various forms of NMC including $\text{Li}[\text{Ni}_{0.33}\text{Mn}_{0.33}\text{Co}_{0.33}]\text{O}_2$ (NMC111) and $\text{Li}[\text{Ni}_{0.4}\text{Mn}_{0.4}\text{Co}_{0.2}]\text{O}_2$ (NMC442) have been used to maximize lifetime and performance while minimizing cost. Li-ion cells containing NMC442 will be the main, but not exclusive, focus of the work presented in this thesis.

There are several other positive electrode materials that have been developed for Li-ion cells. Another layered positive electrode is $\text{Li}[\text{Ni}_x\text{Co}_y\text{Al}_{1-x-y}]\text{O}_2$ (NCA), where x is typically 0.8 and y is typically 0.15. NCA provides good storage calendar life,¹⁹ but has high impedance during cycling leading to capacity loss.²⁰ LiMn_2O_4 , a spinel structure, has low cost but also low capacity.¹² LiFePO_4 , an olivine structure, has good safety properties but low energy density.¹²

As indicated in Figure 1.1, the potential of positive electrodes used in consumer electronic devices is typically at or below 4.4 V vs Li/Li^+ . This is to enhance the capacity

and lifetime while preventing continuous electrolyte oxidation. Positive electrode materials suitable for high potential operation is an active area of research.

Surface coatings on the positive electrode materials have been designed in attempt to improve performance, and will be discussed in Chapter 2.

1.2.2 NEGATIVE ELECTRODE

The negative electrode active material is typically blended with a conductive additive, such as carbon black, and a polymeric binder, such as styrene-butadiene rubber (SBR) and carboxymethyl cellulose (CMC). This ensures good electronic conductivity, good adhesion to the current collector, and good mechanical strength. Thin copper foil is used as the current collector for the negative electrode due to its electrochemical stability.

In the first commercialized Li-ion battery, Sony initially employed petroleum coke as a negative electrode material.¹² Lithium metal has also been used for negative electrodes, as it has high capacity, but it also has several safety issues.¹² Therefore, the negative electrode of a Li-ion cell is typically graphite. Graphite has a theoretical capacity of 372 mAh/g,²¹ which is significantly lower than the theoretical capacity of some alloys used as negative electrode materials. Alloys can achieve higher capacity, and therefore better energy density, but often at the expense of other problems. For example, silicon has a high theoretical capacity of 3579 mAh/g²² in $\text{Li}_{15}\text{Si}_4$ but exhibits a severe volume expansion of 280%,²³ which can lead to electrode damage,²⁴ loss of electronic contact,^{25–}²⁷ high irreversible capacity loss during the first cycle,^{24,28} and poor cell lifetime.^{24,29}

1.2.3 SEPARATOR

A thin porous material is used as a separator to mechanically separate the positive and negative electrode, avoiding an internal short, but is permeable to the electrolyte, maintaining ionic conductivity. Separators are typically a polypropylene and/or polyethylene material, used for their chemical stability, suitable porous structure allowing for good Li-ion transport and good performance at high temperature.¹²

Different separator materials and configurations have been designed to improve cell performance and cell safety. For example, layered separators have been used to prevent thermal runaway in the event of a short circuit. This type of separator consists of a layer of polypropylene (melting point of 165°C), then a layer of polyethylene (melting point of 135°C), and another layer of polypropylene.¹² During a short circuit the polyethylene layer would melt, but remain in place due to the polypropylene separators, and prevent Li ions from transferring between the two electrodes, thereby preventing thermal runaway.¹² Ceramic-coated polyethylene separators have been used to achieve better thermal stability and improved capacity retention compared to polyethylene separators without the coating.³⁰ Polyethylene terephthalate separators have been investigated due to its good thermal stability, high tensile strength, and high discharge capacity in cells.³¹

1.2.4 ELECTROLYTE SYSTEMS

An electrolyte, typically liquid, is necessary to facilitate the transfer of charge between the positive and negative electrodes. The electrolyte consists of a lithiated salt dissolved in a mixture of solvents. Commonly used salts in Li-ion cells include lithium

hexafluorophosphate (LiPF_6), lithium bis(trifluoromethylsulfonyl)imide ($\text{LiN}[\text{CF}_3\text{SO}_2]_2$ or LiTFSI), lithium bis(fluorosulfonyl)imide (LiFSI), and lithium tetrafluoroborate (LiBF_4). LiPO_2F_2 is a salt that has recently been used in Li-ion cells.^{32,33} Figure 1.3 shows the chemical structures of these salts. LiPF_6 is the most commonly used salt with carbonate solvents and is highly conducting.³⁴ LiTFSI has high conductivity and thermal stability, but is also expensive and can corrode aluminum current collectors.³⁴ LiTFSI can be used in small concentrations as an additive, instead of as a salt, in order to take advantage of its highly conductive properties while minimizing cost and corrosion. However, some researchers have found good performance of cells containing super-concentrated electrolytes with up to 21M LiTFSI .^{35,36} LiFSI has similar conductivity to LiPF_6 and better thermal stability.³⁴ LiBF_4 has moderate conductivity, high thermal stability and good safety properties,³⁷ but leads to poor performance in cells operated to high potential, most likely due to high impedance at the negative electrode.³⁸

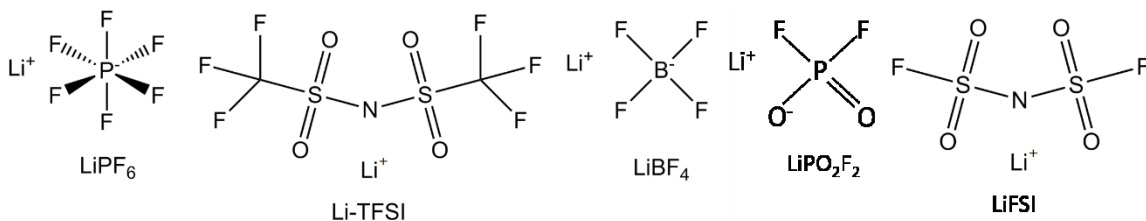


Figure 1.3 The chemical structures of commonly used salts for electrolytes in Li-ion cells.

Carbonate solvents are the most commonly, but not exclusively, used solvents in Li-ion cells. They are attractive due to their high dielectric constant and ability to dissolve high concentrations of Li salts.³⁷ Common carbonate solvents include ethylene carbonate

(EC), ethyl methyl carbonate (EMC), diethyl carbonate (DEC), dimethyl carbonate (DMC) and propylene carbonate (PC). PC was originally used as a solvent due to its high dielectric constant, but can cause degradation in graphitic electrodes leading to capacity fade, lithium plating and poor cycling.³⁹ EC is a similar molecule to PC, but is able to form an effective passivating film on the negative electrode which helps to prevent electrolyte decomposition.³⁹ EC results in low capacity fade and low irreversible capacity but is solid at room temperature.³⁷ By combining EC with other solvents, such as EMC or DEC, the freezing point of the electrolyte is reduced while maintaining the beneficial properties of EC. For these reasons EC:EMC is a common and useful solvent mixture and will be used in much of the work presented in this thesis.

More recently, fluorinated carbonates have been suggested to have superior anodic stability to EC and EMC, among other advantages.⁴⁰ In particular, Xia et al. have shown that when charged to 4.5 V, NMC442/graphite cells containing fluoroethylene carbonate (FEC) mixed with bis (2,2,2-trifluoroethyl) carbonate (TFEC) and the additive prop-1-ene-sultone (PES) outperformed all cells studied with non-fluorinated electrolytes.⁴¹ While the impedance from the positive electrode was found to be small, Xia et al. found that the impedance coming from the negative electrode in the FEC:TFEC containing cells was high compared to that in the EC:EMC containing cells. Figure 1.4 shows the chemical structures of the aforementioned electrolyte solvents.

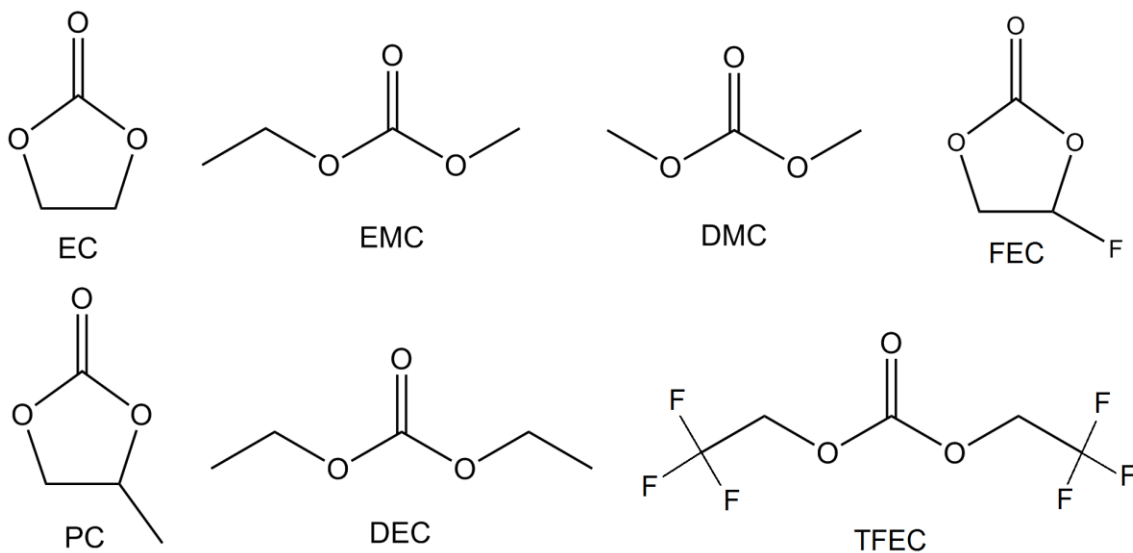


Figure 1.4 The chemical structures of commonly used electrolyte solvents.

1.2.5 ELECTROLYTE ADDITIVES

Electrolyte additives play a crucial role in the success of Li-ion batteries in modern applications. Electrolyte additives, chemicals present in the electrolyte typically up to five weight percent, can improve the lifetime,^{42,43} reduce the capacity loss,^{43,44} enhance the safety,^{43,45,46} decrease the flammability,⁴⁷ effect the temperature range,⁴⁸ and increase the usable voltage range^{11,49,50} achieved by Li-ion cells. The benefit of additives is most powerfully illustrated by Burns et al., who showed that the lifetime of LCO cells could be increased by up to 20 times when the electrolyte contained additives when compared to cells without additives.⁴²

It has been shown that cells containing a combination of additives have superior performance to those containing a single additive.^{42,51,52} Ma et al. studied cells containing a combination of vinylene carbonate (VC), a sulfur-containing additive (methylene

methane disulfonate [MMDS] or 1,3,2-dioxathiolane-2,2-dioxide [DTD]), and tris(-trimethyl-silyl)-phosphate (TTSP), and/or tris(-trimethyl-silyl)-phosphite (TTSPi).⁴³ Ma et al. determined that the ternary and quaternary additive mixtures improved the cycling performance and safety while reducing the impedance when compared to cells containing VC alone.⁴³ Although VC is perhaps the most famous and widely used additive, it is ineffective when used in cells operated to potentials above 4.2 V.⁵³ The superiority of PES over VC when used in NMC442/graphite pouch cells has been shown by Xia et al.⁵⁴ and Nelson et al.,⁴⁴ particularly with respect to gas reduction and performance at high potential. Although MMDS has been shown to reduce electrolyte oxidation and impedance at the positive electrode when used in NMC442/graphite pouch cells and reduce the volume of gas produced,^{49,55} DTD has been shown to have superior performance in NMC442/graphite pouch cells when in combination with other additives,⁴³ particularly when subjected to extended periods of time at high potential.¹⁰ DTD has been shown to function as a film-forming additive for the solid electrolyte interphase on the negative electrode in NMC/graphite pouch cells.^{56,57} TTSPi has been shown to have superior performance to TTSP, as it reduced impedance, reduced charge end point capacity slippage and improved the coulombic efficiency of NMC/graphite Li-ion cells, particularly when in combination with other additives.⁵⁸ NMC/graphite Li-ion cells containing PES, DTD, and TTSPi will be the main focus of the work presented in this thesis. The importance of electrolyte additives will be further discussed in Chapter 2.

Hundreds of additives have been studied and used to improve various aspects of Li-ion cells. Fifty such additives have been tabulated by Nelson,¹³ including the chemical

structure and primary function of each additive in Li-ion cells. Figure 1.5 shows the chemical structures of the aforementioned electrolyte additives. Despite the extensive study of electrolyte additives for Li-ion cells, their fate and function are often not understood.

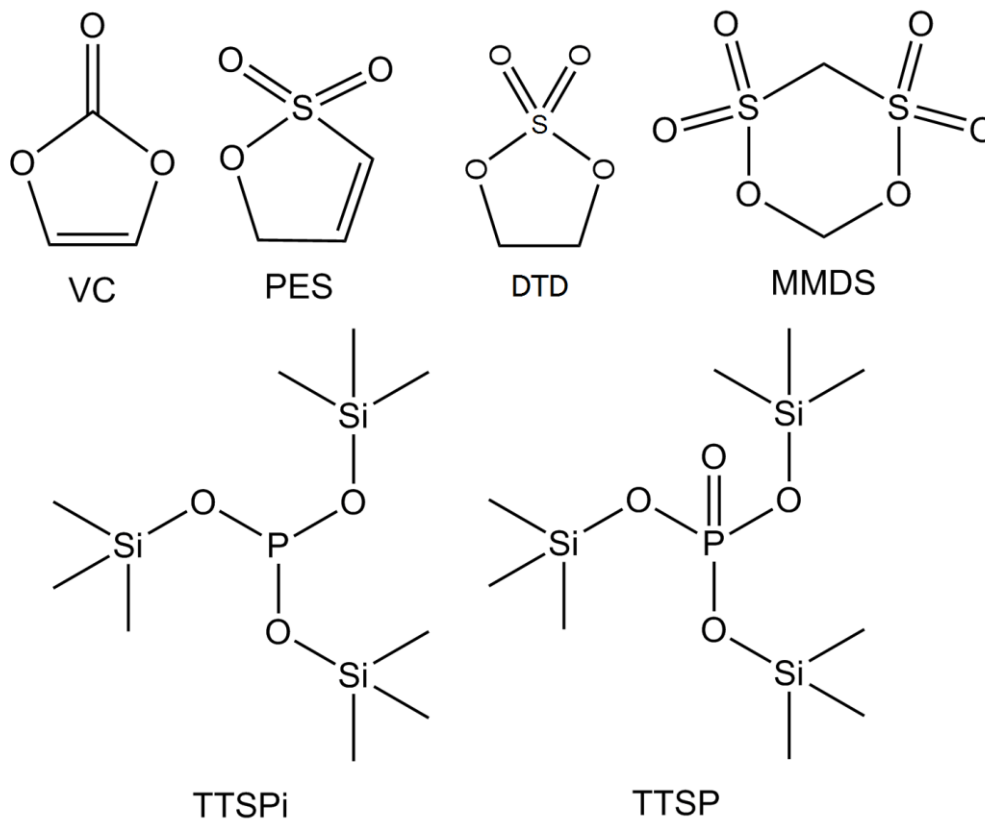


Figure 1.5 The chemical structures of the electrolyte additives discussed previously.

1.3 THESIS OUTLINE

Chapter 2 of this thesis discusses the role of electrolyte additives and their influence on the solid electrolyte interphase present on both the positive and negative electrodes.

Chapter 3 gives a description of the experimental methods used throughout this work and emphasizes the importance of experiments that are representative of real-life Li-ion cell usage. Chapter 3 will present equivalent circuit models used in the literature to represent the solid electrolyte interphase layers.

Chapter 4 presents the effect of positive electrode coatings and electrolyte additives on the performance of Li-ion cells operated to high potential. An analysis of impedance spectra will show the usefulness of symmetric cells.

Chapter 5 presents a comparison of commercial Li-ion cells to in-house Li-ion cells. Differential voltage analysis will provide insight to the failure of commercial Li-ion cells.

Chapter 6 presents the effects of various cell components on the performance and impedance of Li-ion cells under a variety of experimental conditions. An equivalent circuit model used to fit measured impedance spectra will be introduced.

Chapter 7 presents a comparison of different types of NMC/graphite pouch cells and electrolyte systems and their effect on impedance growth. An equivalent circuit model is used to fit impedance spectra.

Chapter 8 investigates the phenomenon of both reversible and irreversible impedance growth. A literature review will be presented to characterize impedance growth.

Chapter 9 presents results investigating the effect of electrolyte additives on impedance growth at both the positive and negative electrode during high temperature storage.

Analysis of impedance spectra, including analysis of fitting parameters obtained from equivalent circuit modeling, are discussed.

Chapter 10 summarizes the work presented in this thesis and concludes by outlining future work to advance the understanding of the effect of high potential operation on the impedance of lithium-ion cells.

The work presented in this thesis is a continuation of the work presented and experimental techniques explored in the M.Sc. thesis by Nelson.¹³ Some of the results presented in this thesis were previously published in peer-reviewed journals, including:

- K. J. Nelson, D. W. Abarbanel, J. Xia, Z. Lu, and J. R. Dahn, *J. Electrochem. Soc.*, **163**, A272–A280 (2016).

CHAPTER 2. SOLID ELECTROLYTE INTERPHASES AND THE ROLE OF ELECTROLYTE ADDITIVES

Lithium-ion (Li-ion) cells have finite lifetimes due to parasitic reactions that occur within the cell, consuming electrolyte, active material, and rendering some lithium trapped and/or electrochemically inactive. Despite the instability of the charged electrodes in contact with the electrolyte, Li-ion cells are able to function due to passive layers that form on both the positive and negative electrodes. These layers, called solid electrolyte interphases (SEI) by Peled,⁵⁹ can prevent parasitic reactions and enable the successful function of Li-ion cells. Unfortunately, these SEI layers which are initially helpful can also hinder the performance and lifetime of Li-ion cells. The SEI layers on the positive and negative electrodes can have different compositions and also behave very differently.

2.1 SEI AT THE NEGATIVE ELECTRODE

The SEI layer on the negative electrode has garnered significant interest from the battery community. During the first charge of a Li-ion cell, a passivating film forms from the reaction of the electrolyte, particularly the electrolyte solvent, with the negative electrode. This passivating film, called the SEI, is an ionic conductor and electronic insulator. It has been proposed that the SEI layer consists of dense Li-containing inorganic compounds at the surface of the negative electrode and porous organic compounds, some of which contain lithium,^{60,61} close to the electrolyte interface.⁶²⁻⁶⁵ This SEI layer hinders further electrolyte degradation and decomposition, therefore slowing the consumption of lithium. The formation of the SEI layer can therefore enable good cycle life and cell performance.

Following the first charge of the cell, the SEI continues to grow. At fixed temperatures, the negative electrode SEI thickness continues to grow at a rate approximately proportional to $t^{-1/2}$, where t is the time since the beginning of cycling.^{66,67} SEI growth results in irreversible capacity loss due to trapped Li. The growth rate of the SEI can be altered at high temperatures,⁶⁶ where the rate of parasitic reactions may increase, and at “extreme” voltages (high or low potential), where the rate of parasitic reactions may also increase. An ideal SEI layer prevents capacity loss and electrolyte consumption by preventing parasitic reactions while remaining passive.

Peled et al. introduced an “advanced model” of the SEI on lithium and graphite negative electrodes in 1997.⁶² They described the SEI structure as a mixture of insoluble products on the negative electrode that results from reactions between reduced species and the bulk electrolyte. Peled et al. thought that the order in which electrolyte components were reduced on the negative electrode dictated where certain species were located within the SEI.⁶² These species included inorganic compounds such as lithium oxide (Li_2O), lithium fluoride (LiF), and lithium carbonate (Li_2CO_3) in addition to semicarbonates and polyolefins.⁶²

There has been substantial research aiming to characterize the SEI and study the composition under a variety of conditions.^{60,61,68–70} Although several models of the SEI have been proposed, some of which will be discussed in Chapter 3, it has been difficult to analyze and characterize the SEI, due to its size and sensitivity to water and oxygen.^{65,71} It is difficult to determine the composition of the SEI layer, particularly how the

composition changes with time and voltage. There has been controversy over the components of the negative electrode SEI. For example, the presence of Li_2CO_3 is debated among researchers.

Ganesh et al. performed ab initio molecular dynamics simulations of the graphite negative electrode SEI, in the presence of ethylene carbonate (EC), to learn about electrolyte reduction.⁶³ They determined that cyclic carbonates are reduced on the graphite negative electrode and that Li_2CO_3 is a vital, stable component of the SEI that should be expected near the electrode surface in the SEI. As lithium hexafluorophosphate (LiPF_6) in the electrolyte decomposed, LiF formed on the graphite negative electrode surface.⁶³ Ganesh et al. determined that the surface of the electrode and the presence of LiPF_6 in the electrolyte had a strong impact on the type of species that were reduced on the electrode surface.⁶³ They determined that inorganic species remained close to the graphite electrode surface while organic species were closer to the electrolyte. Shi et al. used a computational study to show that Li_2CO_3 was one of the main stable negative electrode SEI components.⁷²

Zhao et al. detected Li_2CO_3 in the SEI layer on natural graphite in the presence of EC and dimethyl carbonate (DMC) using thermogravimetric-differential thermal analysis combined with mass spectrometry (TG-DTA/MS) and X-ray photoemission spectroscopy (XPS), but only in Li/graphite cells cycled for 50 cycles and longer.⁷³ Li_2CO_3 was not present in the negative electrode SEI for cells undergoing short-term cycling. Zhao et al. also determined that the observed graphite XPS peak faded with increasing cycle number,

confirming their hypothesis that the negative electrode SEI became thicker as the cycle number increased.⁷³ They found that the main components in the negative electrode SEI were lithium oxalate, lithium alkyl carbonate, hydrocarbons, oxygen-containing polymeric species, and, after prolonged cycling, Li_2CO_3 .⁷³ They observed that, in EC:DMC based electrolyte, EC and DMC were reduced and decomposed to form lithium ethylene dicarbonate (LEDC) and lithium methyl carbonate (LMC), respectively.^{73,74}

Alternatively, Edström et al. suggested that the presence of Li_2CO_3 observed by other researchers was an artifact.⁶⁵ Li_2O could form from trace amounts of water in Li-ion cells and then react with CO_2 to form Li_2CO_3 . Edström et al. studied Li/graphite cells with LiPF_6 in EC and diethyl carbonate (DEC) and only detected Li_2CO_3 in the negative electrode SEI when the sample was exposed to ambient atmosphere.⁶⁵ Harilal et al. agreed with Edström et al. as they observed Li_2CO_3 in the negative electrode SEI only in samples that had been exposed to air, thus allowing oxygen contaminants to react with Li to form carbonate-containing compounds.⁷⁵

The presence of other components of the negative SEI, such as LEDC and polymeric species, have also been debated by researchers. Nie et al. used binder-free graphite electrodes to study the composition of the negative electrode SEI using transmission electron microscopy (TEM) with energy dispersive X-ray spectroscopy (EDX) and nuclear magnetic resonance (NMR) spectroscopy.⁶⁰ They determined that, in the presence of LiPF_6 in EC, the SEI was mainly composed of LEDC, from the reduction of EC, and LiF. They determined that, in the presence of LiPF_6 in ethyl methyl carbonate (EMC) or

EC:EMC, the SEI was mainly composed of LEDC, LiF, and low concentrations of LMC.⁶⁰ In both cases, these components were found throughout the SEI layer, in disagreement with previous work that suggested that the SEI consisted of a layer of dense inorganic compounds on the surface of the graphite and a layer of porous organic compounds close to the electrolyte. Nie et al. determined that the SEI was thicker in the presence of EC:EMC compared to without EC.⁶⁰ In this study, Nie et al. did not detect Li_2CO_3 as an SEI component, nor did they detect polymeric species.⁶⁰ However, they only analyzed the SEI composition between the first and fifth cycles. It is possible that polymeric species and Li_2CO_3 form during subsequent cycles, similar to the findings by Zhao et al.⁷³

In another experiment, however, Nie and Lucht⁶¹ detected low concentrations of Li_2CO_3 , in addition to LEDC, in the negative electrode SEI, which is inconsistent with their previous findings. Nie and Lucht studied the SEI formed by electrolyte containing EC and various salts, including LiPF_6 , LiBF_4 , LiTFSI, and LiFSI.⁶¹ They explained that the detected peaks of Li_2CO_3 overlap with the detected peaks of LEDC, and that perhaps a low concentration of Li_2CO_3 already existed on the negative electrode surface.

Lu et al. reported a new mechanism of negative electrode protection in the presence of concentrated electrolytes.⁷⁶ Upon changing of the potential of Li/graphite cells, an electric field on the electrode surface in contact with the concentrated electrolyte induced a reversible passivation layer. Lu et al. used a variety of electrolytes including LiTFSI with 1,3-dioxolane (DOL) and LiPF_6 with EC:EMC or propylene carbonate (PC).⁷⁶ Upon

polarization of the electrode in the presence of highly concentrated electrolyte, a compact surface layer was formed and continued to grow, protecting the electrode surface from the bulk electrolyte. Upon removal of the field, a thin and porous layer resulted after a 20 minute rest, and could disappear completely, meaning there was no permanent SEI.⁷⁶ The formation of this layer was reversible. This work presented a phenomena that requires further investigation and understanding.

It is clear that the composition, thickness, and growth of the SEI are influenced by cell chemistry, electrolyte, and cycling conditions used, and cannot be correctly described by a single model. Electrolyte additives can have a dramatic effect on the SEI, and will be discussed in section 2.3. Furthermore, the type of Li salt used in the electrolyte can alter the ratio of inorganic and organic species present in the negative electrode SEI.⁶⁵

2.2 SEI AT THE POSITIVE ELECTRODE

The SEI layer at the positive electrode was first suggested by Thomas et al. in 1989.⁷⁷ Guyomard and Tarascon⁷⁸ studied EC and PC based electrolyte that decomposed due to oxidation in a LiMn_2O_4 /graphite cell, and determined that this decomposed electrolyte formed a passivating film, or SEI, on the electrode surface. They suggested that, following the initial formation of the SEI layer, further electrolyte oxidation was prevented.⁷⁸ Alternatively, Aurbach et al.⁷⁹ found that the SEI layer continued to grow during cycling and storage experiments in LiNiO_2 and LiMn_2O_4 half cells with LiPF_6 in EC and DMC, thus not entirely preventing electrolyte oxidation. This claim was supported by a measured increase in impedance during cycling,⁷⁹ which could indicate

the growth of the SEI layer and the inability of the layer to effectively allow the transfer of charge between the electrode and the electrolyte.

Although it has historically received significantly less interest from the battery community, it is now understood that the positive electrode SEI plays a crucial role in obtaining higher energy density Li-ion cells by enabling performance at high potentials, thus leading to an increase in cell capacity. Important factors when choosing an electrolyte are the anodic stability and oxidation potential of the components, both of which affect the negative and positive electrode SEI layers. Moshkovich et al. studied several salts and solvents, including DMC, DEC, EC, LiPF₆, and LiTFSI on Au, Pt, and Al metal electrodes.⁸⁰ They determined that the onset oxidation potential for all solutions tested was below 4 V vs Li/Li⁺. However, Li-ion cells with a variety of positive electrode materials have been shown to have good performance when cycled to potentials above 4 V.^{10,11,51,81,82} The reactions shown to occur on the metal electrodes must be inhibited by practical positive electrode materials as a result of the formation of an SEI layer on the electrode, which suppresses the catalytic nature of the electrode surface. This means that the stability and passivating nature of the positive electrode SEI is important for Li-ion cells to be able to cycle to potentials above 4 V. Although Li-ion cells have shown good performance when cycled to potentials above 4 V, transition metal ions from the positive electrode can catalyze electrolyte decomposition at lower potentials.^{50,83} Transition metal dissolution can lead to structural changes in the positive electrode material and result in capacity fade. For example, LiMn₂O₄ half cells exhibited a large capacity fade due to Mn dissolution, which was accelerated at high temperatures.⁸⁴ However, it is not clear that

transition metal dissolution is a major contributing factor to capacity fade in full Li-ion cells, particularly those with NMC positive electrodes.⁸⁵ It is possible that other factors, such as the presence of HF,⁸⁶ shuttle-type reactions, or the loss of lithium due to growth of the SEI layers, are more significant than Mn dissolution in practical Li-ion cells.

Moshkovich et al. also determined that the oxidation products resulted from the decomposition of the solvents used and that the choice of salt did not affect the products formed during oxidation.⁸⁰ They observed the presence of CO and CO₂ in addition to organic compounds with carbonyl groups. CO₂ observed in the positive electrode SEI may diffuse toward the negative electrode, resulting in the detection of lithium oxalate in the negative electrode SEI.^{87,88} The interactions between the positive and negative electrodes are important in the study of the composition and function of the SEI layers.

Broussely et al. suggested that reduction products at the negative electrode diffuse to the positive electrode and oxidize, resulting in SEI growth.⁸⁹ Dedryvère et al. proposed that organic species formed at the positive electrode due to solvent decomposition at high potential may diffuse through the electrolyte to the surface of the negative electrode during long-term cycling.⁹⁰ Xiong et al. studied the interaction between Li[Ni_{1-x-y}Mn_xCo_y]O₂ (NMC) and graphite electrodes at 4.2 or 4.4 V and 60°C in the presence of LiPF₆ in EC and EMC.⁹¹ They found that when only the positive electrode was in contact with the electrolyte, a significant amount of CO₂ formed, whereas negligible amounts of CO₂ formed in the full cell. They also found that the impedance of the SEI on the positive electrode in absence of the negative electrode was three times larger than the impedance

of the SEI on the positive electrode in a full cell.⁹¹ They suggested that species were oxidized at the positive electrode and migrate to the negative electrode, where they were reduced.⁹¹ This work highlights the importance of the interactions between positive and negative electrodes to enable good cycling at high temperatures and/or high potential.

Coatings on the positive electrode have been studied to enable good cycling performance at high potential and increase the stability of the electrolyte to oxidation at high potential.^{37,71} The coating can act as an artificial interphase similar to the SEI, ideally limiting the amount and reducing the rate of parasitic reactions. With both LiCoO₂ and NMC positive electrodes, AlF₃ was found to be an effective coating.⁹² Chen et al. found that cells with LiCoO₂ could be cycled up to 4.54 V with better capacity retention and rate capability when the positive electrode was coated with AlF₃.⁹² The coating provided a barrier between the active material and the electrolyte. Sun et al. found that cells with NMC had reduced positive electrode reactivity when in contact with electrolyte and had increased stability when coated with AlF₃.⁹³

Song et al. found that a coating of LaPO₄ on NMC was effective at reducing transition metal dissolution and could therefore improve cycling stability.⁹⁴ Mohan and Kalaignan found that cells with LiMn₂O₄ coated with LaPO₄ had excellent cycling and structural stability up to 4.5 V and high reversible capacity at elevated temperatures.⁹⁵ Xia et al. found that, without electrolyte additives, LaPO₄-coated NMC442/graphite cells improved the cycling performance up to 4.5 V compared to cells without the electrode coating.⁹⁶

The effect of a LaPO₄ coating on the cycling performance and impedance of NMC/graphite cells operated to high potential will be discussed in detail in Chapter 4.

2.3 EFFECT OF ELECTROLYTE ADDITIVES ON THE SOLID ELECTROLYTE INTERPHASES

Electrolyte additives play an important role in the formation and growth of both the positive and negative electrode SEI layers, and have been an important topic of study in recent years. The undesirable properties of electrolyte salts and solvents can be modified by using electrolyte additives. Electrolyte additives can be preferentially reduced or oxidized to greatly improve the formation and stability of the negative or positive electrode SEI. As mentioned in Chapter 1, the structure and function of 50 electrolyte additives have been tabulated by Nelson.¹³ Selected recent and/or important studies of the effect of electrolyte additives on the positive and negative electrode SEI layers are presented here.

The additive prop-1-ene-1,3-sultone (PES) has been shown to reduce gas evolution and improve cycling performance at high potential in NMC/graphite cells.^{44,54} It has been suggested that PES is a film-forming additive,^{44,54,97} meaning it enables the production of a stable SEI on the negative electrode. Self et al. used XPS measurements to show that when PES was reduced, it formed lithium sulfite and organic sulphate SEI components.⁹⁸ Madec et al. used XPS to investigate the effect that electrolyte containing PES and/or vinylene carbonate (VC) had on the positive and negative electrode SEI layers in NMC/graphite cells during SEI formation and after cycling to 4.2 V.⁹⁹ The SEI formed in

the presence of control electrolyte (no additives) was 12 nm thick on the graphite surface and 2 nm thick on the NMC surface after the formation cycle.⁹⁹ On the graphite surface, there was a significant amount of inorganic compounds, such as LiF and Li₂O, formed from the degradation of the electrolyte salt (LiPF₆) and the electrolyte solvents (EC and EMC). The SEI layers on both the positive and negative electrode were thinner and contained a higher fraction of organic species when PES and/or VC were present in the electrolyte.⁹⁹ This is evidence that VC and PES stabilize the reactivity of LiPF₆ during SEI formation. Despite leading to the formation of a thinner negative electrode SEI, the presence of PES in the electrolyte has been shown to increase the impedance of the negative electrode SEI compared to electrolyte without PES.⁵⁴ However, PES reduced the impedance of the positive electrode SEI.⁵⁴

Bernhard et al. investigated the effect of VC on the graphite negative electrode SEI and gas evolution with Li/graphite cells in the presence of water-containing electrolyte compared to water-free electrolyte.¹⁰⁰ They found that by pre-cycling the cell in the presence of VC, the SEI that formed was able to reduce the amount of H₂ gas evolution in water-containing electrolyte compared to the amount of H₂ gas that evolved in a cell with pristine graphite (no SEI formed from VC).¹⁰⁰

Petibon et al. investigated the impact of phenyl carbonates, including methyl phenyl carbonate, diphenyl carbonate and ethyl phenyl carbonate, as additives in NMC/graphite cells. Through gas chromatography-mass spectrometry (GC-MS) analysis they determined that phenyl carbonates are SEI-modifiers rather than SEI-formers, meaning

that they are not preferentially reduced, but react with byproducts of the reduction of EC and EMC and affect the surface of the positive and negative electrodes. Furthermore, the impedance of cells containing phenyl carbonates was low compared to cells containing VC, and also led to low gas evolution in cells cycled to 4.2 V.

Although electrolyte additives play a crucial role in the formation and growth of the SEI layers, choice of appropriate electrolyte solvents can also have a dramatic effect on the SEI layers, and therefore impedance and cycling performance, of Li-ion cells. For example, the negative electrode SEI of NMC/graphite pouch cells in the presence of EC:EMC based electrolytes containing PES, 1,3,2-dioxathiolane-2,2-dioxide (DTD), and tris-(trimethyl-silyl)phosphite (TTSPi) was thought to be stable.⁸² This was evidenced by negligible impedance growth of the negative electrode SEI and little capacity fade when exposed to 4.4-4.5 V for extended periods of time.⁸² Conversely, NMC/graphite pouch cells containing fluoroethylene carbonate (FEC) and bis(2,2,2-trifluoroethyl) carbonate (TFEC) based electrolytes with PES exhibited severe impedance growth at the negative electrode, indicating an unstable negative electrode SEI, despite exhibiting superior cycling performance to cells containing EC:EMC based electrolytes.⁴¹

2.4 ROCK SALT SURFACE LAYER ON NMC POSITIVE ELECTRODES

NMC/graphite cells operated to high potential exhibit severe capacity loss, significant impedance growth, electrolyte dry-out, and other detrimental issues as discussed in Chapter 1.^{10,82,101} While some of these problems are attributed to changes in the SEI

layers, they may be the result of a surface reconstruction that occurs at high potentials. Lin et al. used X-ray absorption spectroscopy (XAS), atomic-scale scanning transmission electron microscopy (STEM) and electron energy loss spectroscopy (EELS) to investigate the surface reconstruction of NMC positive electrodes.¹⁰² While layered NMC positive electrode materials have an $R\bar{3}m$ structure, Lin et al. found that upon cycling to high potential a spontaneous surface reconstruction to a rocksalt structure ($Fm\bar{3}m$) occurred.¹⁰² Additionally, a layer containing LiF and organic species formed on the surface, and was found to be approximately 4 nm thick after 20 cycles between 2.5 and 4.7 V. The clear Li-ion diffusion pathways that exist in the $R\bar{3}m$ structure are blocked by the reconstruction to the $Fm\bar{3}m$ structure, which can explain sudden and severe impedance growth and capacity fade that occurs in NMC cells exposed to high potential.^{10,82,102} Similar rocksalt layers have been reported on NCA positive electrodes.^{103–106}

Abraham et al. used XAS, EELS, scanning electron microscopy (SEM), and transmission electron microscopy (TEM) to investigate the surface reconstruction of $\text{LiNi}_{0.8}\text{Co}_{0.2}\text{O}_2$ positive electrodes.^{107,108} They determined that while the bulk had the expected layered crystal structure, the surface had a NiO-like rocksalt crystal structure. They found that the rocksalt surface layer thickened during accelerated aging which could increase the impedance associated with the positive electrode SEI layer.¹⁰⁷ Abraham et al. found the rocksalt surface layer to be approximately 2-5 nm thick.¹⁰⁸ This rocksalt layer has a negative effect on Li-ion conductivity and diffusion.

Li et al. investigated the effect of additives (PES and VC) and upper cutoff potential (4.1 V and 4.3 V) on the formation of a rocksalt layer on $\text{Li}[\text{Ni}_{0.8}\text{Mn}_{0.1}\text{Co}_{0.1}]\text{O}_2$ (NMC811).¹⁰⁹ Using STEM, they found that there was no growth of a rocksalt layer for the cells cycled to 4.1 V. In those cycled to 4.3 V, the cells without any additives had the thickest rocksalt surface layer.¹⁰⁹ When cycled to 4.3 V, cells containing additives suppressed the growth of the rocksalt layer. The formation, growth, and effects of the rocksalt structure on NMC positive electrode materials requires further investigation. This includes the effect of the rocksalt layer on conductivity and diffusion, and the subsequent change to impedance associated with the positive electrode and positive electrode SEI. Impedance growth in Li-ion cells operated to high potentials is characterized throughout the remainder of this thesis. Chapter 8 discusses possible explanations, such as the formation of a rocksalt layer, for reversible and irreversible impedance growth.

CHAPTER 3. EXPERIMENTAL METHODS

3.1 POUCH CELLS AND CELL CHEMISTRIES

Li-ion cells are typically manufactured in either a soft pouch cell casing or in a hard cylindrical can. Cylindrical 18650-sized cells are used in Tesla vehicles and power tools while pouch cells are typically used in cell phones and tablets. Pouch cells are ideal for experimental purposes and were used in this work. Pouch cells are machine-made, resulting in high repeatability between cells, and can be obtained dry (without any electrolyte), allowing freedom and control over the electrolyte systems and electrolyte additives used for study. Due to the high repeatability of cells, any differences between cells during experiments can be attributed solely to the different electrolyte and cell components in the cell as well as the experimental conditions used.

Figure 3.1a shows a photograph of a dry $\text{Li}[\text{Ni}_{0.4}\text{Mn}_{0.4}\text{Co}_{0.2}]\text{O}_2$ (NMC442)/graphite pouch cell as received from LiFUN Technologies (Zhuzhou City, China). Cell details are described in Appendix A. The pouch cells were manufactured and vacuum sealed in a dry room before shipping to Dalhousie University. The labelled jelly roll contains the wound electrodes and separator. The vacuum seals are indicated as well as the positive and negative electrode tabs. Please note there is also a vacuum seal at the tab edge. The gas bag exists to hold gas produced during cell testing. Due to the evolution of gas, clamps can be used to ensure a consistent stack pressure in the cell, and force any gas produced into the gas bag and away from the jelly roll. Figure 3.1b shows a photograph of a clamped cell using two silicone rubber pieces to provide even clamping over the entire

jelly roll, and aluminum shims to ensure tightness of the clamp. The clamping pressure is approximately 122 kPa (1.2 atm), as measured by a pressure gauge (LCKD, Omega Engineering) for a Li-ion cell clamped as shown in Figure 3.1b.

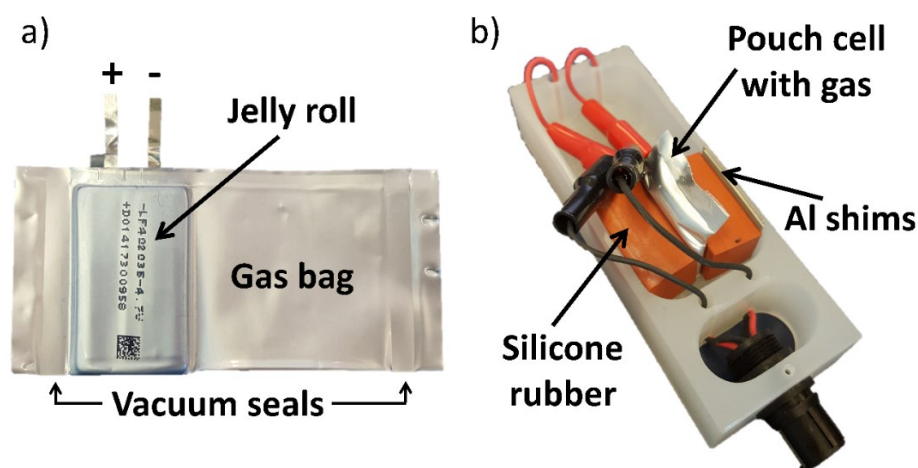


Figure 3.1 Photograph of a) an NMC442/graphite wound pouch cell from LiFUN Technologies and b) a clamped pouch cell using silicone rubber and Al shims.

The work in this thesis mostly involved experiments using machine made NMC/graphite wound pouch cells balanced for 4.4 V or 4.7 V operation. The control electrolyte used for most experiments was 1M LiPF_6 in ethylene carbonate (EC): ethyl methyl carbonate (EMC) 3:7 by weight. As explained in section 1.2.4, these solvents and salt have properties which lead to good cycling performance. Pouch cells required 0.85 grams of electrolyte. The use of alternative electrolyte systems is discussed in Chapters 6 and 7.

3.2 LITHIUM ION CELL CYCLING EXPERIMENTS

Cycling experiments, including short-term high precision^{66,110–113} tests and long-term tests,^{89,112,114} are essential to probe the effect of various experimental conditions,

including choice of electrolyte solvents, electrolyte additives, salt concentration, testing temperature, and voltage range. The discharge capacity of a cell typically decreases as a function of cycle number due to parasitic reactions that can consume electrolyte and/or render lithium electrochemically inactive. Monitoring the discharge capacity of a cell, and the subsequent fade in capacity, is a useful indicator of the effectiveness of the SEI at the negative electrode to prevent parasitic processes.

The rate of charge or discharge of a cell (C-rate) indicates the current applied to a cell during cycling. A C-rate of 1C means that a full charge takes approximately 1 hour. For a 240 mAh cell, a C-rate of C/20 means that a full charge will take 20 hours, and that 12 mA will be applied to the cell.

Cycling experiments that are representative of real-life Li-ion cell usage are imperative. Practical applications that use Li-ion cells often leave the cells at high potentials for extended periods of time after charging. This high potential exposure can be detrimental to cell performance and is not observed under simple continuous cycling experiments.¹⁰ Furthermore, aggressive cycling can aid in determining differences between electrolytes and electrolyte additives in a timely fashion.

Figure 3.2 shows an example of an aggressive testing protocol designed to expose cells to high potentials for extended periods of time.^{10,82} Under this experimental protocol, cells were cycled between 2.8 V and the upper cutoff potential (shown as 4.4 V in Figure 3.2), including a 24 hour hold at the top of charge. Cells underwent two cycles between 2.8 V and the upper cutoff potential at C/5 followed by three cycles between 2.8 V and the

upper cutoff potential with a C/5 charge and a C/2.5 discharge. All five cycles included a 24 hour hold at the top of charge. The five cycles were followed by a charge-discharge cycle, normally at C/20 or C/10, without a hold at the top of charge. After the charge-discharge cycle, the cells were cycled again for 5 cycles and the protocol was repeated. This type of protocol will be described as charge-hold-discharge cycling.

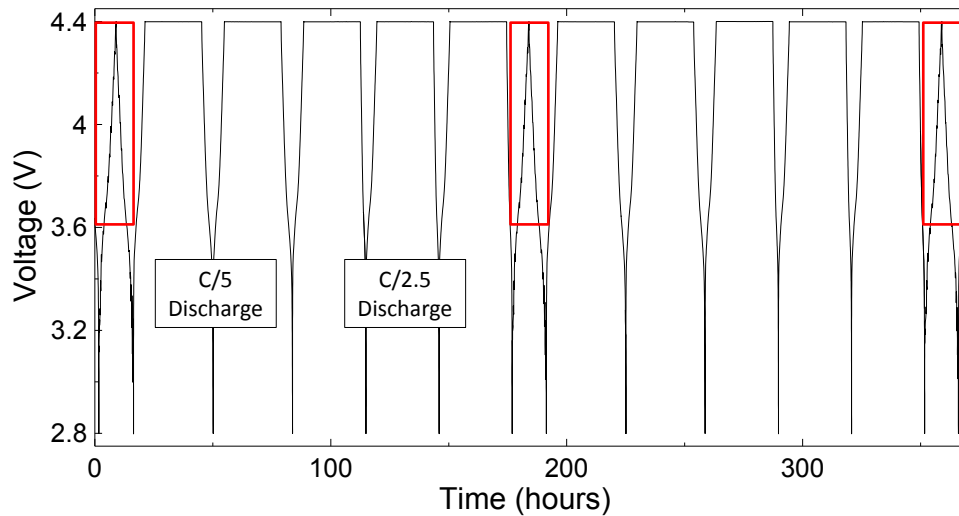


Figure 3.2 The charge-hold-discharge method used in much of the work presented in this thesis. The method includes two cycles at C/5, followed by three cycles with a C/5 charge and a C/2.5 discharge. All five cycles include a 24 hour hold at the top of charge, shown as 4.4 V in this figure.

Figure 3.3 emphasizes the aggressiveness of the charge-hold-discharge method shown in Figure 3.2, for two NMC442/graphite pouch cells containing 1M LiPF₆ EC:EMC with 2% by weight prop-1-ene-1,3-sultone (PES), 1% by weight methylene methane disulfonate (MMDS), and 1% by weight tris-(trimethyl-silyl) phosphite (TTSPi). Figure 3.3a and Figure 3.3b show the discharge capacity of two cells as a function of time and cycle number, respectively. One cell underwent continuous charge-discharge cycling between 2.8 and 4.4 and 4.5 V (the increase in upper cutoff potential is indicated by the

dashed vertical line). The other cell underwent charge-hold-discharge cycling in which the hold was at 4.4 V for 24 hours. Both experiments were performed at 40°C. Despite the excellent capacity retention of the cell during continuous charge-discharge cycling, the hold at high potential led to severe discharge capacity fade. Figure 3.3 dramatically demonstrates the aggressiveness of holding cells at high potentials for extended periods of time, and the importance of testing cells using this protocol to learn about “real-life” performance.^{10,82}

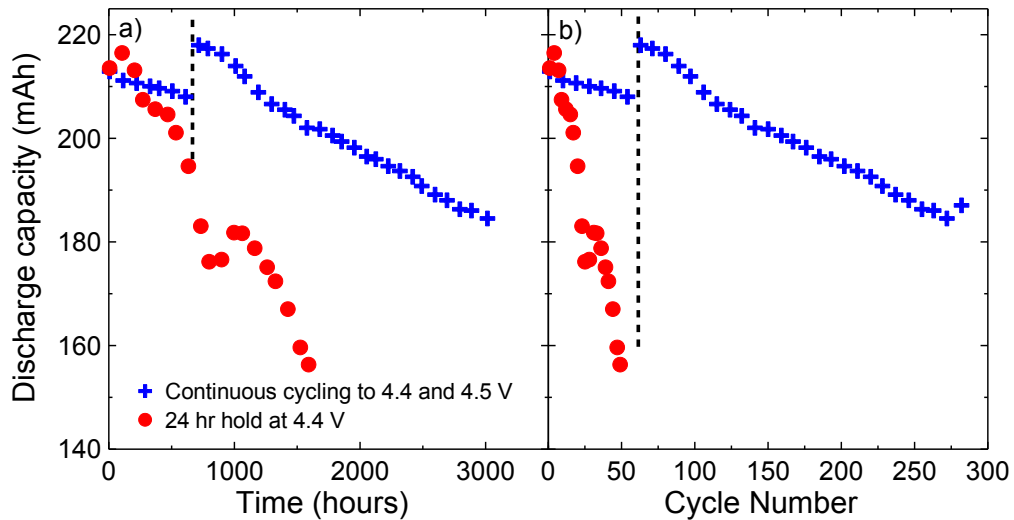


Figure 3.3 The discharge capacity for cells containing 2% PES + 1% MMDS + 1% TTSPi undergoing cycling tests according to continuous charge-discharge cycling or charge-hold-discharge cycling as a function of a) time and b) cycle number.

Machine made wound pouch cells balanced for 4.7 V operation were obtained dry (no electrolyte added) from LiFUN Technologies (Zhuzhou City, China) for the work presented in this thesis, unless otherwise noted. The pouch cells were manufactured without electrolyte and vacuum sealed in a dry room in China by LiFUN Technologies before shipping to Dalhousie University. Cell details are described in Appendix A.

As part of the cell filling process, cells were cut open, in air, and then immediately heated to 80°C or 100°C for 14 hours under vacuum to remove any residual water. The pouch cells were then moved into an argon-filled glove box and filled with 0.85 g of electrolyte. Cells were vacuum sealed after electrolyte filling using a compact vacuum sealer (MTI Corp.). This procedure will be referred to as the ‘standard filling’ procedure.

Cells underwent a formation cycle at $40. \pm 0.1^\circ\text{C}$, consisting of a 24 hour hold at 1.5 V to ensure adequate electrolyte wetting followed by a C/20 charge to 3.5 V. After this step, cells were transferred into an argon-filled glovebox, cut open just below the heat seal to release generated gas and then vacuum sealed again. After degassing, the cells were charged to 4.5 V at C/20 followed by a C/20 discharge to 3.8 V. This procedure will be referred to as the ‘standard formation cycle’. The temperature boxes used for the measurements presented in this work are stable to $\pm 0.1^\circ\text{C}$ and are within one degree Celsius of the set temperature.

3.3 GAS VOLUME MEASUREMENTS

During formation of the positive and negative electrode SEI layers and during cycling experiments, gas can be produced inside Li-ion cells. Gas production can lead to battery safety issues, manufacturing obstacles, loss of electrical contact, and change in cell volume. Gas production can be accelerated in cells operated to high potential.^{5,87,115} It is therefore important to prevent or reduce gas evolution. Accurate measurements of the gas produced inside a cell are necessary to determine the effect of electrolyte additives and

cell components on gas evolution. In-situ and ex-situ measurements of gas evolution employing Archimedes principle are possible for pouch cells.

Ex-situ measurements of gas evolution were done by weighing pouch cells before and after an experimental test, such as before and after a formation cycle or a cycling experiment. The pouch cells were suspended from a balance and placed in nanopure water with $\rho = 0.998 \text{ g/mL}$ (20°C). The apparent change in the weight of the pouch cell as measured by the balance before and after formation or cycling, Δm , is a direct measure of the volume, Δv , of gas produced during formation or cycling as described by $\Delta v = -\Delta m/\rho$. This procedure is discussed in depth by Aiken et al.¹¹⁶ The pouch cells used in this work typically have an initial volume, without gas evolution, of about 2.5 mL.

3.4 ELECTROCHEMICAL IMPEDANCE SPECTROSCOPY

Electrochemical impedance spectroscopy (EIS) can be used to measure the real and imaginary components of cell impedance in response to a small AC signal over a range of frequencies. When an AC potential on the order of mV is applied to the cell, a current response that is linear with the amplitude of the AC potential is invoked. The impedance, in ohms, is calculated at each frequency as the ratio of the applied voltage, in volts, to the measured current, in amps. It is important to know that for the system undergoing measurements, such as a full Li-ion cell, that an AC amplitude is chosen such that the signal is strong and the system remains in a linear region. Figure 3.4a, Figure 3.4b, and Figure 3.4c show the current-voltage Lissajous curves for a Li-ion cell at 3.8 V measured at selected frequencies using a 1 mV, 10 mV, or 20 mV AC potential, respectively. As

the amplitude of the AC potential increases, the current response becomes non-linear during high frequency measurements, as shown by the 100 kHz curve in Figure 3.4b and the 1 kHz and 100 kHz curve in Figure 3.4c. Figure 3.4 indicates that using a 1-10 mV potential is appropriate for a full Li-ion cell. For the measurements presented in this work, an amplitude of 2 or 10 mV was chosen depending on the system used.

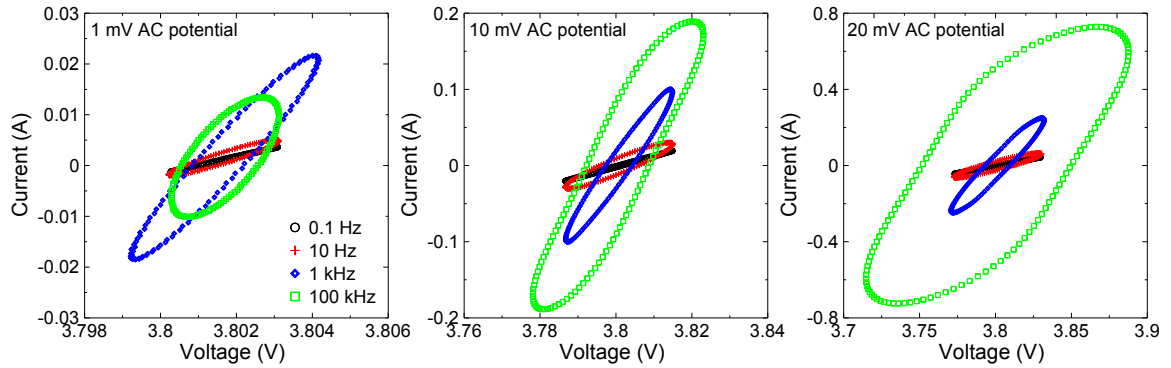


Figure 3.4 The current-voltage Lissajous figures for impedance measurements of a Li-ion cell using an applied a) 1 mV AC potential, b) 10 mV AC potential, and c) 20 mV AC potential shown for selected frequencies.


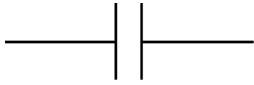


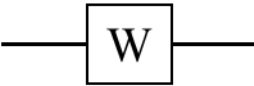
EIS measurements can be used to learn about the effects that electrolyte additives, experimental conditions, and cell chemistry have on the cell impedance, including charge transfer processes, interfacial processes, and solution resistances. EIS measurements can be performed quickly without altering the cell. The impedance, Z_{eq} , of circuit elements in series and parallel are shown by Equations 3.1 and 3.2, respectively.

$$\text{Series: } Z_{eq} = Z_1 + Z_1 + \dots + Z_n \quad (3.1)$$

$$\text{Parallel: } Z_{eq} = \left[\frac{1}{Z_1} + \frac{1}{Z_2} + \dots + \frac{1}{Z_n} \right]^{-1} \quad (3.2)$$

Table 3.1 shows the schematic of circuit elements and their corresponding impedance. The capacitance of a capacitor, in farads, is represented by C , the resistance of a resistor, in ohms, is represented by R , and the inductance of an inductor, in henrys, is represented by L . The angular frequency, ω , is equal to $2\pi f$, where f is the frequency in hertz. Table 3.1 introduces constant phase elements (CPE) and Warburg elements. A CPE is an imperfect capacitor and models the behaviour of a double layer capacitor. It can be used to represent an effective capacitance resulting from a distribution of time constants. The impedance of a CPE depends on the measured frequency, ω , an exponent, φ , ranging from 0 to 1, and the variable Q , which has units of $F s^{\varphi-1}$. The exponent, φ , is less than 1 for an imperfect capacitor, and equal to 1 for an ideal capacitor. A Warburg element models the diffusion processes in a Li-ion cell. The impedance of a Warburg diffusion element depends on the measured frequency, ω , and a Warburg coefficient, A_W .

Table 3.1 Circuit elements and their calculated impedance. Adapted from Nelson.¹³

Component	Circuit Symbol	Impedance, $Z(\omega)$
Resistor		R
Capacitor		$\frac{1}{i\omega C}$
Inductor		$i\omega L$
Constant Phase Element		$\frac{1}{Q(i\omega)^\varphi}$
Warburg Element		$\frac{A_W}{\omega^{1/2}} - \frac{iA_W}{\omega^{1/2}}$

EIS spectra are often displayed in a Nyquist plot, in which the imaginary component of impedance is plotted as a function of the real component of impedance. A Nyquist plot of a Li-ion cell typically has a depressed semi-circular shape and the real component of impedance normally decreases as frequency increases. EIS spectra can also be displayed in a Bode plot, in which either the real or imaginary component of impedance is plotted as a function of frequency on a logarithmic scale. This is useful as the impedance at each measured frequency is shown.

In a simplified model, a single electrode in electrolyte can be described by a circuit comprised of a resistor, R_p , and capacitor, C_p in parallel (an RC circuit) and in series with a resistor, R_s . The resistor, R_p , is due to the resistance of to the electrode SEI, including charge transfer resistance. The SEI layer has some surface charge and in the electrolyte there are oppositely charged ions near the SEI surface. These two parallel layers of charge are an electric double layer, and have a double layer capacitance, C_p . The resistance R_s represents the electrolyte or solution resistance. Figure 3.5 shows a Bode and Nyquist representation of the impedance spectrum obtained from this simple circuit model for a single electrode in electrolyte. In Figure 3.5c, the diameter of the semicircle corresponds to the value of R_p (0.3Ω) and the shift of the semicircle from zero in the real axis corresponds to R_s (0.05Ω).

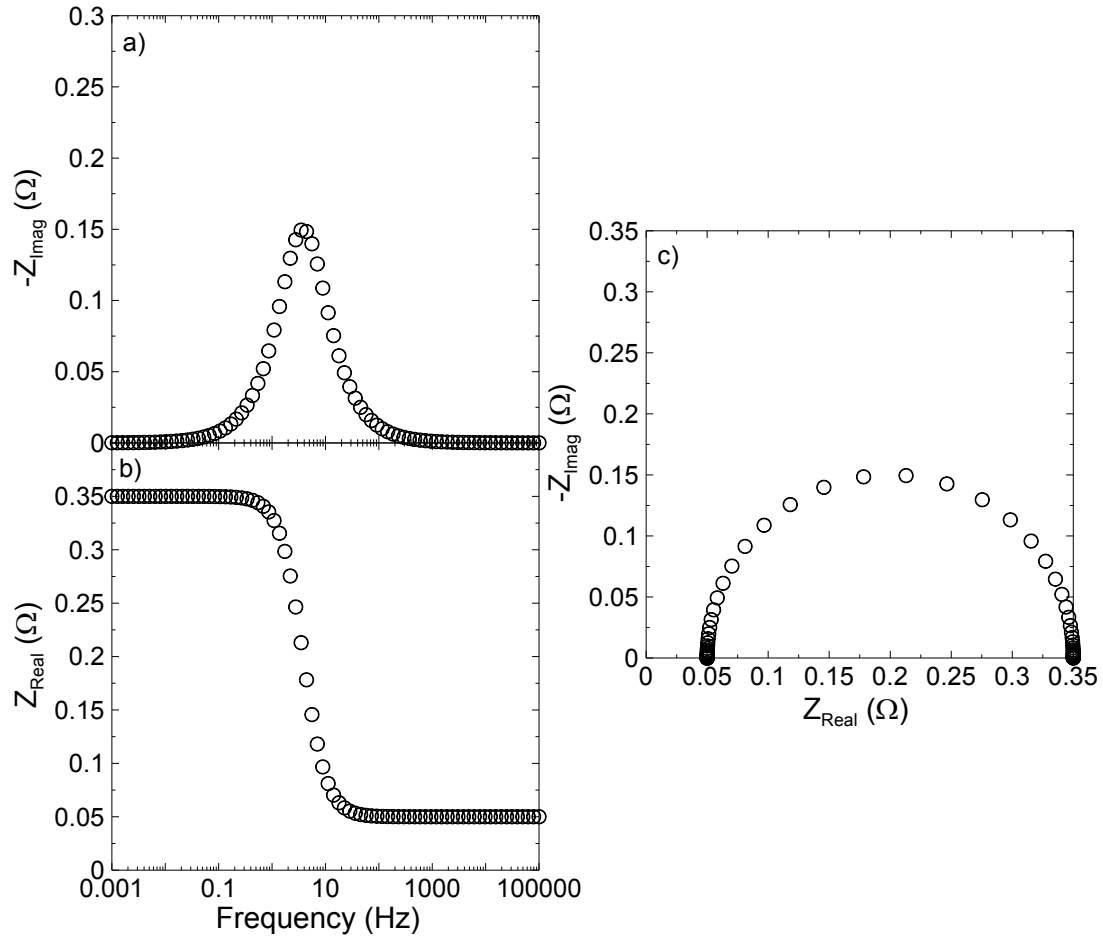


Figure 3.5 An a) imaginary Bode, b) real Bode, and c) Nyquist representation of the impedance spectrum for an RC circuit in series with a resistor. The series resistor has a resistance of 0.05 Ω, and the parallel RC circuit has resistance 0.3 Ω and capacitance 0.15 F.

The spectrum shown in Figure 3.5c resulting from an RC circuit in series with a resistor is not an accurate depiction of the spectrum obtained from a full Li-ion cell. Figure 3.6 shows two impedance spectra measured for a real full Li-ion cell shown in a Nyquist representation. Figure 3.6a shows an impedance spectrum with a single-peak feature and Figure 3.6b shows an impedance spectrum with a two-peak feature. The spectra are not a single semicircle, as shown in Figure 3.5, but are actually made up of several depressed

semi circles. An effective resistance, R_{ct} , represents the combination of charge transfer resistances (both positive and negative electrodes) and the resistance due to the motion of ions through the SEI layers (both positive and negative electrodes). The shift of the spectrum from zero on the real axis at high frequency typically corresponds to the solution resistance, R_s , plus any inductive contribution from the experimental setup. This ‘high frequency intercept’ (HFI) will be discussed in detail in the remainder of this thesis.

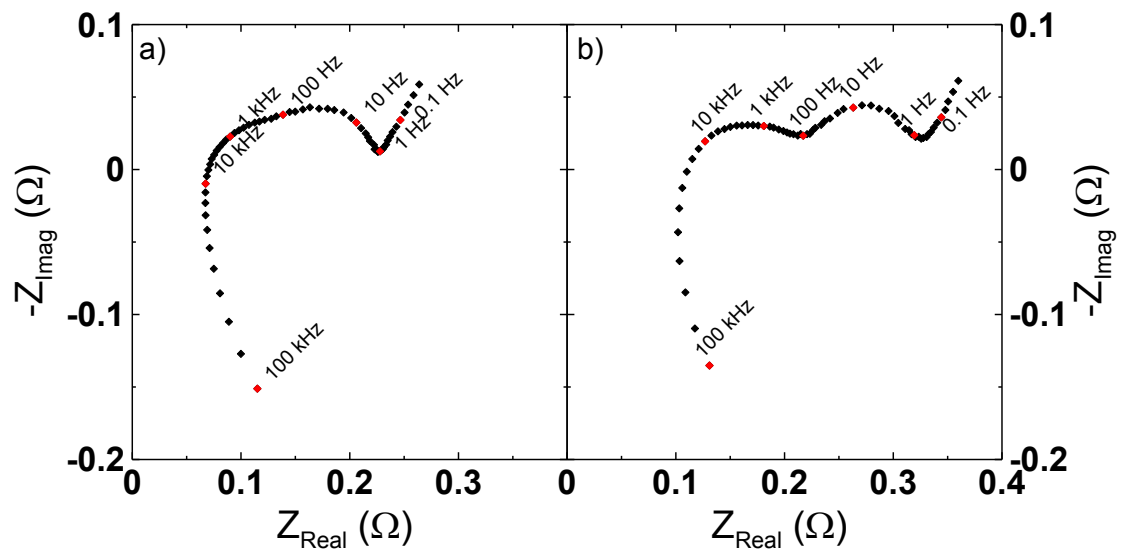


Figure 3.6 Example of Nyquist plot for a cell exhibiting a) a single-peak impedance spectrum and b) a two-peak impedance spectrum.

The high frequency tail that occurs at low values of the real axis, as shown in Figure 3.6 is due to the inductive contribution of the experimental setup. This is demonstrated in Figure 3.7, which shows the contribution to impedance from the four-wire system used to obtain the spectra shown in Figure 3.6. Figure 3.7 shows the impedance spectrum obtained from measuring EIS of a short circuit from 40 mHz to 100 kHz on the four-wire system at 40°C. The short circuit was made by connecting the alligator clips of an empty

cell container (the Teflon container shown in Figure 3.1b) together, meant to capture the entire contribution due to the experimental setup under real conditions.

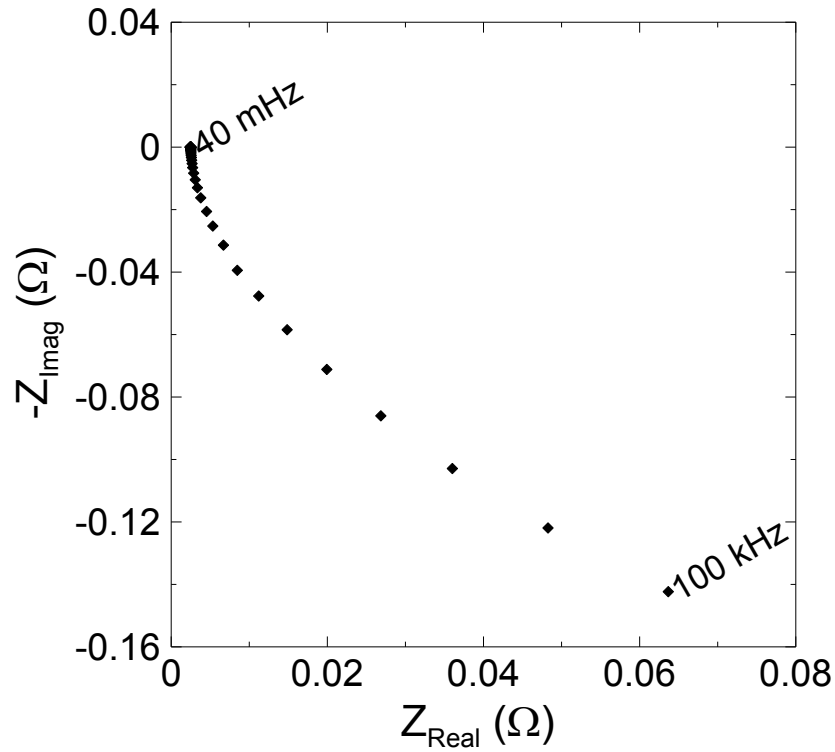


Figure 3.7 Example of the contribution of the equipment to the measured impedance, obtained by measuring EIS of a short circuit using the four-wire system.

Figure 3.8 shows the Bode plots corresponding to the data shown in Figure 3.6. Figure 3.8a and Figure 3.8b show the imaginary impedance Bode plot for the same cell shown in Figure 3.6a and Figure 3.6b, respectively. Figure 3.8c and Figure 3.8d show the real impedance Bode plot for the same cell shown in Figure 3.6a and Figure 3.6b, respectively.

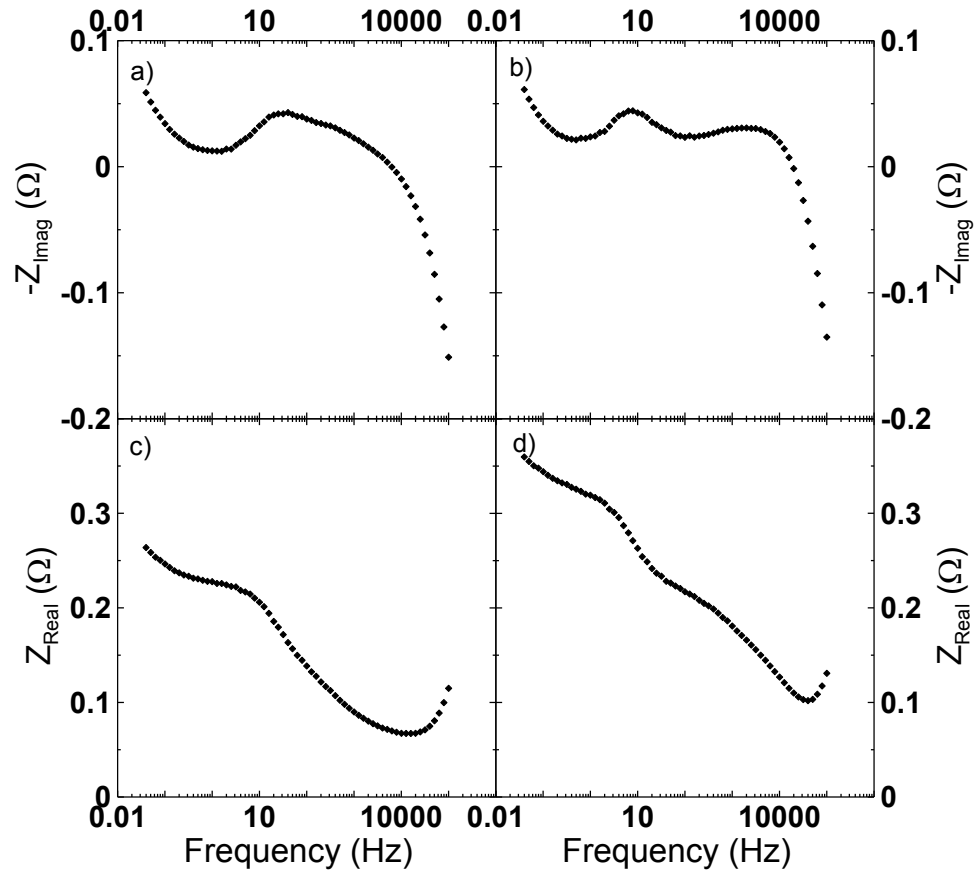


Figure 3.8 Example of an imaginary Bode plot for a cell exhibiting a) a single-peak feature and b) a two-peak feature. Example of a real bode plot for a cell exhibiting c) a single-peak feature and d) a two-peak feature.

In order to more accurately represent the impedance spectra for a Li-ion cell, a transmission line model^{117,118} can be used. Figure 3.9 shows a simplified diagram and a transmission line model of the positive electrode in electrolyte.^{82,119} Figure 3.9b shows a schematic of the positive electrode with the current collector on the left and the separator on the right. The positive electrode is shown to be five particles thick, and the corresponding transmission line model in Figure 3.9a contained five links. The number of links in the model was chosen because SEM images of NMC positive electrode particles

indicated a particle diameter ranging between 15-20 μm ,^{42,120} and the positive electrode thickness was measured to be approximately 105 μm .¹²¹

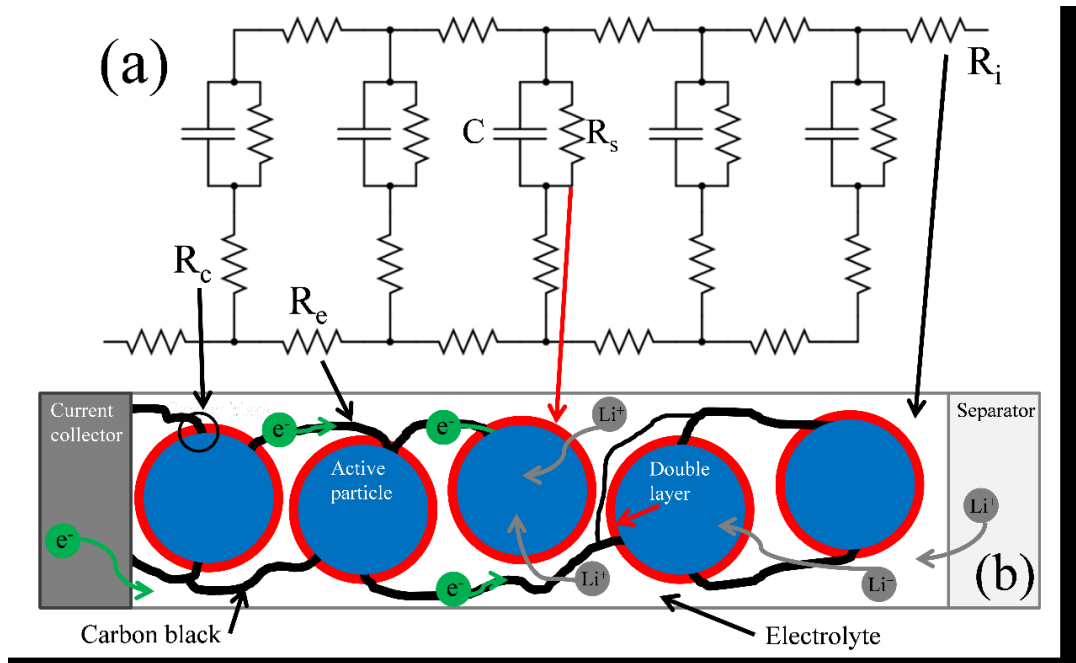


Figure 3.9 a) Discrete transmission line model circuit of the positive electrode used to interpret impedance spectra with the current collector at the left and the separator at the right.^{82,119} b) Schematic of a Li-ion cell positive electrode with each relevant effect highlighted and connected to its corresponding circuit component. Work done and figure produced by Dan Abarbanel, 3rd year B. Sc. Student, Physics and Atmospheric Science, Dalhousie University (2015).

Each component of the schematic shown in Figure 3.9b has a corresponding circuit element shown in Figure 3.9a. The circuit elements R_e , R_i , R_s , R_c , and C represent the resistance of the electronic path from particle to particle through the carbon black, the resistance of the ionic path from particle to particle through the electrolyte solution, the charge transfer resistance of the SEI layer at each particle surface, the contact resistance between the carbon black and the active particles, and the double layer capacitance of the

SEI layer at the particles surfaces, respectively. Nelson et al.⁸² and Abarbanel et al.¹¹⁹ showed that this equivalent circuit was able to effectively model the depressed semicircular impedance spectra of a full cell. However, with a large number of circuit parameters, it can be difficult to make meaningful interpretations of how the circuit parameters change with time, cycle number, and voltage.

In order to reduce the number of circuit parameters, a constant phase element can be used to model the imperfect electrode surface. By replacing the capacitor in an RC circuit with a CPE, it is possible to obtain depressed semicircular impedance spectra. Figure 3.10 shows Bode and Nyquist representations of the impedance spectra obtained from a circuit consisting of a resistor in parallel with a CPE. Figure 3.10 also shows the impedance spectra obtained for an RC circuit. As previously mentioned, when the exponent, ϕ , is equal to one, the CPE is equivalent to an ideal capacitor. Therefore when the exponent, ϕ , is equal to one, the circuit is equivalent to an RC circuit. As the exponent, ϕ , decreases, the semicircle shown in Figure 3.10c becomes more depressed. Therefore, it is possible to reasonably fit impedance spectra from real Li-ion cells by using constant phase elements in place of ideal capacitors.

Table 3.2 shows simplified models of an electrode and of a full Li-ion cell, using either capacitors or constant phase elements. In the simplified models, both the positive and negative electrode can be described by a circuit comprised of a resistor and capacitor in parallel. The resistances, R_p and R_n , are due to the resistance of the positive and negative electrode SEI, respectively. The resistance, R_s , represents the electrolyte resistance and

the resistance, R_e , represents the electronic resistance. In the models using capacitors, the SEI layers have some surface charge and in the electrolyte there are oppositely charged ions near the SEI surface. These two parallel layers of charge are an electric double layer, and have a double layer capacitance, C_p and C_n , on the positive and negative electrode respectively. In the simplified models using CPEs, the critical frequency is represented by ω_c , and is affected by the effective capacitance of the CPE.

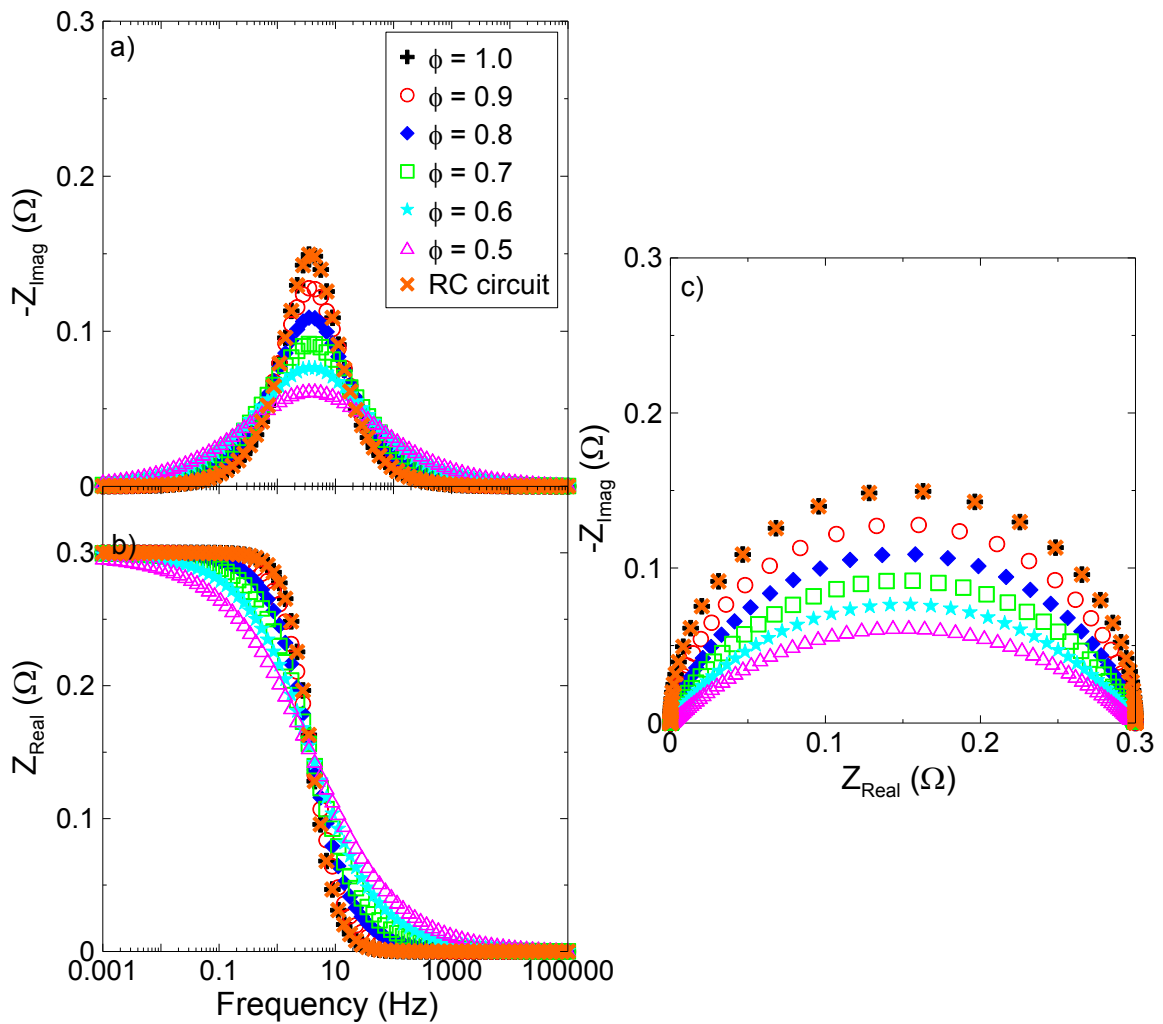


Figure 3.10 a) Imaginary Bode, b) real Bode, and c) Nyquist representations of the impedance spectra for a circuit consisting of a CPE in parallel with a resistor with values of ϕ ranging from 0.5 to 1.0.

Table 3.2 Simplified equivalent circuit models for Li-ion electrodes and Li-ion cells, and their calculated impedance. Adapted from Nelson.¹³

Component	Circuit Symbol	Impedance, $Z(\omega)$
Positive Electrode in Electrolyte (using C)		$R_s + R_e + \frac{R_p}{1 + \omega^2 C_p^2 R_p^2}$ $- \frac{R_p^2 i \omega C_p}{1 + \omega^2 C_p^2 R_p^2}$
Simplified model of full Li-ion cell (using C)		$R_s + R_e + \frac{R_n}{1 + \omega^2 C_n^2 R_n^2}$ $- \frac{R_n^2 i \omega C_n}{1 + \omega^2 C_n^2 R_n^2}$ $+ \frac{R_p}{1 + \omega^2 C_p^2 R_p^2}$ $- \frac{R_p^2 i \omega C_p}{1 + \omega^2 C_p^2 R_p^2}$
Positive Electrode in Electrolyte (using CPE)		$R_s + R_e + \frac{R_p}{1 + \left(\frac{i\omega}{\omega_c}\right)^\varphi}$
Simplified model of full Li-ion cell (using CPE)		$R_s + R_e + \frac{R_p}{1 + \left(\frac{i\omega}{\omega_{c1}}\right)^\varphi}$ $+ \frac{R_n}{1 + \left(\frac{i\omega}{\omega_{c2}}\right)^\varphi}$

EIS measurements can be performed quickly without altering the cell, which means that these measurements can also be done in-situ. Ex-situ measurements presented in this thesis were taken using two different systems; a two-wire setup and a four-wire setup. A four-wire system uses two separate pairs of wires to separate current and voltage, which eliminates the resistance due to the leads present in a two-wire measurement. As the impedance of a Li-ion cell is below 1000 Ω , the lead resistances can provide significant error. Therefore, the four-wire measurements are advantageous. The two-wire setup consists of a BioLogic VMP3 battery tester equipped with an EIS board. The four-wire setup consists of a BioLogic SP-150. Both systems will be used in this thesis.

3.5 AUTOMATIC EIS AND CYCLING

EIS measurements can be made during cycling experiments. This allows for the study of impedance as a function of time, cycle number, and voltage, which is essential to characterize how Li-ion cells are affected by experiments representative of real-life use at high potential.

Two systems capable of EIS measurements coupled with cycling experiments were used in this work, both using a frequency response analyzer (FRA) for EIS measurements. The two-wire system consists of Neware (Shenzhen, China) cyclers connected to computers with Gamry FRA cards via appropriate computer controlled relays. The relay switching was controlled to connect the cells to the Neware charger or to the Gamry FRA cards so the cell remained at open circuit voltage while the FRA measured the impedance spectra of a cell. The four-wire system consists of Neware cyclers connected to a Gamry

Interface 5000E potentiostat. This system also uses computer controlled relays to ensure the cells remain at open circuit voltage while undergoing an impedance measurement. Chapter 6 and 7 will demonstrate the usefulness of measuring impedance with a four-wire system.

The typical protocol used for cycling experiments coupled with automatic impedance measurements is described by Figure 3.2. Typically, impedance is measured every 0.1 V during charge and discharge during the red outlined regions of the cycles indicated in Figure 3.2. Figure 3.11 shows an example of the impedance spectra measured of a Li-ion cell undergoing the charge-hold-discharge cycling method described in Figure 3.2. Each spectrum shown was measured at 3.8 V every 12 cycles. The blue spectrum is the measurement from cycle 2, and the orange spectrum is the measurement from cycle 74.

Figure 3.11a shows the impedance spectra plotted on axes that are not equally scaled and Figure 3.11b shows the impedance spectra plotted on equally scaled axes. While it is common practice to plot impedance spectra on equally scaled axes, as shown in Figure 3.11b, the depressed spectra measured for full Li-ion cells are better illustrated on axes that are not equally scaled. Therefore, throughout this thesis, impedance spectra will be shown on plots without equally scaled axes, as shown in Figure 3.11a, in order to clearly show the features of multiple spectra at once.

As described in section 3.4 and indicated in Figure 3.11a, the width of the impedance spectrum along the real axis, R_{ct} , is the combination of charge transfer resistances (both positive and negative electrodes) and the resistance due to the motion of ions through the

SEI layers (both positive and negative electrodes). The shift of the spectra from zero on the real axis are due to changes in the electronic and/or ionic path resistance plus the inductive contribution from the experimental setup, as shown in Figure 3.7.^{82,119}

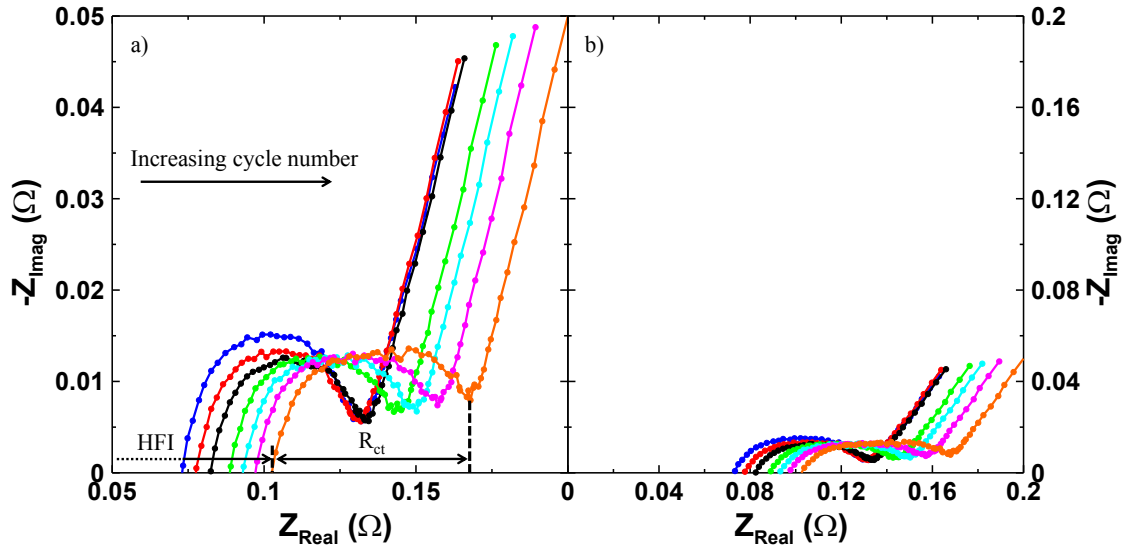


Figure 3.11 Impedance spectra of a Li-ion cell undergoing charge-hold-discharge cycling. The spectra shown were measured at 3.8 V. The arrow indicates the trend of the data with increasing cycle number. The data points shown were measured from 40 mHz to 6300 Hz.

The usefulness of cycling experiments coupled with automatic EIS measurements, particularly to understand the performance of Li-ion cells operated to high potentials has been shown by Nelson et al.,^{10,82} and is summarized by Figure 3.12. Figure 3.12a shows the discharge capacity as a function of time for an NMC/graphite cell cycled continuously to 4.4 and 4.5 V and an NMC/graphite cell undergoing charge-hold-discharge cycling. Figure 3.12b shows the same discharge capacity plotted as a function of cycle number. As discussed in section 3.2, the cell undergoing charge-hold-discharge cycling with a 24 hour hold at 4.4 V had severe capacity fade after only 50 cycles, despite

a similar cell having excellent capacity retention for 300 continuous charge-discharge cycles. Figure 3.12c and Figure 3.12d show R_{ct} as a function of voltage for the cell undergoing charge-hold-discharge testing and continuous cycling, respectively.

The cell undergoing the charge-hold-discharge cycling exhibited severe impedance growth over 50 cycles (~1700 hours). The cell undergoing continuous cycling had very low impedance at all voltages and all 285 cycles (~3000 hours). Figure 3.12 dramatically demonstrates the aggressiveness of holding cells at high potential for extended periods of time, and the usefulness of cycling experiments coupled with automatic impedance measurements.^{10,82} Chapter 4 and 5 will investigate the effect of these aggressive charge-hold-discharge cycling tests on a variety of cell chemistries. Chapters 6 and 7 will further illustrate the importance of monitoring impedance growth as a function of time, cycle number, and voltage.

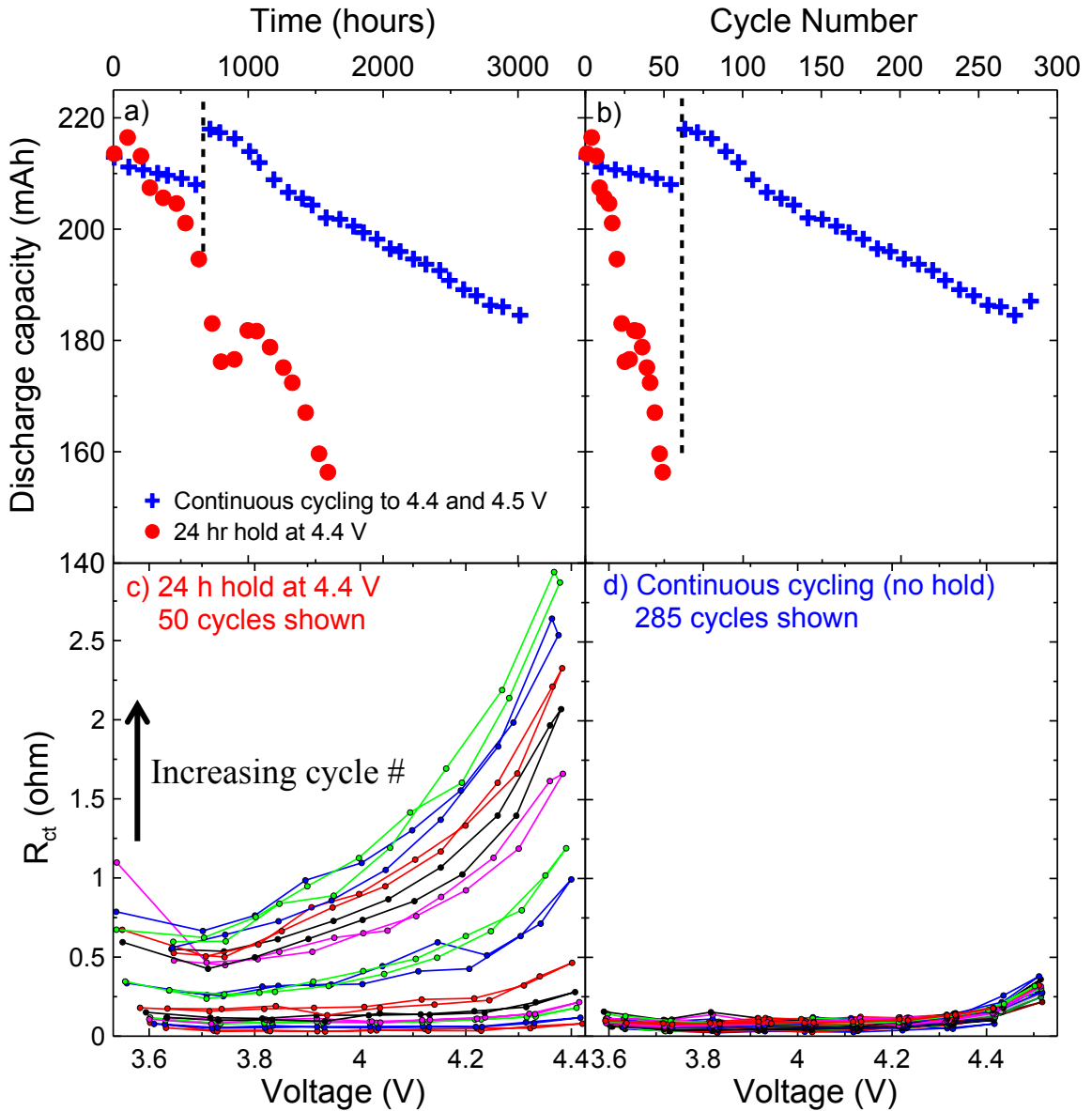


Figure 3.12 The discharge capacity for cells containing 2% PES + 1% MMDS + 1% TTSPi undergoing cycling tests and FRA measurements according to continuous charge-discharge cycling or charge-hold-discharge cycling as a function of a) time and b) cycle number. The combination of charge transfer resistance (both positive and negative electrodes) and resistance due to motion of ions through the SEI layers (both positive and negative electrodes), R_{ct} , as a function of voltage measured during every FRA cycle for c) the cell undergoing charge-hold-discharge cycling and d) the cell undergoing continuous charge-discharge cycling.

3.6 SYMMETRIC CELLS

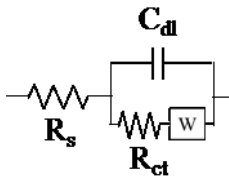
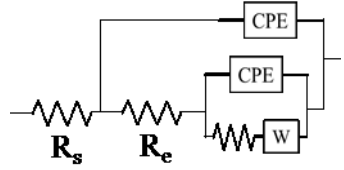
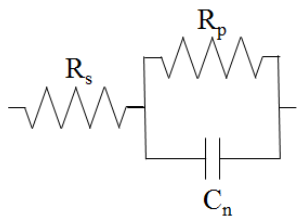
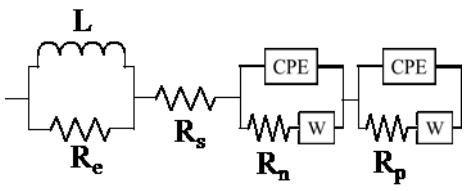
When testing various electrolyte systems, electrolyte additives, cell chemistries and experimental conditions, it is necessary to determine if changes are made to the positive electrode or to the negative electrode, and their respective SEI layers. Impedance measurements of a full cell include information about the impedance of both the positive and negative electrodes. However, the contributions from each electrode often overlap and are not distinguishable from impedance measurements made on full Li-ion cells. Symmetric coin cells^{19,122,123} can be used to determine the source of impedance growth in a Li-ion cell.

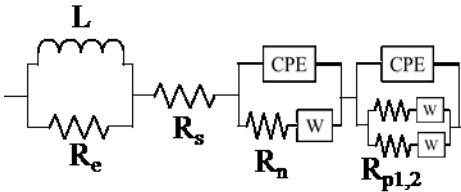
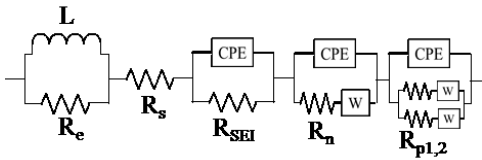
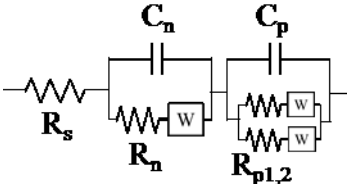
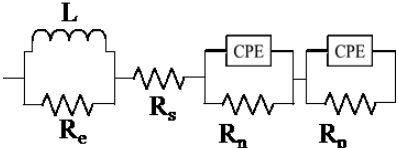
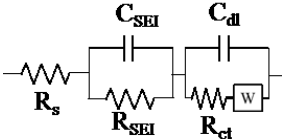
Coin-type cells can be assembled from the positive and negative electrodes from a dismantled full pouch cell, typically after a cycling or storage experiment. A symmetric coin cell consists of either two positive electrodes or two negative electrodes punched from the electrodes from a full pouch cell in addition to a separator, typically polypropylene blown microfiber (BMF), and control electrolyte. BMF separators are available from 3M Co. with a thickness of 0.275 mm and 3.2 mg/cm². Full pouch cells are typically dismantled, in an argon-filled glovebox, at 3.8 V or approximately 50% state of charge. The potential of the assembled symmetric coin cells is approximately 0.0 V. After assembling symmetric cells, EIS measurements can be taken as described in section 3.4. These EIS measurements provide separate information for the impedance contribution from the positive side (electrode and SEI layer), and from the negative side (electrode and SEI layer).

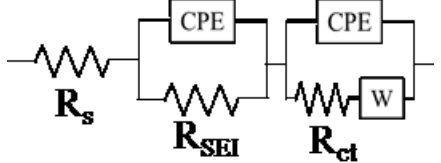
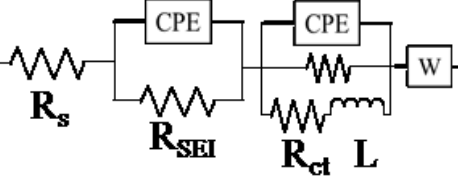
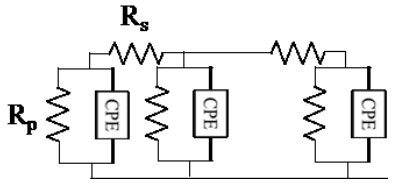
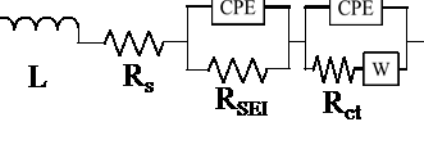
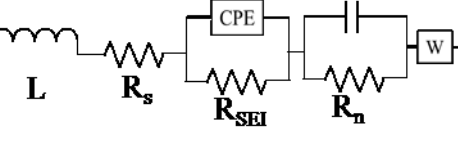
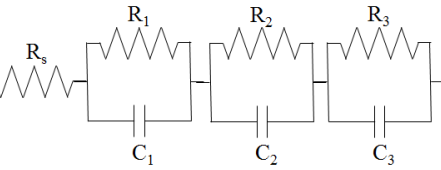
3.7 EQUIVALENT CIRCUIT MODELS FROM LITERATURE

Several equivalent circuit models are used across literature to fit the impedance spectra measured from Li-ion cells. Many of these models, although different, have common features. Table 3.3 presents a small selection of these models, including the circuit diagram and comments about the components used.

Table 3.3 List of equivalent circuit models from literature used to fit impedance spectra of Li-ion cells.

Circuit and Reference	Notes
<p>1. Randles et al.¹²⁴</p> 	<ul style="list-style-type: none"> -only accounts for a single semicircle, which is not accurate for a full Li-ion cell -includes solution resistance -does not include inductive component -includes Warburg diffusion
<p>2. Atebamba et al.¹²⁵</p> 	<ul style="list-style-type: none"> -accounts for multiple semicircles -includes solution resistance -does not include inductive component -includes Warburg diffusion
<p>3. Liaw et al.¹²⁶</p> 	<ul style="list-style-type: none"> -simple model that could be used to fit a single electrode in electrolyte -only accounts for a single perfect semicircle, which is not accurate for a full Li-ion cell -includes solution resistance -does not include inductive component from equipment and wound current collector -does not account for Warburg diffusion
<p>4. Osaka et al.¹²⁷</p> 	<ul style="list-style-type: none"> -positive and negative electrode electrochemical reactions are represented by an interfacial capacitance in parallel with charge transfer resistance with Warburg impedance -accounts for multiple depressed semicircles -includes solution resistance -includes inductive component from equipment and wound current collector -includes Warburg diffusion

Circuit and Reference	Notes
<p>5. Osaka et al.¹²⁷</p> 	<ul style="list-style-type: none"> -similar to circuit #4, but includes variation in Li-ion diffusion length in the positive electrode -includes two diffusion elements used to represent two types of active material with two different radii -variation in capacitance in particles represented by CPE -introducing variety in positive electrode particle size, fitting error decreased compared to circuit #4 -accounts for multiple depressed semicircles -includes solution resistance -includes inductive component from equipment and wound current collector -includes Warburg diffusion
<p>6. Osaka et al.¹²⁷, Mukoyama et al.¹²⁸</p> 	<ul style="list-style-type: none"> -similar to circuit #5, but component of SEI introduced -accounts for multiple depressed semicircles -includes solution resistance -includes inductive component from equipment and wound current collector -includes Warburg diffusion
<p>7. Osaka et al.¹²⁹</p> 	<ul style="list-style-type: none"> -similar to circuit #5, but uses C instead of CPE -use of capacitors (instead of CPE) may provide physically relevant information, but may produce inaccurate fits -accounts for multiple semicircles -includes solution resistance -does not include inductive component from equipment and wound current collector -includes Warburg diffusion
<p>8. Suresh et al.¹³⁰</p> 	<ul style="list-style-type: none"> -similar to circuit #4, but does not include Warburg diffusion -accounts for multiple depressed semicircles -includes solution resistance -includes inductive component from equipment and wound current collector
<p>9. Zhang et al.¹³¹</p> 	<ul style="list-style-type: none"> -accounts for multiple semicircles -includes solution resistance -includes inductive component from equipment and wound current collector -includes Warburg diffusion

Circuit and Reference	Notes
<p>10. Itagaki et al.¹³²</p> 	<p>-proposed as a model for the positive electrode, including R CPE circuits for the active material/current collector interface and for the SEI layer</p> <ul style="list-style-type: none"> -accounts for multiple depressed semicircles -includes solution resistance -does not include inductive component -includes Warburg diffusion
<p>11. Itagaki et al.¹³²</p> 	<p>-proposed as a model for the negative electrode, including R CPE circuits related to the SEI layer and to the electric double-layer</p> <ul style="list-style-type: none"> -accounts for multiple depressed semicircles -includes solution resistance -includes inductive component -includes Warburg diffusion
<p>12. Nara et al.¹³³</p> 	<ul style="list-style-type: none"> -transmission line model -accounts for multiple depressed semicircles -includes solution resistance -does not include Warburg diffusion
<p>13. Nara et al.¹³³, Dong et al.¹³⁴</p> 	<ul style="list-style-type: none"> -similar to circuit #10, but includes the inductive component from equipment and wound current collector -accounts for multiple depressed semicircles -includes solution resistance -includes Warburg diffusion
<p>14. Buller et al.¹³⁵</p> 	<ul style="list-style-type: none"> -accounts for multiple depressed semicircles -includes solution resistance -includes inductive component from equipment and wound current collector -includes Warburg diffusion
<p>16. Huang et al.¹³⁶, Agarwal et al.¹³⁷</p> 	<ul style="list-style-type: none"> -accounts for multiple semicircles -includes solution resistance -does not include inductive component -does not include Warburg diffusion -the circuit described in Agarwal et al.¹³⁷ is similar to that described by Huang et al.¹³⁶

CHAPTER 4. EFFECTS OF UPPER CUTOFF POTENTIAL AND SURFACE COATING ON THE IMPEDANCE OF NMC/GRAPHITE POUCH CELLS^a

The work of Nelson et al.¹⁰ is extended to include studies up to 4.5 V to probe the performance and impedance of cells containing the additives prop-1-ene-1,3-sultone (PES), 1,3,2-dioxathiolane-2,2-dioxide (DTD), and tris-(trimethyl-silyl) phosphite (TTSPi). Although the effectiveness of this ternary additive combination has been shown to withstand continuous charge-discharge and charge-hold-discharge cycling to 4.4 V,^{10,43,138} it is important to study and understand the performance of these additives when the upper cutoff potential is increased. This is important to improve the energy density of Li-ion cells by obtaining higher capacity from increasing the upper cutoff potential. Furthermore, studying the effect of extended periods of time at high potential on the cycling performance and impedance growth of cells is imperative since practical applications of Li-ion cells often leave the cells at high potential for extended periods of time after charging.

As discussed in section 2.2, coatings on the positive electrode, such as LaPO₄, can act as an artificial solid electrolyte interphase (SEI) and limit the rate of parasitic reactions, improve cycling stability and improve capacity retention in cells without electrolyte

^a The results presented in this chapter were published in K. J. Nelson, D. W. Abarbanel, J. Xia, Z. Lu, and J. R. Dahn, *J. Electrochem. Soc.*, **163**, A272–A280 (2016) for which the candidate wrote the first draft of the entire manuscript. The contribution of the co-authors (other than the candidate) is indicated in the captions of the figures where appropriate.

additives.⁹⁴⁻⁹⁶ This work compares LaPO₄-coated and uncoated Li[Ni_{0.4}Mn_{0.4}Co_{0.2}]O₂ (NMC442)/graphite cells with upper cutoff potentials selected from 4.4, 4.425, 4.45, 4.475, or 4.5 V to examine the impact of the upper cutoff potential on performance. The electrochemical impedance spectra were analyzed using a transmission line model to determine how the charge transfer impedance and the impedance of the electronic/ionic path change with cycle number as a function of the upper cutoff potential selected.

4.1 EXPERIMENTAL

The cells used were 180 mAh NMC442/graphite wound pouch cells with a 3 wt. % LaPO₄ coating on the NMC442 active material (referred to as coated cells) and 240 mAh NMC442/graphite wound pouch cells (referred to as uncoated cells). The coated cells had a thinner positive electrode than the uncoated cells and therefore had smaller capacity. The NMC442 was prepared by Umicore Co. and the LaPO₄ coating was applied by 3M Co. to the active material. The cells were filled with 1M LiPF₆ in ethylene carbonate (EC): ethyl methyl carbonate (EMC) (BASF) in a ratio of 3:7 by weight with 2% by weight each of PES (Lianchuang Medicinal Chemistry Co., 98.20%), DTD (Aldrich, 98%), and TTSPi (TCI America, >95%). This additive combination will be referred to as PES222. All cells underwent the standard filling procedure and formation cycle as described in section 3.2.

After the formation cycle, these cells were placed in a 40. ± 0.1°C temperature box connected to a system capable of two-wire electrochemical impedance spectroscopy (EIS) measurements coupled with cycling capabilities, as described in Chapter 3.5. Cells

underwent charge-hold-discharge cycling as shown in Figure 3.2, in which the upper cutoff potential was 4.4, 4.425, 4.45, 4.475, or 4.5 V. Cells were removed after 84 cycles, or approximately 2250 hours.

Following all cycling experiments, selected pouch cells were dismantled and the electrodes were used to assemble positive and negative electrode symmetric coin cells,^{19,122,123} as described in section 3.6, in order to determine the source of impedance growth. The size of the punched electrodes was 1.36 cm². Once assembled, EIS measurements were taken at 10. ± 0.1°C from 10 mHz to 100 kHz using ten points per decade. The cell potentials were approximately 0.0 V because these were symmetric cells.

4.2 RESULTS

Figure 4.1a and Figure 4.1b show the discharge capacity versus cycle number of the 180 mAh coated and 240 mAh uncoated cells, respectively. Each cell has two distinct data sets that display the difference in capacity between the two C/5 (higher capacity cycles) and the three C/2.5 discharge segments (lower capacity cycles). Figure 4.1a shows that coated cells had severe discharge capacity fade at a high rate after only 20 cycles and at both rates by the end of testing when cycled above 4.425 V. Uncoated cells, however, exhibited very small capacity fade for cells cycled up to 4.45 V during all cycles. As shown in Figure 4.1b, the uncoated cell cycled to 4.5 V began to exhibit severe capacity fade after 30 cycles for C/2.5 cycling and after 45 cycles for C/5 cycling, and the cell cycled to 4.475 V began to exhibit severe capacity fade after 35 cycles for C/2.5 cycling

and after 60 cycles for C/5 cycling. Uncoated cells had significantly better capacity retention than coated cells, and small capacity fade in cells up to 4.45 V, unlike the coated cells.

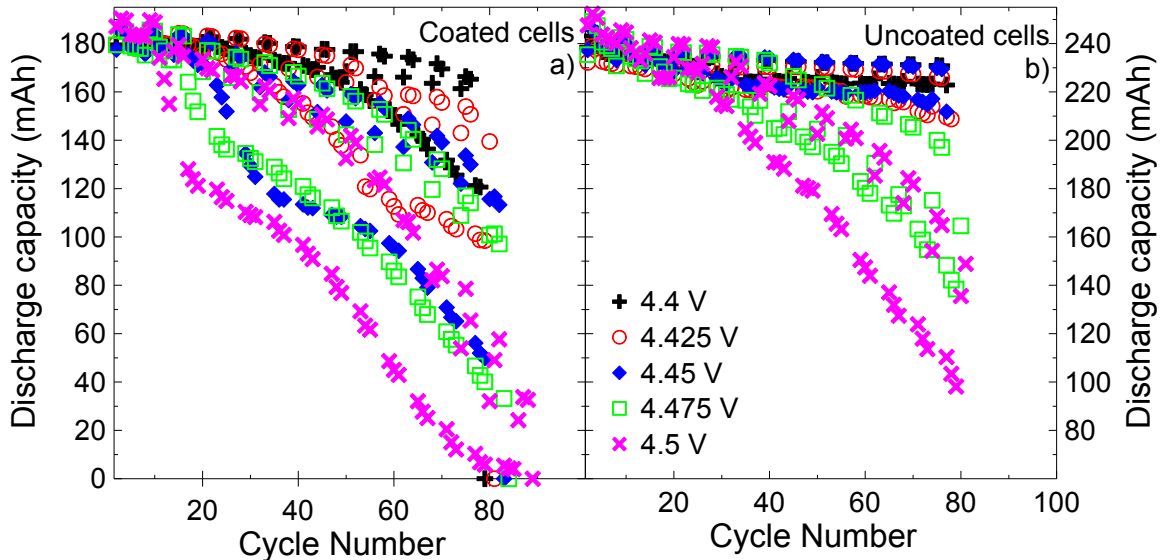


Figure 4.1 The discharge capacity of a) LaPO_4 -coated and b) uncoated NMC442/graphite pouch cells undergoing charge-hold-discharge cycling tests and FRA measurements at 40°C with upper cutoff potentials between 4.4 and 4.5 V. Each cell has two distinct sets of data points displaying the capacity of the two C/5 (high capacity) and the three C/2.5 (lower capacity) discharge segments.

Figure 4.2 shows the impedance spectra collected by the FRA at all voltages during cycles 26, 50, and 74 for the coated (top panels) and uncoated (bottom panels) cells cycled with an upper cutoff potential of 4.4 V. With an upper cutoff of 4.4 V, the coated cell had very small impedance at cycles 26 and cycles 50, but grew significantly by cycle 74, particularly at high potential. By contrast, the uncoated cell showed very little change in impedance spectra with cycle number. The uncoated cell exhibited very small increases in the high frequency real component of the impedance spectra with cycle

number (from ~ 1.1 to 1.15Ω), which indicates a minor increase in the electrolyte resistance or electrode resistance with cycle number. While the overall shift of the high frequency component with cycle number was the same for all potentials measured, at each cycle there was a clear difference in the high frequency component with potential. This indicates that, at low potentials, the ionic or electronic path resistance was larger than at high potentials. This may be due to a dynamic SEI layer on the positive or negative electrode that changes with potential. The coated cell exhibited much larger shifts in the high frequency real component of the impedance spectra with cycle number (from 1.5 to 1.7Ω), indicating a larger increase in the electrolyte or electrode resistance with cycle number compared to the uncoated cell. Furthermore, while the high frequency component of the coated cell was the same at all measured potentials for cycle 26 and cycle 50, the high frequency component measured at low potentials during cycle 74 shifted to higher values compared to those measured at high potentials. This indicates that a change to the electronic or ionic path resistance occurred at high cycle number and low potential.

Figure 4.3 shows the impedance spectra collected by the FRA for all voltages during cycles 26, 50, and 74 for the coated (top panels) and uncoated (bottom panels) cells cycled with an upper cutoff of 4.475 V . In all panels, the widths of the spectra grew with increasing voltage from 3.7 V . The coated cell exhibited significant impedance growth with both cycle number and voltage. At high potentials and large cycle numbers, the spectra from the coated cell are incomplete – the FRA does not scan to low enough frequency to capture the entire spectra.

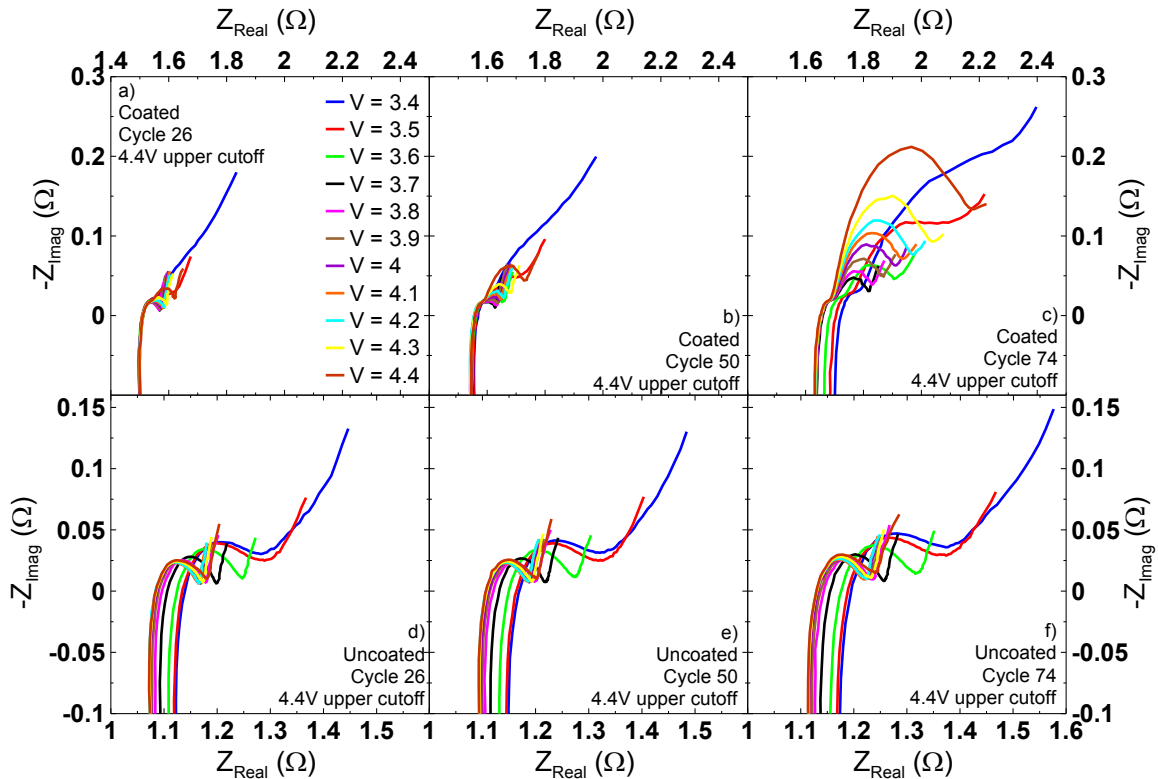


Figure 4.2 The impedance spectra as measured by the FRA for the coated cell at a) cycle 26, b) cycle 50 and, c) cycle 74 and for the uncoated cell at d) cycle 26, e) cycle 50, and f) cycle 74, both with an upper cutoff of 4.4 V. Note the different y axis scale for the coated and uncoated cells.

The uncoated cell exhibited impedance growth, albeit much less than shown by the coated cell. At high potential and large cycle number, the uncoated cell exhibited two peaks in the spectra. This is most likely due to a change in either the positive or negative electrode when the cell was repeatedly subjected to high potential. The uncoated cell exhibited small increases in the high frequency real component of the impedance spectra with cycle number, which indicates a minor increase in the electrolyte resistance or electrode resistance with cycle number. This increase was the same at all potentials measured. The coated cell exhibited much larger shifts in the high frequency real

component of the impedance spectra with cycle number, indicating a larger increase in the electrolyte or electrode resistance with cycle number compared to the uncoated cell. Furthermore, while the high frequency component of the coated cell was the same at all measured potentials for cycle 26, the high frequency component measured at low potentials during cycle 50 and 74 shifted to higher values compared to those measured at high potentials. This indicates that a change to the electronic or ionic path resistance occurred at high cycle number and low potential.

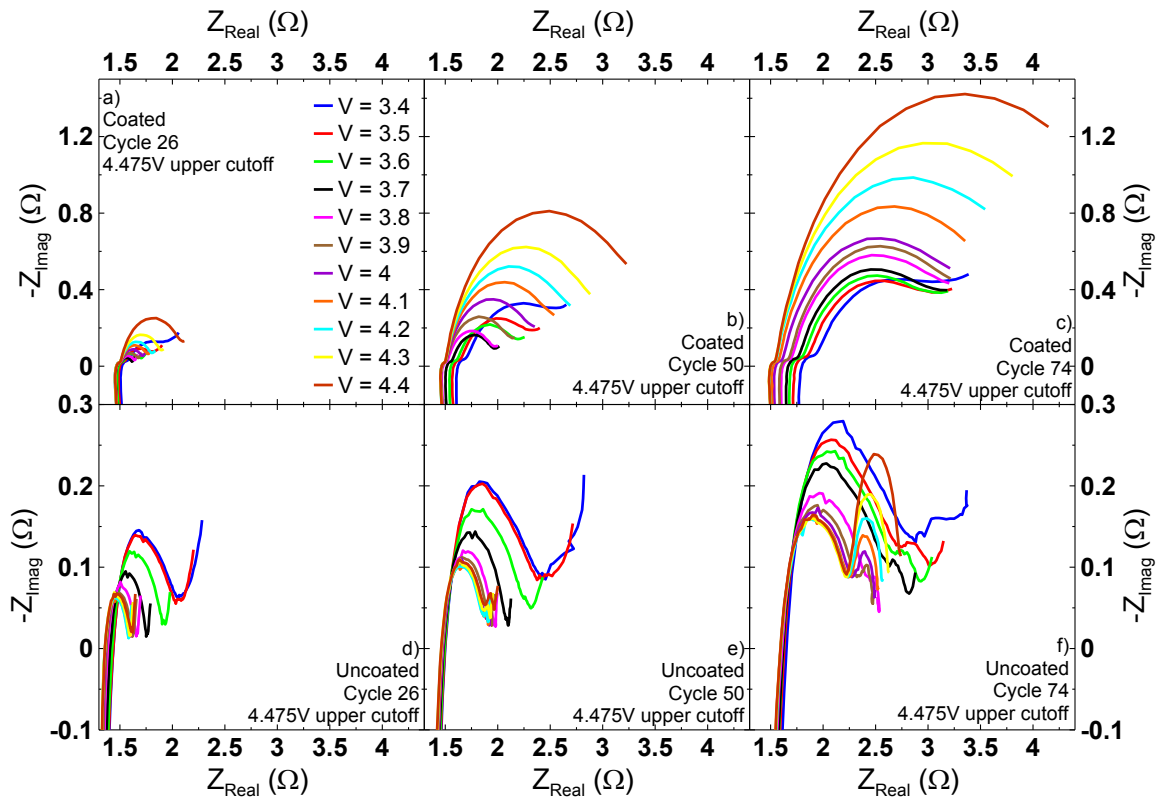


Figure 4.3 The impedance spectra as measured by the FRA for the coated cell at a) cycle 26, b) cycle 50 and, c) cycle 74 and for the uncoated cell at d) cycle 26, e) cycle 50, and f) cycle 74, both with an upper cutoff of 4.475 V.

In order to distinguish the contributions from the positive and negative electrode to the impedance growth, the coated and uncoated pouch cells charged to upper cutoff potentials of 4.4 V and 4.45 V were dismantled and assembled into positive and negative symmetric cells after 84 cycles. Figure 4.4 summarizes the EIS data for the symmetric cells. Figure 4.4a shows the impedance spectra of the positive electrode symmetric cells made from the coated pouch cells. Figure 4.4b shows the impedance spectra of the positive electrode symmetric cells made from the uncoated pouch cells and the inset shows a close-up view of the spectra. Similarly to the spectra shown in Figure 4.2 and Figure 4.3, the uncoated symmetric cells have much smaller impedance than the symmetric cells made from the coated electrodes. Figure 4.4a and Figure 4.4b show that the upper cutoff potential had a dramatic effect on the impedance from the positive electrode. Figure 4.4c and Figure 4.4d show the impedance spectra of the negative electrode symmetric cells made from the coated and uncoated pouch cells, respectively. The contribution to impedance from the negative electrode had negligible dependence on the upper cutoff potential, and was also unaffected by the use of a LaPO_4 coating on the positive electrode. Figure 4.4 clearly shows that the impedance growth exhibited by the cells charged to potentials above 4.4 V was dominated by contributions from the positive electrode and positive electrode SEI, which were heavily dependent on the upper cutoff potential.

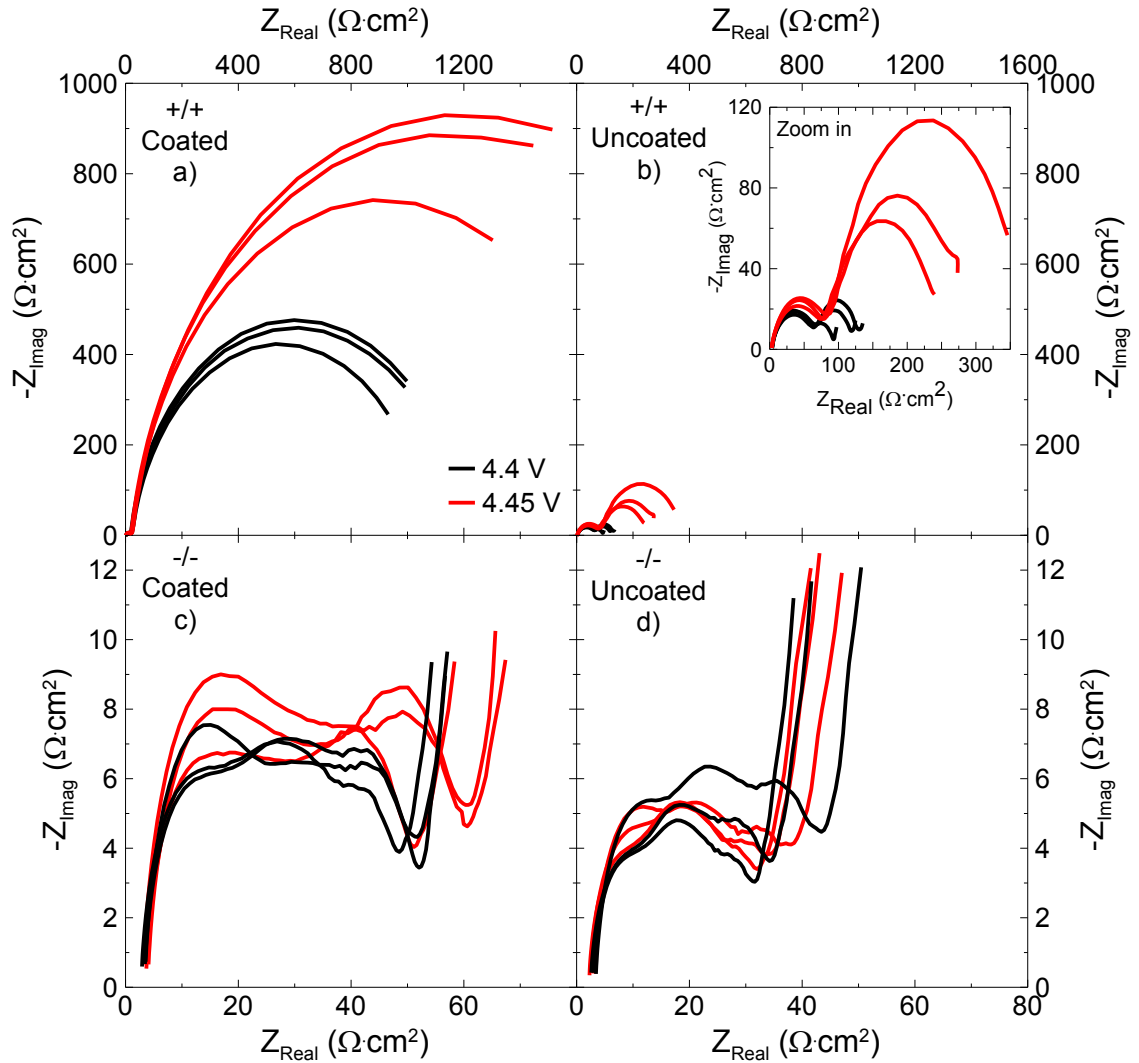


Figure 4.4 The impedance spectra measured at $10. \pm 0.1^\circ\text{C}$ for the a) coated positive symmetric cell, b) uncoated positive symmetric cell, c) coated negative symmetric cell, and d) uncoated negative symmetric cell made from the respective pouch cells charged to 4.4 and 4.45 V.

In order to interpret the changes to the impedance spectra shown in Figure 4.2 and Figure 4.3, a transmission line model of the positive electrode^{117,118} was used as shown in Figure 4.5a. In Figure 4.5a, the current collector is at the left and the separator is at the right. The circuit elements R_s , R_i , R_e , and C represent the resistance of the electronic path from particle to particle, the resistance of the ionic path from particle to particle, the charge

transfer resistance at each particle surface, and the double layer capacitance at the particles surfaces, respectively. The impedance of the circuit was solved analytically and also using LTSpice.¹³⁹ Both solutions gave identical results. The blue curves in Figure 4.5b show how the impedance spectrum changes if R_s is increased sequentially from 0.2 to 3.0 Ω at fixed values of R_e , R_i and C . The red curves in Figure 4.5b show how the impedance spectrum changes if R_e is increased sequentially from 0.25 to 0.3 Ω while R_s , R_i and C are held fixed. It is worth noting that the same effect as shown by the red curves could be obtained by fixing R_e and increasing R_i . Figure 4.5b shows that increasing R_s causes the width of the impedance spectrum along the real axis to increase while increasing R_e causes the high frequency intercept, and the whole impedance spectrum, to shift to the right. Figure 4.5c combines the effects of increases in R_s and R_e to approximately mimic the changes observed in the impedance spectra shown in Figure 4.3d-f for data collected at 3.8 V.

The purpose of Figure 4.5 is to demonstrate that changes in the charge transfer resistance are primarily responsible for the changes in the impedance spectra in Figure 4.2 and Figure 4.3, although both R_e and R_i could increase somewhat. A recent paper by Metzger et al.¹⁴⁰ suggested that oxidation of carbon black, leading to reduction of electronic conductivity of the positive electrode, was an important factor for cells exposed to high potentials. The data in Figure 4.2, Figure 4.3, and Figure 4.5 suggest that at potentials of 4.5 V and lower in these NMC442/graphite cells with PES222 electrolyte additive, decreases in electronic conductivity of the electrode are of minor impact compared to the increases in the charge transfer resistance.

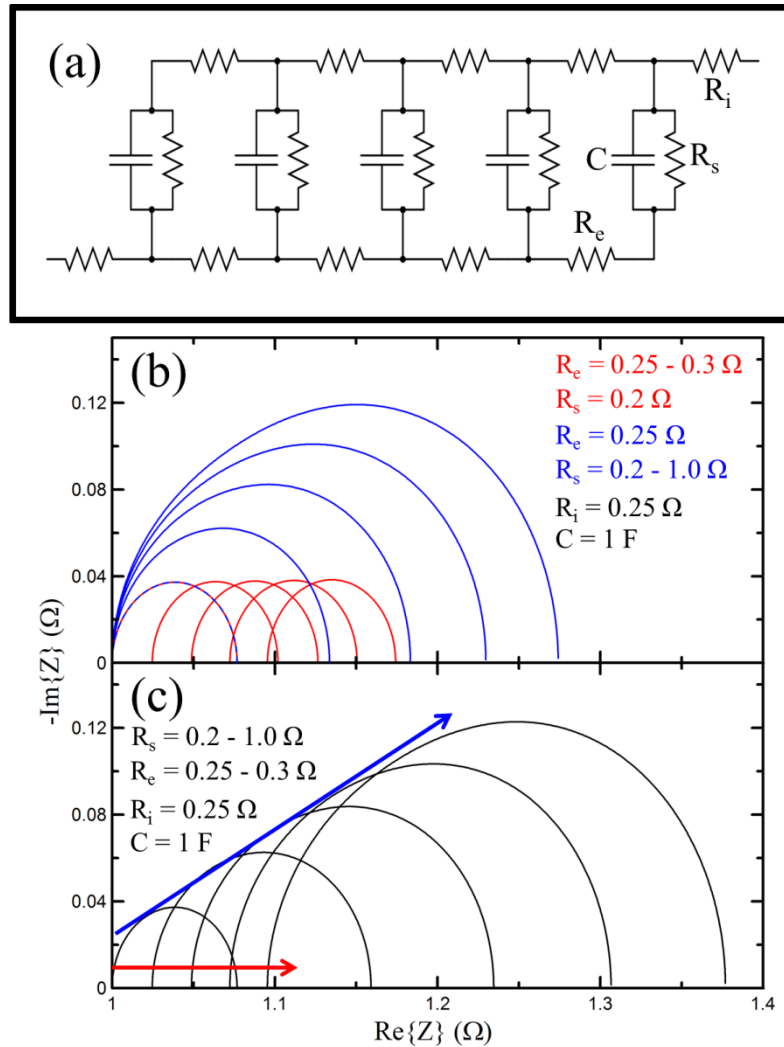


Figure 4.5 a) A transmission line model of the positive electrode used to interpret impedance spectra with the current collector at the left and the separator at the right. b) A Nyquist plot showing how the impedance spectrum changes if R_s is increased sequentially from 0.2 to 3.0 Ω at fixed values of R_e , R_i and C (blue curves) and how the impedance spectrum changes if R_e is increased sequentially from 0.25 to 0.3 Ω while R_s , R_i and C are held fixed (red curves). c) A Nyquist plot showing the effects of increases in both R_s and R_e to approximately mimic the changes observed in the impedance spectra shown in Figure 4.3d-f for data collected at 3.8 V. Work done and graph produced by Dan Abarbanel, 3rd year B. Sc. student, Physics and Atmospheric Science, Dalhousie University (2015).

Figure 4.6 shows R_{ct} (the combination of charge transfer resistances from both the positive and negative electrodes as well as the resistance due to the motion of ions through the SEI layers at both the positive and negative electrodes) as a function of potential for the cells described by Figure 4.2 and Figure 4.3. R_{ct} , for one electrode, is approximately equivalent to R_s in Figure 4.5. The value of R_{ct} plotted in Figure 4.6 was taken to be the widths, along the real axis, of the impedance spectra measured in Figure 4.2 and Figure 4.3 (as well as for other cycles not shown). Since incomplete spectra were measured for the coated cells at high potential and at large cycle numbers, as shown in Figure 4.3, R_{ct} for the incomplete spectra were taken as the differences between the real part of the impedance at the lowest measured frequency and where the high frequency data crossed the real axis. This means that R_{ct} for the coated cells was grossly underestimated when compared to the uncoated cells. This is an approximation, and it is possible to obtain more accurate values of R_{ct} through spectra fitting using equivalent circuit models. This will be discussed in Chapters 6, 7, and 9.

Each panel in Figure 4.6 shows R_{ct} measured during every other charge and discharge of the FRA cycle, every 12 cycles, for the coated and uncoated cells with the upper cutoff as indicated in each panel. The arrow in Figure 4.6b indicates the trend of the data with increasing cycle number and applies to all panels. Figure 4.6 shows that uncoated cells cycled up to 4.45 V had virtually no increase in R_{ct} with potential or with cycle number. Uncoated cells up to 4.475 and 4.5 V, however, show an increase in R_{ct} with cycle number. All LaPO_4 -coated cells exhibited impedance growth with cycle number and with increasing potential. Although the coated cell cycled to 4.4 V had small impedance

growth, R_{ct} was five times larger than the uncoated cell to the same potential. The LaPO_4 -coated cell cycled up to 4.425 V had fifteen times larger impedance growth than the uncoated cell cycled to the same potential and the LaPO_4 -coated cells cycled to 4.45 V and above exhibited extreme impedance growth.

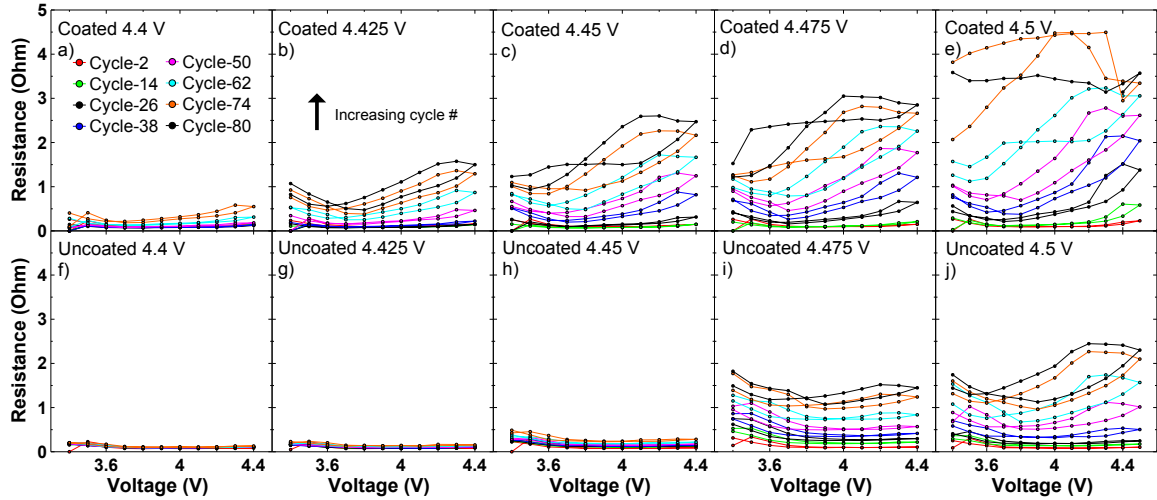


Figure 4.6 The combination of charge transfer resistance (both positive and negative electrodes) and resistance due to motion of ions through the SEI layers (both positive and negative electrodes), R_{ct} , as a function of voltage measured every 12 cycles. The arrow in panel b) indicated the trend of the data with increasing cycle number, and applies to all panels.

Figure 4.7 shows the values of R_{ct} (c and d) and the changes in R_e (or R_i or a combination of R_e and R_i) (a and b) extracted from the impedance spectra of LaPO_4 -coated cells (red) and from uncoated cells (black) at 3.4 V (circles) and at 4.4 V (crosses) for cells cycled to 4.4 V (a and c) and to 4.475 V (b and d). Figure 4.7 shows that increases in R_{ct} and R_e were less than 0.1 ohm for uncoated cells charged to 4.4 V over 84 aggressive charge-hold-discharge cycles at 40°C. By contrast, impedance increases occurred in LaPO_4 -coated cells after 40 cycles. Figure 4.7b and Figure 4.7d show that both R_{ct} and R_e

increased with cycle number for all cells charged to 4.475 V. However, the increases in R_{ct} were about 5 to 10 times larger than the increases in R_e . Again, it is worth noting that R_{ct} was underestimated for the coated cells in Figure 4.7d because the full semicircle was not accessed at the lowest frequency measured (see Figure 4.3b and Figure 4.3c).

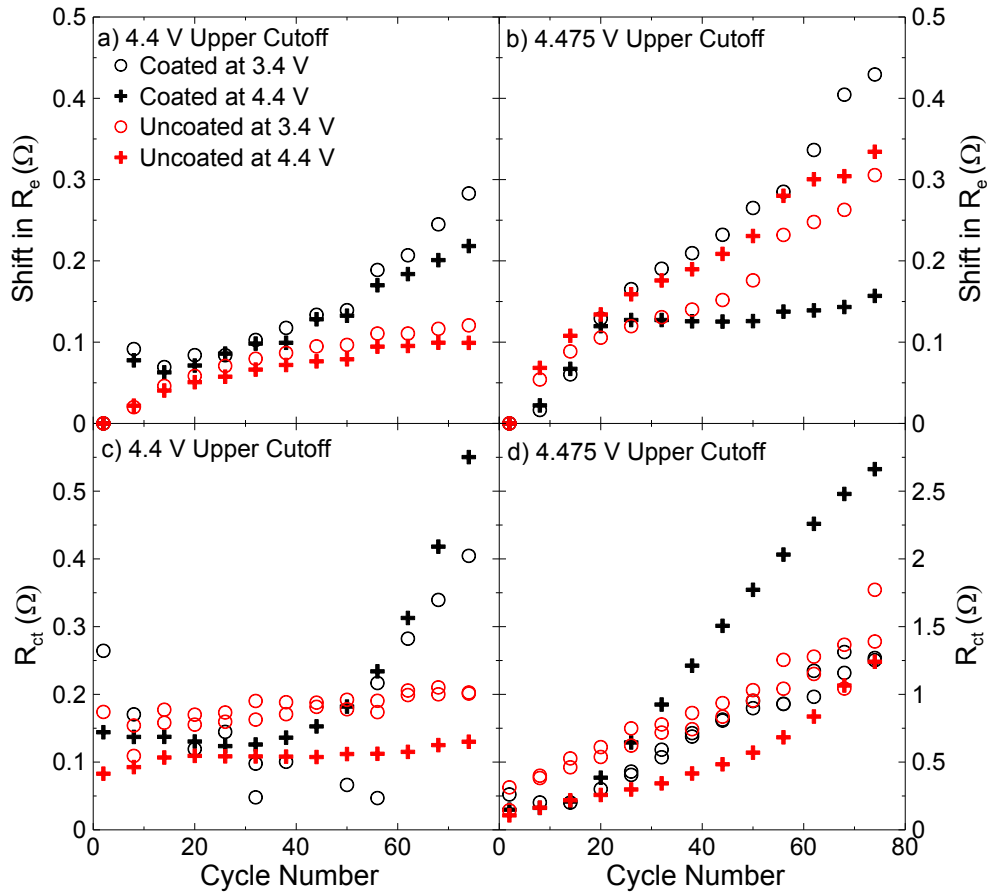


Figure 4.7 The values of R_{ct} (c and d) and the changes in R_e (or R_i or a combination of R_e and R_i) (a and b) extracted from the impedance spectra of LaPO_4 -coated cells (red) and from the uncoated cells (black) at 3.4 V (circles) and at 4.4 V (crosses) for cells cycled to 4.4 V (a and c) and to 4.475 V (b and d).

Figure 4.7c shows that the R_{ct} measured at 4.4 V for the coated cell cycled to 4.4 V stayed constant until approximately 50 cycles, after which there was a sharp increase in

impedance. Similarly, Figure 4.7d shows that the R_{ct} measured at 4.4 V for the coated cell cycled to 4.475 V stayed constant until approximately 25 cycles, after which there was a sharp increase in impedance. Figure 4.8a and Figure 4.8b show the difference between the average charge and discharge voltage, ΔV , as a function of cycle number for the coated and uncoated cells cycled to 4.4 V and 4.475 V, respectively. A smaller value of ΔV means there is smaller polarization and thus smaller cell impedance.¹⁴¹ While the uncoated cells showed a steady increase in ΔV , the coated cells cycled to 4.4 V and 4.475 V showed a sharp increase in ΔV after 50 and 25 cycles, respectively. This corresponds to the cycle at which a sharp increase in R_{ct} was observed for the same cells in Figure 4.7c and Figure 4.7d. It is possible that the LaPO_4 coating on the positive electrode was stripped away during cycling, and was accelerated at high potentials, This may lead to parasitic reactions and an increase in charge transfer resistance and ΔV .

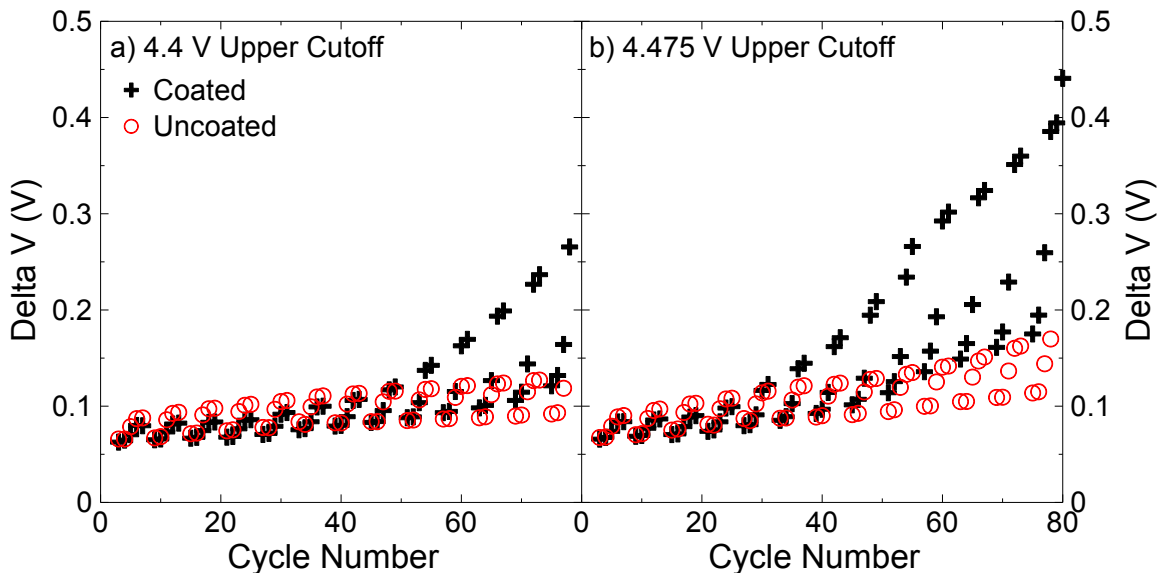


Figure 4.8 The difference between the average charge and discharge voltage, ΔV , as a function of cycle number for the coated (crosses) and uncoated (circles) cells cycled to a) 4.4 V and b) 4.475 V.

Figure 4.9a and Figure 4.9b show the volume of gas evolved in coated and uncoated cells, respectively, during each segment of formation and during the 84 charge-hold-discharge cycles coupled with the FRA. In general, the coated cell produced more gas during formation and during cycling than the uncoated cells. The initial volume of the pouch cells was 2.2 mL so an increase in volume of 0.4 mL represents a 20% expansion. This would be problematic for pouch-type Li-ion cells that operate without restraining clamps. Therefore, gas generation during such aggressive cycling represents a further problem that must be solved.

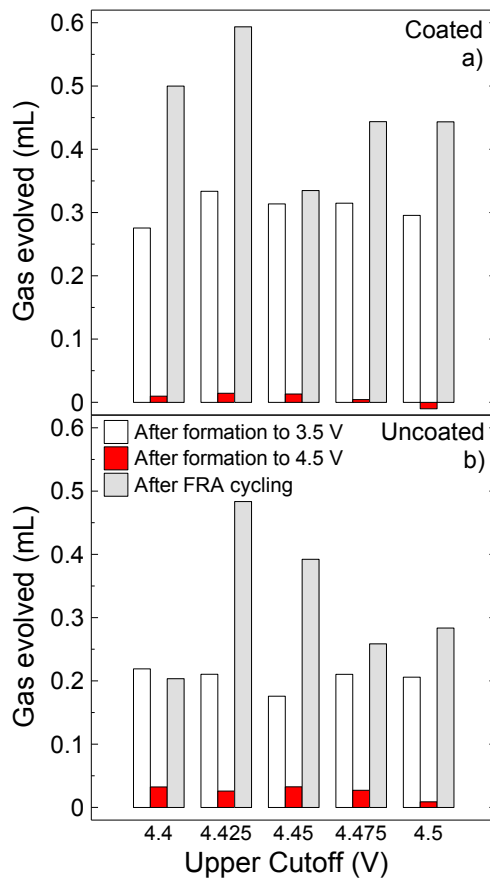


Figure 4.9 The volume of gas produced in a) coated and b) uncoated cells during both segments of formation and after the completion of 84 charge-hold-discharge cycles.

4.3 CONCLUSION

Impedance growth is the biggest obstacle to high-potential NMC/graphite Li-ion cells. The charge transfer resistance of the positive electrode increases much more (10x) than resistances associated with either the electronic or ionic path within the electrodes. Although positive electrode coatings may reduce the impedance of cells with control electrolyte, the work here shows that the use of certain electrolyte additive combinations was effective at reducing impedance growth and improving capacity retention in uncoated cells. The LaPO₄-coated cells used in this work demonstrated severe impedance growth and capacity fade when tested aggressively above 4.40 V. The uncoated cells performed well up to 4.45 V, where virtually no impedance growth or capacity fade was measured under the aggressive charge-hold-discharge test at 40°C, but the same cells failed when the upper cutoff was increased by only 25 mV to 4.475 V. This demonstrates the impact of the upper cutoff potential on cell lifetime and impedance growth. It is possible that the SEI layer on the positive electrode created by the PES222 additive set was itself oxidized and destroyed when the upper potential increases above 4.45 V (at 40°C) in the uncoated cells, leading to the formation of a rock salt surface layer.^{102,109}

The usefulness of automated impedance measurements coupled with cycling experiments has been demonstrated and, in addition, the importance of performing experiments representative of “real-life” Li-ion cell use. Results collected on high potential Li-ion cells during continuous high-rate charge-discharge cycling at 20°C are simply not representative of aggressive conditions that Li-ion cells can face.

This work, however, also raises a number of issues and stresses the need for follow-up experiments. As shown in Figure 4.2 and Figure 4.3, using a two-wire system to make impedance measurements resulted in an incredibly large inductive contribution from the equipment. This contribution can affect the accuracy of the high frequency data obtained, which is necessary to learn about changes to the electronic and ionic path resistances. Similar experiments utilizing four-wire measurements will be presented in Chapters 6 and 7. This work will emphasize the benefits of a four-wire system. The benefit of fitting impedance spectra using equivalent circuit models will be presented in Chapters 6, 7, and 9. Furthermore, it is necessary to explore the performance and impedance of other cell chemistries in experiments representative of “real-life” Li-ion cell use, as well as other electrolyte solvents, electrolyte additives, separators, current collectors, conducting diluents, and electrode surface coatings. Studies that investigate the effect of these changes on the performance of cells will be discussed in Chapter 5, 6, 7, 8, and 9.

CHAPTER 5. A COMPARISON OF NMC/GRAPHITE POUCH CELLS AND COMMERCIALY AVAILABLE LCO CELLS TESTED TO HIGH POTENTIAL

It is important to increase the voltage range of Li-ion cells to increase their energy density and reduce their overall cost. Li-ion cells in consumer electronic devices and electric vehicles often remain at high potentials for extended periods of time after charging. This means that testing protocols that assume a charge is always immediately followed by a discharge are not practical in predicting the lifetime and/or failure of Li-ion cells. Experiments that are representative of “real-life” Li-ion cell use are imperative to fully understand the performance of such cells.^{10,82}

Electrolyte additives and electrode materials have a dramatic effect on the lifetime and performance of cells cycled to high potentials. For example, as shown in Chapters 3, Li[Ni_{0.4}Mn_{0.4}Co_{0.2}]O₂ (NMC442)/graphite cells filled with ethylene carbonate (EC): ethyl methyl carbonate (EMC) based electrolyte containing the additives prop-1-ene-1,3-sultone (PES), methylene methane disulfonate (MMDS), and tris-(trimethyl-silyl) phosphite (TTSPi) had 88% capacity retention after 285 cycles when cycled continuously to 4.4 and 4.5 V.¹⁰ NMC442/graphite cells containing the same additive combination had severe capacity fade (72% retention) after only 50 cycles when cycled to 4.4 V with a potential hold at the top of charge for 24 hours.¹⁰ Nelson et al. showed that replacing MMDS for 1,3,2-dioxathiolane-2,2-dioxide (DTD) in cells resulted in dramatically improved capacity retention (92% retention after 65 cycles to 4.4 V with a potential hold

at the top of charge for 24 hours), demonstrating the importance of suitable electrolyte additives.¹⁰ Furthermore, with a LaPO₄ coating, NMC442/graphite cells containing the additives PES, DTD, and TTSPi cycled to 4.4 V with a 24 hour hold had 89% capacity retention after 80 cycles, and only 17% capacity retention after 80 cycles to 4.5 V, as shown in Chapter 4.⁸² Similar NMC442/graphite cells but without the LaPO₄ coating had 93% capacity retention after 80 cycles to 4.4 V, and 58% capacity retention after 80 cycles to 4.5 V.⁸² This demonstrates the effect that different electrode materials and different upper cutoff potentials have on the performance on Li-ion cells.

Commercially available LiCoO₂ (LCO)/graphite cells with upper cutoff potentials of 4.35 or 4.4 V are common and such cells^b are rated to have capacity retentions of > 75% after 300 cycles at 23-25°C.¹⁴²⁻¹⁴⁴ Shim et al. showed that LCO cells coated with Li_{1+x}Al_xTi_{2-x}(PO₄)₃ rated for 4.4 V had > 85% capacity retention and > 60% capacity retention after 500 and 700 cycles, respectively, at 23°C.¹⁴⁵ However, the cells were cycled at 1C, meaning the cells exhibited 40% capacity fade after only 2.5 months of testing. These cycle tests were made without extended hold periods at the top of charge so it is interesting to consider what the capacity retention would be if 24 hour holds at the top of charge were included in the protocols. NMC/graphite cells that can be charged to 4.4 V are not commonly found in the marketplace. NMC materials are preferable to LCO materials for the positive electrode due to the decreased cost associated with less cobalt

^b LCO cell model ICR1865030B had > 70% capacity retention after 300 cycles to 4.35 V at 25°C.¹⁴³ LCO cell model ICR18650B1 had > 75% capacity retention after 300 cycles to 4.35 V at 23°C.¹⁴⁴ LCO cell model ICR18650C1 had > 75% capacity retention after 300 cycles to 4.35 V at 23°C.¹⁴²

and more nickel and manganese present in the electrode.¹⁴⁻¹⁶ The work done by Nelson et al.^{10,82} and Li et al.¹⁴⁶ suggest that it is possible to have high performance NMC/graphite cells with appropriate electrolyte additives and electrode properties. It is therefore useful to compare such cells to commercially available Li-ion cells to learn if NMC/graphite cells with appropriate additive combinations are useful and competitive when compared to high potential cells made by industry. In this work, an NMC442/graphite pouch cell cycled aggressively to 4.4 V is compared to commercially available LCO cells tested under the same experimental conditions.

5.1 EXPERIMENTAL

Commercial LCO cells designed for high potential were obtained in order to compare to high potential NMC cells filled with additive combinations invented by Dahn et al.¹⁴⁷ The three types of commercial LCO cells had recommended upper cutoff voltages of 4.2, 4.35, or 4.4 V. These cells underwent an unknown formation procedure by the commercial supplier. These cells were prismatic cells and had capacities of 240, 260, and 265 mAh, respectively.

For comparison, a machine-made 240 mAh NMC442/graphite wound pouch cell balanced for 4.7 V operation was used. This cell underwent the standard filling procedure and formation cycle. The pouch cell was filled with 1M LiPF₆ in EC:EMC:PES:DTD:TTSPi 28:66:2:2:2. This additive combination will be referred to as PES222, and its positive effects on the performance of NMC/graphite cells have been documented.^{10,43,51,82,138}

After formation, all cells (both LCO and NMC) were placed in a $40. \pm 0.1^\circ\text{C}$ temperature box connected to a system capable of two-wire electrochemical impedance spectroscopy (EIS) measurements coupled with cycling capabilities, as described in Chapter 3.5. Cells underwent charge-hold-discharge cycling as shown in Figure 3.2. LCO cells were cycled between 3.0 V and an upper cutoff potential of 4.2, 4.35, or 4.4 V, depending on the rated upper cutoff potential of the cells. The NMC cell was cycled between 2.8 V and 4.4 V. The impedance was measured every 0.05 V (for LCO cells) and every 0.1 V (for the NMC cell) between 3.9 V and the upper cutoff potential from 40 mHz to 100 kHz. LCO cells were removed after 50 cycles, or 1600 hours and the NMC cell was removed after 84 cycles, or 2250 hours.

5.2 RESULTS

Figure 5.1 shows the fractional discharge capacity retention as a function of cycle number. Each cell has two distinct curves showing both the two C/5 and the three C/2.5 discharge segments. The cycles at C/5 had higher capacity than the cycles at C/2.5 due to cell polarization as expected. Figure 5.1 shows that the capacity retention of the LCO cells became worse as the upper cutoff potential increased. All LCO cells had worse capacity retention during the C/5 cycles than the NMC cell. Only the LCO cell cycled to 4.2 V had comparable performance to the C/2.5 cycles for the NMC cell. This means that although the commercial LCO cells were designed to withstand cycling to high potentials, they are unable to withstand an aggressive protocol that includes significant time spent at high potential at 40°C .

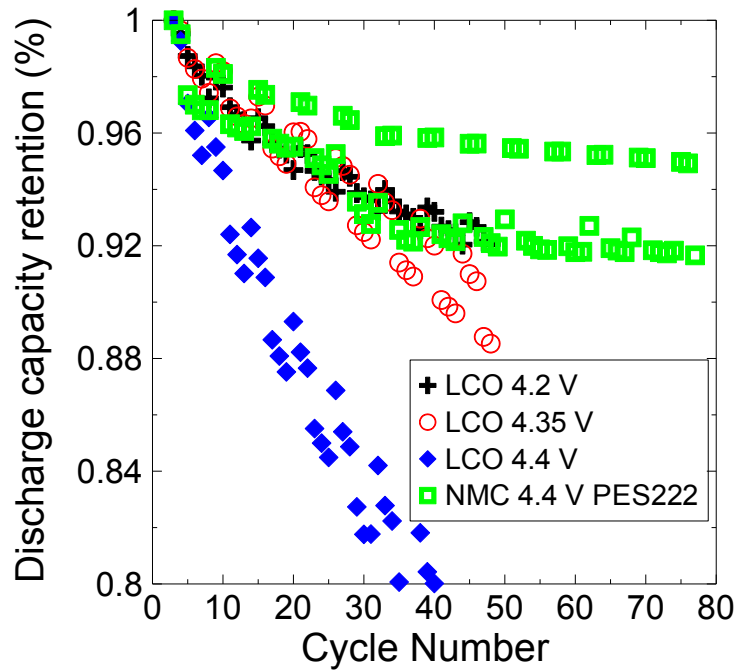


Figure 5.1. The fractional discharge capacity of the LCO and NMC cells undergoing charge-hold-discharge cycling at 40°C to the potentials indicated. Each cell has two distinct sets of data points displaying the capacity of the two C/5 (higher capacity) and the three C/2.5 (lower capacity) discharge segments.

Figure 5.2 shows R_{ct} as a function of potential for the cells shown in Figure 5.1. As shown in Figure 3.11, R_{ct} is the combination of the charge transfer resistances from both the positive and negative electrodes, and the resistance due to the motion of ions through the SEI layers at both the positive and negative electrodes. Figure 5.2a, Figure 5.2b, and Figure 5.2c show R_{ct} measured over 44 cycles for the LCO cells and Figure 5.2d shows the R_{ct} measured over 74 cycles for the NMC cell. The upper cutoff potential for each cell is shown in the label. Figure 5.2 shows that the NMC cell had the smallest overall impedance and smallest impedance growth. The impedance of the LCO cells increased with increasing upper cutoff voltage, corresponding to the capacity fade shown in Figure 5.1.

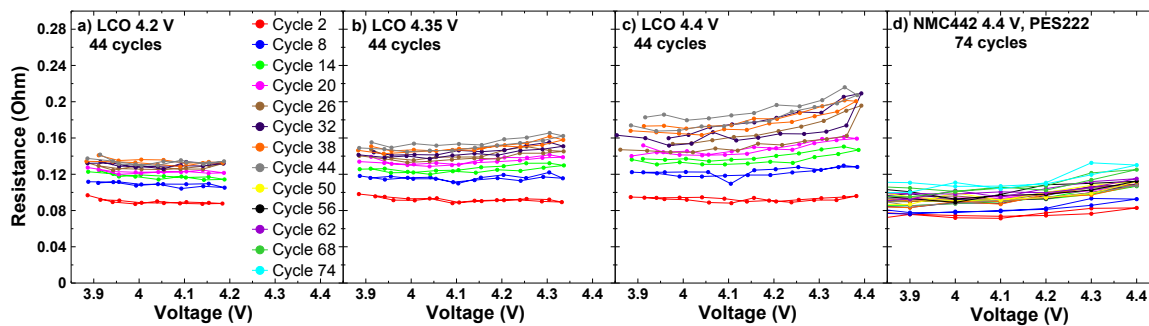


Figure 5.2 The combination of charge transfer resistance (both positive and negative electrodes) and resistance due to motion of ions through the SEI layers (both positive and negative electrodes), R_{ct} as a function of potential measured every 6 cycles.

Figure 5.3 shows the impedance spectra measured for the 4.2 V LCO cell, the 4.4 V LCO and the NMC cell. Figure 5.3a and Figure 5.3d show the impedance spectra for the 4.2 V LCO cell measured every 6 cycles at 3.9 and 4.2 V, respectively. Figure 5.3b and Figure 5.3e show the impedance spectra for the 4.4 V LCO cell measured every 6 cycles at 3.9 and 4.4 V, respectively. Figure 5.3c and Figure 5.3f show the impedance spectra for the 4.4 V NMC cell measured every 6 cycles at 3.9 and 4.4 V, respectively. The impedance growth for both the LCO and NMC cells cycled to 4.4 V was smaller at 3.9 V compared to at 4.4 V, whereas it was comparable at both 3.9 V and 4.2 V for the LCO cell cycled to 4.2 V. The shift of the spectra in the real axis, typically corresponding with changes to the electronic or ionic path resistance,^{82,119} were small for the LCO cells, but more significant for the NMC cell. This means that the ionic and/or electronic path resistance increased for the NMC cell cycled to 4.4 V over the 84 cycles. The overall impedance growth, or change in R_{ct} , for the 4.2 V LCO cell was significant, particularly between the first two EIS measurements. This increase was shown in Figure 5.2a. The overall impedance growth, or change in R_{ct} , was large for the 4.4 V LCO cell at 3.9 V and even

larger at 4.4 V. This was shown in Figure 5.2c. The overall impedance growth, or change in R_{ct} , was very small over all cycles for the NMC cell measured at 3.9 and 4.4 V. This was shown in Figure 5.2d. It is clear from the severe capacity fade exhibited by the 4.4 V LCO cell in Figure 5.1 that changes to R_{ct} have a significant impact on the cycling performance of LCO at high potential, and that changes to the electronic or ionic path resistance do not contribute significantly to capacity fade. More work is required to investigate ways to reduce changes to the electronic and ionic path resistances in NMC442/graphite cells and this will be discussed in Chapter 6.

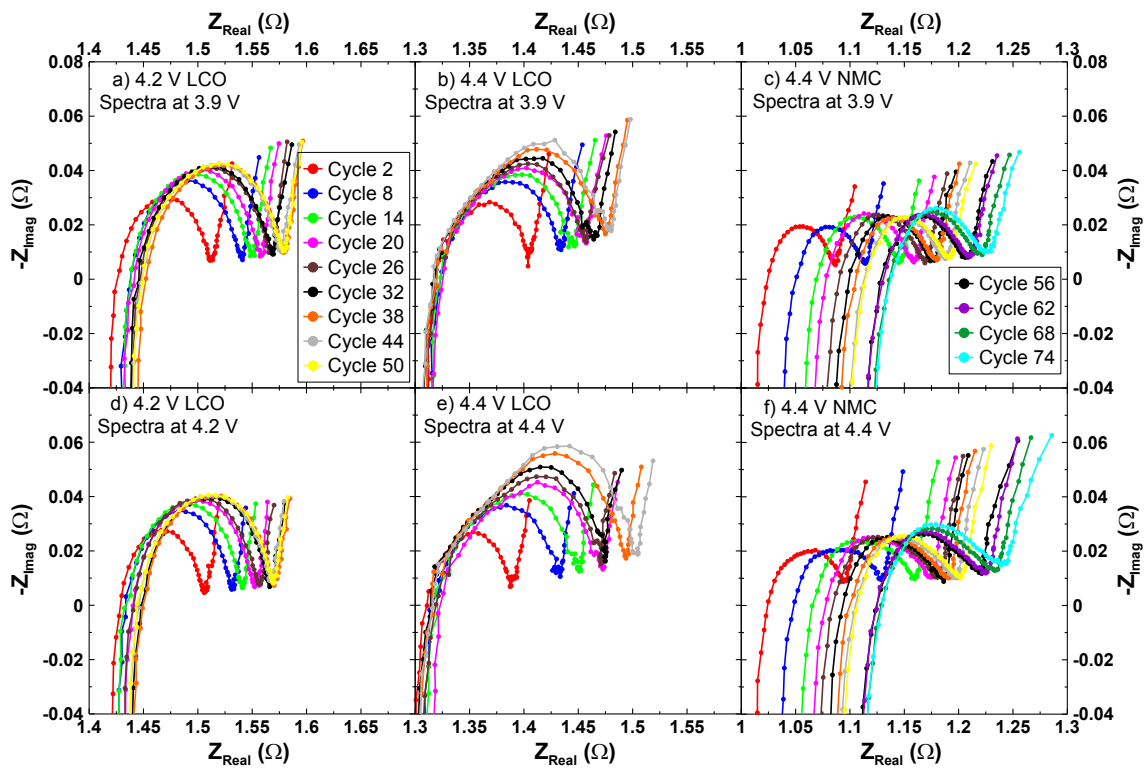


Figure 5.3 The impedance spectra for the LCO cell cycled to 4.2 V measured at a) 3.9 V and d) 4.2 V. The impedance spectra for the LCO cell cycled to 4.4 V measured at b) 3.9 V and e) 4.4 V. The impedance spectra for the NMC cell cycled to 4.4 V measured at c) 3.9 V and f) 4.4 V. The large high frequency tail is due to the inductive contribution from the two-wire system.

Differential voltage analysis was introduced by Bloom et al. and Honkura et al.^{148–150} Figure 5.4 shows differential voltage analysis (dV/dQ vs. Q) for the LCO cells, comparing measurements for a “fresh” cell (cycle 1) and after 50 charge-hold-discharge cycles. This data was collected at C/20 and 40°C using an ultra high precision charger.¹¹³ Figure 5.4 shows the differential voltage analysis aligned at the bottom of discharge. This was done to illustrate and understand the cause of capacity fade for the LCO cells as shown in Figure 5.1. Figure 5.4a shows that, at 4.2 V, the features related to the negative electrode align when the dV/dQ analysis is aligned at the bottom of discharge. At 4.35 and 4.4 V, these features do not align. In Figure 5.4a, the width of x remains constant during the 50 charge-hold-discharge cycles. The width of z shrinks during the 50 charge-hold-discharge cycles shown by z' . The dV/dQ analysis for the cell cycling to 4.2 V is consistent with SEI growth at the negative electrode, and is further illustrated by Figure 5.5.

Figure 5.5 shows an example voltage curve for LCO and graphite as a function of the fraction of available Li. The dashed curve for graphite indicates how the voltage curve changes after 50 charge-hold-discharge cycles. The voltage curve for LCO remains unchanged. The width of x corresponds to the amount of capacity available between the fully discharged state and the LiC_{12} graphite step. After 50 charge-hold-discharge cycles, the graphite curve shifts relative to the LCO curve, due to growth of the negative electrode SEI. The width of x remains the same. The width of z corresponds to the amount of capacity available between the LiC_{12} graphite step and the fully charged state. The width of z shrinks since the graphite curve shifts to higher values relative to the LCO

curve during the 50 cycles, shown by z' . Figure 5.5 therefore explains the differential voltage analysis shown in Figure 5.4a.

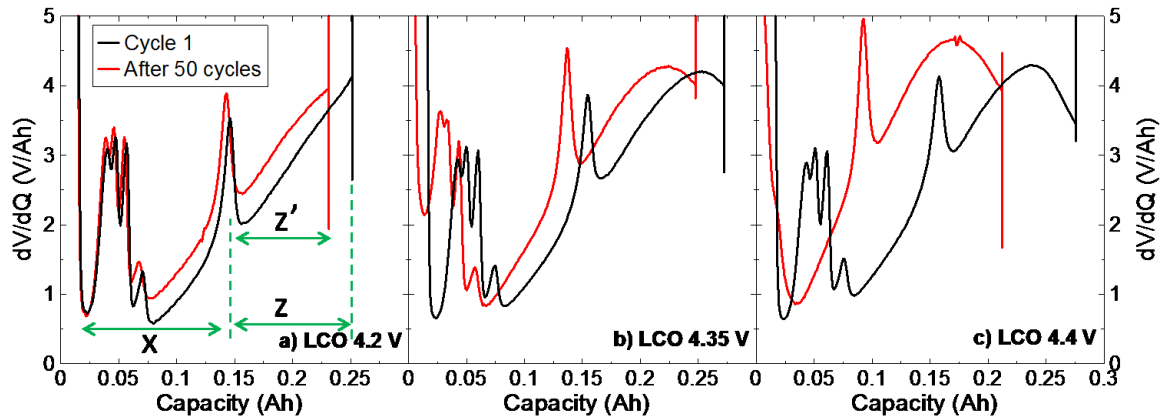


Figure 5.4 The differential voltage analysis (dV/dQ vs. Q) for the LCO cells aligned at the bottom of discharge for a fresh cell (cycle 1) and after 50 charge-hold-discharge cycles to a) 4.2 V, b) 4.35 V, and c) 4.4 V. The data were collected at C/20 at 40°C.

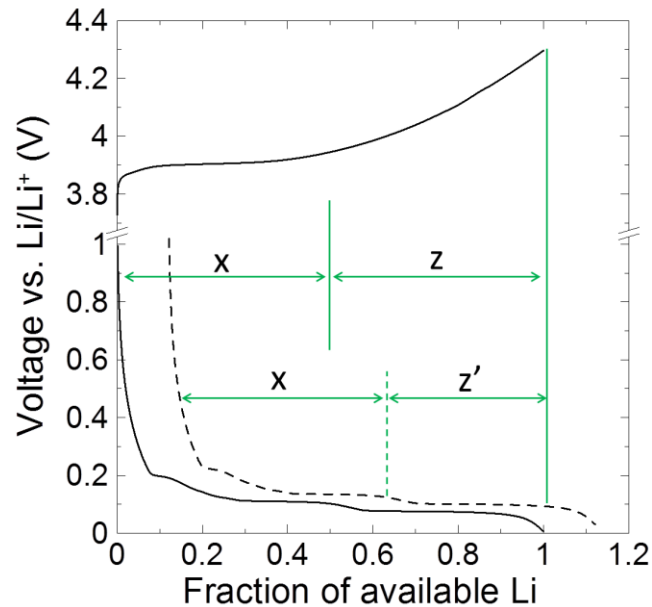


Figure 5.5 The voltage (vs. Li/Li^+) as a function of the fraction of available Li for LCO and graphite. The dashed curve indicates the proposed SEI growth, and subsequent shift of the V-Q curve of the negative electrode after 50 charge-hold-discharge cycles.

Figure 5.6 shows the differential voltage analysis aligned at the top of charge for the LCO cells, comparing measurements for a “fresh” cell (cycle 1) and after 50 charge-hold-discharge cycles. This was done to illustrate and understand the cause of capacity fade for the LCO cells as shown in Figure 5.1. Figure 5.6b shows that, at 4.35 V, the features align fairly well when the dV/dQ analysis is aligned at the top of charge. Figure 5.6c shows that, at 4.4 V, the features at high capacity align when the dV/dQ analysis is aligned at the top of charge, but the graphite features associated with the stage 4 and 3 phases are completely missing. The width of z remains constant during the 50 charge-hold discharge cycles, but the width of x shrinks, shown by x' . This suggests major positive electrode damage and is further illustrated by Figure 5.7.

Figure 5.7 shows an example voltage curve for LCO and graphite as a function of available Li. The dashed curve for LCO indicates that the voltage curve shrinks, due to positive electrode damage, relative to the graphite curve after 50 charge-hold-discharge cycles. The width of z corresponds to the amount of capacity available between the fully charged state and the LiC_{12} graphite step, and the width of z remains constant before and after the 50 cycles. The width of x corresponds to the amount of capacity between the fully discharged state and the LiC_{12} graphite step. After 50 cycles, it is likely that the positive electrode has severe damage resulting in loss of active mass at the positive electrode in addition to continual growth of the positive electrode SEI layer resulting in possible loss of electric contact to some particles. This is indicated by the width of x' . Continual growth of the positive electrode SEI layer was illustrated by the impedance growth of the spectra shown in Figure 5.3a and Figure 5.3c.

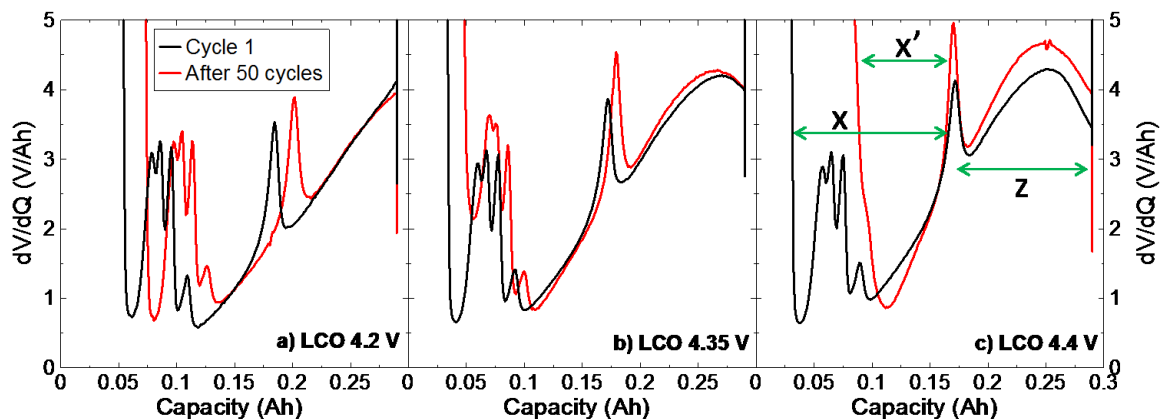


Figure 5.6 The differential voltage analysis for the LCO cells aligned at the top of charge for a fresh cell (cycle 1) and after 50 charge-hold-discharge cycles to a) 4.2 V, b) 4.35 V, and c) 4.4 V. The data were collected at C/20 at 40°C.

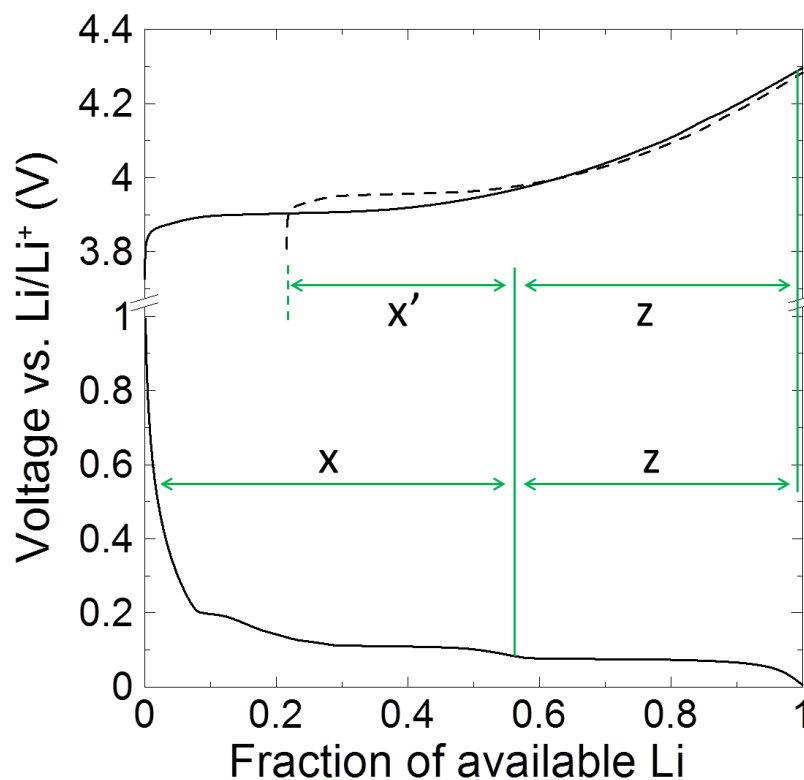


Figure 5.7 The voltage (vs. Li/Li^+) as a function of the fraction of available Li for LCO and graphite. The dashed curve indicates the impact of the proposed positive electrode damage and subsequent shrinkage of the positive electrode V-Q curve after 50 charge-hold-discharge cycles.

Figure 5.7 therefore explains the differential voltage analysis and missing graphite features shown in Figure 5.6c, the severe capacity loss shown by the 4.4 V cell in Figure 5.1 and the impedance growth shown in Figure 5.2.

Figure 5.8 shows the differential voltage analysis for the NMC cell, comparing measurements for a “fresh” cell (cycle 1) and a cell after 84 charge-hold-discharge cycles. For both cases, there are curves representing “measured” dV/dQ curves and “calculated” dV/dQ curves. The measured curves were numerically derived from the voltage and capacity data collected during cycling at C/50 and 40°C, similar to the data shown in Figure 5.4 and Figure 5.6. The calculated curves were obtained from the difference between the voltage-capacity curves of NMC/Li and graphite/Li half cells. By scaling the half cell voltage-capacity curves for electrode mass and incorporating a relative shift between the curves, it was possible to match the calculated dV/dQ vs Q to the measured dV/dQ vs Q. This procedure was performed by the software described by Dahn et al.¹⁵¹ The electrode masses and relative shift are important parameters that the software determined by least squares fitting of the measured and calculated dV/dQ vs Q curves. It was not possible to assemble half cells from the electrodes of the commercial LCO/graphite full cell, and therefore not possible to obtain calculated dV/dQ curves for the LCO cells. Therefore, calculated curves were not presented in Figure 5.4 and Figure 5.6.

Unlike for the LCO cells, the width between the features in Figure 5.8 does not shrink after charge-hold-discharge cycling for the NMC cell. The capacity shown is the same

for cycle 1 and cycle 84, which agrees with the minimal capacity fade shown in Figure 5.1. There are minor changes to the dV/dQ curve after cycling, possibly due to changes to the electrode surfaces.

It is clear that the commercially available “high potential” Li-ion cells tested here are unable to withstand aggressive high potential cycling with extensive hold periods at 40°C at the top of charge due to SEI growth, impedance growth and subsequent severe capacity fade. This work demonstrates the importance of testing high potential Li-ion cells using harsh experiments. Exposure to high potential and elevated temperature for extended periods of time can have detrimental effects on the performance and impedance of Li-ion cells, and such tests are necessary to predict failure during practical cell use.

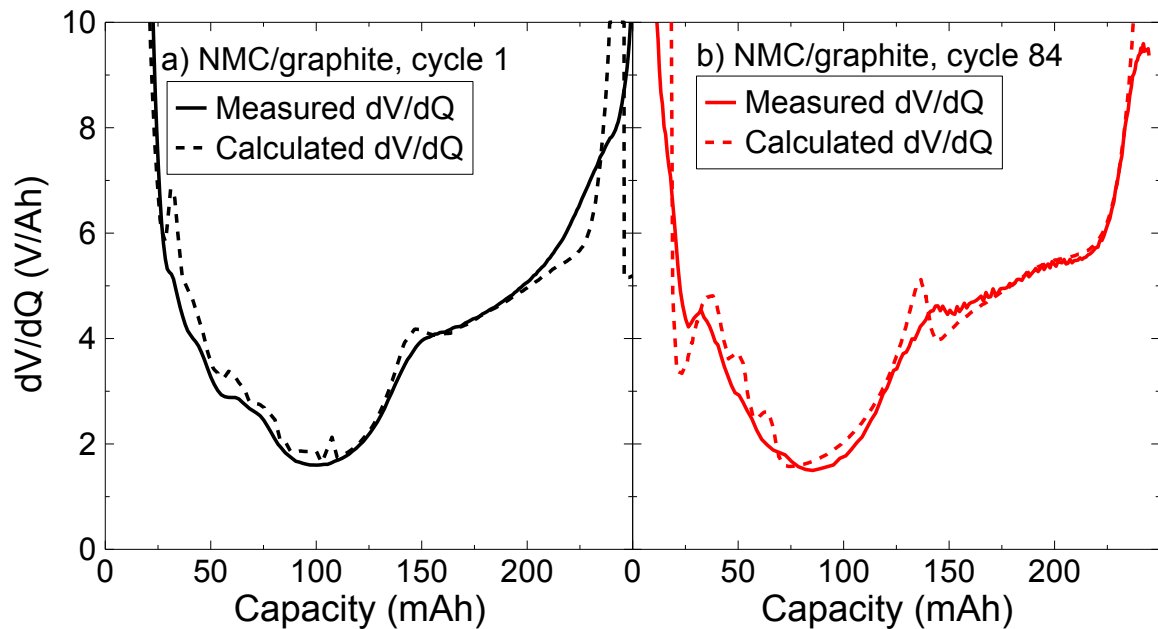


Figure 5.8 The measured and calculated differential voltage analysis for the NMC cell at a) cycle 1, and b) after 84 charge-hold-discharge cycles to 4.4 V. The data were collected at C/50 at 40°C. The calculated profiles were made using the software described by Dahn et al.¹⁵¹

5.3 CONCLUSION

Impedance growth, changes to the positive and negative SEI layers, and electrolyte oxidation all play a role in the performance of Li-ion cells when operated to high potential. In this work, an NMC/graphite pouch cell containing a state-of-the-art electrolyte additive combination and operated to 4.4 V was compared to commercially available “high potential” LCO cells, which were operated to their rated upper cutoff potentials of 4.2, 4.35, and 4.4 V, respectively. The tests at 40°C included a 24 h hold at the top of charge. The NMC cell operated to 4.4 V had good capacity retention and small impedance growth, and was comparable to the 4.2 V LCO cell. The 4.35 and 4.4 V LCO cells, however, had severe capacity fade and large impedance growth. Through differential voltage analysis, it was proposed that the growth of the negative electrode SEI was the cause for the small capacity fade and impedance growth observed for the LCO cell cycled to 4.2 V. It was proposed that major damage to the positive electrode was the cause for the large capacity fade and impedance growth observed for the LCO cells cycled to 4.35 and 4.4 V. Furthermore, the importance of using experiments representative of real-life Li-ion cell use to investigate the performance of high potential cells was demonstrated. The remainder of the work presented in this thesis studies various types of NMC positive electrode materials.

CHAPTER 6. EFFECTS OF VARIOUS CELL COMPONENTS ON THE IMPEDANCE OF NMC/GRAPHITE POUCH CELLS

As discussed in Chapters 4 and 5, choice of cell chemistry, upper cutoff potential, surface coatings, and electrolyte systems impacted the impedance growth of Li-ion cells. During aggressive charge-hold-discharge cycling, severe capacity fade due to impedance growth at the positive electrode occurs.^{10,82,119} An increase in the width, along the real axis, of the AC impedance spectrum, R_{ct} , is primarily due to increases in the resistance of the positive electrode solid electrolyte interphase (SEI) layer, whereas the shift in the high frequency intercept of the impedance spectrum corresponds to increases in the electronic and/or ionic path resistances.^{82,119} Impedance increase is accelerated during aggressive cycling conditions, such as cycling to high potential (4.5 V) or cycling that includes extended periods of time at high potential (4.4 V and above), but can be improved through the use of adequate electrolyte solvents and electrolyte additives. However, irreversible changes to impedance occur in all cells, and it is necessary to investigate the cause of irreversible impedance growth in cells and determine possible solutions.

In this work, $\text{Li}[\text{Ni}_{0.4}\text{Mn}_{0.4}\text{Co}_{0.2}]\text{O}_2$ (NMC442)/graphite pouch cells with a variety of cell components were investigated. The separator was either a ceramic-coated polypropylene (PP) or a ceramic-filled polyethylene terephthalate (PET). The conducting diluent in the positive electrode was either carbon black (CB) or carbon nanotubes (CNT). The positive electrode current collector was either aluminum foil (Al) or carbon-coated Al foil (CC-

Al). The NMC/graphite cells discussed in Chapters 4 and 5 had PP, CB, and Al. That cell type will be considered the 'standard' cell type.

The different separators were chosen to explore their resistance to oxidation at high potential. PET has been shown to have electrochemical stability up to 5.0 V.³¹ PET has been shown to have good thermal stability and tensile strength.³¹ Cells containing PET had better electrochemical stability and higher capacity compared to those containing a PP separator.³¹ Lin Ma (Dalhousie University) showed that PET had better permeability than PP and that cells containing PET had lower impedance during charge-hold-discharge cycling and better performance during high precision cycling experiments.

The different conducting diluents were chosen to explore whether nanotubes could limit carbon degradation. Metzger et al. showed that ethylene carbonate (EC) oxidized rapidly with carbon black in Li-ion cells exposed to high potentials.¹⁴⁰ This oxidation can lead to a reduction of the electronic conductivity of the positive electrode. By eliminating CB from the cell, it is possible that the oxidation of EC would be prevented or reduced. The carbon-coated current collector was used in an attempt to improve the positive electrode/current collector interface. CC-Al has better electrical conductivity, mechanical strength, and adhesion to the electrode material compared to Al foil.¹⁵² It is possible that the carbon-coating can limit the corrosion of Al foil that occurs at high potentials.⁷¹

It is also important to investigate the effects that different electrolyte solvents and electrolyte additives can have on the impedance growth of Li-ion cells. As shown in Chapter 4, standard NMC442/graphite cells containing 1M LiPF₆ EC:ethyl methyl

carbonate (EMC) with 2% by weight each of prop-1-ene-1,3-sultone (PES), 1,3,2-dioxathiolane-2,2-dioxide (DTD), and tris-(trimethyl-silyl) phosphite (TTSPi) endured extended periods of time at high potential with low impedance growth. This additive combination also led to low gas evolution in NMC/graphite cells. Therefore, this electrolyte was chosen to compare the performance of the eight cell types discussed.

Another electrolyte, 1M LiPF₆ EMC:fluoroethylene carbonate (FEC):pyridine phosphorus pentafluoride (PPF) 94:5:1, was also chosen for this study. By eliminating EC from the electrolyte, it is possible that the carbon degradation that occurs at high potentials will be prevented or reduced. Petibon et al. studied electrolyte systems without EC for Li-ion cells.¹⁵³ They showed that NMC442/graphite pouch cells containing EC-free linear alkyl carbonate-based electrolytes had long cycle life when cycled to 4.4 V, and that the EC-free electrolyte, when the salt concentration was greater than 0.4 M, had good conductivity, low impedance, and low electrolyte oxidation. Petibon et al. measured the voltage drop of cells left at open circuit voltage for 500 hours, and found that cells containing EC-free electrolyte had the smallest voltage drop. A smaller voltage drop indicates less electrolyte oxidation at the positive electrode.¹⁵⁴ Xia et al. showed that by using appropriate additives as ‘passivating agents’, EC-free electrolytes resulted in cells with better performance compared to EC-containing cells.¹⁵⁵

6.1 EXPERIMENTAL

The cells used were 180 mAh NMC442/graphite wound pouch cells. The cells contained either a ceramic-coated (Al₂O₃) polypropylene or a ceramic-filled (Al₂O₃) polyethylene

terephthalate separator, carbon black or carbon nanotubes as the conducting material in the positive electrode, and Al foil or a carbon-coated Al foil as the positive electrode current collector. Therefore, there are eight unique cell types.

The PP separator had a porosity of ~40%. The PET separator was manufactured by Freudenberg and had a porosity of ~55%. The Al₂O₃ content of each separator was measured after heating the PP and PET separators to 900°C in air for 2 hours to leave only Al₂O₃. The measurements were repeated for three separator samples of each type to ensure repeatability. The PET separator was 67% Al₂O₃ by weight, and the PP separator was only 11% Al₂O₃ by weight. Table 6.1 summarizes these findings. The errors shown are the range in data for the three repeated measurements.

Table 6.1 Information about the Al₂O₃ content in the PP and PET separator obtained after 900°C heating for 2 hours.

	PP	PET	Al₂O₃
Density	0.946 g/cm ³	1.38 g/cm ³	3.95 g/cm ³
Total separator mass	0.162 ± 0.005 g	0.413 ± 0.002 g	-
Polymer mass	0.143 ± 0.006 g	0.135 ± 0.002 g	-
Al₂O₃ mass	0.0185 ± 0.0005 g	0.278 ± 0.002 g	-
Weight fraction	11% Al ₂ O ₃	67% Al ₂ O ₃	-
Polymer volume	0.151 cm ³	0.098 cm ³	-
Al₂O₃ volume	0.00047 cm ³	0.070 cm ³	-

The carbon black was provided by LiFUN and added at 2 wt. % to the electrode. The CNT was provided by CNano and was added at 0.4 wt. %. The Al foil was provided by LiFUN, and the CC-Al was provided by 3M Co. Cell details are described in Appendix A. All cells underwent the standard filling procedure and formation cycle.

Two separate experiments were done and will be discussed in the following two sections. During both experiments, electrochemical impedance spectroscopy (EIS) measurements were taken regularly during cycling. In this work, an equivalent circuit model was used to fit the measured impedance spectra from all cells. All fitting of the data in this work was done by Samuel Buteau. Adapted from Huang et al.,¹³⁶ Figure 6.1 shows the equivalent circuit model used to fit the measured impedance spectra. R_{ohmic} represents the electronic and/or ionic path resistances and W represents the Warburg diffusion component. There are three $R||\text{CPE}$ circuits, each dependent on the corresponding resistance, R , the critical frequency, ω_c , and the exponent, ϕ . The first $R||\text{CPE}$ is associated with the positive electrode SEI impedance. The second and third $R||\text{CPE}$ are associated with the negative electrode and the contact impedances for both the positive and negative electrode.

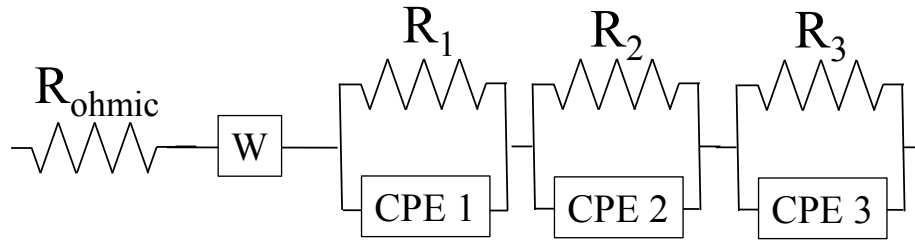


Figure 6.1 The equivalent circuit model used to fit measured spectra. W is a Warburg diffusion element and each CPE is a constant phase element. Adapted from Huang et al.¹³⁶

6.2 CHARGE-HOLD-DISCHARGE CYCLING AT 20°C

6.2.1 EXPERIMENTAL

In this study, the eight cell types were filled with 1M LiPF_6 EC:EMC:PES:DTD:TTSPi 28:66:2:2:2. This additive combination will be referred to as PES222. Cells underwent

charge-hold-discharge cycling to 4.4, 4.45, or 4.5 V at 20°C, as shown in Figure 6.2. These cells will be referred to as the 4.4 V cells, the 4.45 V cells, and the 4.5 V cells, respectively. Two cycles at $C/5$ were followed by three cycles with a $C/5$ charge and a $C/2.5$ discharge. All five cycles included a 24 hour hold at the top of charge. The five cycles were repeated twice for a total of 15 charge-hold-discharge cycles. Cells were then paused at 3.8 V and removed from the cycler so that EIS measurements could be taken. After EIS measurements, cells were placed back on the cycler and the entire protocol was repeated. Four-wire impedance measurements were taken at 3.8 V and 20°C using a Biologic SP-150 and a frequency range from 30 mHz to 100 kHz using 10 points per decade.

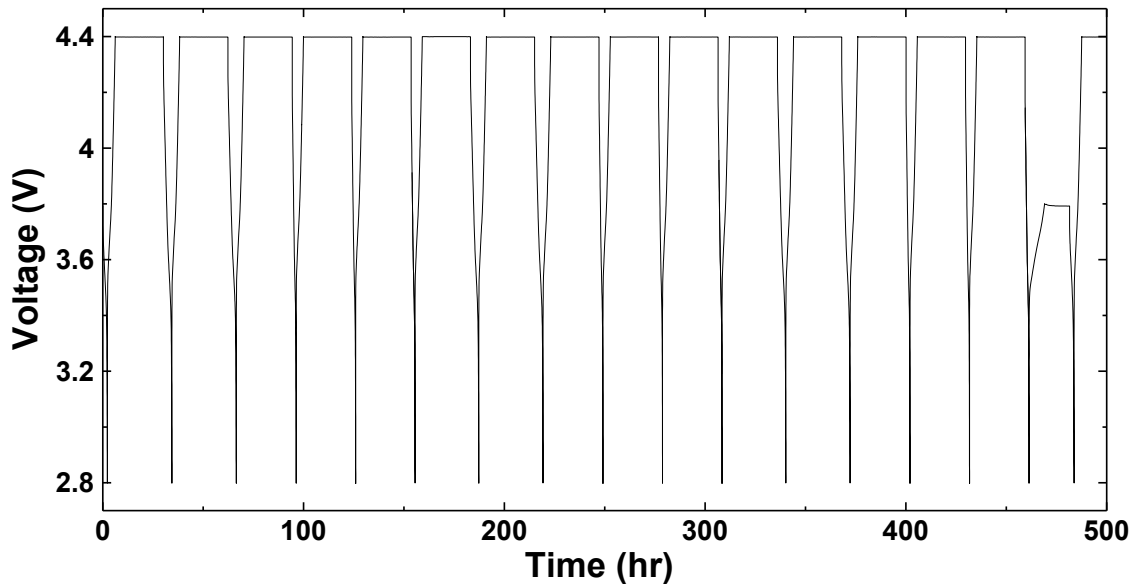


Figure 6.2 The charge-hold-discharge method used in the work presented in this section. The method includes two cycles at $C/5$, followed by three cycles with a $C/5$ charge and a $C/2.5$ discharge. All five cycles include a 24 hour hold at the top of charge, shown as 4.4 V in this figure. After approximately 15 cycles, cells were paused during a potential hold at 3.8 V for EIS measurements.

6.2.2 RESULTS

Figure 6.3 shows the discharge capacity as a function of cycle number for all cells undergoing charge-hold-discharge cycling. Figure 6.3a, Figure 6.3c, and Figure 6.3e show the discharge capacity for the 4.4, 4.45, and 4.5 V cells containing the PP separator, respectively. Figure 6.3b, Figure 6.3d, and Figure 6.3f show the discharge capacity for the 4.4, 4.45, and 4.5 V cells containing the PET separator, respectively. Each cell has two distinct data sets that display the difference in capacity between the two C/5 (higher capacity cycles) and the three C/2.5 discharge segments (lower capacity cycles), as shown in Figure 6.3c as an example. The dashed lines in Figure 6.3a and Figure 6.3b indicate when the cells were moved from a non-temperature controlled room to a temperature-controlled room. All 4.4 V cells exhibited good performance over the 140 cycles, or approximately 6.5 months of cycling, although the cells containing PET had a smaller rate of capacity fade than the cells containing PP. As explained in section 3.2, the charge-hold-discharge cycling protocol is an aggressive test. The 4.4 V cells containing CC-Al exhibited more capacity fade at the end of cycling compared to the cells containing Al.

All 4.45 V cells had good capacity retention until approximately 60 cycles, although the cells containing PET had a smaller rate of capacity fade than the cells containing PP. After 60 cycles, the 4.45 V cells began to show capacity fade in the high rate (C/2.5) cycles. The cells containing PET, CNT and Al had severe capacity fade during both the high and low rate cycles after 60 cycles despite exhibiting excellent capacity retention prior to cycle 60. The 4.5 V cells exhibited constant capacity fade which was accelerated

after 60 cycles for the C/2.5 cycles. There were no clear differences between the cell types for the 4.5 V cells.

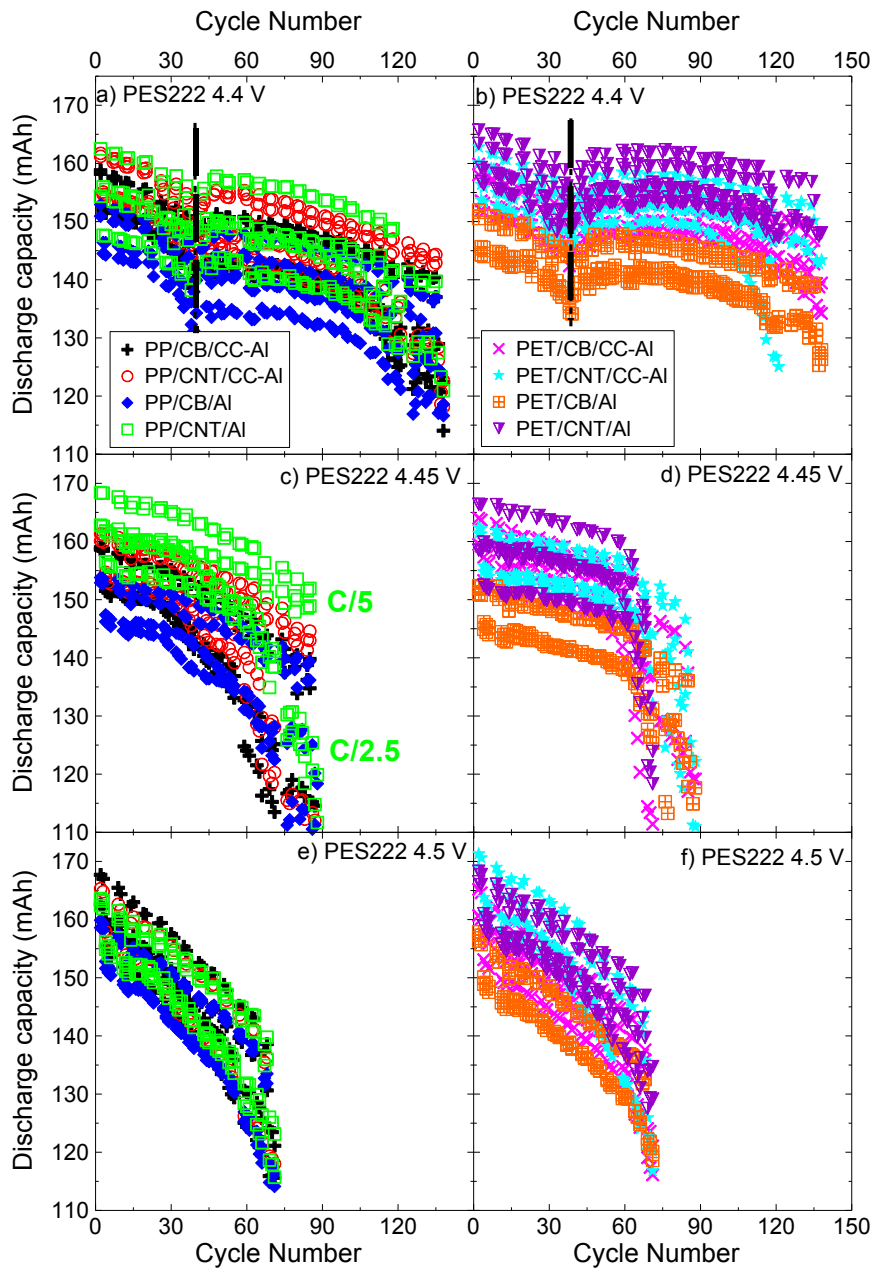


Figure 6.3 The discharge capacity as a function of cycle number for the 4.4 V cells containing a) PP and b) PET, for the 4.45 V cells containing c) PP and d) PET, and for the 4.5 V cells containing e) PP and f) PET as the separator material.

Figure 6.4 shows the impedance spectra measured at 3.8 V and 20°C for the 4.4 V cells, measured approximately every 15 cycles. The top panels of Figure 6.4 show the spectra for the cells containing the PP separator and the bottom panels show the spectra for the cells containing the PET separator. The impedance for all cells containing PP increased with cycle number, and the impedance growth accelerated after 90 cycles. This growth typically corresponds to the impedance associated with the positive electrode SEI layer.^{82,119} The impedance of cells containing PET and CNT decreased from cycle 20 to cycle 75, and then increased with increasing cycle number, albeit at a much smaller rate than the similar cells containing PP. The cell containing PET, CB, and Al exhibited large impedance growth after 75 cycles, although smaller than the similar cell containing PP. The impedance of the cell containing PET, CB, and CC-Al decreased until 75 cycles, and then increased very slightly such that the overall width of the spectrum along the real axis was the same at cycle 20 and at cycle 135. The impedance spectra for all cells shown in Figure 6.4 changed shape as cycle number increased, from spectra with a single-peak feature to spectra with multi-peak features.

From the spectra shown in Figure 6.4, it is clear that PET provided a significant advantage over PP, which was supported by the improved discharge capacity retention shown in Figure 6.3. It is surprising that PET had such a dramatic effect on the overall cell impedance compared to PP. One would expect that the choice of separator would impact the high frequency intercept, as it influences the electronic and ionic path resistances, and not the overall growth in the width of the impedance spectra along the real axis. Furthermore, CC-Al led to smaller impedance growth compared to Al, which

may be due to the ability of the carbon-coating to improve the current collector/electrolyte interface.

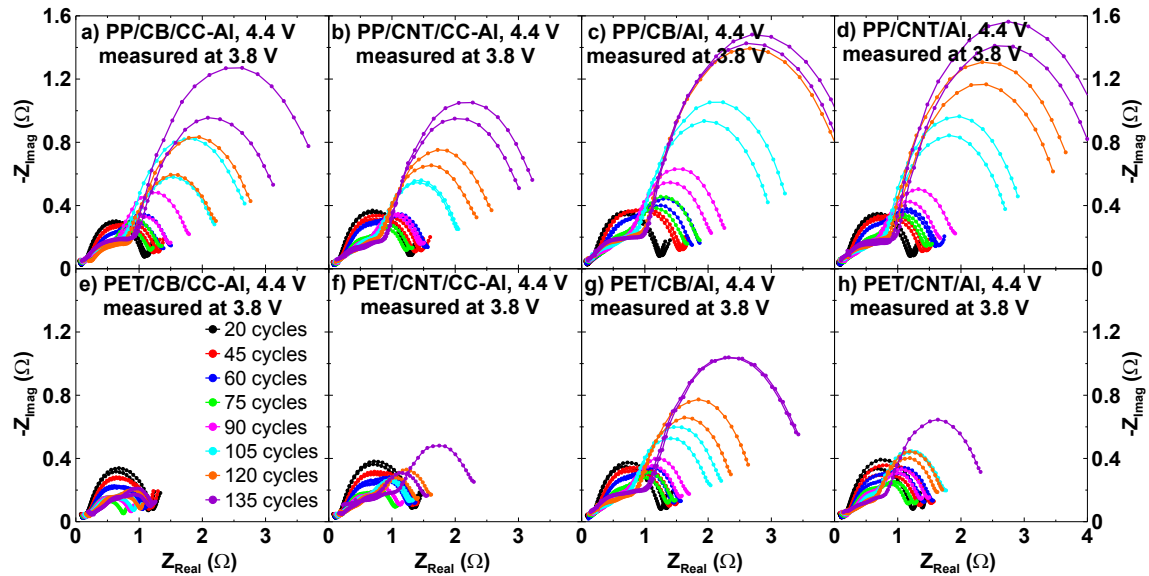


Figure 6.4 The impedance spectra measured at 3.8 V and 20°C every 15 cycles for the cells cycled to 4.4 V. The cells contained either PP or PET, CB or CNT, and CC-Al or Al, as indicated in each panel. Each panel shows results for two pair cells. The electrode area for all cells was 84.7 cm².

Figure 6.5 shows the impedance spectra measured at 3.8 V and 20°C for the 4.45 V cells, measured approximately every 15 cycles. The top panels of Figure 6.5 show the spectra for the cells containing the PP separator and the bottom panels show the spectra for the cells containing the PET separator. The impedance for all cells increased with cycle number, and the impedance growth accelerated after 40 cycles for the PP cells and after 55 cycles for the PET cells. This growth typically corresponds to the impedance associated with the positive electrode SEI layer. The impedance spectra for all cells shown in Figure 6.5 changed shape as cycle number increased, from spectra with a

single-peak feature to spectra with multi-peak features. The impedance growth for all 4.45 V cells was larger than the 4.4 V cells. From the spectra shown in Figure 6.5, it is clear that PET provided a significant advantage compared to PP for the 4.45 V cells, similar to the 4.4 V cells.

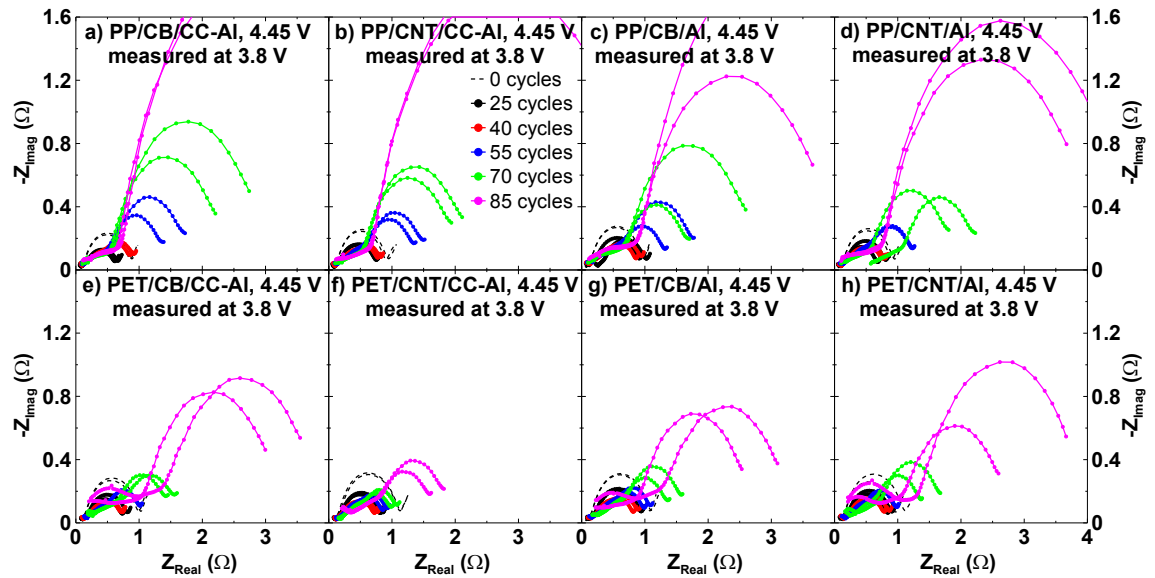


Figure 6.5 The impedance spectra measured at 3.8 V and 20°C every 15 cycles for the cells cycled to 4.45 V. The cells contained either PP or PET, CB or CNT, and CC-Al or Al, as indicated in each panel. Each panel shows results for two pair cells. The electrode area for all cells was 84.7 cm².

Figure 6.6 shows the impedance spectra measured at 3.8 V and 20°C for the 4.5 V cells, measured approximately every 15 cycles. The top panels of Figure 6.6 show the spectra for the cells containing the PP separator and the bottom panels show the spectra for the cells containing the PET separator. Please note that the scale of the axes in Figure 6.6 is larger than in Figure 6.4 and Figure 6.5. The impedance for all cells increased with cycle number. After 70 cycles, the 4.5 V cells had impedance growth at least three times larger

than the 4.45 V cells and at least six times larger than that 4.4 V cells at the same cycle number. At 4.5 V, all cell types had similar impedance growth, indicating that the various cell components explored in this work could only make an impact when the upper cutoff potential was below 4.5 V. This agrees with the discharge capacity versus cycle number shown in Figure 6.3, in which all cells have similar capacity fade.

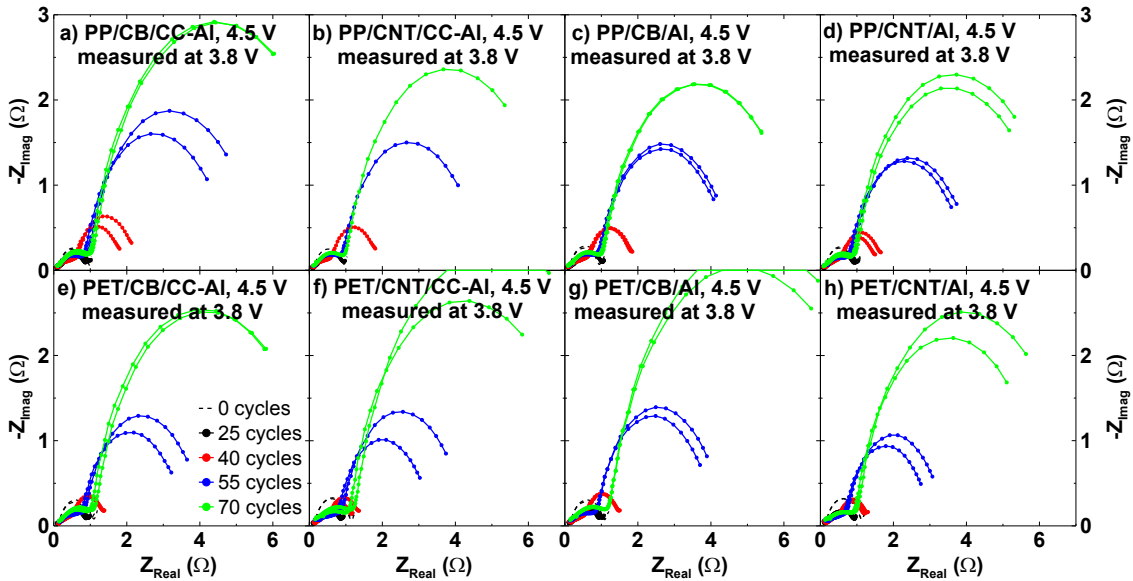


Figure 6.6 The impedance spectra measured at 3.8 V and 20°C every 15 cycles for the cells cycled to 4.5 V. The cells contained either PP or PET, CB or CNT, and CC-Al or Al, as indicated in each panel. Each panel shows results for two pair cells. The electrode area for all cells was 84.7 cm².

Figure 6.7 shows selected impedance spectra and the corresponding fitting results from the equivalent circuit model (Figure 6.1) for the 4.4 V cell containing PP, CB, CC-Al and PES222. Figure 6.7a shows the Nyquist representations of the selected spectra, Figure 6.7b shows the imaginary Bode representations and Figure 6.7c shows the real Bode

representations. There is good agreement between the measured spectra and the spectra obtained from fitting in all cases.

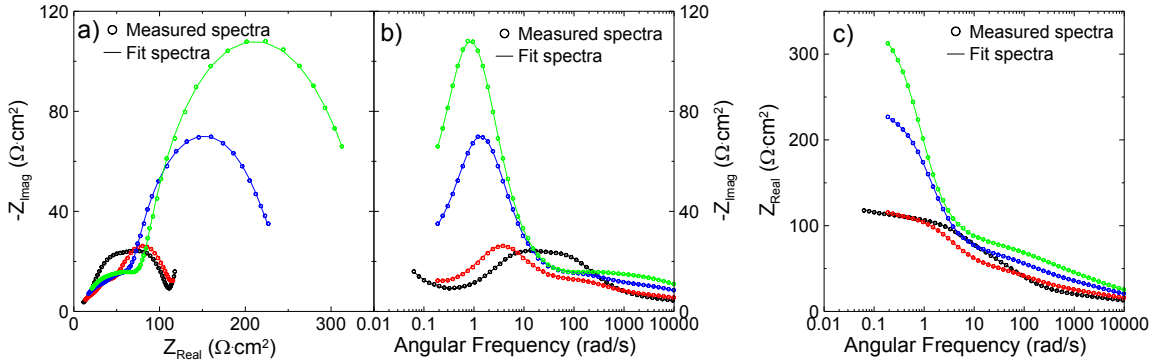


Figure 6.7 Selected impedance spectra and the corresponding fit for a 4.4 V cell containing PP, CB and CC-Al, measured during cycles 45, 75, 105 and 135, shown in a) Nyquist representation, b) imaginary Bode representation, and c) real Bode representation.

Figure 6.8 shows the impedance spectra for a cell containing PP/CB/Al and PES222 cycled to 4.4 V and the resulting symmetric cell impedance spectra measured after dismantling the full pouch cell and assembling symmetric coin cells, as described in section 3.6. Figure 6.8a shows the Nyquist representations of the spectra, Figure 6.8b shows the imaginary Bode representations and Figure 6.8c shows the real Bode representations. The green spectrum is the measured full pouch cell. The red spectrum is the negative symmetric cell. The blue spectrum is the positive symmetric cell. The black spectrum is the spectrum for the positive and negative symmetric cell added together at each measured frequency. All spectra are area normalized appropriately. Figure 6.8 shows that the positive symmetric cell impedance is significantly larger than the negative symmetric cell impedance, similar to the findings discussed in Chapter 4. It is clear that the full pouch cell is not the same as the sum of the positive and negative symmetric cell,

likely due to differences in the cell geometry and assembly. Both the positive and negative symmetric cell had two semicircular features, and the full pouch cell had three. It is clear that the largest feature at low frequency for the full pouch cell resulted from the positive electrode SEI. It is less clear which processes contribute to the two smaller features of the full pouch cell spectra that occur at mid-high frequency. In this work, therefore, the two features at mid-high frequency range (labelled as the 2nd and 3rd R||CPE component in Figure 6.1) will be generally attributed to the negative electrode SEI and the contact impedances from both the positive and negative electrode.

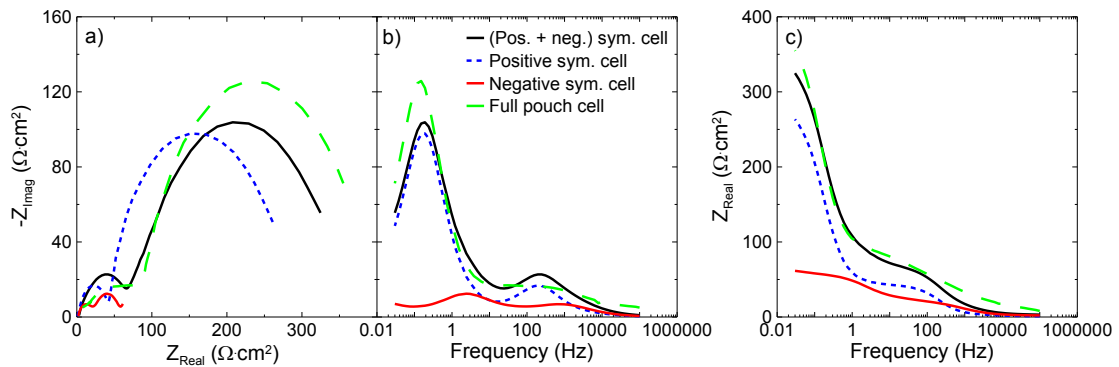


Figure 6.8 Impedance spectra for a full 4.4 V pouch cell containing PP, CB and CC-Al and the resulting symmetric coin cell impedance spectra shown in a) Nyquist representation, b) imaginary Bode representation, and c) real Bode representation.

Figure 6.9 and Figure 6.10 show the fitting results as a function of cycle number for the resistors in the equivalent circuit model (Figure 6.1) for cells containing CB and CNT, respectively. Each panel shows the fitting parameters for the cells cycled to 4.4, 4.45, and 4.5 V, although data was not available for cycle 0 for the 4.4 V cells. Figure 6.9a and Figure 6.10a show the results for parameter R_1 , which was associated with the positive electrode SEI. Figure 6.9c and Figure 6.10c show the results for parameter R_2 , and Figure

6.9d and Figure 6.10d show the results for parameter R_3 . These parameters were associated with the negative electrode and the contact resistance. Figure 6.9b and Figure 6.10b show the results of parameter R_{ohmic} , which was associated with the electronic and ionic path resistances.

Figure 6.9a and Figure 6.10a show clear trends of R_1 with increasing upper cutoff potential. In all cases, R_1 increased with cycle number, and this impedance growth was larger and occurred faster when the upper cutoff potential was increased. This agrees with the work presented in Chapters 4 and 5. While there were no clear differences in R_1 for cells containing CB compared to CNT, cells containing PET had lower growth in R_1 compared to cells containing PP. The parameter R_1 was significantly larger than R_2 , R_3 , and R_{ohmic} for all cells. Figure 6.9c and Figure 6.10c show that R_2 initially decreased with cycle number and then became constant. Cells cycled to 4.45 and 4.5 V reached a steady state earlier than cells cycled to 4.4 V. There were no clear differences in R_2 between the cell types. Figure 6.9d and Figure 6.10d show that R_3 increased with cycle number for all cells, and that the onset of this growth was larger and occurred faster when the upper cutoff potential increased. Figure 6.9b and Figure 6.10b show that R_{ohmic} increased slightly for the 4.4 V cells and increased significantly for the 4.45 and 4.5 V cells. R_{ohmic} increased most significantly for cells containing PET.

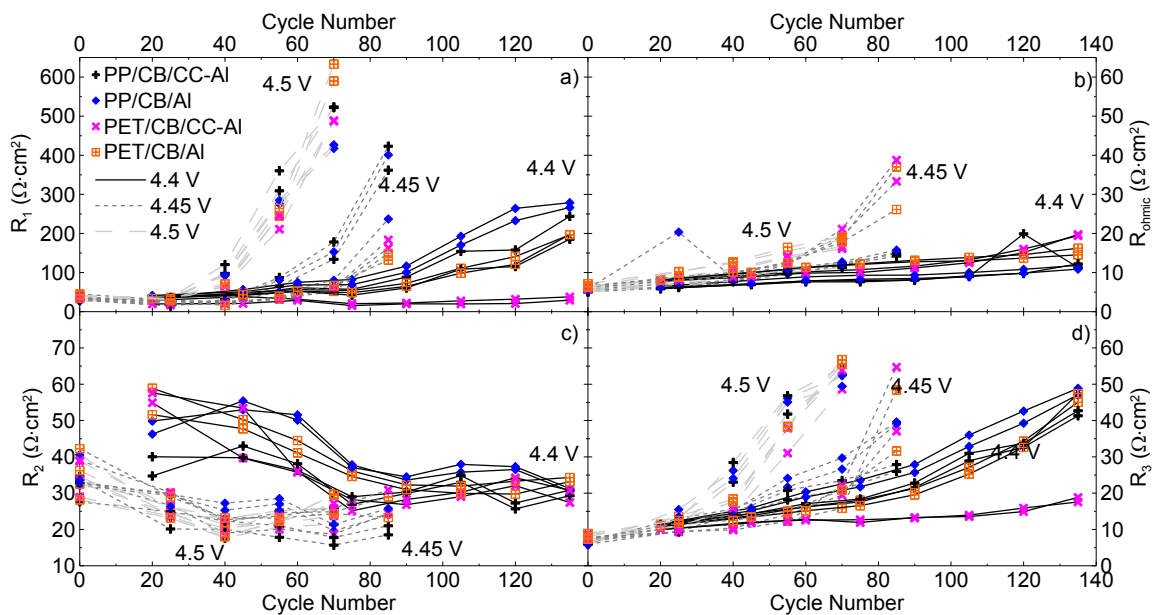


Figure 6.9 Parameters for the resistances a) R_1 , b) R_{ohmic} , c) R_2 , and d) R_3 obtained from fitting the impedance spectra of cells containing CB using an equivalent circuit model. The error bars, from fitting, are equal size or smaller than the symbols.

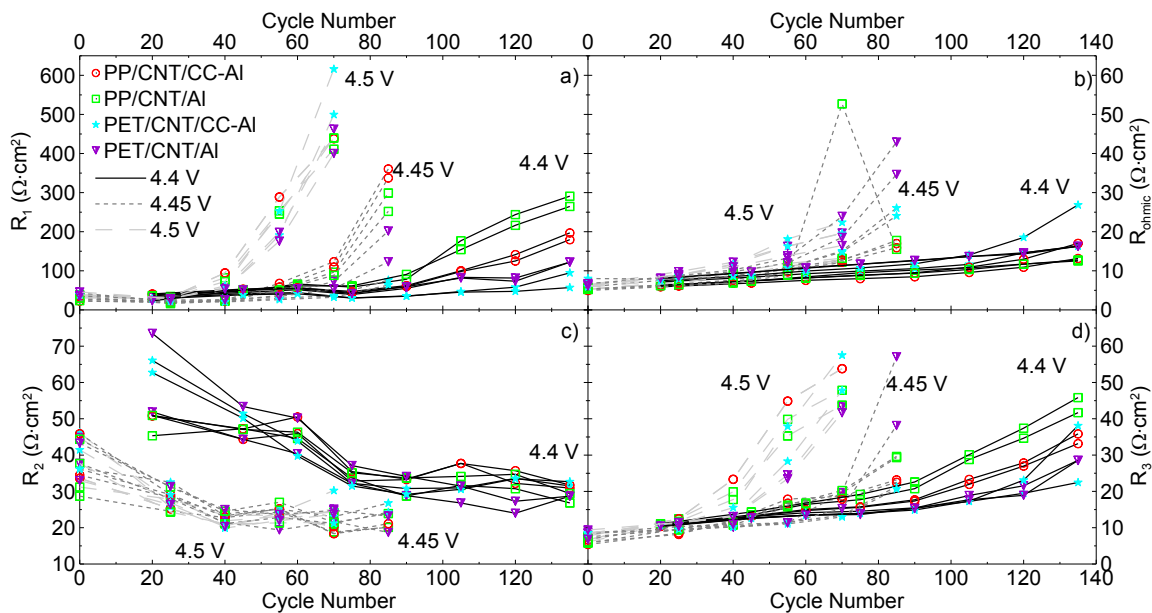


Figure 6.10 Parameters for the resistances a) R_1 , b) R_{ohmic} , c) R_2 , and d) R_3 obtained from fitting the impedance spectra of cells containing CNT using an equivalent circuit model. The error bars, from fitting, are equal size or smaller than the symbols.

Figure 6.11 shows the fitting results for the parameter R_1 from the equivalent circuit model for all cells compared to the value of R_{ct} . R_{ct} was taken as the approximate widths of the impedance spectra along the real axis shown in Figure 6.4, Figure 6.5, and Figure 6.6. R_{ct} was calculated as the difference between the real components of impedance corresponding to the minima in the imaginary component at both high and low frequency. In cases in which the impedance growth was too large to observe the Warburg diffusion tail at low frequency, the difference was taken as the minima of the high frequency component and the value measured at the lowest frequency. This means that R_{ct} was underestimated for several spectra.

Figure 6.11a and Figure 6.11c show the value of R_1 and R_{ct} , respectively, for the cells containing CB. Figure 6.11b and Figure 6.11d show the value of R_1 and R_{ct} , respectively, for the cells containing CNT. The trends of R_1 and R_{ct} were similar, demonstrating that R_{ct} was an acceptable indication of impedance growth as a function of time and cycle number. The method used to obtain R_{ct} was quick and easy, so it will be used throughout this thesis to provide a general analysis of impedance growth in Li-ion cells. Fitting using an equivalent circuit model will also be used to study selected cells to provide more detailed analysis of impedance growth.

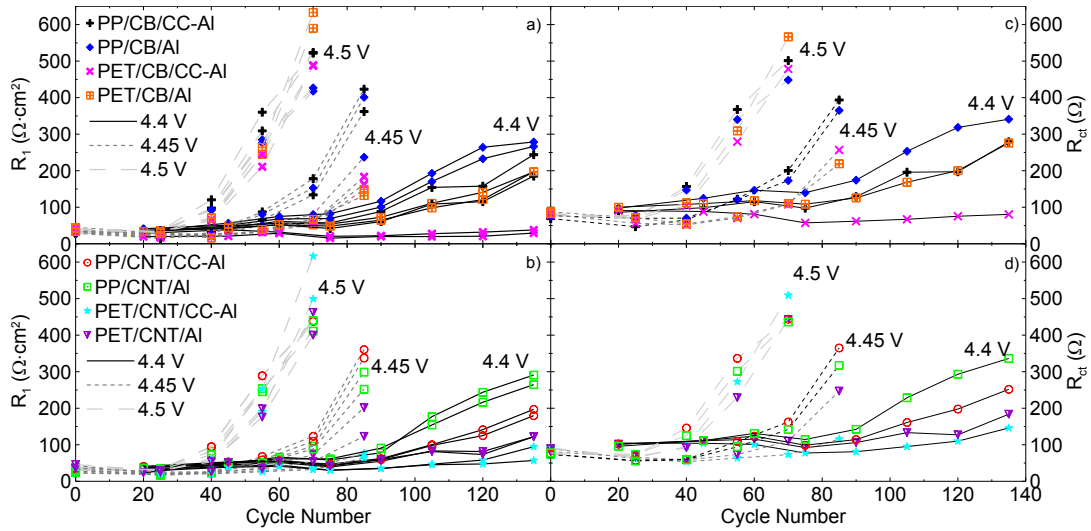


Figure 6.11 Parameters for the resistance, R_1 , obtained from fitting the impedance spectra of cells containing a) CB and b) CNT using an equivalent circuit model compared to the entire widths of the impedance spectra along the real axis, R_{ct} , for the cells containing c) CB and d) CNT. The error bars, from fitting, are equal size or smaller than the symbols.

Figure 6.12 and Figure 6.13 show the fitting results as a function of cycle number for the effective capacitance for the constant phase elements in the equivalent circuit model (Figure 6.1) for cells containing CB and CNT, respectively. For each $R||CPE$ circuit, an effective capacitance can be calculated from the corresponding resistance and the critical frequency, ω_c , obtained from the fit, using $\omega_c = 1/RC_{eff}$. In Figure 6.12 and Figure 6.13, each panel shows the fitting parameters for the cells cycled to 4.4, 4.45, and 4.5 V, although data is not available for cycle 0 for the 4.4 V cells. Figure 6.12a and Figure 6.13a show the results of parameter C_1 , which corresponds to the effective capacitance associated with the positive electrode SEI. Figure 6.12b and Figure 6.13b show the results of parameter C_2 and Figure 6.12c and Figure 6.13c show the results of parameter C_3 . These parameters correspond to the effective capacitance associated with the negative electrode and the contact impedances.

The trends of the data were the same regardless of the upper cutoff potential. In general for all cells in Figure 6.12 and Figure 6.13, C_1 tended to increase initially, and then stabilized as cycle number increased. C_2 was constant throughout cycling. C_3 initially decreased dramatically and then decreased slightly as cycle number increased. C_1 was largest and C_3 was smallest for all cells.

If capacitance remained constant during cycling but the corresponding resistance increased, then that may indicate that the SEI layer thickness was not changing (at 3.8 V) but becoming more resistive. This may be due to the formation of a rocksalt layer,¹⁰² such that while the thickness does not increase, Li diffusion becomes blocked. It would be valuable to monitor capacitance as a function of voltage, in addition to cycle number, to learn about the dependence on state-of-charge. For example, if capacitance changes with voltage, then it is possible that the thickness of the SEI layer, the surface area, or the dielectric constant is changing.

As explained in Figure 6.8, the source of C_2 and C_3 is unclear, but R_1 and C_1 are a direct result of the positive electrode SEI. It is worth doing a sample calculation of the SEI thickness that would result from $C_1=0.004 \text{ F/cm}^2$. The positive electrode has a specific surface area of 45 cm^2 per cm^2 of electrode area. Therefore, equation 6.1 can be used to determine the thickness of the positive electrode SEI where

$$C_1 = \frac{A\varepsilon_0}{d} \quad (6.1)$$

$$0.004 \frac{\text{F}}{\text{cm}^2} = \frac{45\varepsilon_0\varepsilon_r}{d}$$

$$d = 0.01 \text{ nm}$$

ϵ_0 is 8.854×10^{-12} F/m, d is the resulting thickness of the positive electrode SEI, and a relative dielectric constant, ϵ_r , of unity has been assumed. Typically, the positive electrode SEI is approximately 1-2 nm thick.¹⁵⁶ Therefore, the assumption used for the dielectric constant must be wrong. Assuming the SEI layer has a dielectric constant similar to EC ($\epsilon_r=90$),^{157,158} the calculated positive electrode SEI thickness becomes 0.9 nm, which is the correct order of magnitude. More work is needed to determine the true dielectric constant for the positive and negative SEI layers.

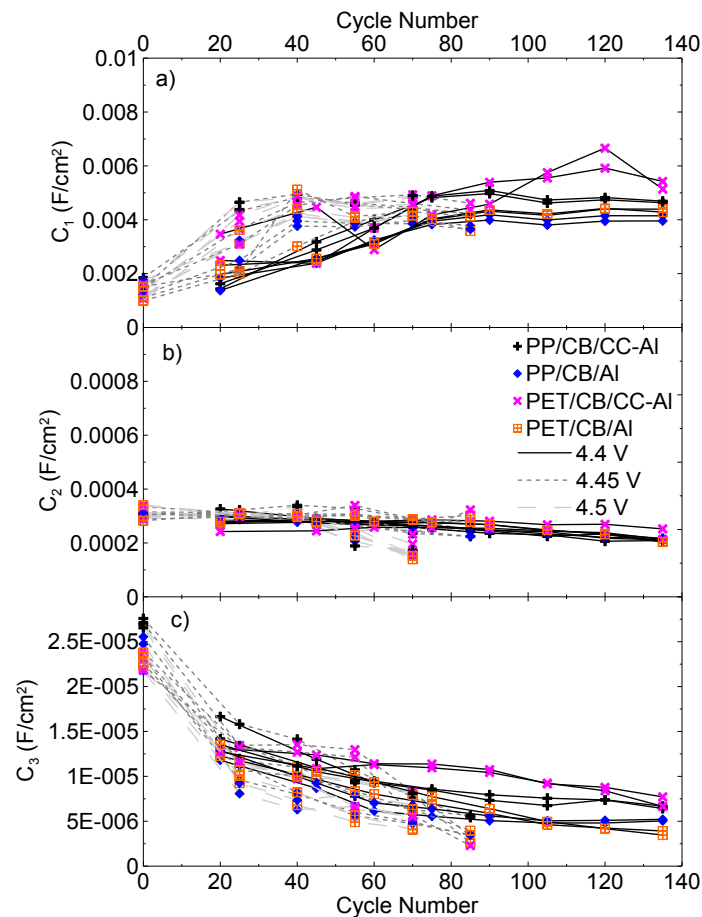


Figure 6.12 Parameters for the effective capacitance a) C_1 , b) C_2 , and c) C_3 obtained from fitting the impedance spectra of cells containing CB using an equivalent circuit model. The error bars, from fitting, are equal size or smaller than the symbols.

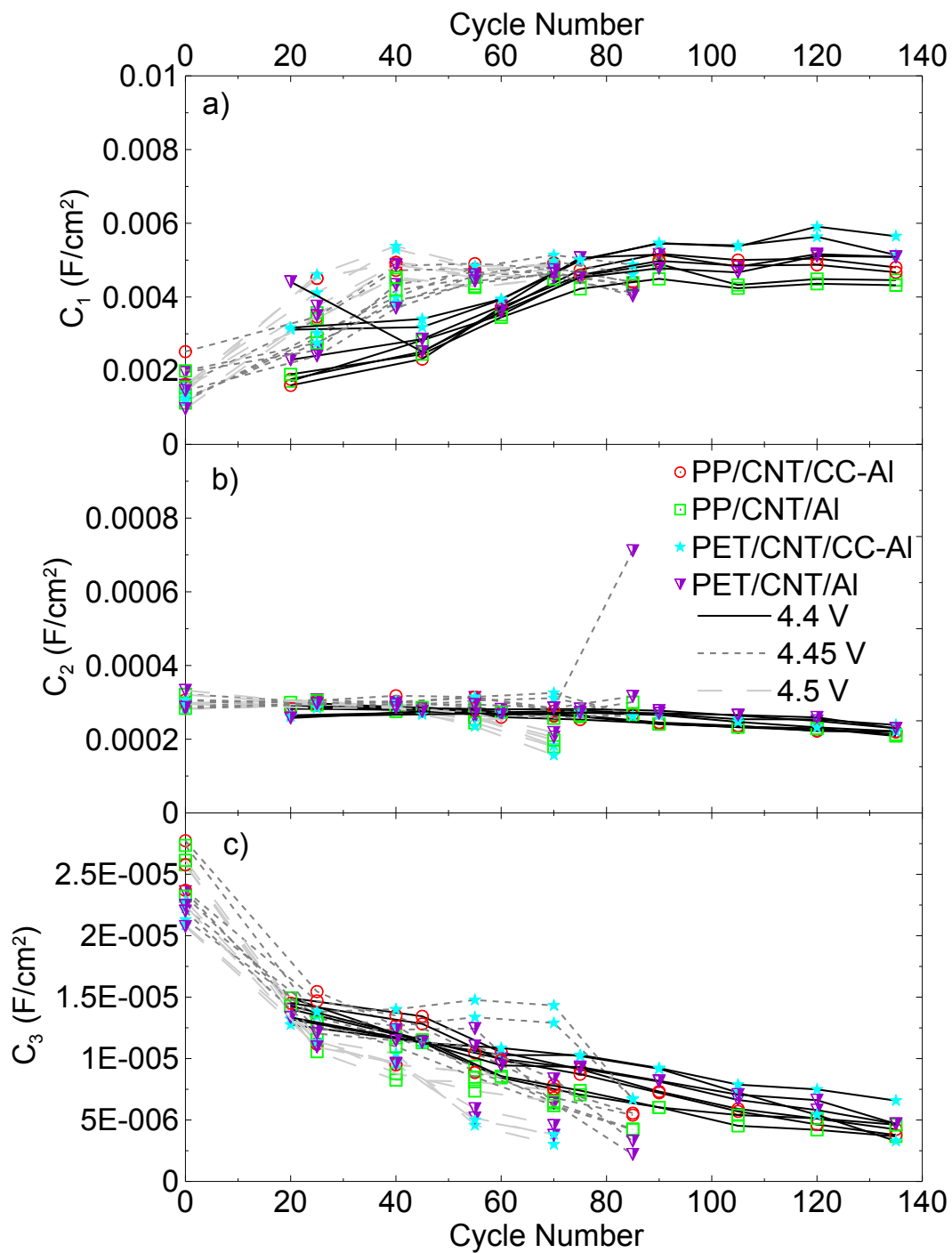


Figure 6.13 Parameters for the effective capacitance a) C_1 , b) C_2 , and c) C_3 obtained from fitting the impedance spectra of cells containing CNT using an equivalent circuit model. The error bars, from fitting, are equal size or smaller than the symbols.

Figure 6.14 shows the volume of gas evolved measured after 135 cycles for the 4.4 V cells and after 70 cycles for the 4.45 and 4.5 V cells. The volume of these pouch cells without gas was approximately 2.2 mL. Figure 6.14a shows that, after 135 cycles, all cells containing CC-Al had larger amounts of gas produced compared to cells containing Al foil, and that cells containing PET had larger amounts of gas produced compared to similar cells containing PP. Figure 6.14b shows that, after 70 cycles, cells containing CC-Al produces more gas than similar cells containing Al. Furthermore, after 70 cycles, the cells cycled to 4.45 and 4.5 V had less gas than cells cycled to 4.4 V after 135 cycles. This means that gas evolution increased with time spent at high potential.

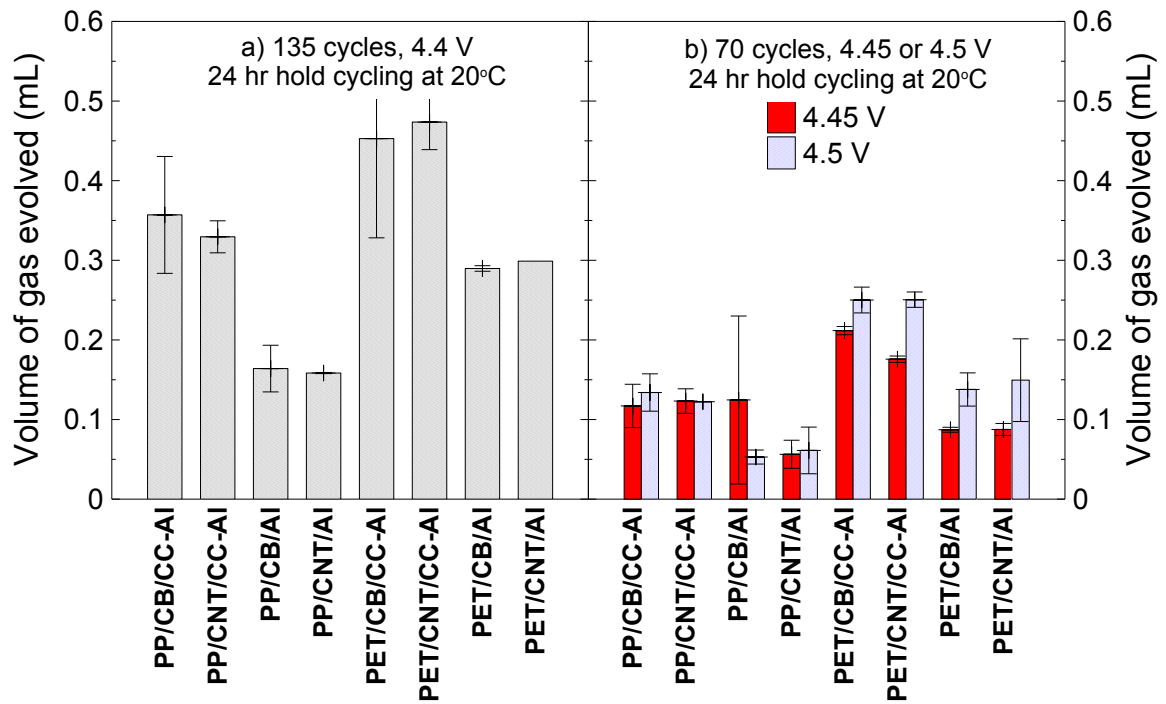


Figure 6.14 The volume of gas evolved after a) 135 cycles for the cells cycled to 4.4 V and b) after 70 cycles for the cells cycled to 4.45 and 4.5 V.

6.3 LONG-TERM CYCLING AT 40°C

6.3.1 EXPERIMENTAL

In this study, the eight cell types were filled with either PES222 or 1M LiPF₆ EMC:FEC:PPF 94:5:1. The latter will be referred to as EC-free cells. Cells underwent cycling to 4.4 V at 40°C. At the top of charge, the cells underwent three short charge-rest periods, intended to mimic CCCV cycling. The cycling was done at C/5. After reaching the top of charge, the cells entered a rest step for 600 seconds, followed by a charge at C/10 to the TOC, followed by a 600 second rest, followed by a C/20 charge to the TOC, followed by a 600 second rest, followed by a C/40 charge to the TOC. After 180 cycles, the upper cutoff voltage was increased to 4.5 V. For the first 300 cycles, cells were paused at 3.8 V to measure EIS every 30 cycles. After 300 cycles, cells were measured less often. Four-wire impedance measurements were taken at 3.8 V and 20°C using a BioLogic SP-150 and a frequency range from 10 mHz to 100 kHz using 10 points per decade.

While some cells were removed early from testing due to poor performance, all cells were removed after 600 cycles, or approximately 9500 hours or 13 months of testing.

Figure 6.15 shows the experimental protocol plotted as cell voltage versus time. Each panel spans twenty hours of cycling. Figure 6.15a shows that, in the beginning of cycling, all cells were cycled to 4.4 V, and had negligible voltage drop during the rest periods at the top of charge. Near the end of cycling, all cells showed capacity fade, and therefore each cycle took a shorter amount of time. Figure 6.15b shows a cell that had minimal

capacity fade near the end of cycling. Figure 6.15c shows a cell that had severe capacity fade near the end of cycling. In this case, each cycle was only 4 hours long, and there was a severe voltage drop during the rest periods at the top of charge. Figure 6.16 shows the same experimental protocol plotted as cell voltage versus time shown in Figure 6.15, but spanning three hours of cycling. Figure 6.16 clearly shows the charge-rest steps at the top of charge.

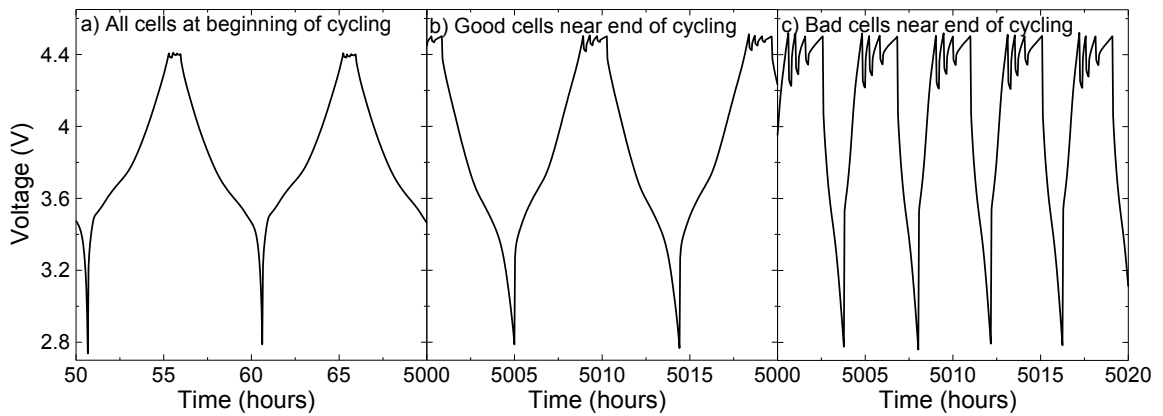


Figure 6.15 The experimental protocol over 20 hours a) near the beginning of cycling, b) near the end of cycling for a cell with little capacity fade, and c) near the end of cycling for a cell with severe capacity fade.

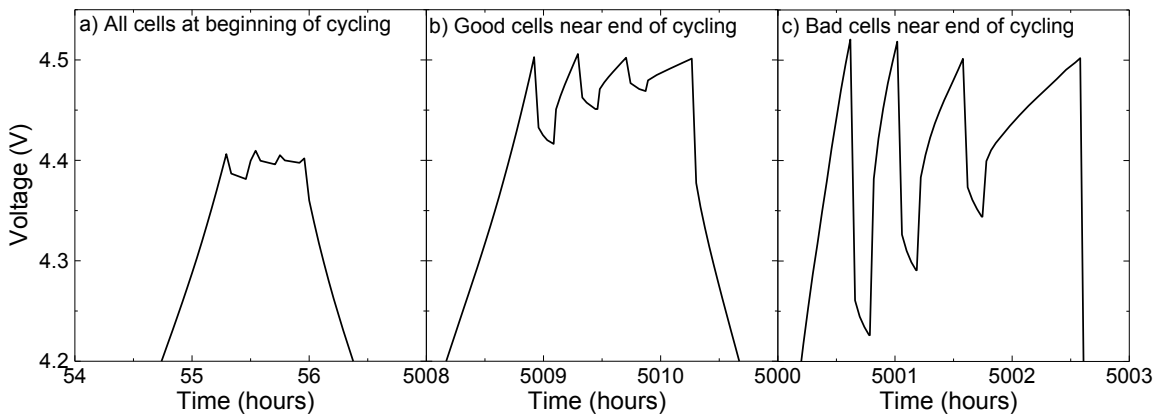


Figure 6.16 The experimental protocol over 3 hours a) near the beginning of cycling, b) near the end of cycling for a cell with little capacity fade, and c) near the end of cycling for a cell with severe capacity fade.

6.3.2 RESULTS

Figure 6.17 shows the normalized discharge capacity as a function of cycle number for all cells. Figure 6.17a and Figure 6.17c show the normalized discharge capacity for the PES222 cells containing PP and PET, respectively. Figure 6.17b and Figure 6.17d show the normalized discharge capacity for the EC-free cells containing PP and PET, respectively. The dashed line in each panel indicates when the upper cutoff potential was increased from 4.4 to 4.5 V. In all cases, cells containing CNT and Al had the best capacity retention and cells containing CB and CC-Al had the worst capacity retention. Cells containing EC-free electrolyte had a smaller rate of capacity fade than cells containing PES222. The rate of fade was accelerated for all cells after the upper cutoff potential was increased to 4.5 V.

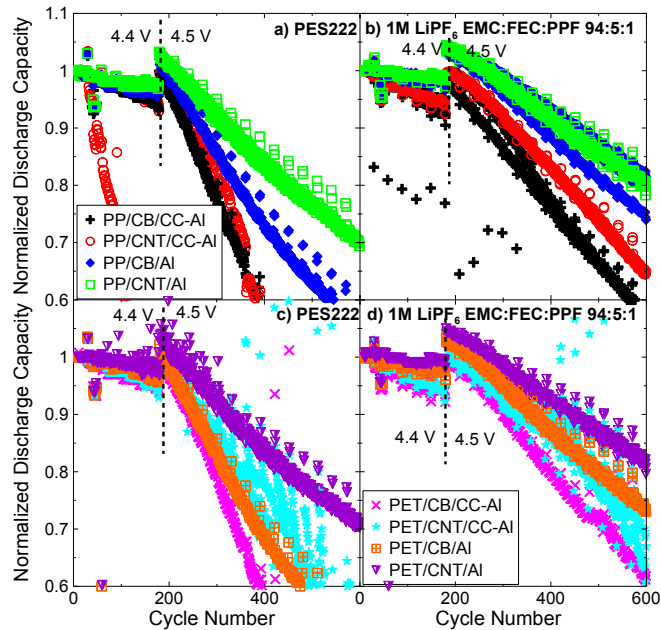


Figure 6.17 The normalized fractional discharge capacity as a function of cycle number for the PES222 cells containing a) PP and c) PET, and for the EC-free cells containing b) PP and d) PET as the separator material.

Figure 6.18 shows the impedance spectra measured at 3.8 V and 20°C for the PES222 cells. The top panels of Figure 6.18 show the spectra for the cells containing the PP separator and the bottom panels show the spectra for the cells containing the PET separator. The impedance for all cells, except the cell containing PP, CNT, and CC-Al, decreased from cycle 30 to cycle 180, after which the upper cutoff potential was increased to 4.5 V and the impedance of all cells increased. Due to the amount of data presented in Figure 6.18, it is difficult to observe trends for each cell type. Fitting results using an equivalent circuit model will be examined to compare cell types.

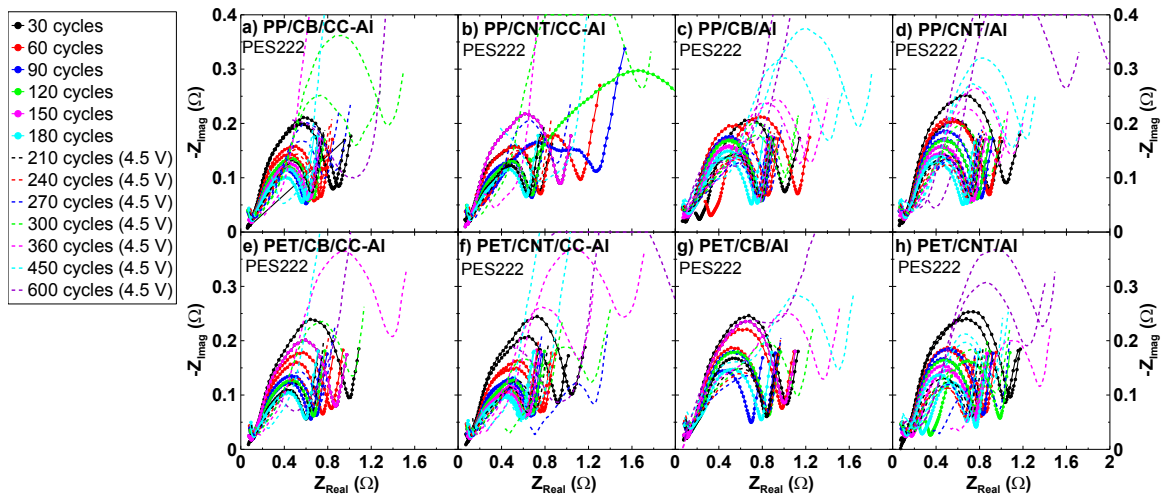


Figure 6.18 The impedance spectra measured at 3.8 V and 20°C for the cells filled with PES222 electrolyte. The cells contained either PP or PET, CB or CNT, and CC-Al or Al, as indicated in each panel. The electrode area for all cells was 84.7 cm².

Figure 6.19 shows the impedance spectra measured at 3.8 V and 20°C for the EC-free cells. The top panels of Figure 6.19 show the spectra for the cells containing the PP separator and the bottom panels show the spectra for the cells containing the PET separator. The impedance for all cells decreased from cycle 30 to 180, and then

increased. The impedance spectra for the EC-free cells have a different shape than those for the PES222 cells. The EC-free cells tend to have more depressed spectra, and easily distinguishable multi-peak features.

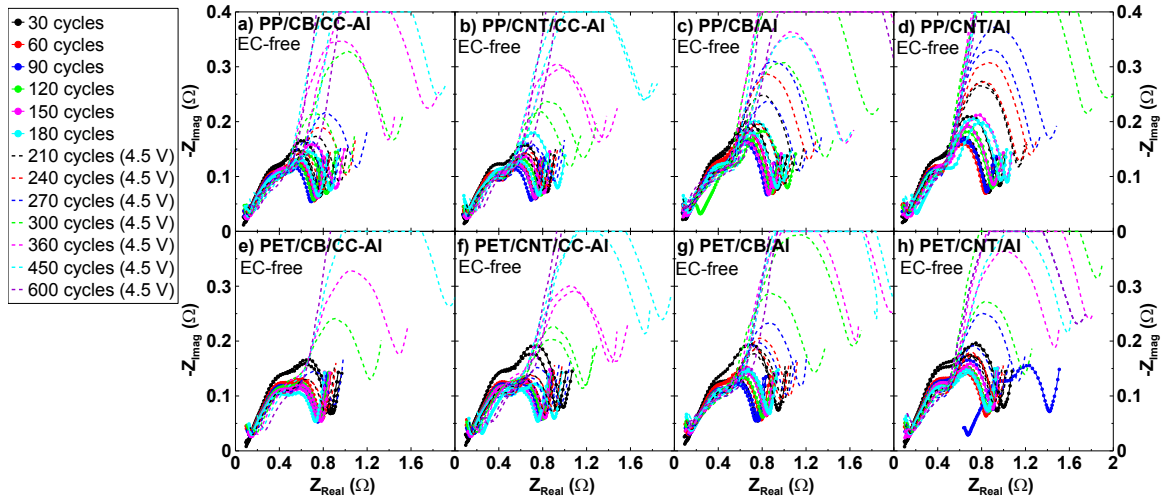


Figure 6.19 The impedance spectra measured at 3.8 V and 20°C for the cells filled with EC-free electrolyte. The cells contained either PP or PET, CB or CNT, and CC-Al or Al, as indicated in each panel. The electrode area for all cells was 84.7 cm².

Figure 6.20 shows selected impedance spectra and the corresponding fitting results from the equivalent circuit model (Figure 6.1) for the cell containing PP, CB, CC-Al and EC-free electrolyte. Figure 6.20a shows the Nyquist representations of the selected spectra, Figure 6.20b shows the imaginary Bode representations and Figure 6.20c shows the real Bode representations. There is good agreement between the measured spectra and the spectra obtained from fitting in all cases.

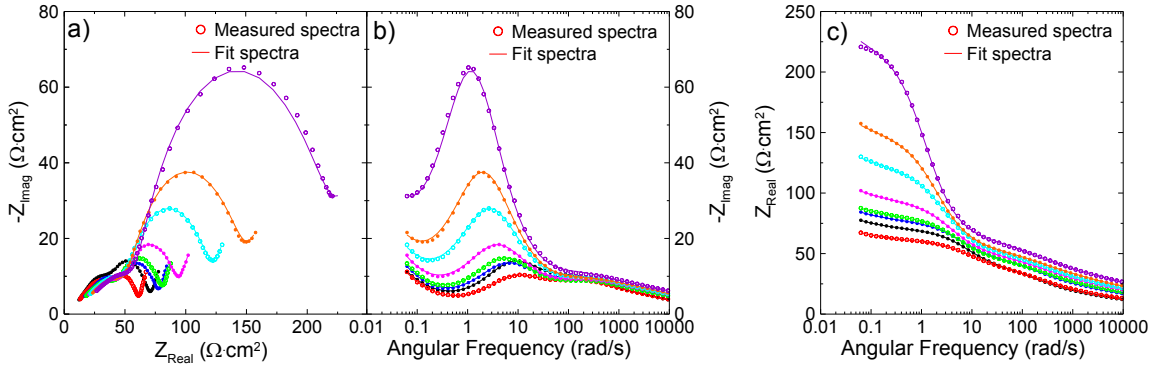


Figure 6.20 Selected impedance spectra and the corresponding fit for the cell containing EC-free electrolyte, PP, CB and CC-Al shown in a) Nyquist representation, b) imaginary Bode representation, and c) real Bode representation. The spectra shown were measured after 30, 90, 150, 210, 270, 300, 360, and 450 cycles.

Figure 6.21 and Figure 6.22 show the fitting results for the resistors in the equivalent circuit model (Figure 6.1) for cells containing CB and CNT, respectively. Each panel shows the fitting parameters for the cells filled with PES222 and EC-free electrolyte. Figure 6.21a and Figure 6.22a show the results of parameter R_1 , which was associated with the positive electrode SEI. Figure 6.21c and Figure 6.22c show the results of parameter R_2 , and Figure 6.21d and Figure 6.22d show the results of parameter R_3 . These parameters were associated with the negative electrode and the contact impedances. Figure 6.21b and Figure 6.22b show the results of parameter R_{ohmic} , which was associated with the electronic and ionic path resistances. R_1 is the largest parameter, and R_2 , R_3 , and R_{ohmic} have similar orders of magnitude. In Figure 6.21 and Figure 6.22, R_1 increased for all cells with cycle number, and R_2 decreased slightly and then remained approximately constant with cycle number. R_3 increased significantly for the cells containing CB and increased slightly or remained constant for cells containing CNT. R_{ohmic} increased with cycle number.

In Figure 6.21a, R_1 increased more for cells containing CC-Al compared to Al. Cells containing EC-free electrolyte and Al foil exhibited larger growth in R_1 compared to cells containing PES222 and Al foil. Cells containing EC-free electrolyte and Al foil had smaller impedance growth than the PES222 cells containing CC-Al foil, which had severe impedance growth. In Figure 6.21c, R_2 was slightly lower for cells containing CC-Al compared to Al. Otherwise, the trend of R_2 with cycle number for each cell type was similar. In Figure 6.21d, R_3 increased more for cells containing Al compared to CC-Al. Using EC-free electrolyte, however, reduced the variation between cell types compared to PES222 electrolyte. In Figure 6.21b, the change in R_{ohmic} was small for all cells except those containing CC-Al and PES222 electrolyte. R_{ohmic} increased more for cells containing CC-Al compared to Al.

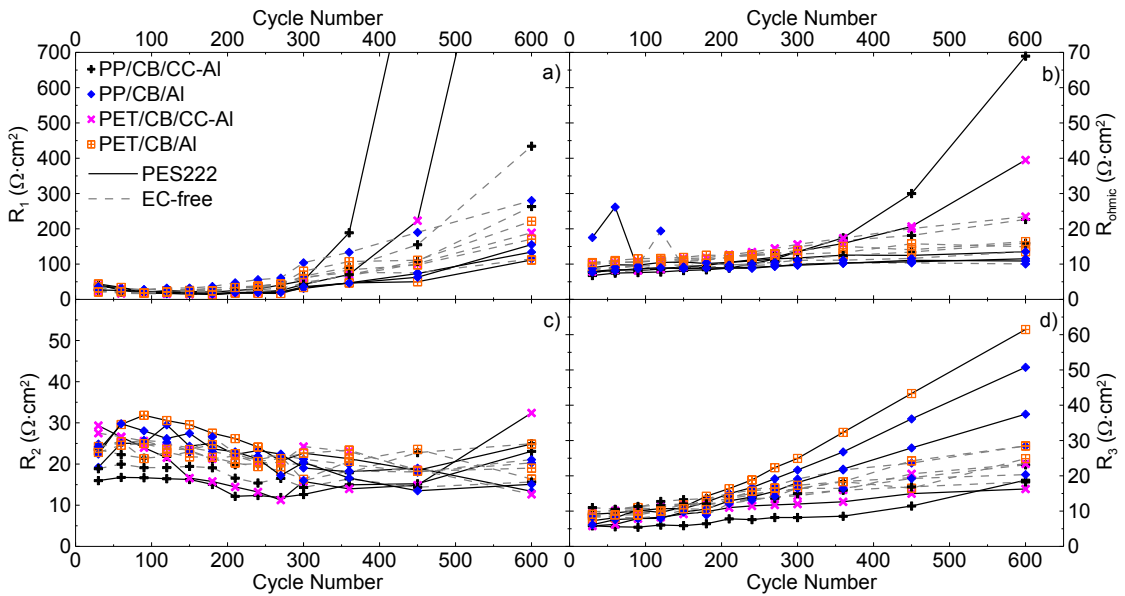


Figure 6.21 Parameters for the resistances a) R_1 , b) R_{ohmic} , c) R_2 , and d) R_3 obtained from fitting the impedance spectra of cells containing CB using an equivalent circuit model. The error bars, from fitting, are equal size or smaller than the symbols.

In Figure 6.22a, R_1 increased more for cells containing CC-Al compared to Al. Cells containing EC-free electrolyte exhibited larger growth in R_1 compared to cells containing PES222, except for the PES222 cells containing CC-Al, which had severe impedance growth. The trend of R_2 with cycle number for each cell type was similar. In Figure 6.22d, R_3 increased more for cells containing CC-Al compared to Al. Compared to cells containing CB, R_3 increased much less for cells containing CNT. Using EC-free electrolyte reduced the variation between cell types compared to PES222 electrolyte. In Figure 6.22b, the change in R_{ohmic} was small for all EC-free cells and large for PES222 cells. R_{ohmic} increased more for cells containing CC-Al compared to Al. The noise in some of the data shown in Figure 6.22b is possibly due to poor connections during EIS measurements.

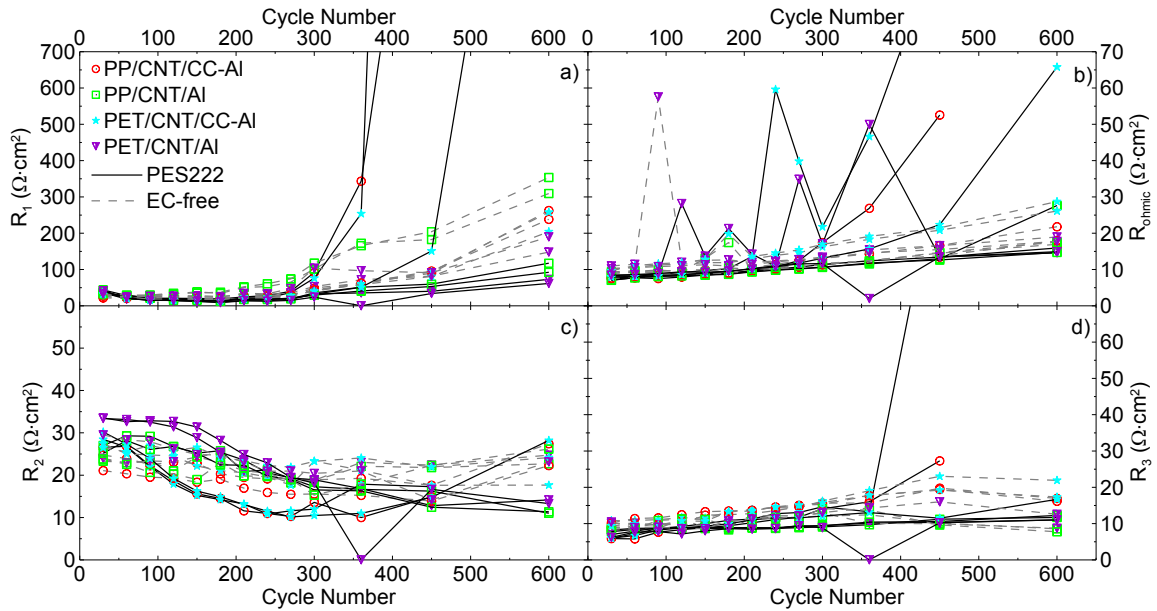


Figure 6.22 Parameters for the resistances a) R_1 , b) R_{ohmic} , c) R_2 , and d) R_3 obtained from fitting the impedance spectra of cells containing CNT using an equivalent circuit model. The error bars, from fitting, are equal size or smaller than the symbols.

Figure 6.23 shows the fitting parameter, R_1 , as a function of cycle number for all cells, highlighting the first 300 cycles. With an upper cutoff potential of 4.4 V, all cells showed a slightly decreasing or approximately constant value for R_1 . After the upper cutoff potential was increased to 4.5 V, as indicated by the dashed red line, all cells exhibited an increase in R_1 with cycle number. This shows that increasing the upper cutoff potential by 0.1 V had a severe impact on the impedance growth of all cells, corresponding to the accelerated rate of capacity fade shown in Figure 6.17.

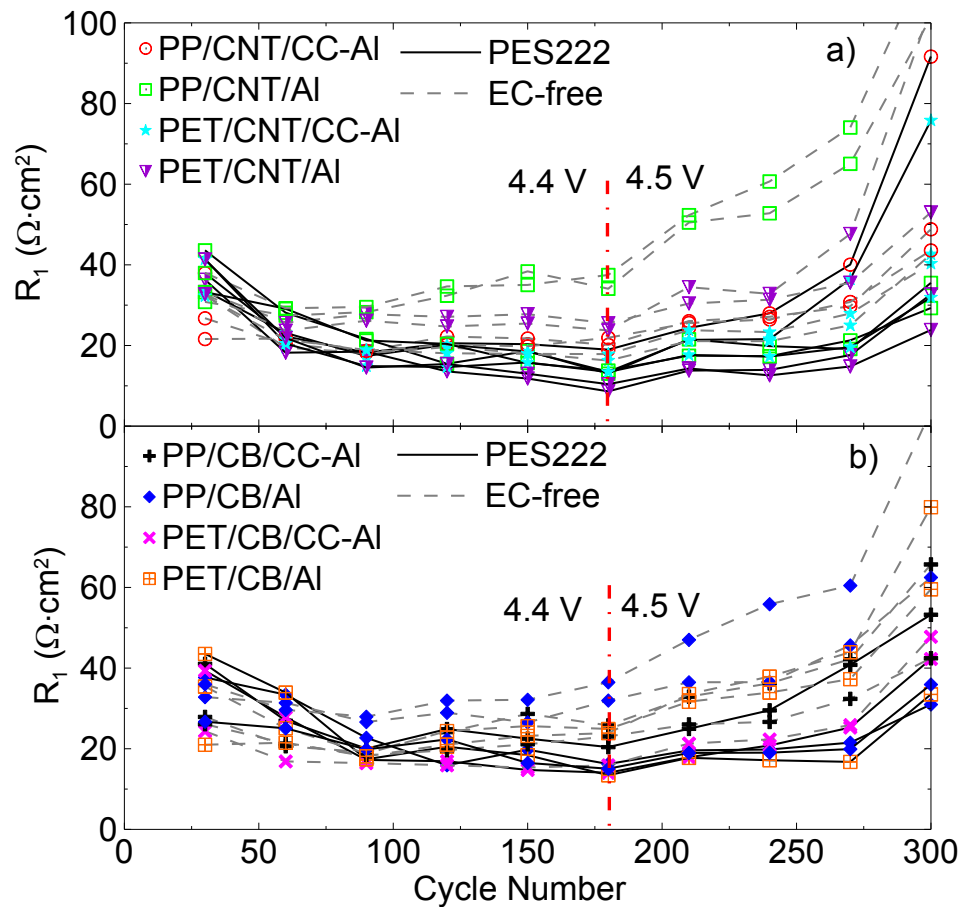


Figure 6.23 Parameters for the resistance R_1 obtained from fitting the impedance spectra of cells containing a) CB and b) CNT using an equivalent circuit model for the first 300 cycles. The error bars, from fitting, are equal size or smaller than the symbols.

Figure 6.24 and Figure 6.25 show the fitting results as a function of cycle number for the effective capacitance for the constant phase elements in the equivalent circuit model (Figure 6.1) for cells containing CB and CNT, respectively. For each R||CPE circuit, an effective capacitance can be calculated from corresponding resistance and the critical frequency, ω_c . Each panel shows the fitting parameters for the PES222 and EC-free cells. Figure 6.24a and Figure 6.25a show the results of parameter C_1 , which corresponds to the effective capacitance associated with the positive electrode SEI. Figure 6.24b and Figure 6.25b show the results of parameter C_2 and Figure 6.24c and Figure 6.25c show the results of parameter C_3 . These parameters are associated with the negative electrode and contact impedances.

The trends of the data were the same regardless of the upper cutoff potential. In general for all cells in Figure 6.24 and Figure 6.25, C_1 tended to increase initially, and then stabilized as cycle number increased. For PES222 cells, C_2 was constant until approximately 180 cycles, at which time the upper cutoff potential was increased to 4.5 V, and then began to increase for all cells. For EC-free cells containing CB, C_2 was approximately constant throughout cycling. For EC-free cells containing CNT, C_2 increased after 300 cycles for cells containing PET and remained constant for cells containing PP. C_2 increased more for cells containing PES222 compared to EC-free electrolyte. C_3 initially decreased slightly and then remained constant for cells containing CB. C_3 remained constant for cells containing CNT. C_1 was largest and C_3 was smallest for all cells.

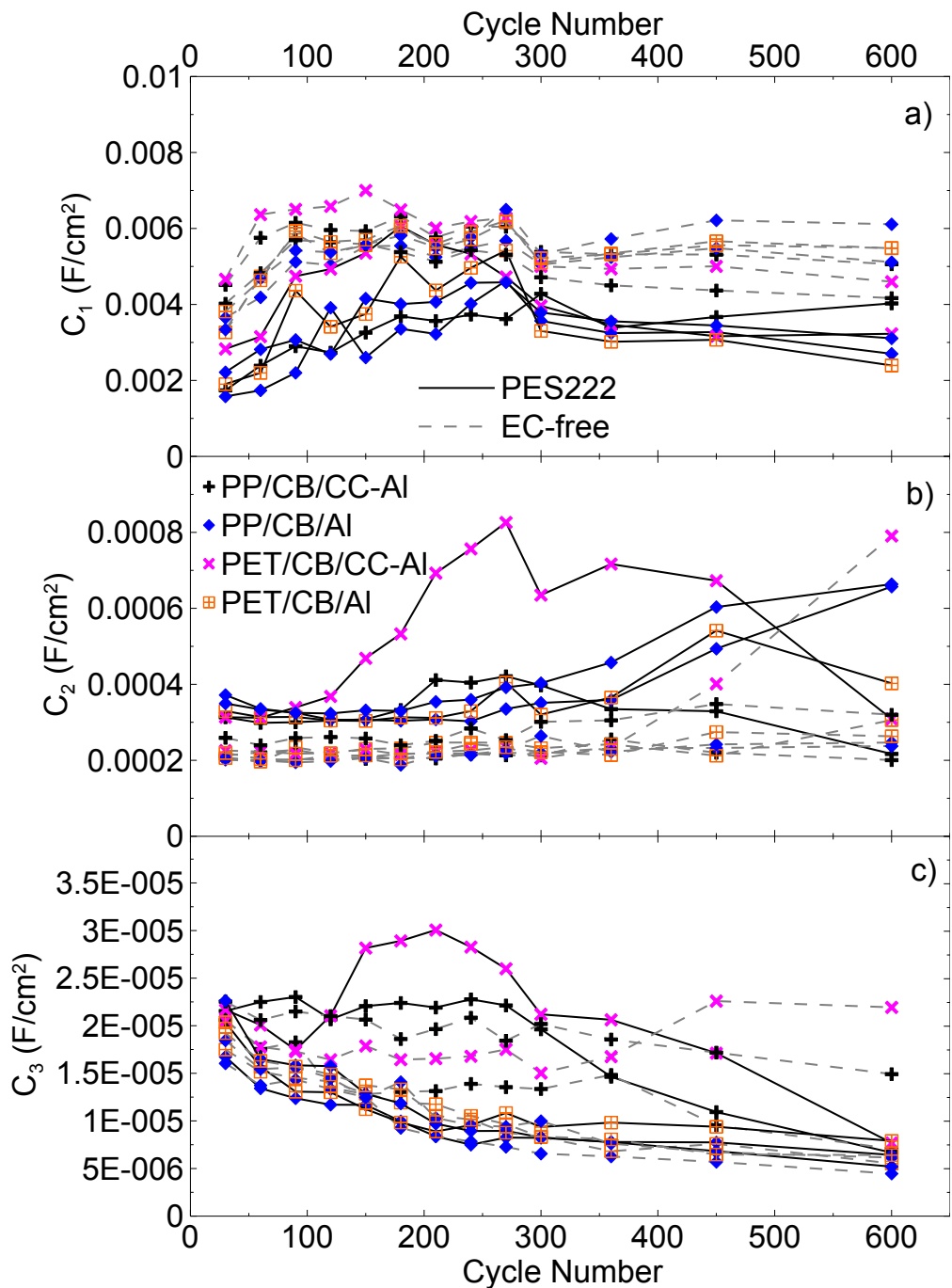


Figure 6.24 Parameters for the effective capacitance a) C_1 , b) C_2 , and c) C_3 obtained from fitting the impedance spectra of cells containing CB using an equivalent circuit model. The error bars, from fitting, are equal size or smaller than the symbols.

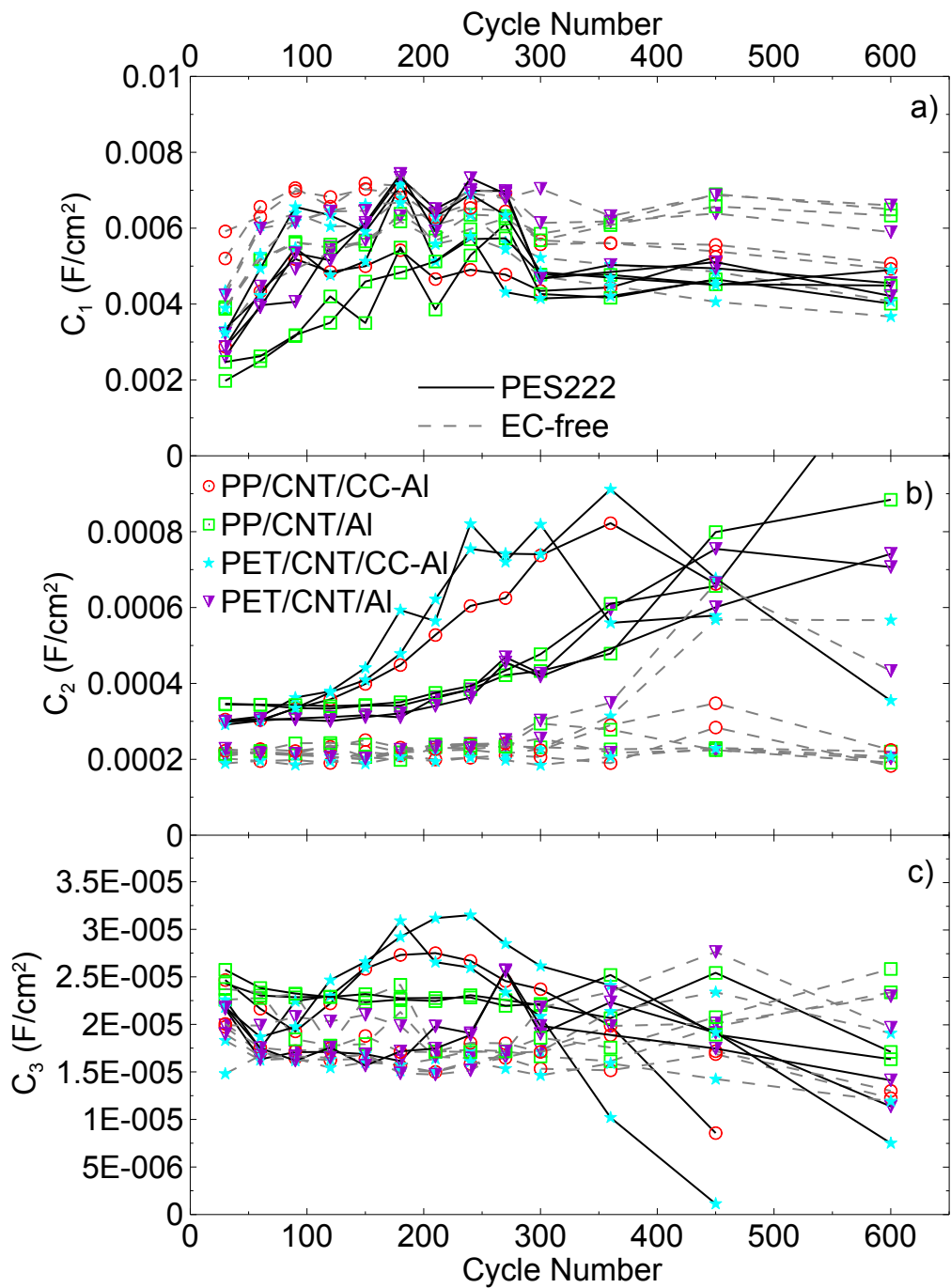


Figure 6.25 Parameters for the effective capacitance a) C_1 , b) C_2 , and c) C_3 obtained from fitting the impedance spectra of cells containing CB using an equivalent circuit model. The error bars, from fitting, are equal size or smaller than the symbols.

Figure 6.26 shows the volume of gas evolved for all cells measured after 90 cycles (when the upper cutoff potential was 4.4 V), and after 600 cycles. After 90 cycles, all cells containing CC-Al had large amounts of gas produced inside the cell, while the cells containing Al foil had little to no gas produced. The volumes of these pouch cells without gas were approximately 2.2 mL, meaning the evolution of >0.5 mL of gas was significant. After 600 cycles, all cells showed >0.5 mL of gas evolution, however the CC-Al cells showed the most gas produced at approximately 2 mL. After 600 cycles, EC-free cells results in more gas evolved. The dramatic gas evolution resulting from the presence of CC-Al presents issues for using this foil in practical Li-ion cells.

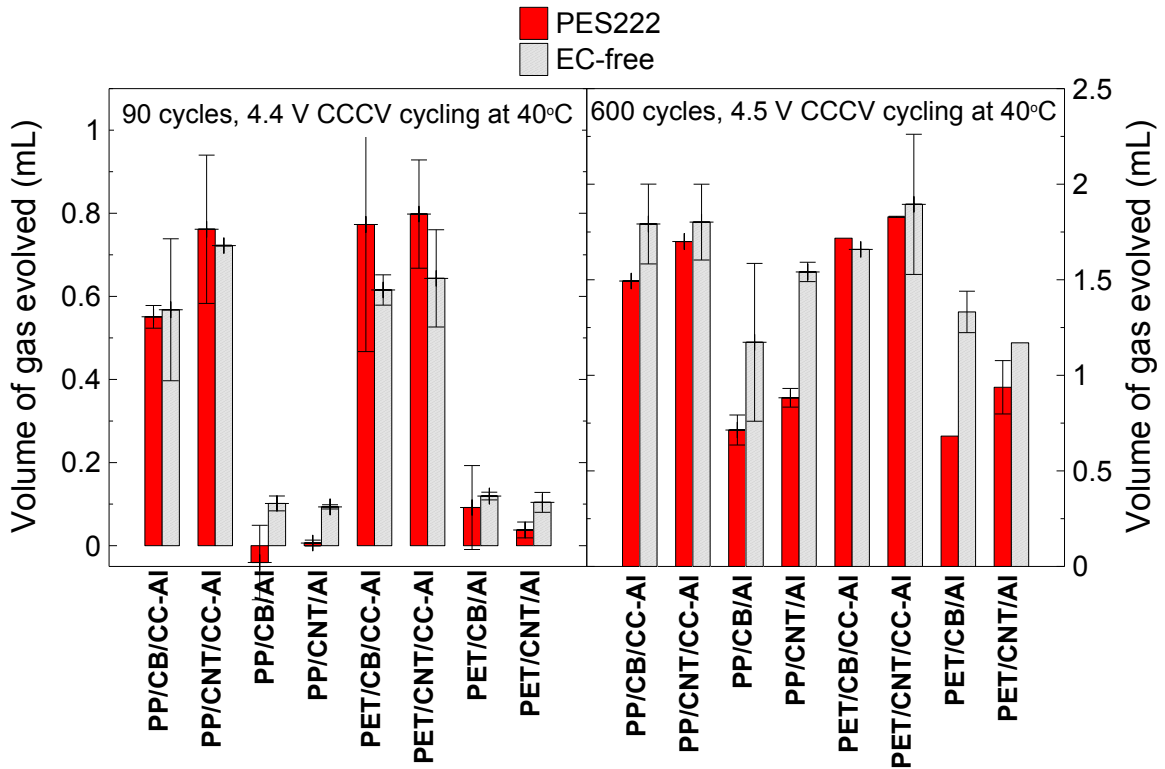


Figure 6.26 The volume of gas evolved after 90 and 600 cycles. Please note the different scale in the y axes.

Figure 6.27 shows the fitting results for the resistor, R_1 , in the equivalent circuit model (Figure 6.1) plotted as a function of time for all cells containing PES222 undergoing charge-hold-discharge cycling at 20°C and continuous cycling at 40°C. As previously discussed, R_1 is associated with the positive electrode SEI. Figure 6.27 shows that for the first 4000 hours of testing, cells cycled continuously at 40°C had little to no growth in R_1 and cells undergoing charge-hold-discharge cycling at 20°C, except the cell containing PET, CB, and CC-Al, had significant growth in R_1 . In particular, cells containing Al foil undergoing charge-hold-discharge cycling at 20°C had significantly larger growth in R_1 compared to cells containing Al foil undergoing continuous cycling at 40°C during the first 4000 hours of testing. This indicates that, although R_1 increased as experiment time increased, it was time spent at high potential that most impacted the growth in R_1 .

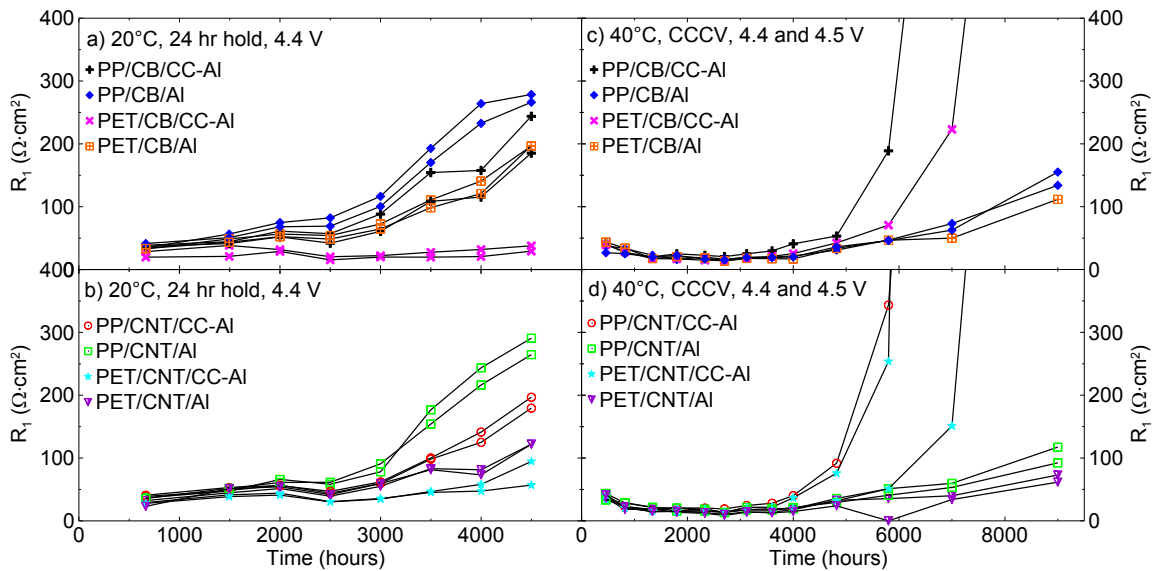


Figure 6.27 Parameters for the resistance R_1 obtained from fitting the impedance spectra of PES222 cells plotted as a function of time for (a,b) cells undergoing charge-hold discharge cycling at 20°C and (c,d) and continuous cycling at 40°C.

6.4 CONCLUSIONS

The work presented here demonstrated the importance and usefulness of monitoring impedance growth as a function of time and cycle number. Charge-hold-discharge cycling at 20°C was an aggressive test that led to impedance growth and capacity loss, which was accelerated when the upper cutoff potential was increased from 4.4 to 4.5 V. Long term cycling at 40°C to 4.4 V was not an aggressive test, but increasing the upper cutoff potential to 4.5 V immediately impacted the capacity retention and impedance of all cells.

In general, cells containing PET had better capacity retention and lower impedance growth compared to cells containing PP. CC-Al foil provided a benefit to cells cycling at 20°C but these cells had severe capacity fade, impedance growth, and gas evolution in cells cycled at 40°C and gas evolution at 20°C.

Quick analysis of the entire width of the impedance spectrum along the real axis, R_{ct} , was a valuable indication of overall cell impedance. However, this value can be underestimated for cells that exhibit large impedance growth. Therefore, fitting impedance spectra using an equivalent circuit model was valuable to characterize the changes of separate processes and monitor how individual impedance components changed over time. The parameter R_1 in the equivalent circuit model was the largest and accounted for the large impedance growth observed in all cells studied. Cells containing PET had smaller impedance growth compared to cells containing PP when the upper cutoff potential was 4.4 and 4.45 V, however all cells had severe impedance growth when

cycled to 4.5 V at 20°C. Therefore, while various cell components can improve the impedance and therefore the capacity retention of cells cycled to 4.4 and 4.45 V, these components were unable to prevent impedance growth at 4.5 V and 20°C that led to severe capacity fade.

It is important to monitor how impedance changes with voltage, in addition to time and cycle number, to better characterize how the positive electrode SEI and other cell components evolve with state of charge and cycle number. Changes to the SEI thickness and SEI composition, as well as the formation and growth of a rocksalt surface layer can affect impedance growth with cycle number and with voltage. Electrolyte dryout and gas evolution can also impact impedance growth and can be accelerated at high potentials. Chapter 7 will investigate the impedance of various types of NMC/graphite cells as a function of time, cycle number, and voltage. Work done to fit measured impedance spectra using an equivalent circuit model will be presented in hopes to further understand how the circuit parameters change with time and voltage.

CHAPTER 7. EFFECTS OF VARIOUS ELECTRODE CHEMISTRIES AND ELECTROLYTES ON THE IMPEDANCE OF NMC/GRAPHITE POUCH CELLS

Chapter 6 demonstrated the importance of using four-wire systems to perform electrochemical impedance spectroscopy (EIS) measurements and the value of fitting spectra using equivalent circuit models. While the studies presented in Chapter 6 characterized the changes to various components of the cell impedance, which were then compared to the cycling data, it is imperative to monitor impedance changes as a function of time, cycle number and potential. Experiments using equipment capable of two-wire impedance measurements coupled with cycling experiments were presented in Chapters 4 and 5. In this work, experiments using similar protocols using equipment capable of four-wire impedance measurements coupled with cycling experiments are discussed.

7.1 EXPERIMENTAL

The cells used were 200-300 mAh pouch cells. The cells were either $\text{Li}[\text{Ni}_{0.6}\text{Mn}_{0.2}\text{Co}_{0.2}]\text{O}_2$ (NMC622)/natural graphite (NG) with an Al_2O_3 coating or a proprietary high voltage coating on the positive electrode, single crystal $\text{Li}[\text{Ni}_{0.5}\text{Mn}_{0.3}\text{Co}_{0.2}]\text{O}_2$ (NMC532)/NG or single crystal NMC532/artificial graphite (AG). The studies presented in Chapters 4, 5, and 6 used cells containing artificial graphite, which is a common name for synthetic graphite. Positive electrode surface coatings can be used to reduce parasitic reactions by improving the interface between the electrolyte and the positive electrode.¹⁵⁹ Al_2O_3 has been shown to improve this interface, reduce

electrolyte oxidation, and improve the cycling performance of cells.^{159–161} Glazier et al. found that Al₂O₃-coated NMC622 cells had smaller parasitic heat flow and better long term capacity retention compared to uncoated NMC442 cells.^{159,162} They also found that Al₂O₃-coated NMC622 cells generated significant volumes of gas when exposed to high voltage for extended periods of time.¹⁶²

Li et al. showed that cells containing commercial single-crystal NMC532 with a grain size of ~3 μm were superior to cells containing Al₂O₃-coated and uncoated polycrystalline NMC532.¹⁴⁶ Li et al. used long term cycling tests to show that single crystal cells had better capacity retention than polycrystalline cells cycled to 4.4 V at 40°C and 55°C. Li et al. also showed that single crystal cells had extremely small volumes of gas evolved after holding for 100 hours at 4.4, 4.5, and 4.6 V. Table 7.1 shows the short-form name and the electrode details of the cells presented in this work.

Table 7.1 Cell chemistry and name of the cells presented in this work.

Short-form name	Positive electrode	Negative electrode	Positive Electrode Coating	Electrolytes Used
622A	NMC622	Natural graphite	Al ₂ O ₃	PES211, VC211
622B	NMC622	Natural graphite	Proprietary high voltage coating	PES211, VC211
Rock/NG	Single crystal NMC532	Natural graphite	Proprietary coating	PES211, VC211
Rock/AG	Single crystal NMC532	Artificial graphite	Proprietary coating	2% VC, 2% FEC, EC:EMC:DMC:FEC

All cells underwent the standard filling procedure and formation cycle. The 622A, 622B, and Rock/NG cells were filled with either 1M LiPF₆ EC:EMC:PES:DTD:TTSPi 29:67:2:1:1 (PES211) or 1M LiPF₆ EC:EMC:VC:DTD:TTSPi 29:67:2:1:1 (VC211). The Rock/AG cells were filled with either 1M LiPF₆ EC:EMC:FEC 29:69:2 (2% FEC), 1M LiPF₆ EC:EMC:VC 29:69:2 (2% VC), or 1.2M LiPF₆ EC:EMC:DMC:FEC 24:5:69:2 (EC:EMC:DMC:FEC). After the formation cycle, these cells were placed in a 40. ± 0.1°C temperature box connected to a system capable of four-wire electrochemical impedance spectroscopy measurements coupled with cycling capabilities, as described in Chapter 3.5. Cells underwent charge-hold-discharge cycling as shown in Figure 3.2, in which the upper cutoff potential was 4.1, 4.2, 4.3, or 4.4 V. Most cells were removed after either 120 or 160 cycles, corresponding to approximately 4000 or 5500 hours, respectively.

7.2 RESULTS

7.2.1 CELLS WITH ARTIFICIAL GRAPHITE

Figure 7.1 shows the discharge capacity as a function of cycle number for all cells containing artificial graphite. Figure 7.1a shows the discharge capacity for cells containing 2% VC, Figure 7.1b shows the discharge capacity for cells containing 2% FEC, and both panels show the discharge capacity for cells containing EC:EMC:DMC:FEC. Each cell has two distinct data sets displaying the difference in capacity between the two C/5 (higher capacity cycles) and the three C/2.5 discharge segments (lower capacity cycles). As expected, the initial discharge capacity of all cells increased with increasing upper cutoff potential. Cells cycled to 4.1, 4.2, and 4.3 V had

similar rates of fade, but cells cycled to 4.4 V had severe discharge capacity fade after only 40 cycles. Furthermore, cells cycled to 4.1, 4.2, and 4.3 V showed little difference in capacity between the C/5 and C/2.5 cycles. Cells cycled to 4.4 V, however, exhibited a clear separation of the C/5 and C/2.5 cycles. There is no clear difference in the capacity retention between the three electrolytes used.

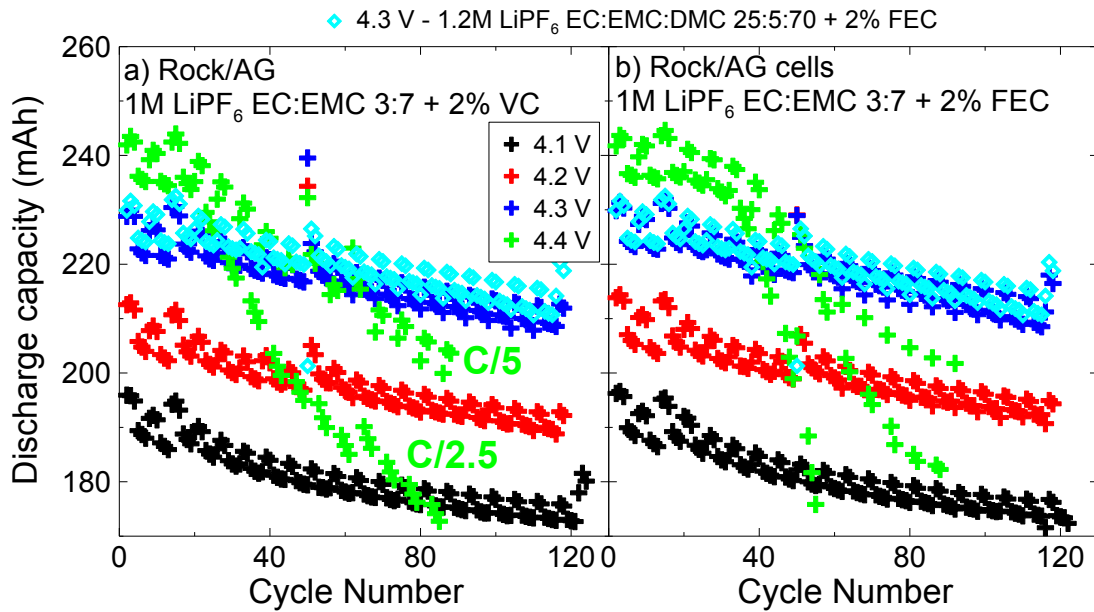


Figure 7.1 The discharge capacity as a function of cycle number for Rock/AG cells containing 1M LiPF₆ EC:EMC and a) 2% VC or b) 2% FEC. Cells containing 1.2M LiPF₆ EC:EMC:DMC 25:5:70 + 2% FEC are shown in both panels. The upper cutoff potential for each cell is indicated by the legend.

Figure 7.2 shows the impedance spectra collected every 6 cycles for Rock/AG cells containing 2% VC. Figure 7.2a and Figure 7.2b show the spectra measured at 3.8 V and 4.2 V, respectively, for the cell cycled to 4.2 V. Figure 7.2c and Figure 7.2d show the spectra measured at 3.8 V and 4.4 V, respectively, for the cell cycled to 4.4 V. Please note the different scale for each axis. The arrow in Figure 7.2a indicates the trend of the

spectra with increasing cycle number and applies to all panels. The cell cycled to 4.2 V exhibited small impedance and small impedance growth at 3.8 V and at 4.2 V. The cell cycled to 4.4 V, however, exhibited severe impedance growth at 3.8 V and 4.4 V, and transitioned from single-peak spectra to multi-peak spectra. This severe impedance growth corresponds to the severe capacity fade for the 4.4 V cell shown in Figure 7.1. In all cases, the cells exhibited a shift in the high frequency intercept (HFI) with increasing cycle number, indicating an increase in the electronic and/or ionic path resistances.

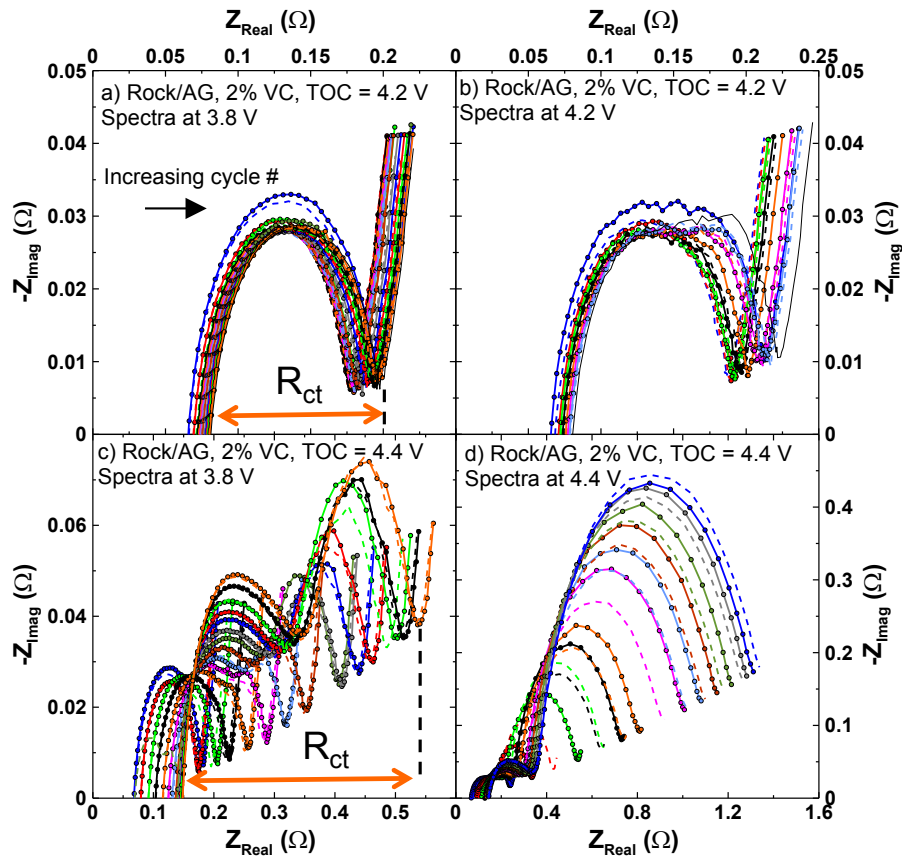


Figure 7.2 The impedance spectra as measured by the 4-wire FRA for the Rock/AG cells containing 2% VC with an upper cutoff potential of 4.2 V (a and b) and 4.4 V (c and d). The spectra were measured at a) 3.8 V, b) 4.2 V, c) 3.8 V, and d) 4.4 V. Please note the different scales for each axis.

Figure 7.3a and Figure 7.3b show the impedance spectra measured at 3.8 V and 4.4 V, respectively, during cycles 2, 44, and 86 for the Rock/AG cells containing 2% VC cycled to 4.4 V. Figure 7.3 also shows the spectra measured during cycles 2 and 44 scaled by the value indicated in the legend. All spectra shown in Figure 7.3 have been shifted to zero along the real axis for clarity and comparison. The spectra measured during cycles 2 and 44 have been scaled to make comparisons with the spectra measured during cycle 86. This has been done to investigate the changes that occur to the impedance growth, and the corresponding changes within Li-ion cells.

In Figure 7.3a, the spectrum measured during cycle 2 has a single feature. By scaling the cycle 2 spectrum, it does not match the spectrum measured during cycle 86, which has two easily distinguishable features. The spectrum measured during cycle 44 has two easily distinguishable features as well, but the size and shape of these two features, when scaled, does not match the spectrum measured during cycle 86. This indicates that changes occurred within the Li-ion cell at 3.8 V and that these changes, and the resulting impedance growth, continued with time and cycle and did not reach a steady state.

In Figure 7.3b, all spectra have two easily distinguishable features. However, the relative size of the two features shown in the spectrum measured during cycle 2 is dramatically different than the relative size of the two features shown in the spectra measured during cycles 44 and 86. Therefore, by scaling the cycle 2 spectrum, it does not match the spectrum measured during cycle 86. Alternatively, by scaling the spectrum measured at cycle 44, the two features closely match the features of the spectrum measured during

cycle 86. This indicates that the chemical changes that occurred within the Li-ion cell at 4.4 V resulted in changes to the shape of the impedance spectra initially, but then reached a steady state. However, the impedance continued to grow with time and cycle number, indicating that at both 3.8 V and 4.4 V, irreversible changes occur as cycling continues.

More work is required to study the scaling of impedance spectra to learn about the changes that occur within Li-ion cells with time, cycle number, and voltage.

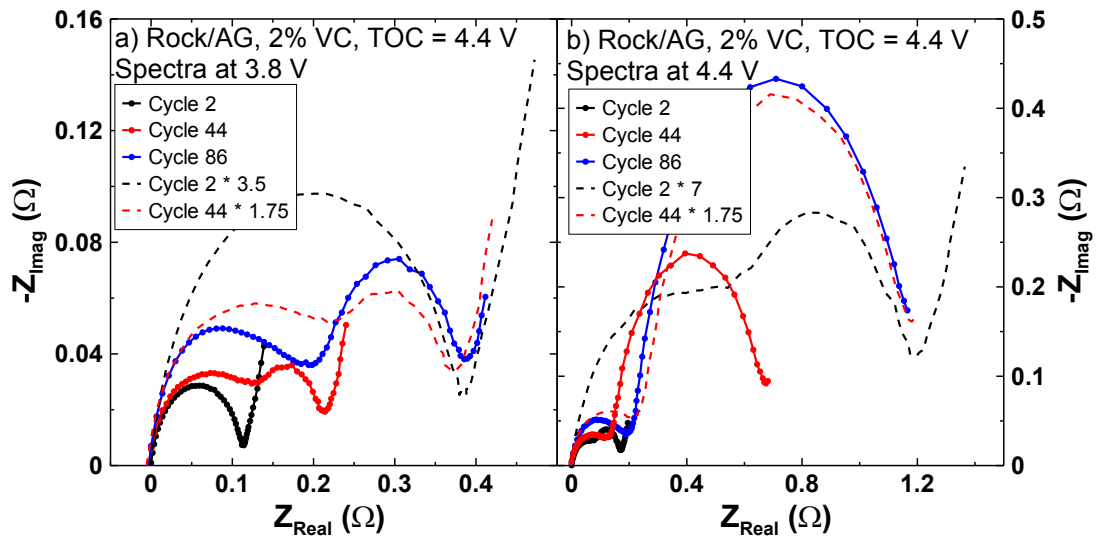


Figure 7.3 The impedance spectra measured at a) 3.8 V and b) 4.4 V for the Rock/AG cells containing 2% VC with an upper cutoff potential of 4.4 V. Spectra shown were measured during cycle 2, 44, and 86. The spectra measured during cycle 2 and 86 have also been scaled (as indicated in the legend) and plotted for comparison.

Figure 7.4 shows R_{ct} (the combination of charge transfer resistances from both the positive and negative electrode as well as the resistance due to motion of ions through the SEI layers at both the positive and negative electrodes) as a function of potential for the Rock/AG cells containing 2% VC (top panels) and 2% FEC (bottom panels). The value

of R_{ct} was taken to be the width of the impedance spectrum along the real axis. In the cases where incomplete spectra were measured due to large impedance growth, as shown in Figure 7.2d, R_{ct} was taken as the difference between the real part of the impedance at the lowest measured frequency and where the high frequency data crossed the real axis. This means that R_{ct} for some cells was underestimated.

The arrow in Figure 7.4a indicates the trend of the data with increasing cycle number and applies to all panels. Figure 7.4 shows that the 2% VC cells cycled to 4.2 V and below had very little impedance growth with potential or with cycle number. The 2% VC cell cycled to 4.3 V shows increased impedance at the top of charge. The 2% VC cell cycled to 4.4 V shows severe impedance growth at all potentials, which was accelerated at high potentials. Compared to the 2% VC cells, the cells containing 2% FEC exhibited higher impedance growth, but showed similar trends with cycle number and potential. While the 2% FEC cells cycled to 4.1 and 4.2 V had small impedance growth, it was larger than that of the 2% VC cells. The 2% FEC cell cycled to 4.3 V shows increased impedance at the top of charge and the 4.4 V cell shows severe impedance growth at all potentials, which was accelerated at high potentials. It is clear that impedance growth was dramatically impacted by the choice of upper cutoff potential and electrolyte additives used.

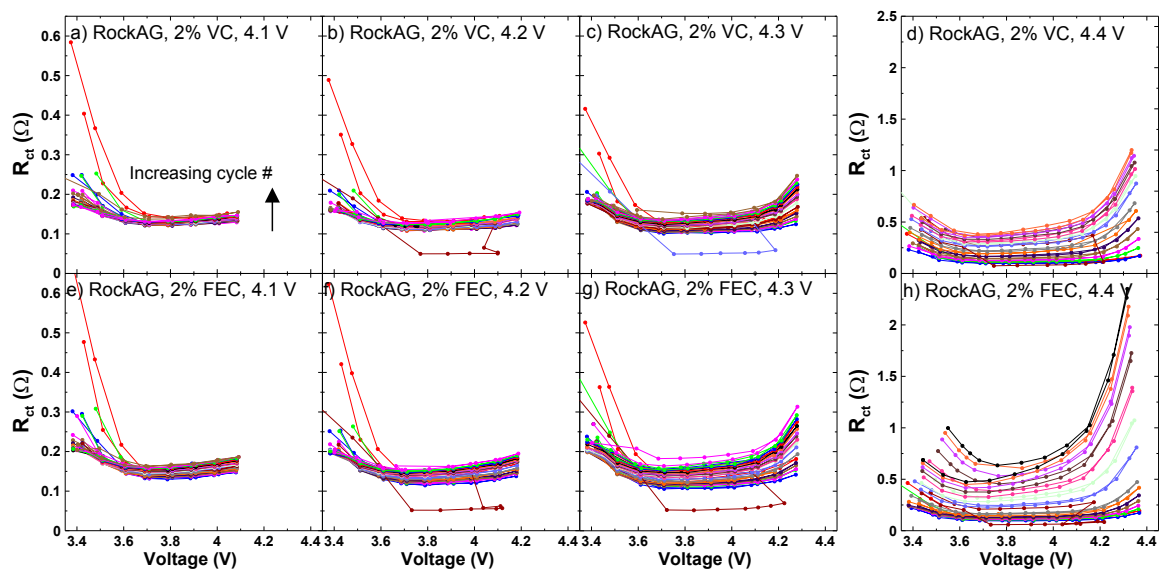


Figure 7.4 The combination of charge transfer resistance (both positive and negative electrodes) and resistance due to motion of ions through the SEI layers (both positive and negative electrodes), R_{ct} , as a function of voltage measured every 6 cycles for the Rock/AG cells containing 2% VC or 2% FEC. The arrow in panel a) indicates the trend of the data with increasing cycle number. Please note that the y-axis scale for panels d) and h) is different than the other panels.

Figure 7.5 shows the value of R_{ct} at 3.8 V (circles) and at the top of charge (crosses) as a function of cycle number for Rock/AG cells containing: a) 2% VC, b) 2% FEC, and c) EC:EMC:DMC:FEC. Figure 7.5a shows that the R_{ct} for 2% VC cells cycled to 4.1 V and 4.2 V were very similar and only slightly larger when measured at the top of charge compared to at 3.8 V. Figure 7.5a shows that the 2% VC cell cycled to 4.3 V had a slightly higher rate of impedance growth at 3.8 V compared to cells cycled to 4.1 V and 4.2 V, and had significant impedance growth at the top of charge. The cell cycled to 4.4 V had severe impedance growth at both 3.8 V and 4.4 V. Figure 7.5b shows that the R_{ct} for 2% FEC cells cycled to 4.1 V and 4.2 V were very similar and that the R_{ct} measured at the top of charge was larger compared to at 3.8 V. Figure 7.5b shows that the 2% FEC

cell cycled to 4.3 V had a slightly higher rate of impedance growth at 3.8 V compared to cells cycled to 4.1 V and 4.2 V, and had significant impedance growth at the top of charge. The cell cycled to 4.4 V had severe impedance growth at both 3.8 V and 4.4 V. Cells containing 2% FEC had a higher rate of impedance growth at all voltages compared to cells containing 2% VC. Figure 7.5c shows that while the initial impedance of cells containing EC:EMC:DMC:FEC was lower than the 4.3 V cells containing 2% VC and 2% FEC, the rate of impedance growth was similar.

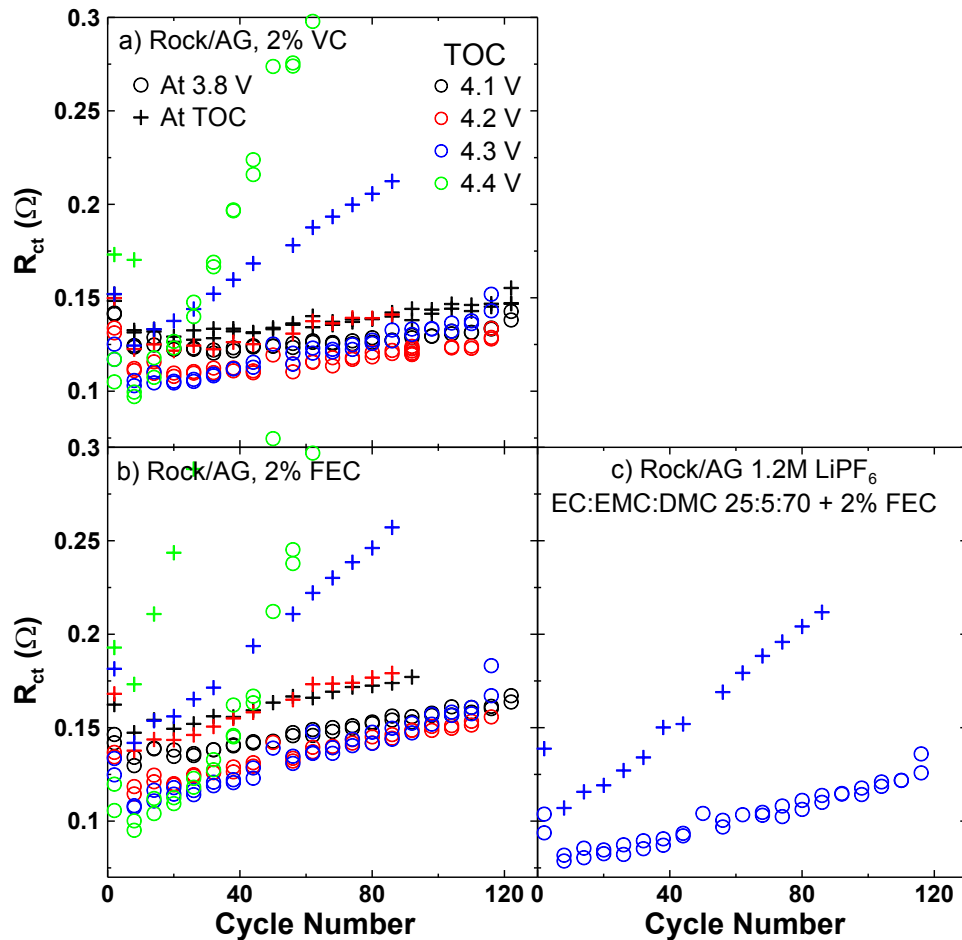


Figure 7.5 The values of R_{ct} , as a function of cycle number, extracted from the impedance spectra of Rock/AG cells filled with a) 2% VC, b) 2% FEC, and c) EC:EMC:DMC:FEC measured at 3.8 V and the top of charge.

Figure 7.6 shows the value of the high frequency intercept at 3.8 V (circles) and at the top of charge (crosses) as a function of cycle number for Rock/AG cells containing a) 2% VC, b) 2% FEC, and c) EC:EMC:DMC:FEC. Figure 7.6a and Figure 7.6b show that while the HFI measured at 3.8 V and at TOC was the same for each cell, the choice of upper cutoff potential significantly impacted the HFI. The rate of growth of the HFI was accelerated by increasing the upper cutoff potential. Figure 7.6c shows that the HFI of cells containing EC:EMC:DMC:FEC was the same when measured at 3.8 V and at 4.3 V, and had a higher rate of increase than the 4.3 V cells containing 2% VC and 2% FEC.

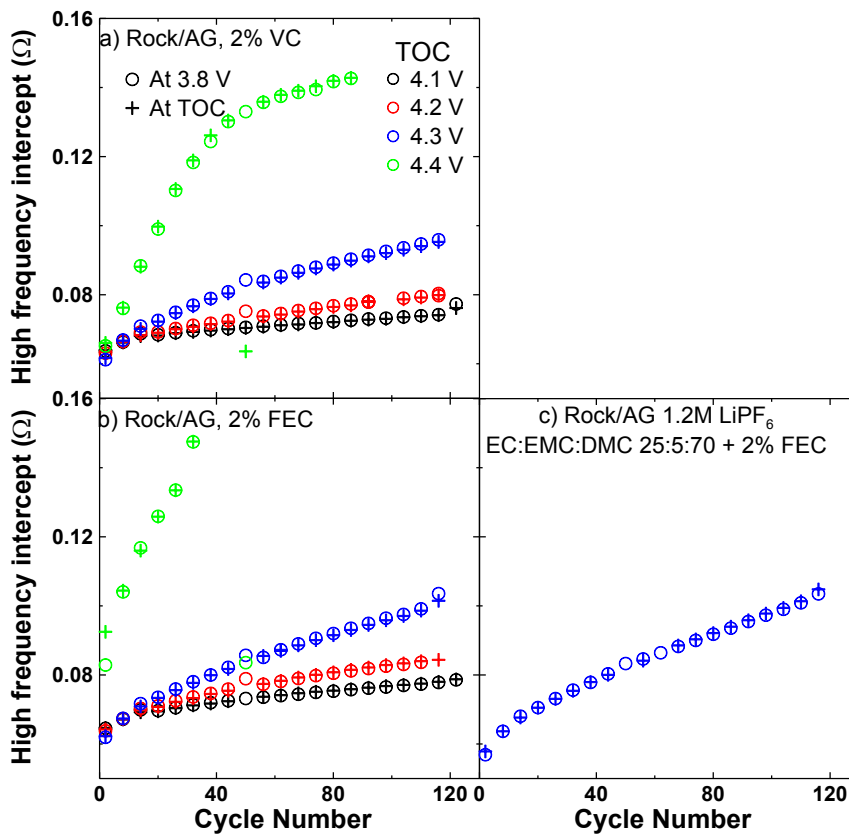


Figure 7.6 The values of the high frequency intercept, as a function of cycle number, extracted from the impedance spectra of Rock/AG cells filled with a) 2% VC, b) 2% FEC, and c) EC:EMC:DMC:FEC measured at 3.8 V and the top of charge.

Figure 7.7 shows the high frequency intercept as a function of measurement potential during the charge and discharge segments of cycles 8 and 80 for the 2% VC cells. For all cells, the high frequency intercept decreased with increasing measurement potential. This trend was shown in Figure 4.2 and Figure 4.3. The change in high frequency intercept was reversible during the charge and discharge segment of a single cycle, however, the high frequency intercept increased irreversibly from cycle 8 to cycle 80. Furthermore, the difference between the high frequency intercept measured at 3.4 V and at the top of charge increased dramatically as the upper cutoff potential of the cell increased.

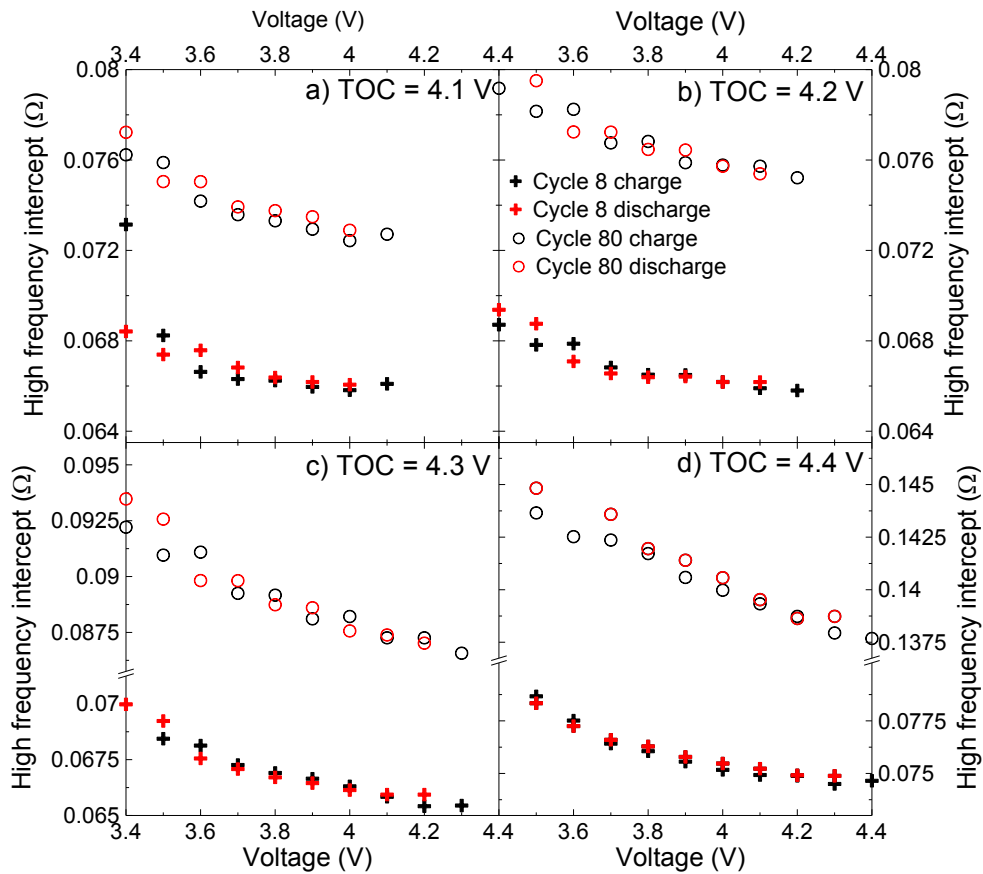


Figure 7.7 The high frequency intercept as a function of potential for the charge and discharge segments of cycles 8 and 80 for the Rock/AG cell containing VC cycled to a) 4.1 V, b) 4.2 V, c) 4.3 V, and d) 4.4 V.

It is useful to monitor the difference between the average charge and average discharge voltage (ΔV) and how it changes with cycle number. A smaller value of ΔV means smaller polarization, and thus smaller overall cell impedance, as discussed in section 4.2.¹⁴¹ Therefore, the change in ΔV with cycle number should correspond to the change in cell impedance with cycle number. Figure 7.8 shows the actual measured change in ΔV as well as the expected change in ΔV calculated from the measured impedance growth. The actual change in ΔV was calculated using

$$\text{Actual change in } \Delta V = \Delta V(\text{cycle } n) - \Delta V(\text{cycle } 3) \quad (7.1)$$

where cycle 3 was used as the reference cycle. The expected change in ΔV was calculated using

$$\text{Calc. change in } \Delta V = 2I\{[HFI + R_{ct}](\text{cycle } n) - [HFI + R_{ct}](\text{cycle } 3)\} \quad (7.2)$$

where cycle 3 was used as the reference cycle, the impedance growth was taken as the sum of the HFI and R_{ct} , and the current used was either the current corresponding to the C/5 or C/2.5 cycles. The factor of 2 was used to incorporate both the charge and discharge contribution.

Figure 7.8 shows the actual change in ΔV during both the C/5 and C/2.5 cycles (diamonds) and the calculated change in ΔV during the C/5 cycles (circles) and the C/2.5 cycles (crosses), as described in the legend. The top panels of Figure 7.8 show the actual and calculated change in ΔV for the Rock/AG cells containing 2% VC, and the bottom panels show that for the Rock/AG cells containing 2% FEC. The upper cutoff potential is indicated in each panel. In general, the actual change in ΔV was larger than the calculated

change in ΔV at the same C-rate, but the rate of increase was the same. This means that, for the cells shown in Figure 7.8, the growth in ΔV was well-matched to the total growth in impedance. In Figure 7.8d and Figure 7.8h, the calculated change in ΔV was significantly smaller than the actual change in ΔV . This indicates that for the Rock/AG cells cycled to 4.4 V, the polarization was larger than the growth in HFI and R_{ct} . Both the actual and calculated change in ΔV for the Rock/AG cells cycled to 4.4 V were significantly larger compared to the cells cycled to 4.3 V and below. This corresponds to the severe capacity fade shown in Figure 7.1 for the cells cycled to 4.4 V. The actual change in ΔV may be larger than the calculated change in ΔV because of increases to the Warburg diffusion, which is not included in EIS measurements when impedance growth becomes large, but is included in ΔV growth. The formation and growth of a rocksalt layer^{102,109} would slow Li-ion diffusion and compromise the diffusional path. Due to time constraints, impedance measurements to very low frequency were not done. This means that the Warburg diffusion component was not always captured, and was excluded from the calculated change in ΔV , which only considers the HFI and R_{ct} .

Figure 7.9 shows the actual and calculated change in ΔV for the Rock/AG cell containing EC:EMC:DMC:FEC. The change in ΔV was calculated using equations 7.1 and 7.2, as described above. The actual change in ΔV was larger than the calculated change in ΔV at the same C-rate, but the rate of increase was the same. The actual and calculated changes in ΔV shown in Figure 7.9 are similar to those shown in Figure 7.8 for the 4.3 V cells. Therefore, the change in ΔV for all Rock/AG cells was significantly impacted by choice of upper cutoff potential, but not influenced by choice of electrolyte additives used.

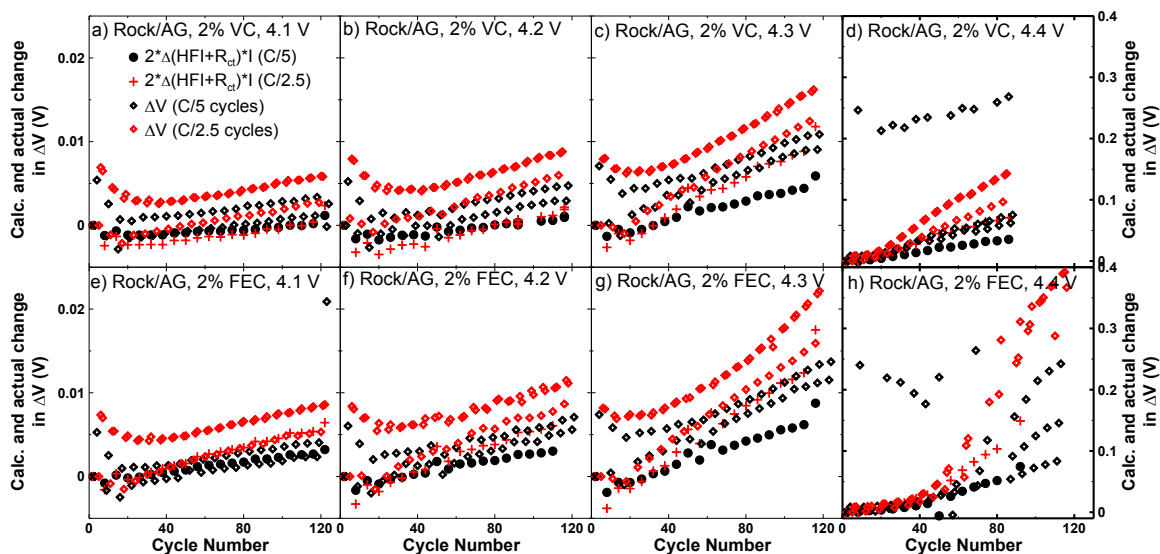


Figure 7.8 The actual and calculated change in ΔV (obtained using equations 7.1 and 7.2) during the C/5 and C/2.5 cycles for the Rock/AG cells containing 2% VC (top panels) and 2% FEC (bottom panels). The upper cutoff potential is indicated in each panel. Please note the different scale for the axes in panel d) and h).

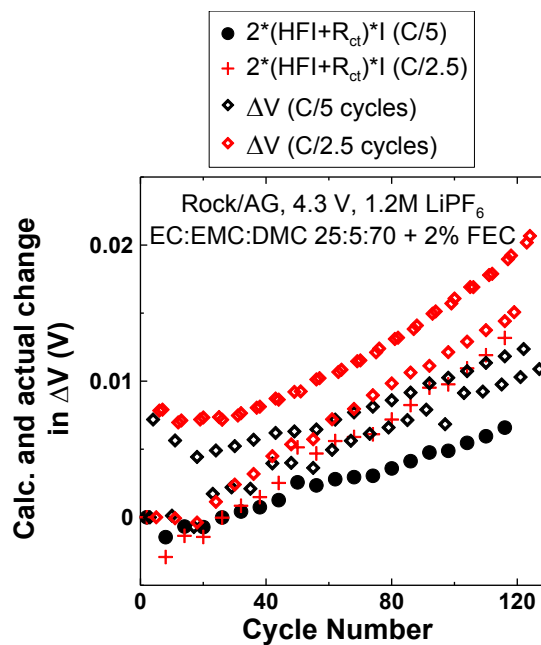


Figure 7.9 The actual and calculated change in ΔV (obtained using equations 7.1 and 7.2) during the C/5 and C/2.5 cycles for the Rock/AG cells containing EC:EMC:DMC:FEC. The upper cutoff potential is indicated in each panel.

Figure 7.10 shows the discharge capacity as a function of time for selected Rock/AG cells shown in Figure 7.1 that underwent charge-hold-discharge cycling compared to similar cells that underwent C/3 charge-discharge cycling (C/3 data from Jing Li, Dalhousie University). Figure 7.10a shows the capacity for 2% FEC cells cycled to 4.2 V and 4.3 V. Figure 7.10a shows that the capacity retention as a function of time during charge-hold-discharge cycling was similar to that during continuous cycling. Figure 7.10b shows the capacity for EC:EMC:DMC:FEC cells cycled to 4.3 V. Figure 7.10b shows that while the capacity during charge-hold-discharge cycling was larger than during continuous cycling, the rate of capacity fade was the same. This means that holding for 24 hours at 4.2 and 4.3 V was not detrimental to cell lifetime. However, based on work in Chapter 5, it is expected that cells held at 4.4 V would be much worse than cells cycled continuously to 4.4 V. Long term data was not available.

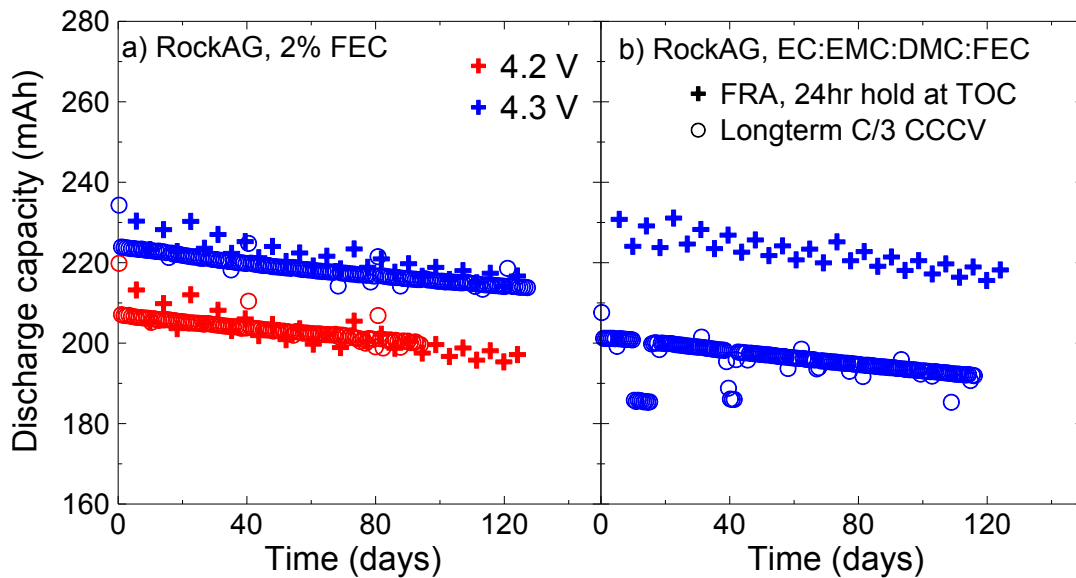


Figure 7.10 The discharge capacity as a function of time for Rock/AG cells that underwent charge-hold-discharge cycling and charge-discharge cycling at 40°C containing a) 2% FEC and b) EC:EMC:DMC:FEC.

Figure 7.11 shows the difference between the average charge and discharge voltage, ΔV , as a function of time for selected Rock/AG cells shown in Figure 7.1 that underwent charge-hold-discharge cycling compared to similar cells that underwent C/3 charge-discharge cycling (C/3 data from Jing Li, Dalhousie University). Figure 7.11a shows ΔV for the 2% FEC cells cycled to 4.2 V and 4.3 V. Figure 7.11 shows that the ΔV as a function of time during charge-hold-discharge cycling had similar rate of increase compared to that during continuous cycling. Figure 7.11b shows that the ΔV for EC:EMC:DMC:FEC cells cycled to 4.3 V was smaller than for cells containing 2% FEC, but the rate of increase was the same. Based on work in Chapter 5, it is expected that cells held at 4.4 V would be much worse than cells cycled continuously to 4.4 V. Long term data was not available.

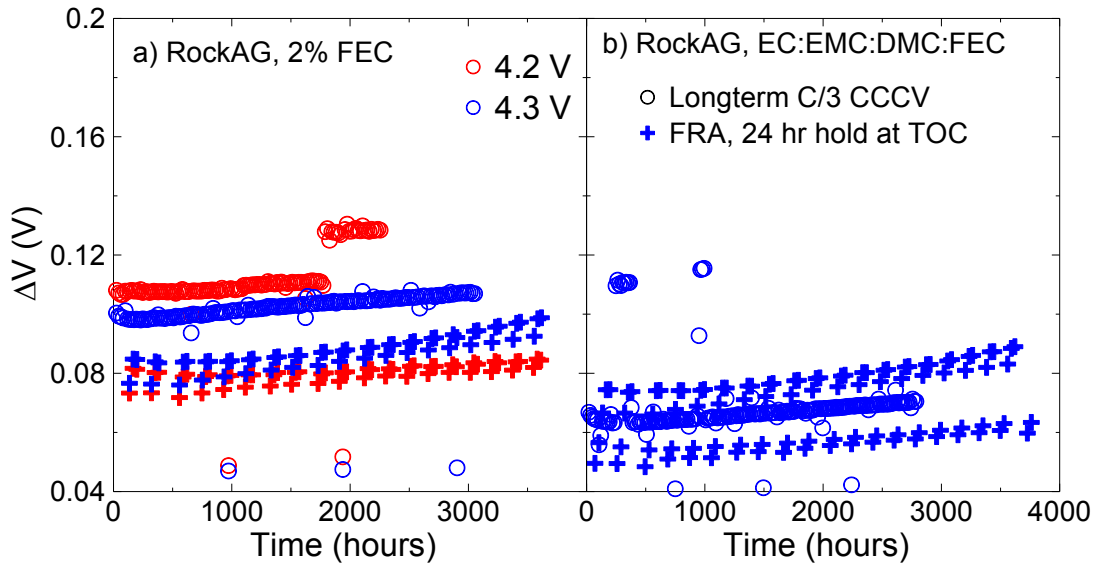


Figure 7.11 ΔV as a function of time for Rock/AG cells that underwent charge-hold-discharge cycling and charge-discharge cycling at 40°C containing a) 2% FEC and b) EC:EMC:DMC:FEC.

7.2.2 CELLS WITH NATURAL GRAPHITE

Figure 7.12 shows the discharge capacity as a function of cycle number for all cells containing natural graphite. Figure 7.12a, Figure 7.12c, and Figure 7.12e show the discharge capacity for cells containing PES211 with an upper cutoff potential of 4.1, 4.2, and 4.3 V, respectively. Figure 7.12e also shows the discharge capacity for Rock/NG cells containing PES211 with an upper cutoff potential of 4.4 V. Figure 7.12b, Figure 7.12d, and Figure 7.12f show the discharge capacity for cells containing VC211 with an upper cutoff potential of 4.1, 4.2, and 4.3 V, respectively. 622A and 622B cells cycled to 4.1, 4.2, and 4.3 V had similar rates of capacity fade. Rock/NG cells containing PES211 had similar rates of capacity fade when cycled up to 4.3 V, but had severe discharge capacity fade after only 40 cycles when cycled to 4.4 V. Rock/NG cells cycled to 4.1 and 4.2 V containing VC211 had higher rates of capacity fade compared to the 622A and 622B cells, indicating that the electrolyte additives used had a significant impact on the performance of Rock/NG cells, but negligible difference in 622A and 622B cells.

Figure 7.13 shows the impedance spectra collected every 6 cycles for 622A cells containing PES211 (top panels) and VC211 (bottom panels), both with an upper cutoff potential of 4.3 V. Figure 7.13a and Figure 7.13b show the spectra measured at 3.8 V and 4.2 V, respectively, for the PES211 cell cycled to 4.3 V. Figure 7.13c and Figure 7.13d show the spectra measured at 3.8 V and 4.3 V, respectively, for the VC211 cell cycled to 4.3 V. The arrow in Figure 7.13a indicates the trend of the spectra with increasing cycle number and applies to all panels. Figure 7.13 shows that for both cells, the spectra were very similar at 3.8 and 4.3 V. Both the overall widths of the impedance spectra and the

high frequency intercepts grew with cycle number. The spectra measured at 4.3 V for both cells were slightly larger than those measured at 3.8 V.

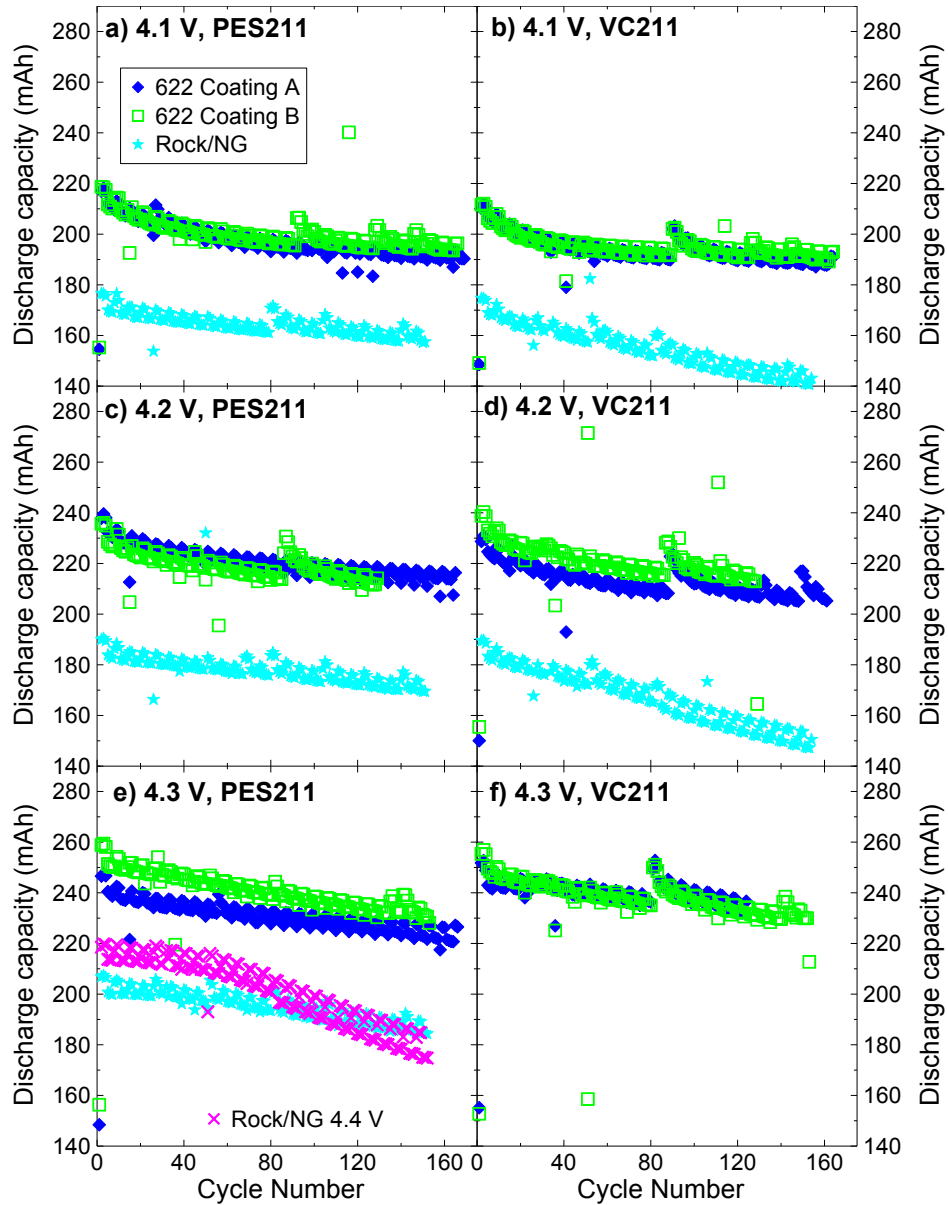


Figure 7.12 The discharge capacity as a function of cycle number for cells cycled to 4.1 V containing a) PES211 or b) VC211, cells cycled to 4.2 V containing c) PES211 or d) VC211, and cells cycled to 4.3 or 4.4 V containing e) PES211 or f) VC211. The cell type is indicated by the legend. The cells underwent charge-hold-discharge cycling at 40°C, as described by Figure 3.2.

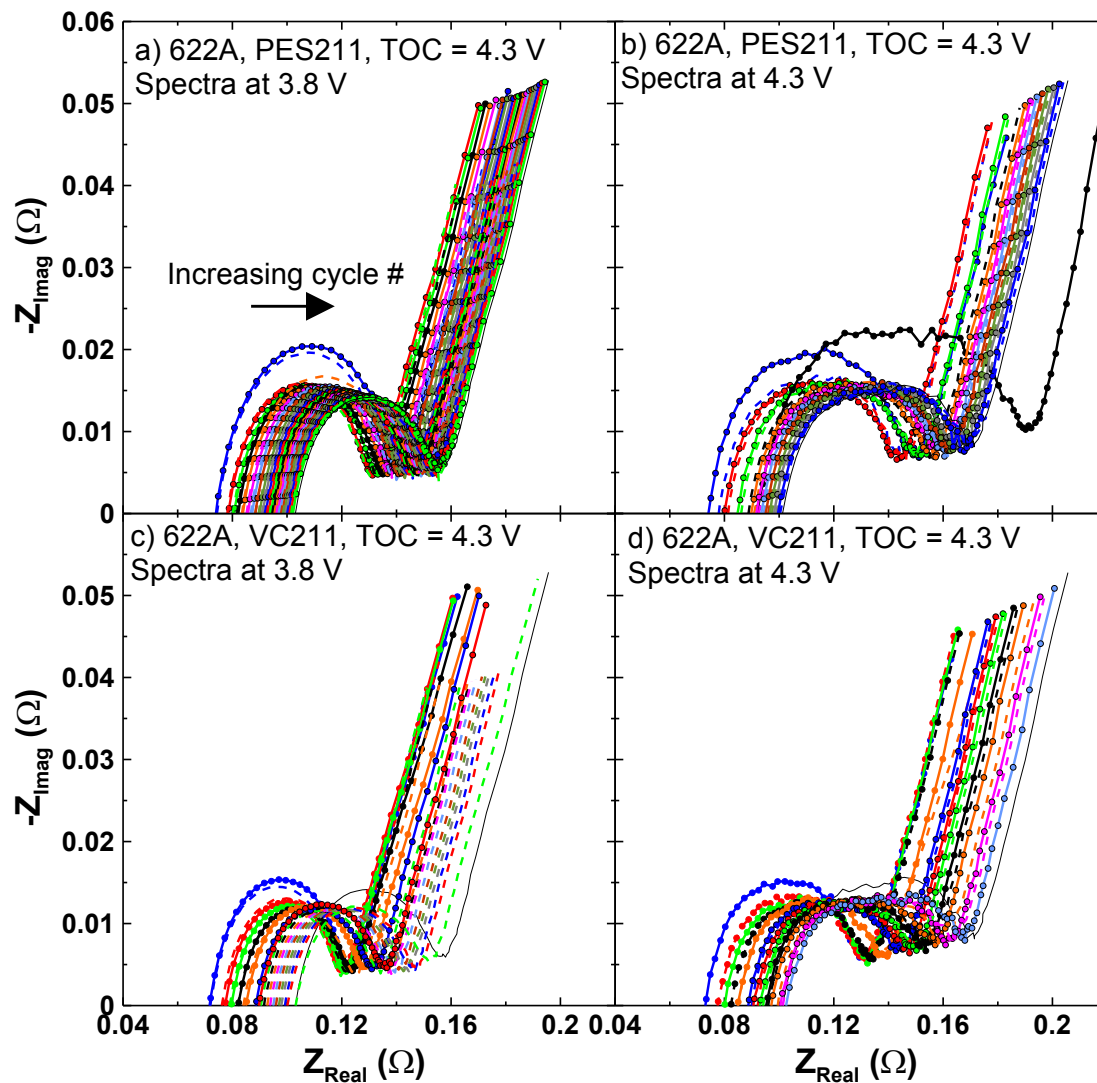


Figure 7.13 The impedance spectra as measured by the 4-wire FRA for the 622A cells cycled to 4.3 V containing a) PES211 and measured at 3.8 V, b) PES211 and measured at 4.3 V, c) VC211 and measured at 3.8 V, and d) VC211 and measured at 4.3 V.

Figure 7.14 shows the impedance spectra collected every 6 cycles for Rock/NG cells containing PES211 cycled to 4.3 V or 4.4 V. Figure 7.14a and Figure 7.14b show the spectra measured at 3.8 V and 4.3 V, respectively, for the Rock/NG cell cycled to 4.3 V. Figure 7.14c and Figure 7.14d show the spectra measured at 3.8 V and 4.4 V,

respectively, for the Rock/NG cell cycled to 4.4 V. The arrow in Figure 7.14a indicates the trend of the spectra with increasing cycle number and applies to all panels. Figure 7.14 shows that for both cells, the high frequency intercept increased with cycle number. Figure 7.14 shows that for the Rock/NG cell cycled to 4.3 V, the impedance was larger at 4.3 V compared to at 3.8 V. Figure 7.14 shows that, while the overall impedance was larger at 4.4 V compared to at 3.8 V for the Rock/NG cell cycled to 4.4 V, the shape of the spectra were dramatically different. In Figure 7.14c, the mid-to-high frequency feature grew with increasing cycle number. This is very different than the impedance growth observed for nearly all other cells presented in this thesis. Typically, the low frequency feature associated with the positive electrode SEI layer exhibits the most growth. The growth of the mid-to-high frequency feature shown in Figure 7.14c may indicate that, at 3.8 V, the negative electrode impedance increased. It is possible that particle cracking occurs for natural graphite after prolonged cycling, leading to an increase in the negative electrode impedance. Park et al. found that carbon-coated natural graphite and the SEI film formed on the NG formed cracks caused by the volume change during continuous cycling.¹⁶³ Park et al. claimed that the volume change and subsequent cracks led to electrolyte decomposition and capacity fading.¹⁶³ Figure 7.14d shows that the impedance at 4.4 V increased with cycle number, and that both the low frequency feature and the mid-to-high frequency feature grew with increasing cycle number.

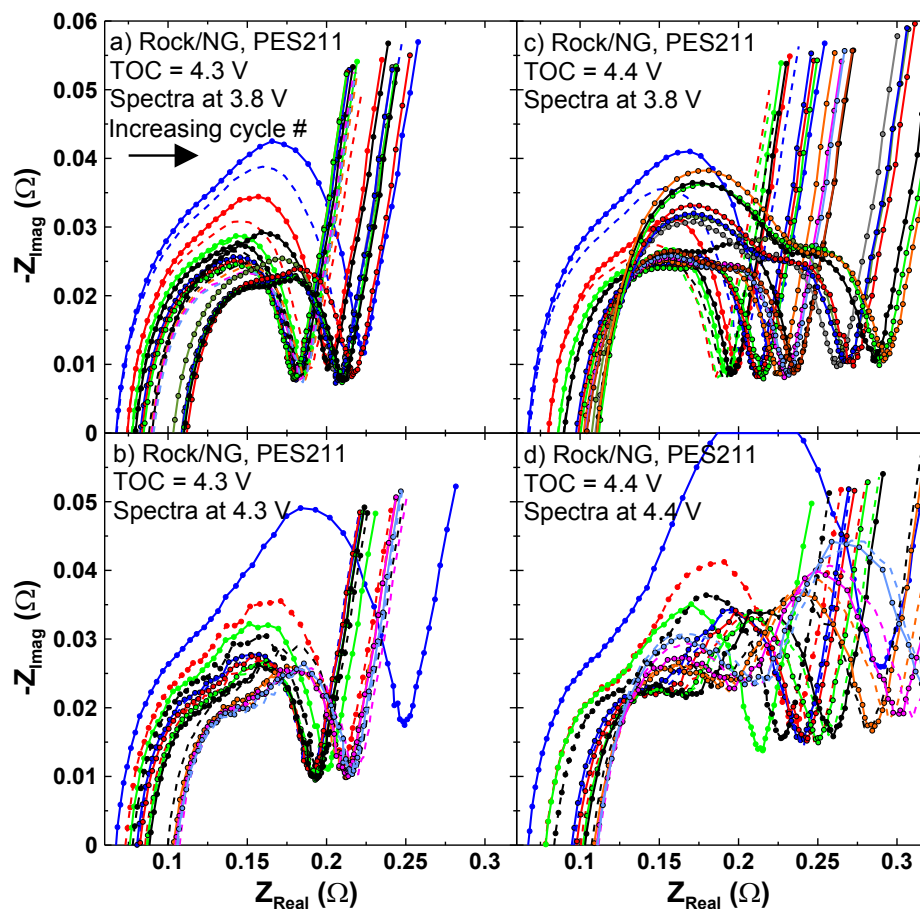


Figure 7.14 The impedance spectra as measured by the 4-wire FRA for the Rock/NG cells containing PES211 a) cycled to 4.3 V and measured at 3.8 V, b) cycled to 4.3 V and measured at 4.3 V, c) cycled to 4.4 V and measured at 3.8 V, and d) cycled to 4.4 V and measured at 4.4 V.

Figure 7.15 shows the value of R_{ct} at 3.8 V (circles) and at the top of charge (crosses) as a function of cycle number for cells containing NG. Figure 7.15a and Figure 7.15d show R_{ct} for 622A cells containing PES211 and VC211, respectively. Figure 7.15b and Figure 7.15e show R_{ct} for 622B cells containing PES211 and VC211, respectively. Figure 7.15c and Figure 7.15f show R_{ct} for Rock/NG cells containing PES211 and VC211, respectively. The 622A cells containing PES211 cycled to 4.1 V and 4.2 V were very similar and were the same when measured at 3.8 V and the TOC. Comparatively, the

622A cells containing PES211 cycled to 4.3 V had similar impedance when measured at 3.8 V and had larger impedance when measured at the TOC. The 622A cells containing VC211 cycled to 4.1 V and 4.2 V were very similar and were the same when measured at 3.8 V and the TOC. Comparatively, the 622A cells containing VC211 cycled to 4.3 V had similar impedance when measured at 3.8 V and had larger impedance when measured at the TOC. The rate of impedance growth in the 622A cells containing VC211 was larger than in cells containing PES211.

The 622B cells containing PES211 cycled to 4.1 V and 4.2 V were very similar and were the same when measured at 3.8 V and the TOC. Comparatively, the 622B cells containing PES211 cycled to 4.3 V had a higher rate of impedance growth at both 3.8 V and at the TOC. The 622B cells containing VC211 cycled to 4.1 V and 4.2 V were very similar and were the same when measured at 3.8 V and the TOC. Comparatively, the 622B cells containing VC211 cycled to 4.3 V had a higher rate of impedance growth at both 3.8 V and the TOC.

The Rock/NG cells containing PES211 cycled to 4.1 V and 4.2 V were very similar and were the same when measured at 3.8 V and the TOC. The Rock/NG cells containing PES211 cycled to 4.3 V had a higher rate of impedance growth at both 3.8 V and at the TOC. The Rock/NG cells cycled to 4.4 V had severe impedance growth at both 3.8 V and the TOC. The Rock/NG cells containing VC211 cycled to 4.1 V and 4.2 V were very similar and were the same when measured at 3.8 V and the TOC. The Rock/NG cells had larger impedance and impedance growth compared to the 622A and 622B cells. The

Rock/NG cells containing PES211 cycled to 4.1 and 4.2 V had smaller impedance growth than the similar cells containing VC211.

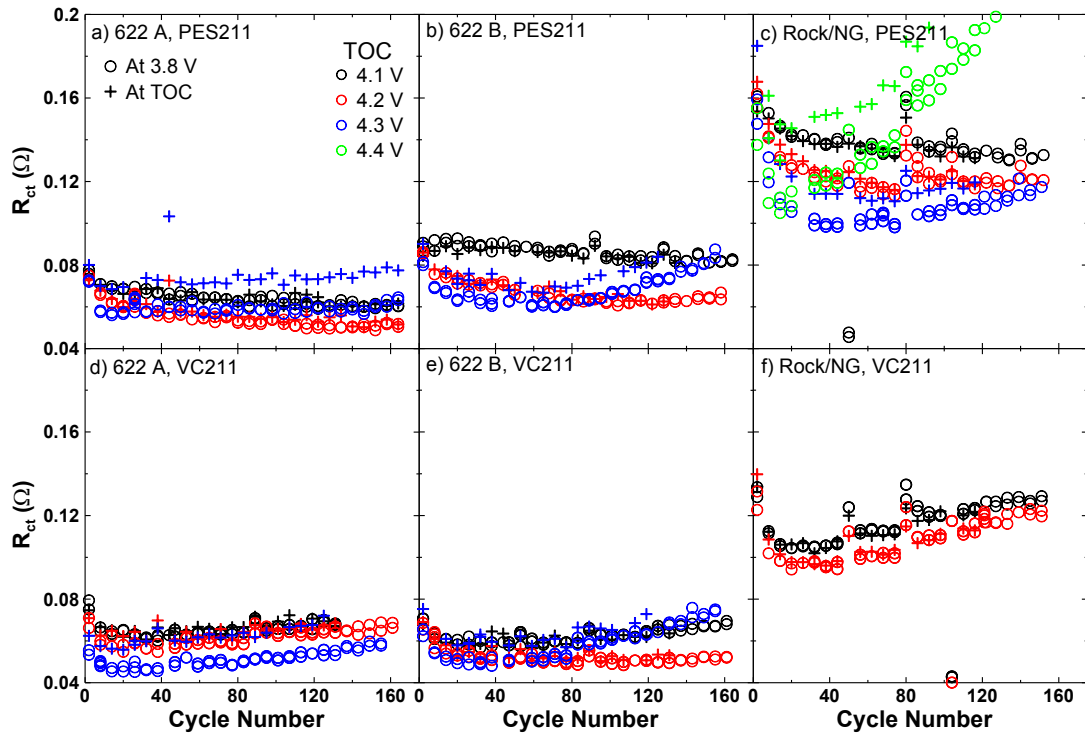


Figure 7.15 The values of R_{ct} , as a function of cycle number, extracted from the impedance spectra of (a,d) 622A, (b,e) 622B, and (c,f) Rock/NG cells filled with PES211 (a-c) and VC211 (d-f) measured at 3.8 V and the top of charge.

Figure 7.16 shows the value of the HFI at 3.8 V (circles) and at the top of charge (crosses) as a function of cycle number for cells containing NG. Figure 7.16a and Figure 7.16d show the HFI for 622A cells containing PES211 and VC211, respectively. Figure 7.16b and Figure 7.16e show the HFI for 622B cells containing PES211 and VC211, respectively. Figure 7.16c and Figure 7.16f show the HFI for Rock/NG cells containing PES211 and VC211, respectively. The jumps in the data are due to an unknown issue. Figure 7.16 shows that while the HFI measured at 3.8 V and at TOC was the same for

each cell, the choice of upper cutoff potential significantly impacted the HFI. The rate of growth of the HFI was accelerated by increasing the upper cutoff potential. There were no clear differences between the cells containing PES211 compared to VC211. It is possible that particle cracking occurs for natural graphite after prolonged cycling. Park et al. found that carbon-coated natural graphite and the SEI film formed on the NG formed cracks caused by the volume change during continuous cycling.¹⁶³ Park et al. claimed that the volume change and subsequent cracks led to electrolyte decomposition and capacity fading.¹⁶³ Cells containing NG may therefore have higher values of HFI due to particle cracking. However, impedance data for 622A and 622B with AG are not available for comparisons.

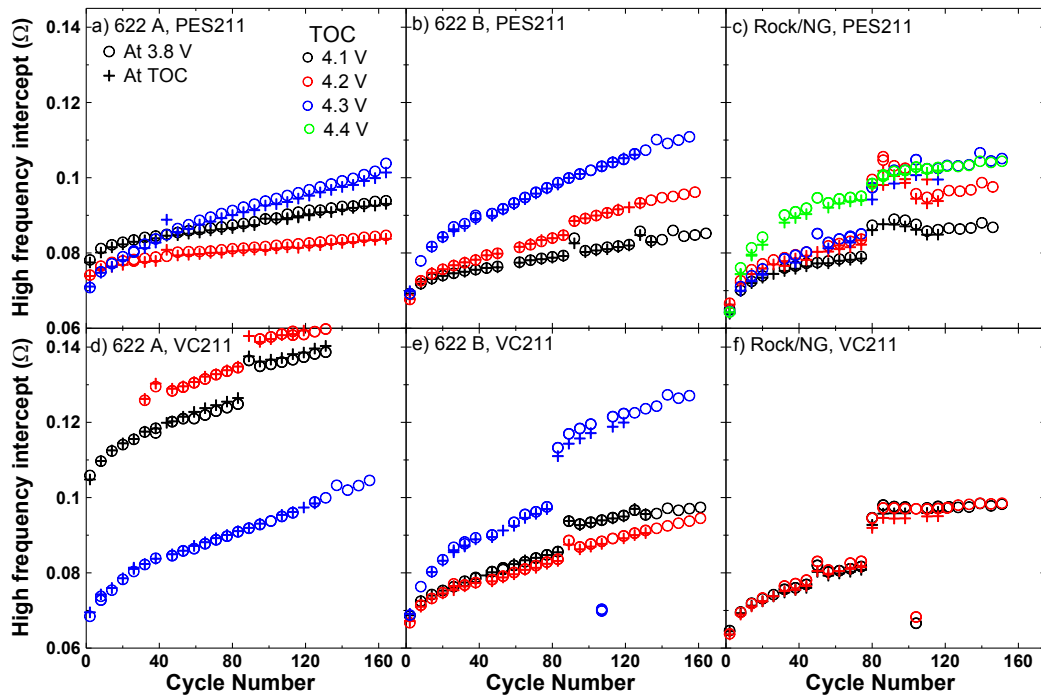


Figure 7.16 The values of the high frequency intercept, as a function of cycle number, extracted from the impedance spectra of (a,d) 622A, (b,e) 622B, and (c,f) Rock/NG cells filled with PES211 (a-c) and VC211 (d-f) measured at 3.8 V and the top of charge.

Figure 7.17 shows the actual and calculated change in ΔV for the 622A cells containing PES211 (top panels) and VC211 (bottom panels). The change in ΔV was calculated using equations 7.1 and 7.2, as described in section 7.2.1. In general, the actual change in ΔV was larger than the calculated change in ΔV . The rate of increase was the same for the 622A cells cycled to 4.1 V and for the 622A cell containing VC211 cycled to 4.2 V. The rate of increase of the calculated and actual change in ΔV for the 622A cells cycled to 4.3 V and for the 622A cell containing PES211 cycled to 4.2 V, however, were not the same. For the 622A cell containing PES211 cycled to 4.2 V, the calculated change in ΔV was low and constant, but the actual change in ΔV had significant growth with cycle number. The reason for this is unknown. While both the actual and calculated change in ΔV increased for the 622A cells cycled to 4.3 V, the actual change increased at a much higher rate than the calculated change. The change in ΔV was significantly impacted by the choice of upper cutoff potential. The rate of increase was accelerated with increasing voltage.

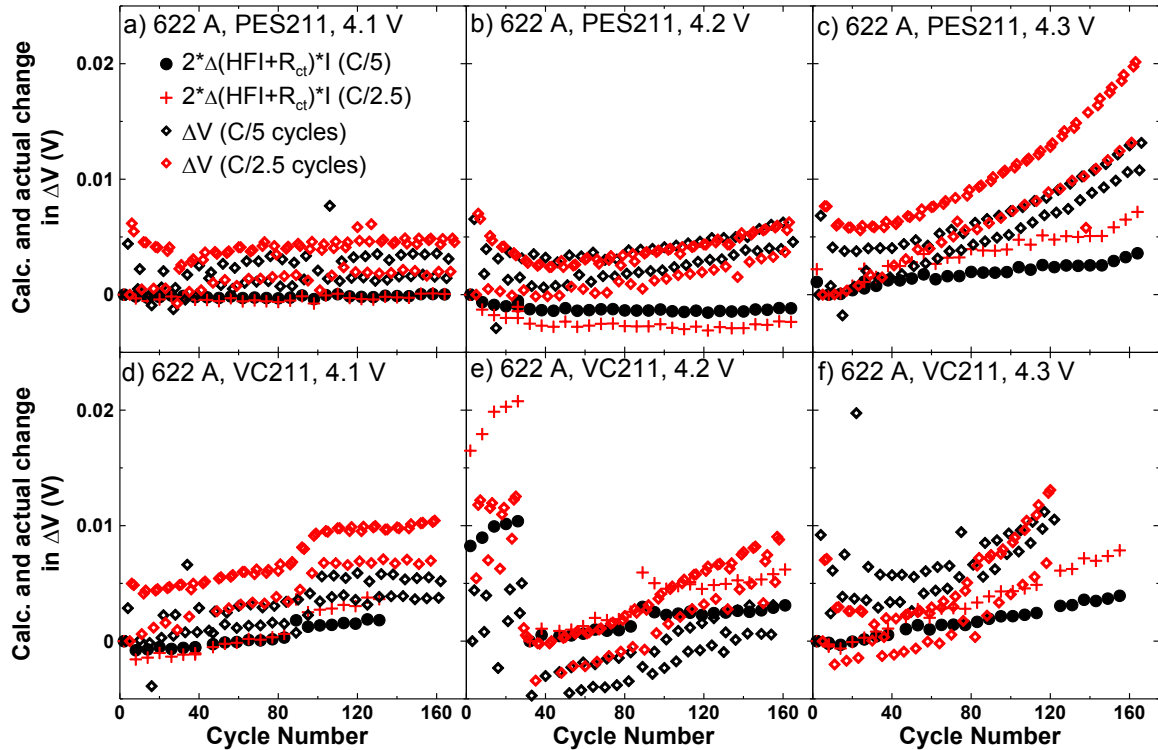


Figure 7.17 The actual and calculated change in ΔV (obtained using equations 7.1 and 7.2) during the C/5 and C/2.5 cycles for the 622A cells containing PES211 (top panels) and VC211 (bottom panels). The upper cutoff potential is indicated in each panel.

Figure 7.18 shows the actual and calculated change in ΔV for the 622B cells containing PES211 (top panels) and VC211 (bottom panels). The change in ΔV was calculated using equations 7.1 and 7.2, as described in section 7.2.1. In general, the actual change in ΔV was larger than the calculated change in ΔV . The rate of increase was the same for the 622B cells cycled to 4.1 V. The rate of increase of the calculated and actual change in ΔV for the 622B cells cycled to 4.2 and 4.3, however, were not the same. While both the actual and calculated change in ΔV increased for the 622B cells cycled to 4.2 and 4.3 V, the actual change increased at a much higher rate than the calculated change. The actual and calculated change in ΔV for the 622A cells shown in Figure 7.17 were approximately

the same for the 622B cells shown in Figure 7.18. The change in ΔV was significantly impacted by the choice of upper cutoff potential, but unaffected by the choice of electrolyte additives used. The rate of increase was accelerated with increasing voltage.

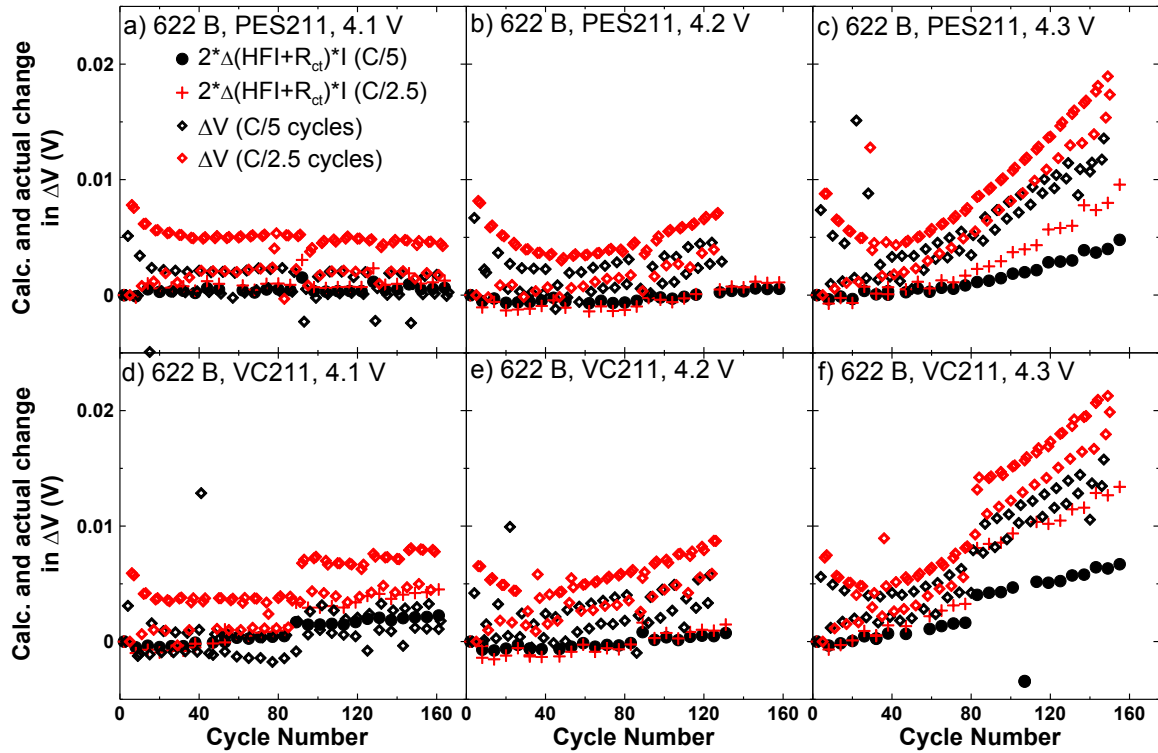


Figure 7.18 The actual and calculated change in ΔV (obtained using equations 7.1 and 7.2) during the C/5 and C/2.5 cycles for the 622B cells containing PES211 (top panels) and VC211 (bottom panels). The upper cutoff potential is indicated in each panel.

Figure 7.19 shows the actual and calculated change in ΔV for the Rock/NG cells containing PES211 (top panels) and VC211 (bottom panels). The change in ΔV was calculated using equations 7.1 and 7.2, as described in section 7.2.1. Unlike the 622A and 622B cells, the calculated change in ΔV for the Rock/NG cells did not match the actual change in ΔV . The calculated change in ΔV for all cells was very low, except the 4.4 V

cell which showed a significant growth. Alternatively, the actual change in ΔV was large for all cells, particularly for cells containing PES211 cycled to 4.3 V and above, and for the VC211 cells cycled to 4.1 and 4.2 V. This means that the measured impedance growth does not account for the severe ΔV growth. The growth in actual ΔV corresponds to the capacity fade exhibited by these cells in Figure 7.12.

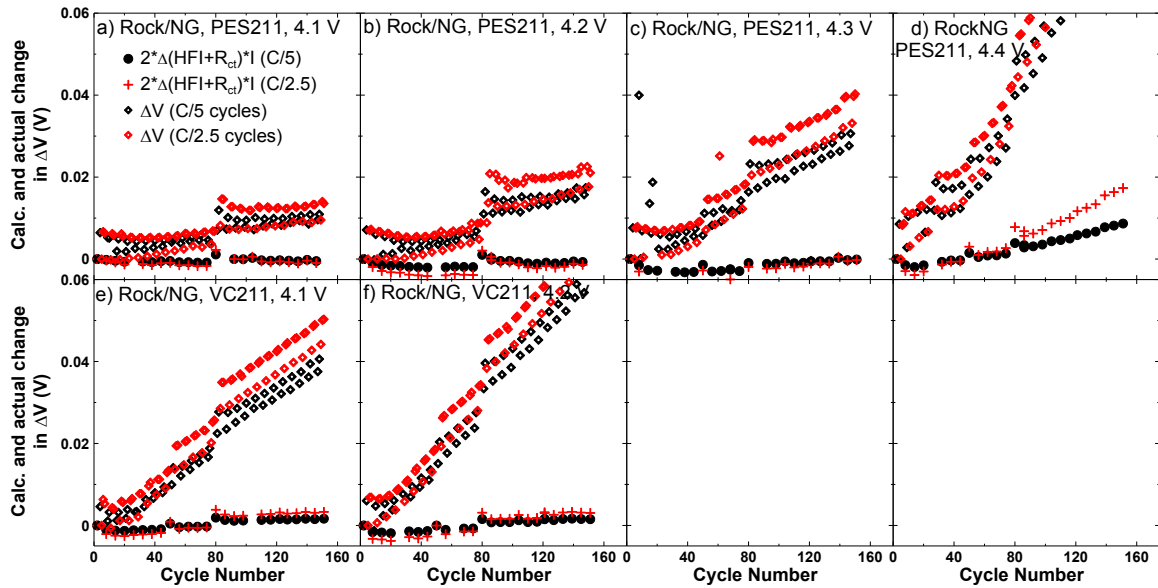


Figure 7.19 The actual and calculated change in ΔV (obtained using equations 7.1 and 7.2) during the C/5 and C/2.5 cycles for the Rock/NG cells containing PES211 (top panels) and VC211 (bottom panels). The upper cutoff potential is indicated in each panel.

Figure 7.20 shows the discharge capacity as a function of time for selected NG cells shown in Figure 7.12 that underwent charge-hold-discharge cycling compared to cells that underwent C/3 charge-discharge cycling (C/3 data from Jing Li, Dalhousie University). The top and bottom panels of Figure 7.20 show the capacity data for cells containing PES211 and VC211, respectively.

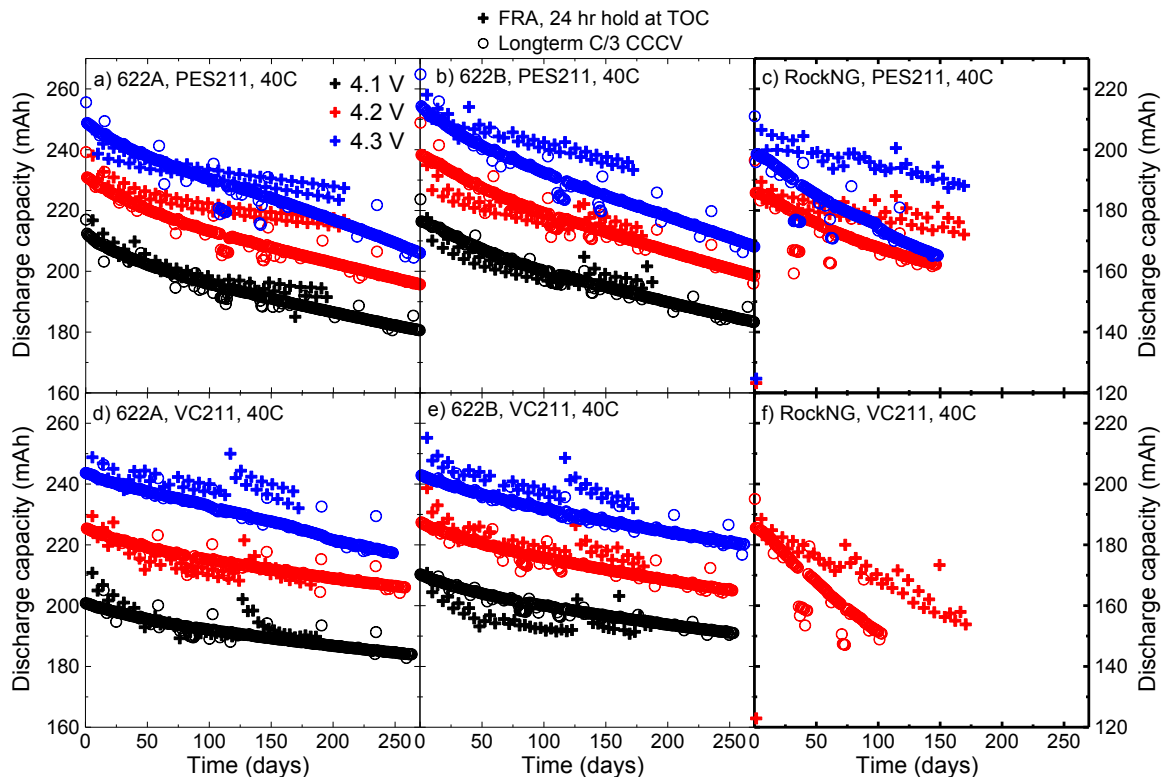


Figure 7.20 The discharge capacity as a function of time for 622A (a,d), 622B (b,e), and Rock/NG (c,f) cells that underwent charge-hold-discharge cycling and charge-discharge cycling at 40°C containing PES211 (a-c) and VC211 (d-f).

Figure 7.20 shows that the capacity retention as a function of time during charge-hold-discharge cycling was similar to that during continuous cycling for the 622A and 622B cells containing VC211 and for the 622A and 622B cells containing PES211 cycled to 4.1 V. The capacity retention versus time for the 622A and 622B cells containing PES211 cycled to 4.2 and 4.3 V, as well as the Rock/NG cells, was worse for the continuously cycled cells compared to the cells undergoing charge-hold-discharge cycling. This difference may be a result of particle cracking that might occur in cells containing natural graphite,¹⁶³ which is accelerated with increasing cycle number. This means that continuously cycled cells, which undergo more cycles per unit time, compared to cells

undergoing charge-hold-discharge cycling would be more affected by particle cracking, therefore leading to larger capacity fade and larger impedance growth. However, at potentials at and above 4.4 V, cells cycled continuously have lower impedance growth and capacity fade compared to cells undergoing charge-hold-discharge cycling.^{10,82} Figure 7.20 shows that Rock/NG cells containing VC211 had larger capacity fade compared to the Rock/NG cells containing PES211.

Figure 7.21 shows the difference between the average charge and discharge voltage, ΔV , as a function of time for selected NG cells shown in Figure 7.12 that underwent charge-hold-discharge cycling compared to similar cells that underwent C/3 charge-discharge cycling (C/3 data from Jing Li, Dalhousie University). The top and bottom panels of Figure 7.21 show ΔV for cells containing PES211 and VC211, respectively. Figure 7.21 shows that ΔV as a function of time during charge-hold-discharge cycling had a similar rate of increase compared to that during continuous cycling for the 622A cells containing VC211 cycled to 4.1 and 4.2 V and for the 622B cells containing VC211 at all potentials. The rate of increase of ΔV for the 622A and 622B cells containing PES211 at all potentials, the 622A cells containing VC211 cycled to 4.3 V, as well as the Rock/NG cells, was worse for the continuously cycled cells compared to the cells undergoing charge-hold-discharge cycling. This difference may be a result of particle cracking that can form in cells containing natural graphite,¹⁶³ which is accelerated with increasing cycle number. This means that continuously cycled cells, which undergo more cycles per unit time, compared to cells undergoing charge-hold-discharge cycling would be more affected by particle cracking, leading to larger capacity fade, and larger impedance

growth and therefore larger cell polarization and ΔV . At 4.4 V, however, cells cycled continuously have smaller capacity fade and impedance growth compared to cells undergoing charge-hold-discharge cycling.^{10,82}

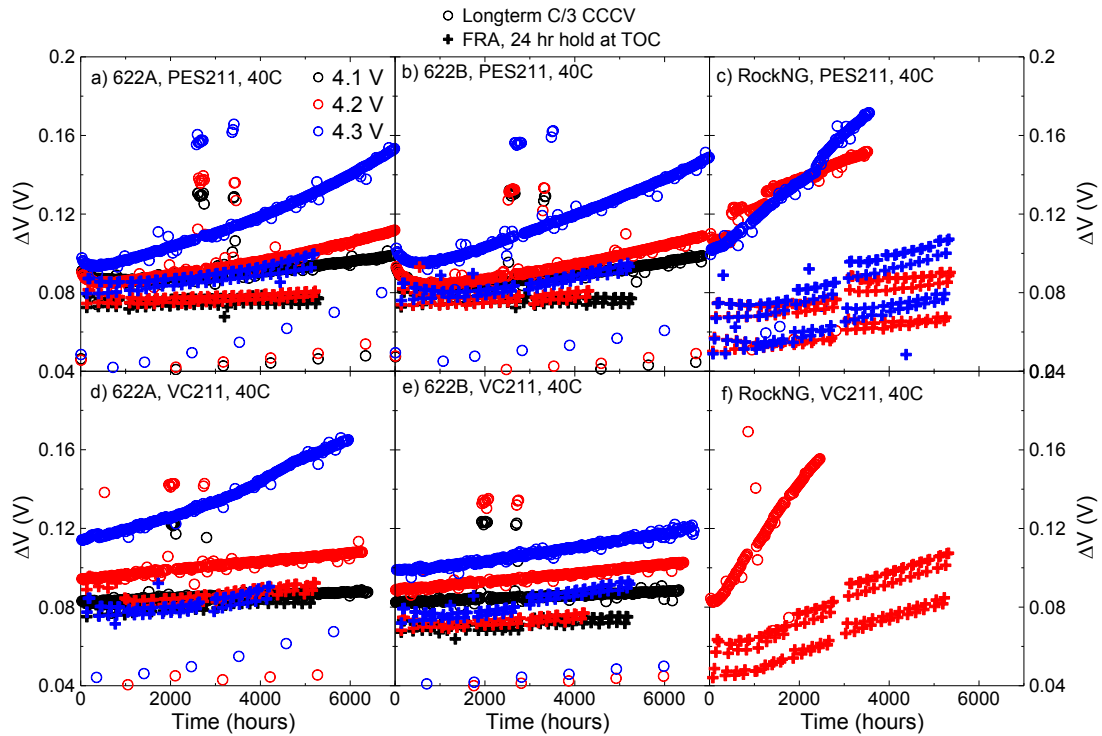


Figure 7.21 ΔV as a function of time for 622A (a,d), 622B (b,e), and Rock/NG (c,f) cells that did charge-hold-discharge cycling and charge-discharge cycling at 40°C containing PES211 (a-c) and VC211 (d-f).

7.2.3 SELECTED FITTING RESULTS

In this work, an equivalent circuit model was used to fit the measured impedance spectra from selected cells. All fitting of this data was done by Samuel Buteau (Dalhousie University, 2017). Adapted from Huang et al.,¹³⁶ Figure 7.22 shows the equivalent circuit model used to fit the measured impedance spectra (similar to Figure 6.1). R_{ohmic} represents the electronic and/or ionic path resistances and W represents the Warburg

diffusion component. There are two $R||CPE$ circuits, each dependent on the corresponding resistance, R , the critical frequency, ω_c , and the exponent, ϕ . The first $R||CPE$ is associated with the positive electrode SEI impedance. The second $R||CPE$ is possibly associated with the negative electrode and the contact impedances.

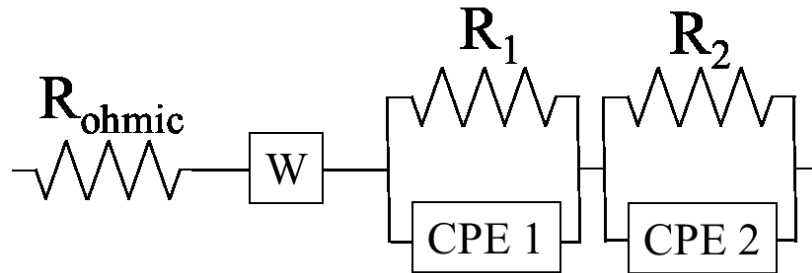


Figure 7.22 The equivalent circuit model used to fit measured spectra. W is a Warburg diffusion element and each CPE is a constant phase element. Adapted from Huang et al.¹³⁶

Figure 7.23 shows the fitting results as a function of impedance measurement number obtained from the equivalent circuit model (Figure 7.22) for Rock/AG cells containing 2% VC cycled to 4.3 V or 4.4 V. Figure 7.23a and Figure 7.23b show the results for parameters R_1 , R_2 , and R_{ohmic} for the cells cycled to 4.3 or 4.4 V, respectively. Figure 7.23c and Figure 7.23d show the results for parameters ω_{c1} and ω_{c2} for the cells cycled to 4.3 or 4.4 V, respectively. Figure 7.23e and Figure 7.23f show the results for parameters ϕ_1 , ϕ_2 , and ϕ_w for the cells cycled to 4.3 or 4.4 V, respectively. The impedance measurements were taken every 0.1 V between 3.4 V and the upper cutoff potential during every 6th cycle. The vertical oscillation of the parameters was due to the effect of measurement potential. The overall trend of the parameters with increasing measurement number was due to the effect of cycle number.

Figure 7.23a shows that R_1 for the Rock/AG cell cycled to 4.3 V was constant at low potentials but increased significantly at high potentials. Figure 7.23a shows that R_2 and R_{ohmic} for the Rock/AG cell cycled to 4.3 V increased with cycle number. Figure 7.23b shows that R_1 for the Rock/AG cell cycled to 4.4 V increased at low potentials and increased dramatically at high potentials. The growth of R_1 was six times larger for the cell cycled to 4.4 V than the cell cycled to 4.3 V. This indicates that the effect of upper cutoff potential significantly impacts R_1 . For the 4.4 V cell, R_2 also increased more than for the 4.3 V cell, but R_{ohmic} was similar. R_{ohmic} for both cells oscillated with the measurement potential, albeit much less than the oscillations of R_1 and R_2 .

Figure 7.23c shows that ω_{c1} initially decreased and then stabilized for the Rock/AG cell cycled to 4.3 V and that ω_{c2} was approximately constant with potential and cycle number. Figure 7.23d shows that ω_{c1} initially decreased and then stabilized for the Rock/AG cell cycled to 4.3 V and that ω_{c2} increased with cycle number. The parameter ω_{c1} decreased more for the cell cycled to 4.4 V compared to the cell cycled to 4.3 V. Figure 7.23e and Figure 7.23f show that the trends of ϕ_1 , ϕ_2 , and ϕ_w were similar for the cells cycled to 4.3 V and 4.4 V. The parameter, ϕ_1 , corresponding to the first R||CPE circuit was the largest, indicating that the corresponding feature was closest to an ideal RC circuit. The parameter ϕ_2 was near 0.5, indicating that the corresponding feature was depressed.

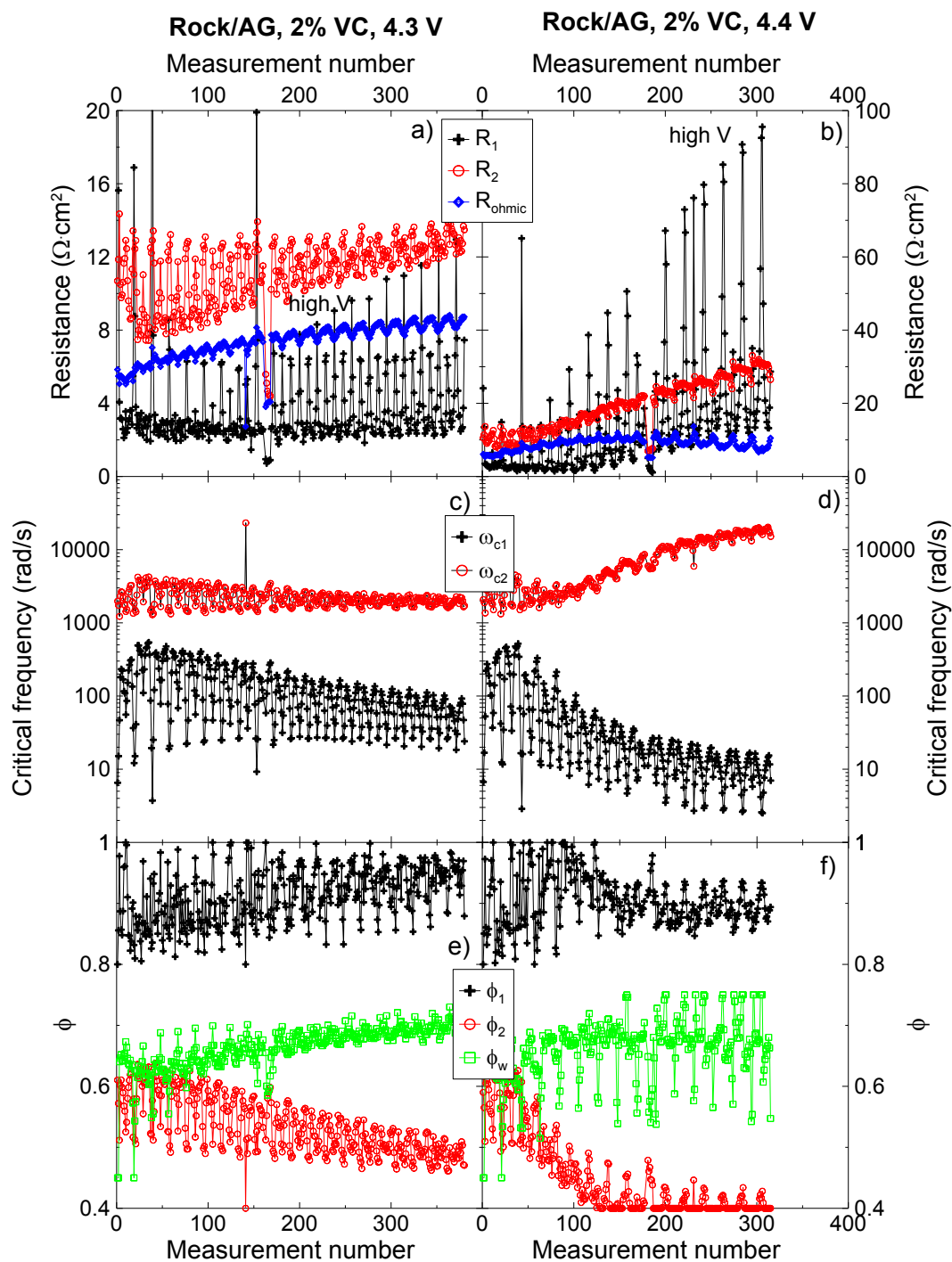


Figure 7.23 Parameters for the resistances (a,b), critical frequencies (c,d), and CPE exponents (e,f) obtained from fitting the impedance spectra using an equivalent circuit model for Rock/AG cells containing 2% VC cycled to 4.3 V (a,c,e) and 4.4 V (b,d,f). Please note the scale of the y-axis in panel a) and b) are different.

Figure 7.24 and Figure 7.25 show the fitting results as a function of impedance measurement number obtained from the equivalent circuit model (Figure 7.22) for 622A cells cycled to 4.2 V or 4.3 V containing PES211 or VC211, respectively. Figure 7.24a and Figure 7.24b show the results for parameters R_1 , R_2 , and R_{ohmic} for the cells cycled to 4.2 or 4.3 V, respectively. Figure 7.24c and Figure 7.24d show the results for parameters ω_{c1} and ω_{c2} for the cells cycled to 4.2 or 4.3 V, respectively. Figure 7.24e and Figure 7.24f show the results for parameters ϕ_1 , ϕ_2 , and ϕ_w for the cells cycled to 4.2 or 4.3 V, respectively. The impedance measurements were taken every 0.1 V between 3.4 V and the upper cutoff potential during every 6th cycle. The vertical oscillation of the parameters was due to the effect of measurement potential. The overall trend of the parameters with increasing measurement number was due to the effect of cycle number.

Figure 7.24 shows very little difference in all parameters, except R_{ohmic} , for the 622A cell cycled to 4.2 V compared to the cell cycled to 4.3 V. Figure 7.24a shows that R_1 for the 622A cell cycled to 4.2 V was approximately constant with potential and cycle number. Figure 7.24a shows that R_2 fluctuated with potential more than R_1 , and decreased slightly with cycle number, whereas R_{ohmic} increased slightly for the 622A cell cycled to 4.2 V. Figure 7.24b shows that R_1 for the 622A cell cycled to 4.3 V increased very slightly with cycle number, R_2 fluctuated with potential but remained constant with cycle number, and R_{ohmic} increased with cycle number.

Figure 7.24c shows that ω_{c1} and ω_{c2} were approximately constant with cycle number for the cells cycled to 4.2 and 4.3 V. Figure 7.24d shows that ω_{c2} fluctuated more with

potential for the cell cycled to 4.3V compared to the cell cycled to 4.2 V. Figure 7.24e and Figure 7.24f show that the trend of ϕ_1 , ϕ_2 , and ϕ_w were similar for the cells cycled to 4.2 V and 4.3 V. The parameter, ϕ_1 , corresponding to the first R||CPE circuit was the largest, indicating that the corresponding feature was closest to an ideal RC circuit.

Figure 7.25 shows the same trends and similar values for all fitting parameters as those shown in Figure 7.24. The similarities between the 622A cells containing PES211 and VC211 indicates that the effect of electrolyte additives used do not significantly impact the impedance growth of cells cycled to 4.3 V and below.

The similarities between the 622A cells cycled to 4.2 V or 4.3 V indicates that the effect of upper cutoff potential only slightly impacts the impedance growth of cells cycled to 4.3 V and below. The differences in the rate of increase of R_{ohmic} were the most significant for all 622A cells.

In order to ensure more accurate tracking of the fitting parameters, and therefore trends in the impedance of each cell with time, cycle number, and voltage, each fitting parameter has a fixed range of allowed values. The fixed range for the fitting parameters was used for all cells presented in this chapter, although only noticeable in the fitting of spectra that are primarily single-featured. For example, the fitting parameters shown in Figure 7.24 and Figure 7.25 have been restricted to a fixed range. The fixed range is most noticeable in Figure 7.24c, Figure 7.24e, Figure 7.24f, Figure 7.25c, Figure 7.25 e, and Figure 7.25f. The fitting parameters shown in Figure 7.24 and Figure 7.25 correspond to the spectra shown in Figure 7.13. These spectra have two features that occur at similar critical

frequencies, which make distinguishing the features more difficult. The fixed range in the fitting parameters is necessary to separate the two features, and ensure that the fit to the appropriate feature is monitored as a function of time, cycle number, and voltage.

Alternatively, the effect of the fixed range on the fitting parameters shown in Figure 7.23 is not apparent. The fitting parameters shown in Figure 7.23 correspond to the spectra shown in Figure 7.2c and Figure 7.2d, which have two easily distinguishable features that occur at clearly different critical frequencies. Therefore, the fixed range in the fitting parameters is not necessary to separate the two features,

While not the ideal solution, the method of fixing the fitting parameters was necessary in this work to keep features of the spectra separate to monitor how each feature changed with time, cycle number, and voltage. More work is required to improve the fitting process.

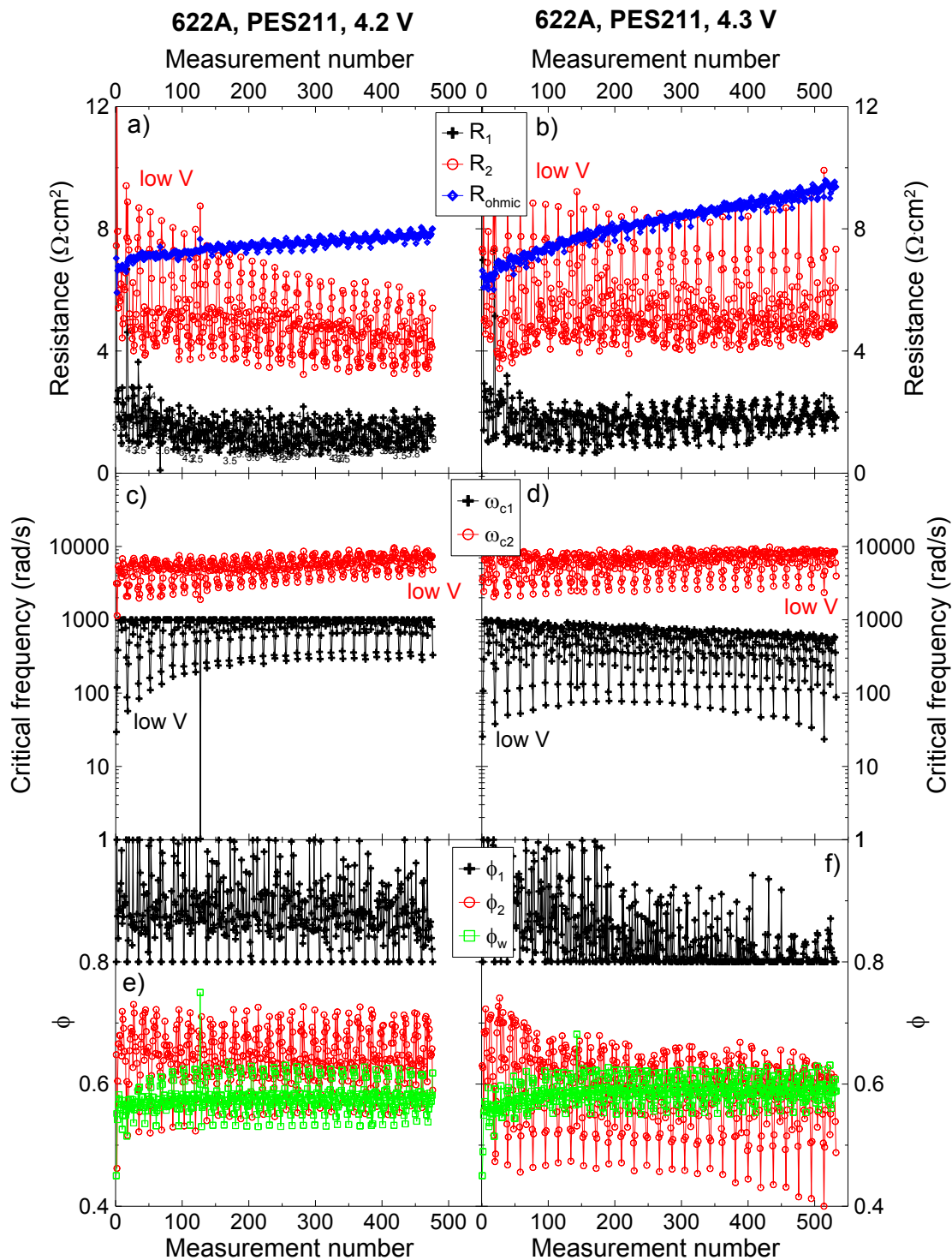


Figure 7.24 Parameters for the resistances (a,b), critical frequencies (c,d), and CPE exponents (e,f) obtained from fitting the impedance spectra using an equivalent circuit model for 622A cells containing PES211 cycled to 4.2 V (a,c,e) and 4.3 V (b,d,f).

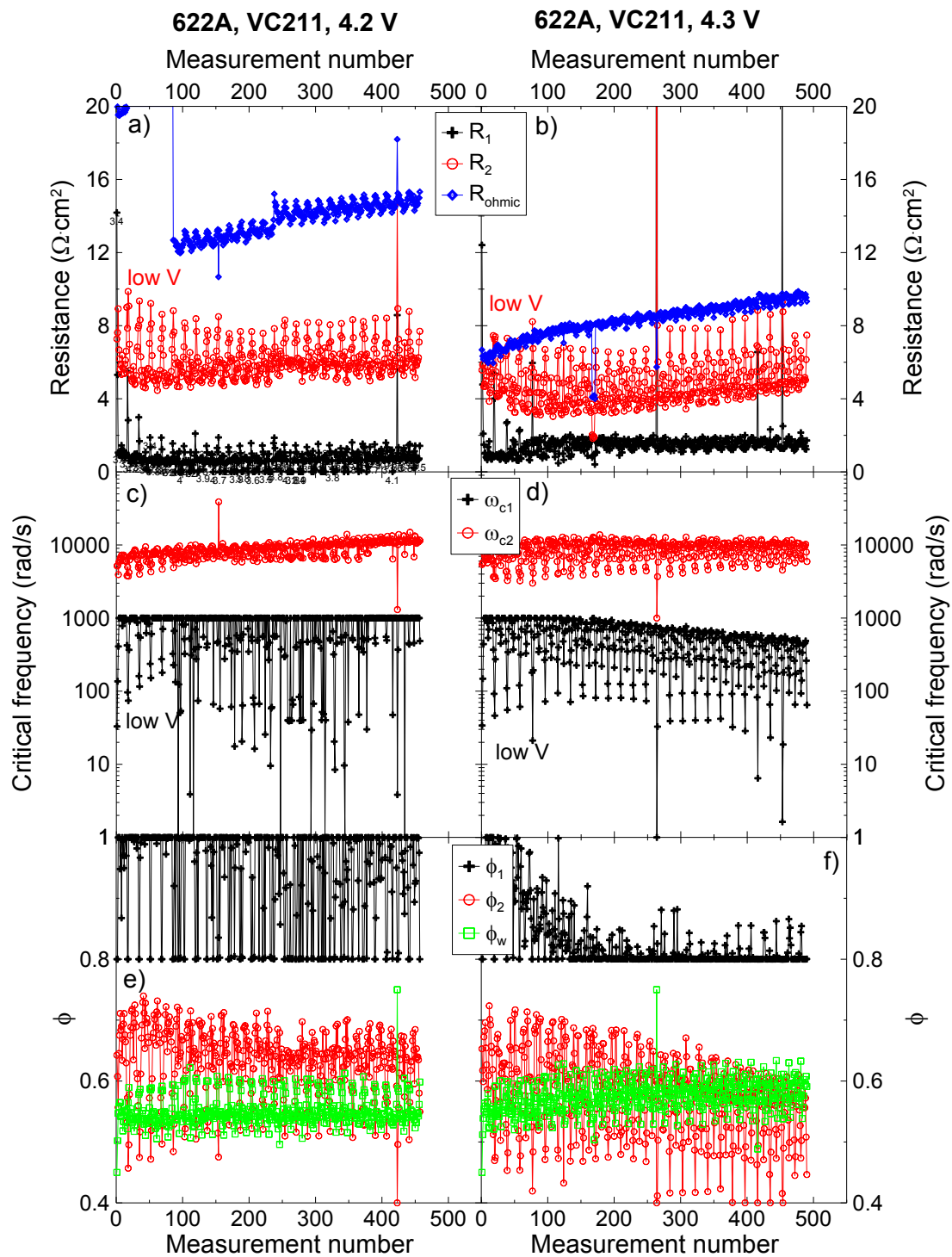


Figure 7.25 Parameters for the resistances (a,b), critical frequencies (c,d), and CPE exponents (e,f) obtained from fitting the impedance spectra using an equivalent circuit model for 622A cells containing VC211 cycled to 4.2 V (a,c,e) and 4.3 V (b,d,f).

Figure 7.26 and Figure 7.27 show the fitting results as a function of impedance measurement number obtained from the equivalent circuit model (Figure 7.22) for 622B cells cycled to 4.2 V or 4.3 V containing PES211 or VC211, respectively. Figure 7.26a and Figure 7.26b show the results for parameters R_1 , R_2 , and R_{ohmic} for the cells cycled to 4.2 or 4.3 V, respectively. Figure 7.26c and Figure 7.26d show the results for parameters ω_{c1} and ω_{c2} for the cells cycled to 4.2 or 4.3 V, respectively. Figure 7.26e and Figure 7.26f show the results for parameters ϕ_1 , ϕ_2 , and ϕ_w for the cells cycled to 4.2 or 4.3 V, respectively. The impedance measurements were taken every 0.1 V between 3.4 V and the upper cutoff potential during every 6th cycle. The vertical oscillation of the parameters was due to the effect of measurement potential. The overall trends of the parameters with increasing measurement number were due to the effect of cycle number.

Figure 7.26 shows very little difference in all parameters, except R_2 for the 622B cell cycled to 4.2 V compared to the cell cycled to 4.3 V. The increase in R_2 for the 622B cell cycled to 4.3 V may be due to particle cracking that can occur on natural graphite. Figure 7.26a and Figure 7.26b show that R_1 for the 622B cells cycled to 4.2 and 4.3 V was approximately constant with potential and cycle number. Figure 7.26a shows that R_2 fluctuated with potential more than R_1 , and decreased with cycle number, whereas R_{ohmic} increased for the 622B cell cycled to 4.2 V. Figure 7.26b shows that R_2 fluctuated with potential and increased with cycle number compared to the 622B cell cycled to 4.2 V. R_{ohmic} increased with cycle number. R_{ohmic} for both cells oscillated with the measurement potential, albeit much less than the oscillations of R_1 and R_2 .

Figure 7.26c and Figure 7.26d show that ω_{c1} was approximately constant with cycle number and ω_{c2} increased with cycle number for the cells cycled to 4.2 and 4.3 V. Figure 7.26e and Figure 7.26f show that the trends of ϕ_1 and ϕ_w were similar for the cells cycled to 4.2 V and 4.3 V, but ϕ_2 decreased for the 622B cell cycled to 4.3 V and remained constant for the cell cycled to 4.2 V. The parameter, ϕ_1 , corresponding to the first R||CPE circuit was the largest, indicating that the corresponding feature was closest to an ideal RC circuit.

Figure 7.27 shows the same trends and similar values for all fitting parameters as those shown in Figure 7.26. The similarities between the 622B cells containing PES211 and VC211 indicates that the effect of electrolyte additives used do not significantly impact the impedance growth of cells cycled to 4.3 V and below.

The similarities between the 622B cells cycled to 4.2 V or 4.3 V indicates that the upper cutoff potential only impacted the growth of R_2 and R_{ohmic} for the cells cycled to 4.3 V and below. The difference in the rate of increase of R_{ohmic} and R_2 were the most significant for all 622B cells.

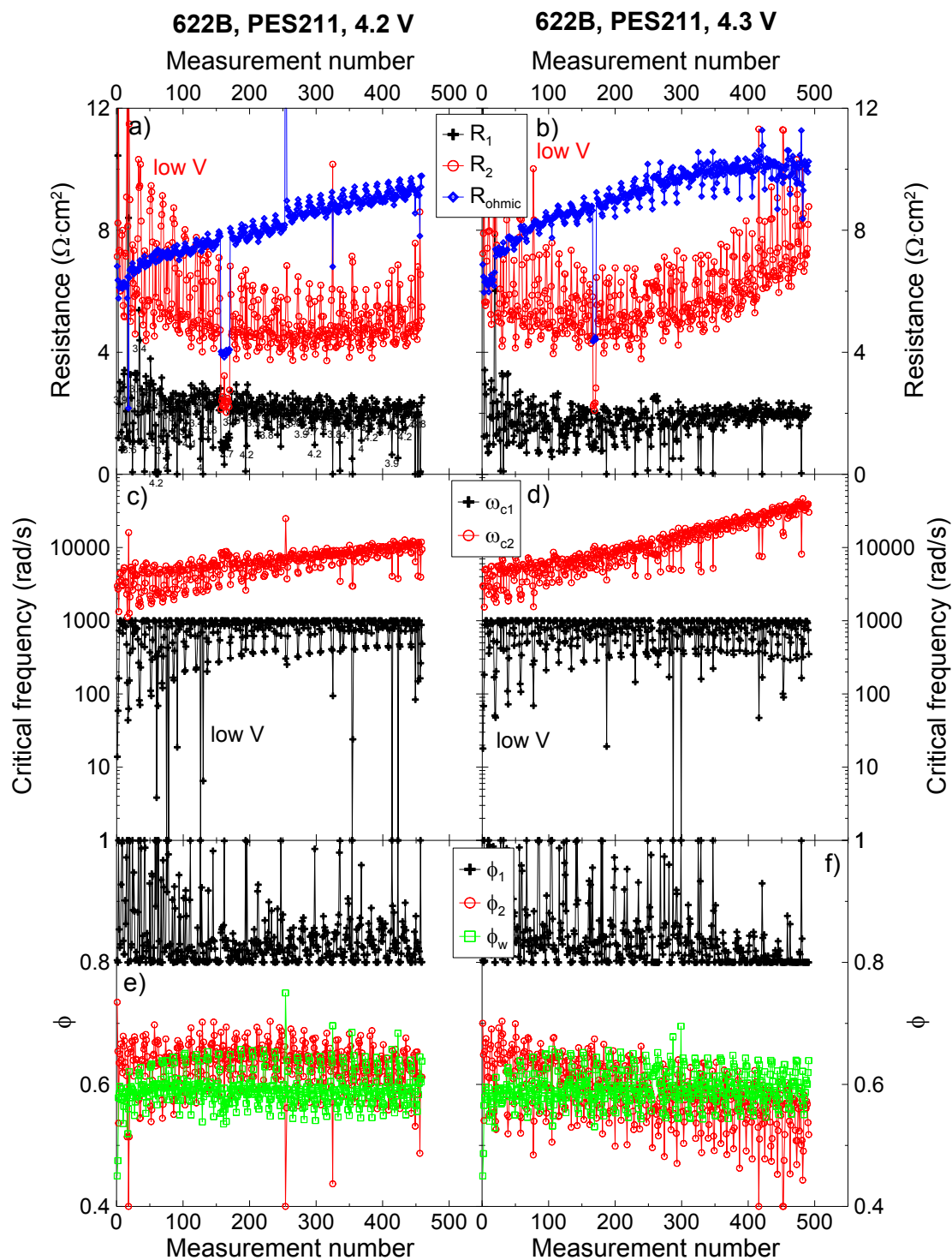


Figure 7.26 Parameters for the resistances (a,b), critical frequencies (c,d), and CPE exponents (e,f) obtained from fitting the impedance spectra using an equivalent circuit model for 622B cells containing PES211 cycled to 4.2 V (a,c,e) and 4.3 V (b,d,f).

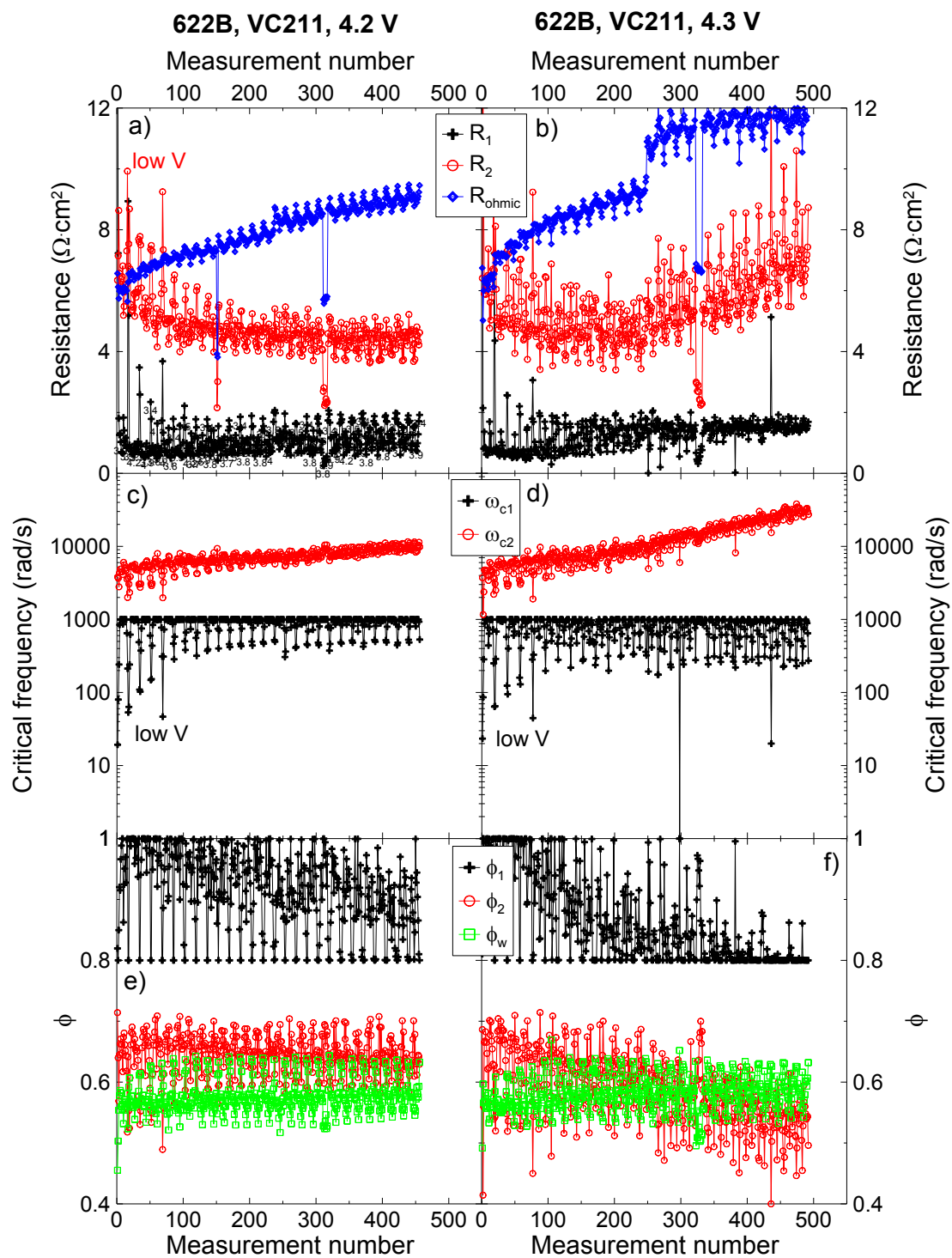


Figure 7.27 Parameters for the resistances (a,b), critical frequencies (c,d), and CPE exponents (e,f) obtained from fitting the impedance spectra using an equivalent circuit model for 622B cells containing VC211 cycled to 4.2 V (a,c,e) and 4.3 V (b,d,f).

Figure 7.28 shows the fitting results as a function of impedance measurement number obtained from the equivalent circuit model (Figure 7.22) for Rock/NG cells containing PES211 cycled to 4.3 V or 4.4 V. Figure 7.28a and Figure 7.28b show the results for parameters R_1 , R_2 , and R_{ohmic} for the cells cycled to 4.3 or 4.4 V, respectively. Figure 7.28c and Figure 7.28d show the results for parameters ω_{c1} and ω_{c2} for the cells cycled to 4.3 or 4.4 V, respectively. Figure 7.28e and Figure 7.28f show the results for parameters ϕ_1 , ϕ_2 , and ϕ_w for the cells cycled to 4.3 or 4.4 V, respectively. The impedance measurements were taken every 0.1 V between 3.4 V and the upper cutoff potential during every 6th cycle. The vertical oscillation of the parameters was due to the effect of measurement potential. The overall trend of the parameters with increasing measurement number was due to the effect of cycle number.

Figure 7.28 shows very little difference in all parameters, except R_1 , R_2 , and R_{ohmic} for the Rock/NG cell cycled to 4.3 V compared to the cell cycled to 4.4 V. Figure 7.28a shows that R_1 for the Rock/NG cell cycled to 4.3 V was approximately constant with potential and cycle number. Figure 7.28a shows that R_2 fluctuated with potential more than R_1 , and increased with cycle number. Figure 7.28a shows that R_{ohmic} increased for the Rock/NG cell cycled to 4.3 V. Figure 7.28b shows that R_1 for the Rock/NG cell cycled to 4.4 V increased with cycle number at high potentials and stayed approximately constant with cycle number at low potentials. Figure 7.28b shows that R_2 for the Rock/NG cell cycled to 4.4 V increased with cycle number much more compared to the Rock/NG cell cycled to 4.3 V. This may be due to an increase in the negative electrode impedance resulting from natural graphite particle cracking. The dramatic increase in R_2 compared to R_1 at 3.8

V was shown in Figure 7.14. R_{ohmic} increased and then stayed approximately constant with cycle number for the Rock/NG cell cycled to 4.4 V.

Figure 7.28c and Figure 7.28d show that ω_{c1} was approximately constant with cycle number and ω_{c2} increased with cycle number for the cells cycled to 4.3 and 4.4 V. Figure 7.28e and Figure 7.28f show that the trend of ϕ_1 and ϕ_w were similar for the cells cycled to 4.3 V and 4.4 V, but ϕ_2 decreased more for the Rock/NG cell cycled to 4.4 V. The parameter, ϕ_1 , corresponding to the first R||CPE circuit was the largest, indicating that the corresponding feature was closest to an ideal RC circuit.

The differences between the Rock/NG cells cycled to 4.3 V or 4.4 V indicates that the upper cutoff potential significantly impacted the impedance growth of the cells cycled to 4.3 and 4.4 V. The difference in the rate of increase of R_1 and R_2 were the most significant for the Rock/NG cells.

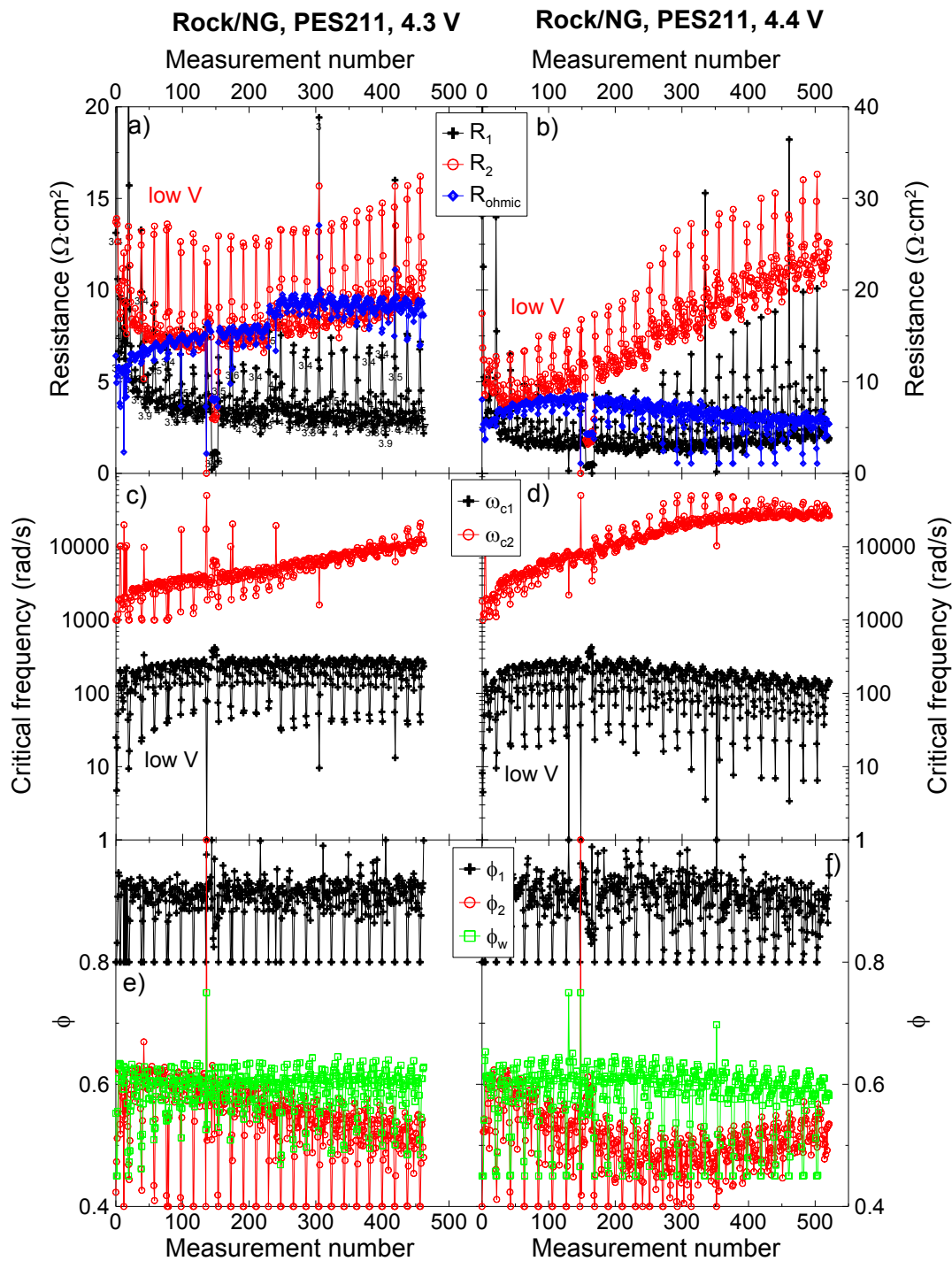


Figure 7.28 Parameters for the resistances (a,b), critical frequencies (c,d), and CPE exponents (e,f) obtained from fitting the impedance spectra using an equivalent circuit model for Rock/NG cells containing PES211 cycled to 4.3 V (a,c,e) and 4.4 V (b,d,f). Please note the scale of the y-axis in panel a) and b) are different.

Figure 7.29 shows a comparison of R_{ct} and R_1 for Rock/AG cells containing 2% VC cycled to 4.2 V or 4.4 V. Some representative spectra were shown in Figure 7.2. Figure 7.29a and Figure 7.29c show R_{ct} obtained from the widths of the impedance spectra along the real axis for the Rock/AG cells cycled to 4.2 or 4.4 V, respectively. The cell cycled to 4.4 V had significant impedance growth at all potentials and accelerated growth at high potentials. Figure 7.29b and Figure 7.29d show R_1 obtained from fitting the impedance spectra of the Rock/AG cells cycled to 4.2 or 4.4 V, respectively, with the equivalent circuit model shown in Figure 7.22. The cell cycled to 4.4 V shows significant impedance growth at all potentials and accelerated growth at high potentials, however smaller than the growth in R_{ct} . The cell cycled to 4.2 V showed no change in R_1 with potential, similar to the trend of R_{ct} with cycle number. However, the value of R_1 was significantly smaller than the value of R_{ct} for the cell cycled to 4.2 V. This is because R_{ct} contains R_1 and R_2 , which are not distinguished from each other. This means that while the trends obtained from R_{ct} match those of R_1 and were therefore useful, fitting the impedance spectra is necessary to obtain quantitative information about the changes to the positive electrode SEI.

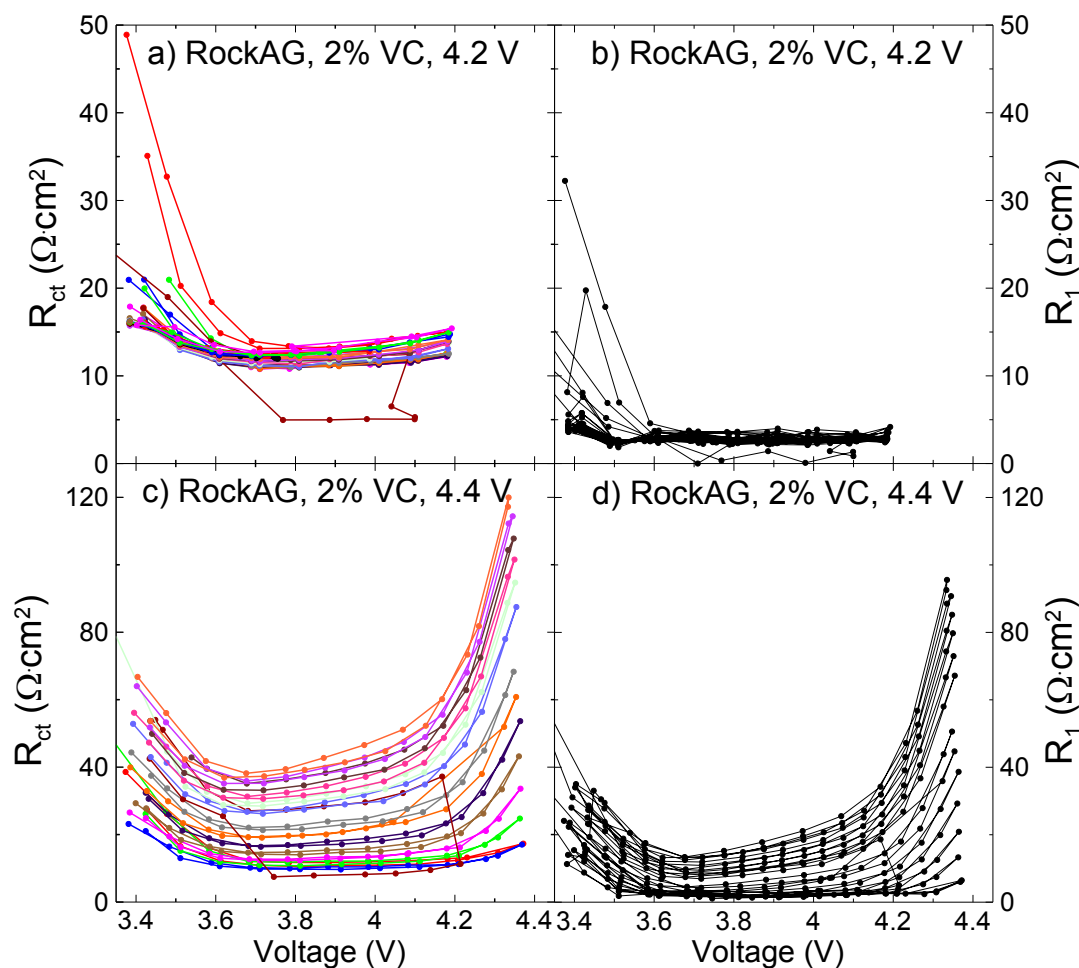


Figure 7.29 The combination of charge transfer resistance (both positive and negative electrodes) and resistance due to motion of ions through the SEI layers (both positive and negative electrodes), R_{ct} , as a function of voltage measured every 6 cycles for the Rock/AG cells containing 2% VC cycled to a) 4.2 V and c) 4.4 V. The parameter, R_1 , obtained from fitting using an equivalent circuit model for the Rock/AG cells containing 2% VC cycled to b) 4.2 V and d) 4.4 V.

Figure 7.30 shows a comparison of the HFI and R_{ohmic} for Rock/AG cells containing 2% VC cycled to 4.2 V or 4.3 V. Figure 7.30a shows the HFI obtained from where the high frequency data of the impedance spectra crosses the real axis for the cells cycled to 4.2 or 4.3 V. Figure 7.30b shows R_{ohmic} obtained from fitting the impedance spectra of the Rock/AG cells cycled to 4.2 or 4.3 V, with the equivalent circuit model shown in Figure

7.22. Both R_{ohmic} and the HFI increase with cycle number, which was accelerated with a higher upper cutoff potential. The values of the HFI were larger than the values of R_{ohmic} , but the trend of the data was the same. This is because the HFI includes the inductive contribution from the equipment and from the wound pouch cell in addition to the electronic and ionic path resistances, whereas the value of R_{ohmic} only includes the electronic and ionic path resistances. The presence of the inductive contribution, which remains approximately constant with cycle number, increases the value of resistance obtained from the high frequency intercept. Therefore the trend of the HFI and R_{ohmic} were the same with cycle number. This means that the quick and simple method of determining the HFI was useful for learning about the electronic and ionic path resistances.

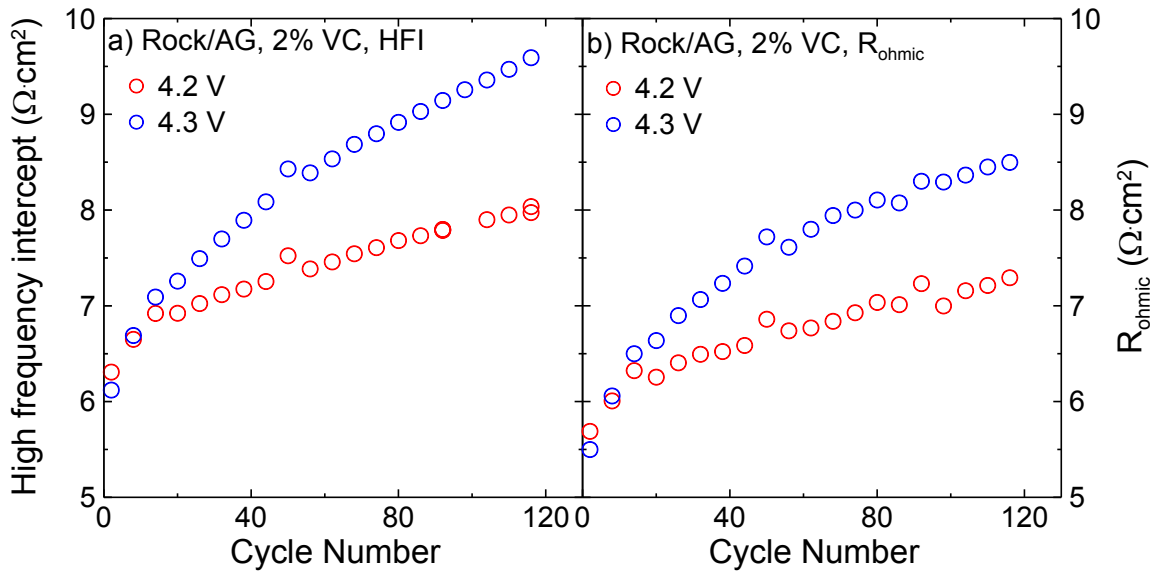


Figure 7.30 a) The values of the high frequency intercept, as a function of cycle number, extracted from the impedance spectra of Rock/AG cells containing 2% VC cycled to 4.2 or 4.3 V. b) The parameter, R_{ohmic} , obtained from fitting using an equivalent circuit model for the Rock/AG cells containing 2% VC cycled to 4.2 or 4.3 V.

7.3 CONCLUSION

The work presented here demonstrated the importance of using a 4-wire system to monitor impedance growth as a function of time, cycle number, and potential and then using an equivalent circuit model to fit the impedance spectra. Oscillations, with measurement potential, in the fitting parameters of R_1 , R_2 , and R_{ohmic} were observed in addition to oscillations in the experimentally determined high frequency intercept. These oscillations with potential are useful in understanding the changes to impedance resulting from changes within the cells. In general for all cells studied here, the capacity fade, impedance growth, and ΔV increased when the upper cutoff potential was increased. For many cells, the change in ΔV was significantly larger than the expected change in ΔV calculated from the corresponding cell impedance growth. This means that there was another process contributing to ΔV growth that was not captured in the measured impedance spectra.

Characterizing the reversible and irreversible nature of impedance growth with various cells chemistries, electrolytes, and upper cutoff potentials is necessary to learn about the processes occurring, and will be explored in Chapter 8.

CHAPTER 8. REVERSIBLE AND IRREVERSIBLE IMPEDANCE GROWTH

The work presented in Chapters 4, 5, 6, and 7 show that impedance growth is one obstacle to high potential NMC Li-ion cells, and that it is a large contributor to Li-ion cell failure at high potential. The overall goal of this work is to enable the successful function of NMC Li-ion cells operated to high potential, in order to achieve higher energy density and lower cost. Chapter 4 showed that impedance growth can be characterized and symmetric cells can be used to narrow the source of impedance growth. Chapters 6 and 7 showed that impedance spectra can be fit using equivalent circuit models to characterize the source of impedance growth and monitor how it changes with time and cycle number. However, there is still a lack of understanding of how and why impedance growth changes with potential. This lack of understanding leads to a lack of sufficient solutions to improve NMC Li-ion cells operated to high potentials. Furthermore, the difference between reversible and irreversible impedance growth needs to be characterized and understood.

In order to characterize impedance growth and learn about the processes that cause impedance growth in NMC Li-ion cells, the impedance at various potentials needs to be measured and understood. As shown in Chapters 4, 5, 6, and 7, impedance can vary greatly with electrode coatings, cell components, separator material, electrolyte additives, upper cutoff potentials, experimental protocol, and testing temperature, all resulting from various processes occurring in Li-ion cells.

8.1 CHARACTERIZATION

To illustrate the changes to impedance that can occur with potential under a variety of cell conditions, consider Figure 8.1. Figure 8.1a shows R_{ct} as a function of potential for an uncoated NMC442/graphite pouch cell filled with 1M LiPF_6 EC:EMC:PES:MMDS:TTSPi 29:67:2:1:1 during the charge and discharge segment of cycles 2, 30, and 50 while undergoing charge-hold-discharge cycling (as shown in Figure 3.2) to 4.4 V. R_{ct} was taken as the width of the impedance spectrum along the real axis, as indicated in Figure 3.11. At cycle 2, the cell had very low impedance that did not change with potential. At cycle 30, the cell impedance increased with increasing potential. At cycle 50, the cell impedance increased dramatically with potential. Most interestingly, the impedance was reversible over one cycle (increased when exposed to high potential during charge, and decreased when exposed to low potential during discharge), but was irreversible over several cycles. This suggests dynamic changes to the SEI layers occurred during exposure to high potential. This also suggests that a temporary process occurred during exposure to high potential that was easily reversed during exposure to low potential.

Figure 8.1b shows R_{ct} as a function of potential for a LaPO_4 coated NMC442/graphite pouch cell filled with 1M LiPF_6 EC:EMC:PES:DTD:TTSPi 28:66:2:2:2 during the charge and discharge segment of cycles 2, 50, and 74 while undergoing charge-hold-discharge cycling (as shown in Figure 3.2) to 4.45 V. At cycle 2, the cell had very low impedance that did not change with potential. At cycle 50, the cell had significantly

larger impedance than at cycle 2, and increased in impedance from 3.8 to 4.4 V during charge and decreased during discharge. At cycle 74, the cell had even larger impedance and again increased in impedance from 3.8 to 4.4 V during charge and decreased during discharge. At cycles 50 and 74, however, the impedance measured during the discharge of the cell was higher than that during the charge of the cell. This suggests a time-dependent response of the SEI layers with potential for EC:EMC-containing coated NMC cells leading to a measured R_{ct} that lagged with time. This also suggests that, although a temporary process may have occurred during exposure to high potential, it was not easily reversed during exposure to low potential.

Figure 8.1c shows R_{ct} as a function of potential for an uncoated NMC442/graphite pouch cell filled with 1M LiPF₆ FEC:TFEC:PES 49:49:2 during the charge and discharge segment of cycle 2, 22, and 34 while undergoing charge-hold-discharge cycling (as shown in Figure 3.2) to 4.5 V. The impedance at all potentials and all cycles was very stable, and did not exhibit the phenomena shown in Figure 8.1a and Figure 8.1b. Figure 8.1 demonstrates the impact that positive electrode coatings, electrolyte solvents, electrolyte additives and upper cutoff potential have on R_{ct} and the impedance growth of NMC Li-ion cells. The impacts of each of these factors needs to be studied quantitatively through the fitting of EIS spectra using equivalent circuit models, as the measurement of R_{ct} alone does not give an indication of the processes occurring in NMC Li-ion cells.

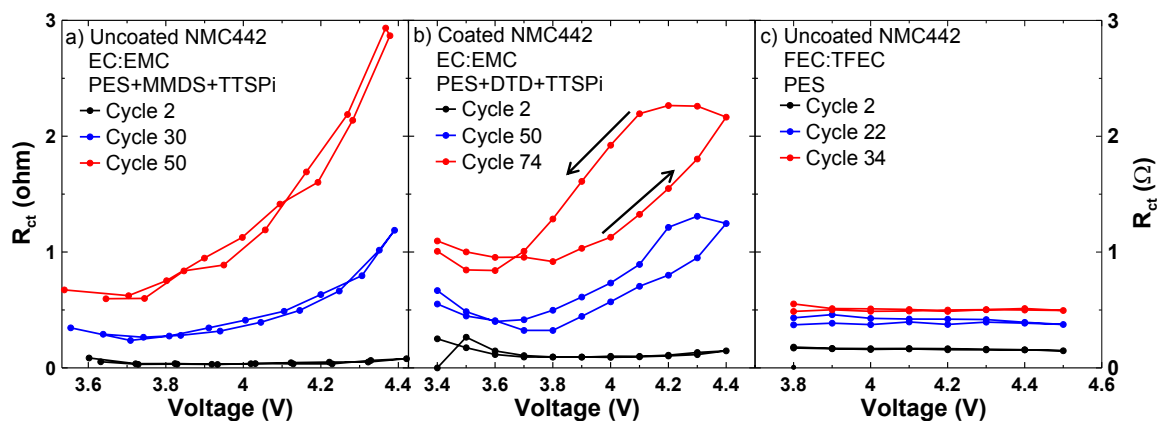


Figure 8.1 R_{ct} plotted as a function of voltage for selected cycles for a) an uncoated NMC442 cell with EC:EMC based electrolyte to 4.4 V, b) a coated NMC442 cell with EC:EMC based electrolyte to 4.45 V, and c) an uncoated NMC442 cell with FEC:TFEC based electrolyte to 4.5 V. All cells underwent charge-hold-discharge cycling. The arrows in panel b) indicate the data measured during charge and discharge.

Xiong et al. studied the effect of two different electrolytes (1M LiPF_6 EC:EMC:PES:DTD:TTSPi 28:66:2:2:2 [PES222] and 1M LiPF_6 FEC:TFEC:PES 49:49:2 [FEC:TFEC]) on the impedance of NMC442 positive electrodes.¹⁶⁴ They observed a significant difference in the impedance of the NMC positive electrode when in the presence of PES222 or FEC:TFEC electrolyte using the “pouch bag method”, meaning they isolated the positive electrode and sealed it inside pouch cell material.¹⁶⁴ They observed large impedance growth after 500 hours of storage at 4.4 V for the isolated positive electrode in the presence of PES222, suggesting that PES222 did not suppress oxidized species from reacting with the charged positive electrode materials. They found that the impedance of the isolated positive electrode for PES222 was an order of magnitude larger than for FEC:TFEC. They suggested this was either because the oxidized species resulting from FEC:TFEC did not react with the charged positive

electrode, or that the SEI layer formed on the positive electrode in the presence of FEC:TFEC prevented oxidized species from reacting with the positive electrode. The work by Xiong et al.¹⁶⁴ may explain the small impedance and small impedance growth shown in Figure 8.1c.

Reversible changes in the high frequency intercept (HFI) over one cycle and irreversible changes over several cycles were also observed in the work presented in this thesis. Figure 4.2, Figure 4.3, and Figure 7.7 most clearly showed that the HFI decreased with increasing measurement potential. The oscillation of the HFI with measurement potential was shown in Figure 7.2, Figure 7.23, Figure 7.24, Figure 7.25, Figure 7.26, Figure 7.27, and Figure 7.28. In all cases, the HFI decreased during charge and reversibly increased during the subsequent discharge, but increased irreversibly over several cycles. It is possible that as potential increased, more species were oxidized on the positive electrode leading to an increase in R_{ct} and a decrease in the HFI. Madec et al. showed that the amount of LiF in both the positive and negative SEI layers increased during charge and decreased during discharge.⁹⁹ Abarbanel et al. showed that the high frequency intercept is affected by the electronic path resistances through carbon black, the ionic path resistances through the electrolyte solution into the electrode pores, and the contact resistance between carbon black and the active material.¹¹⁹ It is possible that the changing content of LiF, among other species, in the positive and negative SEI layers affects the contact resistance between the carbon black and the active material such that R_{ct} can increase while the HFI decreases.

Table 8.1 characterizes the impedance growth of several cells undergoing continuous charge-discharge cycling and charge-hold-discharge cycling. The cell chemistry, electrolyte solvents, electrolyte additives, and upper cutoff potentials are indicated. Table 8.1 indicates if reversible and irreversible impedance growth was exhibited by each cell. Reversible impedance growth means that the value of R_{ct} measured during charge was the same when measured during discharge. Table 8.1 indicates if a hysteresis between the impedance growth during charge and discharge was observed, as shown in Figure 8.1b. Table 8.1 indicates if impedance increased at low voltage (3.6 V and below) or at high voltage (4.2 V and above). If the impedance was not measured at or below 3.6 V or above 4.2 V, the table entry remains blank for that cell. If the impedance measured at all potentials was the same, then Table 8.1 indicates that the impedance was independent of potential. All data in Table 8.1 was measured at 40°C.

Table 8.1 Characterization of impedance growth in Li-ion cells.

Cell Chemistry	Protocol	Electrolyte	Upper Cutoff Potential (V)	Reversible impedance	Irreversible Impedance	Hysteresis	Growth at high V	Growth at low V	Impedance Independent of V
NMC442/AG	24 hr hold	EC:EMC PES:DTD:TTSPi	4.4, 4.425, 4.45	Y	N	N	N	N	Y
			4.475	Y	Y	N	N	N	Y
			4.5	Y	Y	Y	Y	N	N
		EC:EMC PES:MMDS:TTSPi	4.4	Y	Y	N	Y	N	N
		FEC:TFEC PES	4.5	Y	Y	N	N	-	Y
	continuous	EC:EMC VC	4.4	Y	Y	N	Y	N	N
		EC:EMC PES	4.5	Y	Y	N	Y	N	N
		EC:EMC PES:MMDS:TTSPi	4.5	Y	N	N	Y	N	N
		EC:EMC triallyl phosphate	4.5	Y	Y	N	Y	N	N
LaPO ₄ coated NMC442/AG	24 hr hold	EC:EMC PES:DTD:TTSPi	4.4	Y	Y	N	Y	N	N
			4.425, 4.45, 4.475, 4.5	Y	Y	Y	Y	Y	N

Cell Chemistry	Protocol	Electrolyte	Upper Cutoff Potential (V)	Reversible impedance	Irreversible Impedance	Hysteresis	Growth at high V	Growth at low V	Impedance Independent of V
Al ₂ O ₃ coated NMC532/NG	24 hr hold	EC:EMC PES:DTD:TTSPi	4.2, 4.3	Y	Y	N	N	Y	N
		EC:EMC VC:DTD:TTSPi	4.1, 4.2, 4.3	Y	Y	N	N	Y	N
High V coated NMC532/NG	24 hr hold	EC:EMC PES:DTD:TTSPi	4.1, 4.2	Y	N	N	N	Y	N
		EC:EMC VC:DTD:TTSPi	4.1, 4.2, 4.3	Y	N	N	N	Y	N
Al ₂ O ₃ coated NMC622/NG	24 hr hold	EC:EMC PES:DTD:TTSPi	4.1, 4.2	Y	Y	N	N	Y	N
			4.3	Y	Y	N	Y	Y	N
		EC:EMC VC:DTD:TTSPi	4.1, 4.2	Y	N	N	N	Y	N
			4.3	Y	Y	N	Y	Y	N
High V coated NMC622/NG	24 hr hold	EC:EMC PES:DTD:TTSPi	4.1, 4.2, 4.3	Y	N	N	N	Y	N
		EC:EMC VC:DTD:TTSPi	4.1, 4.2, 4.3	Y	N	N	N	Y	N

Cell Chemistry	Protocol	Electrolyte	Upper Cutoff Potential (V)	Reversible impedance	Irreversible Impedance	Hysteresis	Growth at high V	Growth at low V	Impedance Independent of V
Single crystal NMC532/NG	24 hr hold	EC:EMC PES:DTD:TTSPi	4.1, 4.2, 4.3	Y	N	N	N	Y	N
			4.4	Y	Y	N	Y	Y	N
		EC:EMC VC:DTD:TTSPi	4.1, 4.2	Y	N	N	N	Y	N
Single crystal NMC532/AG	24 hr hold	EC:EMC FEC	4.1, 4.2	Y	N	N	N	Y	N
			4.3, 4.3	Y	Y	N	Y	Y	N
		EC:EMC VC	4.1	Y	N	N	N	Y	N
			4.2, 4.3, 4.4	Y	Y	N	Y	Y	N
		EC:EMC:DMC FEC	4.3	Y	Y	N	Y	Y	N

8.2 LITERATURE REVIEW

There is a significant lack of research characterizing how the positive SEI layer changes with time, cycle number, and potential. Characterizing the dynamic behaviour of the positive SEI is of utmost importance to understand the failure of Li-ion cells when operated to high potentials. Typically, researchers investigate the SEI layers at several potentials, but only during a single cycle, or at a single potential during several cycles. While this work is valuable, it often does not illustrate the extent of the complex processes occurring in Li-ion cells. Some of this work, mostly utilizing EIS and X-ray photoelectron spectroscopy (XPS), will be discussed.

Feng et al.¹⁶⁵ measured the impedance of LiFePO₄/graphite cells at ten different potentials between 2.5 and 4.5 V, but only during a single discharge. They found that the electronic and ionic resistances did not change with potential, but the resistance of the positive and negative SEI layers and the charge-transfer impedance of the positive electrode increased at low potential. This increase was thought to be from thickening of the SEI layers. It would be ideal to have impedance measurements during several cycles.

Zhang et al.¹⁶⁶ investigated the impedance of Li-ion cells containing a lithium nickel-based mixed oxide positive electrode and a graphite negative electrode in 1M LiPF₆ EC:EMC 3:7 electrolyte. They used an equivalent circuit model that included the resistance of lithium ion transporting across the SEI layers on the surface of both the positive and negative electrodes, R_{SEI} , and the charge-transfer resistance, R_{ct} . They

claimed that the high frequency feature of the impedance spectrum was due to R_{SEI} , and the feature at medium-low frequency was due to R_{ct} . However, they did not state how they attributed each feature to the corresponding process. Furthermore, the spectra shown did not have clearly distinguishable features. It is not clear if R_{SEI} and R_{ct} can be reliably separated. They determined that the electronic and ionic path resistances and R_{SEI} remained constant with potential, over one cycle, but found that R_{ct} increased at both high and low potentials. They found that the minima in R_{ct} corresponded to the peaks in differential capacity analysis, dQ/dV vs V . It would be ideal to have measurements during several cycles. The work by Zhang et al.¹⁶⁶ may be helpful in explaining reversible impedance growth.

Aurbach et al.⁷⁹ studied the impedance of $LiNiO_2/Li$ and $LiMn_2O_4/Li$ half cells containing various electrolyte salts and solvents. They used an equivalent circuit model that included resistors representing the surface film, R_{film} , present at high frequencies and the interfacial and Li-ion transport resistance, R_{ct} , present at medium-low frequencies. For cells containing $LiAsF_6$, they found that for both positive electrodes studied, R_{film} did not vary with potential, but R_{ct} strongly depended on potential. They found that R_{ct} increased below 3.8 V and above 4.0 V, which agrees with the trends summarized in Table 8.1. It would be ideal to have measurements during several cycles. The work by Aurbach et al.⁷⁹ may be helpful in explaining reversible impedance growth.

Mukoyama et al.¹²⁸ studied the impedance of $LiCoO_2/graphite$ pouch cells during cycling between 2.75 and 4.1 V at 1C and room temperature. They measured impedance at the

top of charge only, at regular intervals during 550 cycles. They used an equivalent circuit model to fit the measured impedance spectra. They found that the total cell resistance increased with cycle number. They found that the electronic and ionic path resistances increased with cycle number. They also found that the resistance related to diffusion at the negative electrode initially decreased during the first 100 cycles, then increased with increasing cycle number and that the resistance related to diffusion at the positive electrode increased with cycle number. Mukoyama et al. included two charge-transfer resistances, in parallel, in the equivalent circuit model to account for two different positive electrode particle sizes. They found that one of the charge transfer resistances remained constant with cycle number and the other increased with cycle number, although they did not explain this difference. Lastly, they determined that the resistances of the SEI layers increased with cycle number. It would be ideal to have impedance measurements at several different potentials.

Lu et al. reported a new mechanism of negative electrode protection in the presence of concentrated electrolytes.⁷⁶ Upon changing of the potential of Li/graphite cells, an electric field on the electrode surface in contact with the concentrated electrolyte induced a reversible passivation layer. Lu et al. used a variety of electrolytes including LiTFSI with 1,3-dioxolane (DOL) and LiPF₆ with EC:EMC or propylene carbonate (PC).⁷⁶ Upon polarization of the electrode in the presence of highly concentrated electrolyte, a compact surface layer was formed and continued to grow, protecting the electrode surface from the bulk electrolyte. Upon removal of the polarization, a thin and porous layer resulted after a 20 minute rest, and could disappear completely, meaning there was no permanent

SEI.⁷⁶ The formation of this layer was reversible. The author of this thesis believes that a permanent SEI, albeit dynamic, must exist on the negative and positive electrodes for the cells presented in this thesis, although it is possible that a type of temporary, reversible passivation layer, as described by Lu et al.,⁷⁶ exists in addition to the permanent SEI layers.

Ciosek Högström et al.¹⁶⁷ used XPS to study LiFePO₄/graphite pouch cells containing 1M LiPF₆ EC:DEC 2:1, cycled between 2.7 and 4.2 V at C/10 for 3.5 cycles. They performed XPS measurements, of the graphite electrodes only, at 3.0 V, 3.3 V, and 4.2 V during the first charge of the full cell, at 2.7 V during the first and third discharge of the cell, and at 4.2 V during the fourth charge of the cell. They found that there was more lithium oxide in the lithiated samples of graphite compared to the delithiated samples of graphite. They estimated that the negative SEI layer thickness was larger at 4.2 V compared to at 2.7 V for all cycles, which was then confirmed using atomic force microscopy. It would be ideal to repeat these measurements for the positive electrodes as well. Furthermore, it would be valuable to repeat these measurements on positive and negative electrode samples after the cells have undergone aggressive cycling conditions (ie. have exhibited severe capacity fade and severe impedance growth). These type of measurements may be incredibly useful in learning about the complex changes that occur to the SEI layers under such aggressive conditions.

Similarly to Ciosek Högström et al.,¹⁶⁷ Madec et al.⁹⁹ used XPS to study both the positive and negative electrode SEI layers from NMC/graphite pouch cells. Madec et al.

investigated the effect that electrolyte containing PES and/or vinylene carbonate (VC) had on the positive and negative electrode SEI layers in NMC/graphite cells during SEI formation and after one cycle to 4.2 V.⁹⁹ The SEI formed in the presence of control electrolyte (no additives) was 12 nm thick on the graphite surface and 2 nm thick on the NMC surface after the formation cycle.⁹⁹ On the graphite surface, there was a significant amount of inorganic compounds, such as LiF and Li₂O, formed from the degradation of the electrolyte salt (LiPF₆) and the electrolyte solvents (EC and EMC). The SEI layers on both the positive and negative electrode were thinner and contained a higher fraction of organic species when PES and/or VC were present in the electrolyte.⁹⁹ This was evidence that VC and PES stabilized the reactivity of LiPF₆ during SEI formation. Madec et al. also investigated the positive and negative SEI layers in NMC/graphite pouch cells containing several other electrolyte additives.^{156,168} These studies are very valuable to learn about the initial formation of positive and negative electrode SEI layers under the influence of different electrolyte additives. It would be ideal to repeat these measurements on positive and negative electrode samples after the cells have undergone aggressive cycling conditions (ie. have exhibited severe capacity fade and severe impedance growth).

Bryngelsson et al. used XPS to study graphite negative electrodes in LiPF₆ and EC:DEC after 3 and 50 cycles. They found that after three cycles, the graphite SEI was different in composition in the lithiated state (0.01 V) compared to in the delithiated state (1.5 V). They also found that the graphite SEI was thicker in the lithiated state compared to the delithiated state. They found that after 50 cycles, the graphite SEI was still thicker in the

lithiated state, but the delithiated state contained a higher concentration of Li_2CO_3 on the surface.

Hayashi et al. used XPS to study $\text{LiNi}_{0.82}\text{Co}_{0.15}\text{Al}_{0.03}\text{O}_2$ positive electrodes. They found that a thick degraded surface layer of positive active material was evident after cycling to 4.2 V. They determined that this degraded layer continuously evolved from a LiNiO_2 layered structure to a NiO structure beginning from the bulk and growing toward the surface. Therefore, the formation of this rocksalt layer was irreversible. The irreversible formation of a rocksalt layer could cause irreversible impedance growth in Li-ion cells, as shown in Figure 8.1.

More recently, Li et al.¹⁶⁹ studied the dynamic nature of interphases on $\text{LiNi}_{0.7}\text{Mn}_{0.15}\text{Co}_{0.15}\text{O}_2$ using, primarily, time-of-flight secondary-ion mass spectrometry (TOF-SIMS) and EIS. They found that a so-called ‘cathode-electrolyte interphase’ (CEI) formed spontaneously from the reactions between carbon black (CB) and the electrolyte. They only studied one type of carbon black as the conducting diluent. The CEI formed even without an applied electrochemical bias, and continued to evolve during cycling. They found that the CEI passivated positive electrode particles. They found that when the CEI was thin, the electrode-electrolyte interphase deteriorated. However, they found that when the CEI was thick, deterioration of the electrode-electrolyte interphase did not occur.

Li et al.¹⁶⁹ determined that a rocksalt layer formed irreversibly, and that this surface reconstruction became thick after 100 cycles. However, Jing Li et al. found that by using

appropriate electrolyte additives, such as PES and vinylene carbonate, the formation and growth of a rocksalt layer on NMC811 electrodes was suppressed. From EIS measurements, they found that the high frequency feature was due to Li-ion migration through the surface films on both the positive and negative electrodes. This feature was small in comparison to the med-low frequency feature attributed to the charge transfer impedance across the positive electrode and surface film interface. They did not state how they attributed each feature to the corresponding process. They found that the charge transfer impedance was significantly impacted by the formation of a rocksalt layer and by active mass dissolution, which was accelerated at high potentials. They found that dissolution products from the positive electrode could migrate to the negative electrode during cycling. Furthermore, Li et al.¹⁶⁹ determined that the CEI partially decomposed when exposed to potentials at 4.5 V and above, which could lead to significant irreversible impedance growth. They did not discuss reversible impedance changes.

Cannarella et al.¹⁷⁰ measured the stack pressure and capacity of commercial Li-ion pouch cells. They found that the stack stress, and therefore the cell thickness, oscillated with charge and discharge, but increased irreversibly over several cycles. They claimed that the oscillation with potential was due to expansion of the LiCoO_2 and graphite electrodes, and that the irreversible increase was possibly due to structural changes within the electrode particles and growth of the SEI layers. They found that commercial Li-ion cells manufactured with higher levels of stack pressure had shorter lifetimes due to mechanical degradation, but low levels of stack pressure improved capacity retention compared to

unconstrained cells. The work by Cannarella et al.¹⁷⁰ may be helpful in explaining irreversible impedance growth.

Jung et al.¹⁷¹ studied the cycling stability of NMC111, NMC622, and NMC811/graphite cells. They found that cells containing NMC111 and NMC622 had good capacity retention when cycled to 4.4 V, but NMC811 cells had good capacity retention only when cycled to 4.0 V and below. They claimed that capacity fade at higher potentials was due to polarization of the positive electrode. This agrees with the findings in Chapter 4 and 6 in which capacity fade and impedance growth of the positive electrode SEI occur in NMC442 cells cycled to potentials above 4.4 V. Jung et al. claimed that the polarization of the positive electrode was due to impedance increases that occurred at high potentials, and that the increase in impedance was due to oxygen release from NMC. Jung et al. believe that the production of CO₂ and CO typically observed in NMC/graphite cells^{87,91} is due to oxygen release from the positive electrode surface. They measured the volume and composition of gas evolved in the NMC/graphite cells during the first four cycles up to 4.8 V for NMC111 and NMC 622, and up to 4.4 V for NMC811. They observed the reduction of EC during the initial formation of the graphite SEI layer. They observed the onset of oxygen evolution at 4.6 V during the first charge, coinciding with the evolution of CO₂ and CO, which stabilized during the subsequent discharge. When the cell potential reached 4.6 V during the second charge, another peak in the oxygen evolution was observed, as well as CO₂ and CO, followed by a plateau during discharge. This work may be useful for understanding reversible and irreversible impedance growth.

Erol et al.^{172,173} studied the impedance of LiCoO₂/carbon coin cells and found that impedance was dependent on potential. The coin cell impedance was irreversibly affected by overcharge, but reversibly affected by overdischarge. The normal range used for cycling was between 3.0 and 4.2 V. with overcharge up to 5 V and overdischarge to 2.2 V. They found that the impedance measured during charge and discharge while cycling within the normal range were identical. However, these measurements were performed at the beginning of life, and should be repeated throughout cycle life. They found that the impedance was the largest at 3.0 V, the impedance between 3.2 and 4.5 V were nearly identical, significant impedance growth occurred at 4.6 V, and severe growth occurred between 4.6 and 5 V. This work may be useful in understanding reversible and irreversible impedance growth.

None of the above papers discuss specific reaction mechanisms or molecules present in the SEI layers that could lead to reversible and/or irreversible impedance growth with potential. While some of the above papers may be helpful in learning about irreversible impedance growth, it is necessary to investigate factors that could cause reversible impedance growth, as shown in Figure 3.12, Figure 5.2, Figure 7.4, and Figure 7.29, for example. Furthermore, it is necessary to be able to explain the impedance changes with cycle number and potential observed in Figure 8.1a, Figure 8.1b, and Figure 8.1c.

8.3 CONCLUSION

It is clear that impedance growth is affected by several factors, including electrolyte systems cell chemistry, upper cutoff potential, and experimental conditions. Impedance

growth can be both reversible over one cycle and irreversible over several cycles. It is clear that while researchers have begun to investigate the dynamic nature of impedance due to the positive and/or negative electrode SEI layers, that more in-depth studies are necessary to characterize, and then understand, impedance growth as a function of time, cycle number, and potential. Much more work is required to understand the dynamic behaviour of the positive electrode SEI. Some suggested projects will be discussed in Chapter 10.

CHAPTER 9. IMPEDANCE OF SYMMETRIC CELLS AFTER FULL CELL STORAGE AT 60°C

Chapters 4 and 5 showed that significant impedance growth occurs when Li-ion cells undergo aggressive cycling tests, such as continuous charge-discharge cycling to 4.5 V, or charge-hold-discharge cycling to above 4.4 V. Figure 4.4 showed that after charge-hold-discharge cycling, there was severe impedance growth due to the positive electrode SEI, demonstrated by the positive symmetric cell impedance. Figure 4.4 also showed that the negative symmetric cell impedance was very small compared to the positive symmetric cell impedance. The work presented in Chapter 4, however, did not investigate in detail the changes to the positive and negative electrode impedance during the first few weeks after the initial formation procedure.

In this work, the impedance of positive and negative symmetric cells was measured after full pouch cells were stored for up to 28 days at high temperature (60°C) and moderate to high voltages (4.2 or 4.4 V). The goal of this work was to understand the changes that occur to the negative and positive electrode when left at open circuit voltage at high temperature.

9.1 EXPERIMENTAL

The cells used were 180 mAh NMC442/graphite pouch cells. All cells underwent the standard filling procedure and formation cycle. Cells were filled with either 1M LiPF₆ ethylene carbonate (EC):ethyl methyl carbonate (EMC) 3:7, 1M LiPF₆ EC:EMC:vinylene

carbonate (VC) 29:69:2, or 1M LiPF₆ EC:EMC:prop-1-ene-1,3-sultone (PES): dioxathiolane-2,2-dioxide (DTD):tris-(trimethyl-silyl) phosphite (TTSPi) 28:66:2:2:2. These cells will be referred to as the control cells, 2% VC cells, and PES222 cells, respectively. Following formation, cells were charged to 4.2 V or 4.4 V and then placed in a 60°C temperature box at open circuit voltage. For each experiment, six or seven identical pouch cells were prepared, and all cells were placed in the same temperature box. At regular intervals, one pouch cell was removed from storage and charged to the initial upper cutoff potential (4.2 or 4.4 V). Electrochemical impedance spectroscopy (EIS) measurements at 20°C were taken of the full pouch cell using a four-wire system. The pouch cell was then disassembled in an argon-containing glovebox from which three positive symmetric coin cells and three negative symmetric coin cells were assembled, as described in section 3.6. After assembly, the symmetric coin cells were placed in a 20°C temperature box and EIS measurements were taken. All EIS measurements were performed at 20°C from 10 or 30 mHz to 100 kHz using a four-wire BioLogic SP-150 potentiostat. The symmetric cell potentials were approximately 0.0 V. All pouch cells, symmetric cells, and EIS measurements were made by Rebecca Tingley.

In this work, an equivalent circuit model was used to fit the measured impedance spectra from selected cells. All fitting of the data in this work was done by Samuel Buteau. Adapted from Huang et al,¹³⁶ Figure 9.1 shows the equivalent circuit model used to fit the measured impedance spectra. R_{ohmic} represents the electronic and/or ionic path resistances and W represents the Warburg diffusion component. There are three $R||CPE$ circuits, each dependent on the corresponding resistance, R , the critical frequency, ω_c , and the

exponent, φ . For a full cell, the first R||CPE is associated with the positive electrode SEI impedance and the second and third R||CPE are associated with the negative electrode and the contact impedances for both the positive and negative electrode. For a symmetric cell, the possible meaning of each R||CPE component will be discussed below.

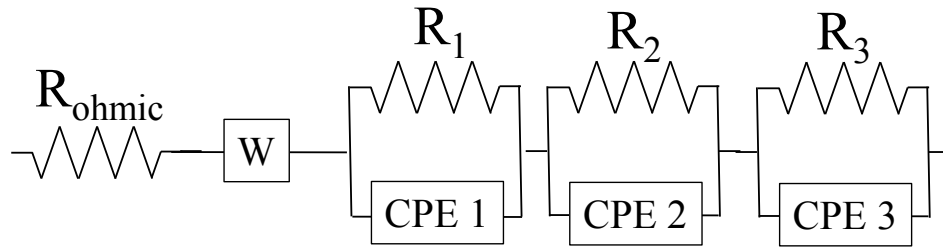


Figure 9.1 The equivalent circuit model used to fit measured spectra. W is a Warburg diffusion element and each CPE is a constant phase element. Adapted from Huang et al.¹³⁶

9.2 RESULTS: CONTROL AND VC CELLS

Table 9.1 summarizes the drop in voltage from 4.2 V for the control pouch cells stored at open circuit voltage and 60°C. In general, the voltage of the control pouch cells decreased with increasing storage time, indicating that electrolyte oxidation at the positive electrode occurred. Each entry in the table is the voltage drop measured of a single cell.

Table 9.1 The drop in voltage during open circuit voltage storage at 60°C for the control cells with initial voltage of 4.2 V.

Days in Storage	2	4	7	14	21
Voltage Drop (V)	0.1236	0.0747	0.1929	0.3472	0.4587

Figure 9.2 shows the measured impedance spectra of the positive and negative symmetric cells assembled from the control cells stored at 60°C and 4.2 V for up to 21 days. The top

panels of Figure 9.2 show the impedance spectra in a Nyquist representation. The middle and bottom panels of Figure 9.2 show the impedance spectra in an imaginary and real Bode plot, respectively. In all cases, the positive symmetric cell impedance was larger than the corresponding negative symmetric cell impedance. In general, the positive symmetric cell impedance increased with increasing storage time, although an oscillatory behaviour was observed. This most likely indicates an increase in impedance of the positive electrode SEI layer, either due to an increase in thickness of the layer, or an increase in resistive species within the layer.

In Figure 9.2, the negative symmetric cell impedance grew with increasing storage time and changed shape. The impedance spectra shown in Figure 9.2 have three depressed “semi-circular” features. The presence of these three features led to the selection of the equivalent circuit model shown in Figure 9.1, in which each feature is represented by a $R||CPE$ component. For the positive symmetric cell impedance, there was a predominant feature at mid-low frequency, and two smaller features at high frequency. For the negative symmetric cell impedance, the features are less distinguishable, and the shape of the spectra changed significantly over the 21 days. This indicates that, for the negative symmetric cells with control electrolyte, the frequency response of the different processes (ie. negative electrode SEI, contact impedance, etc.) overlap. As storage time increased, the negative symmetric cells developed a feature between 1 and 10 Hz.

In Figure 9.2, the predominant feature for the positive symmetric cells occurred at a lower frequency than the predominant feature for the negative symmetric cell. At very

high frequency (> 10 kHz), the positive and negative symmetric cell data were nearly identical.

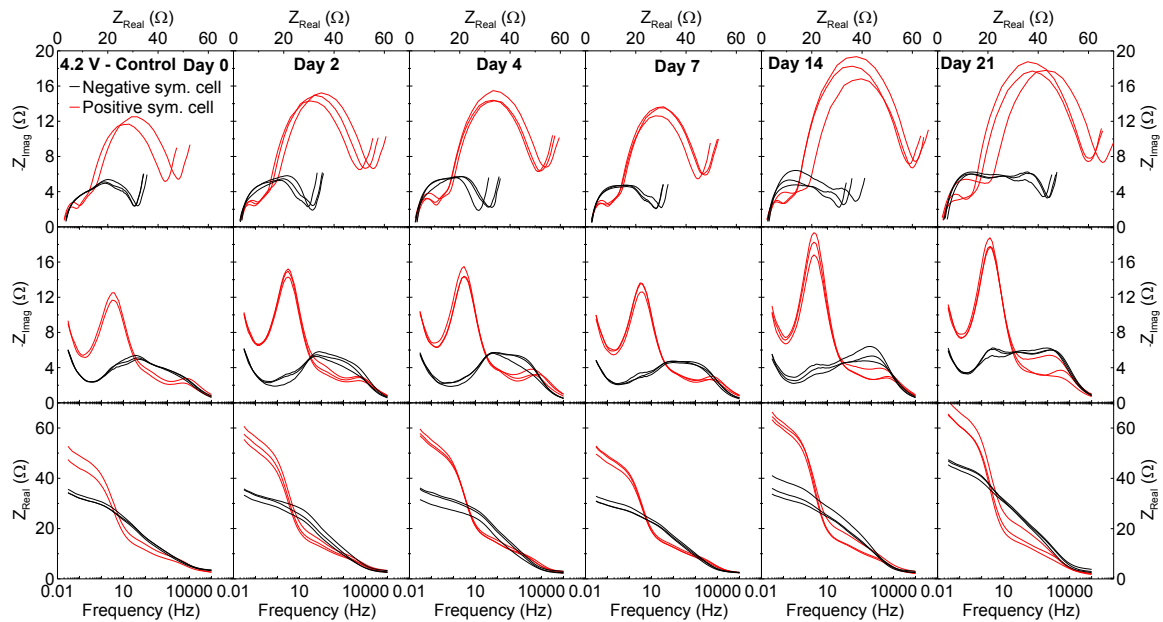


Figure 9.2 The Nyquist representation (top panels), imaginary Bode representation (middle panels), and real Bode representation (bottom panels) for the impedance of positive and negative symmetric cells made from the control pouch cells at 4.2 V, after storage at 60°C . Each panel has three datasets for positive symmetric cells and for negative symmetric cells to demonstrate reproducibility. EIS was measured at 20°C from 10-30 mHz to 100 kHz. The electrode area for all cells was 1.00 cm^2 .

Figure 9.3 shows the impedance spectra of the full control pouch cells measured just prior to disassembly for symmetric cells. While there was no clear trend in the overall impedance growth as a function of storage time, there was a clear change in shape of the spectra as the storage time increased. As storage time increased, the separation of the features became clearer as the low frequency feature became distinguishable from the high frequency feature.

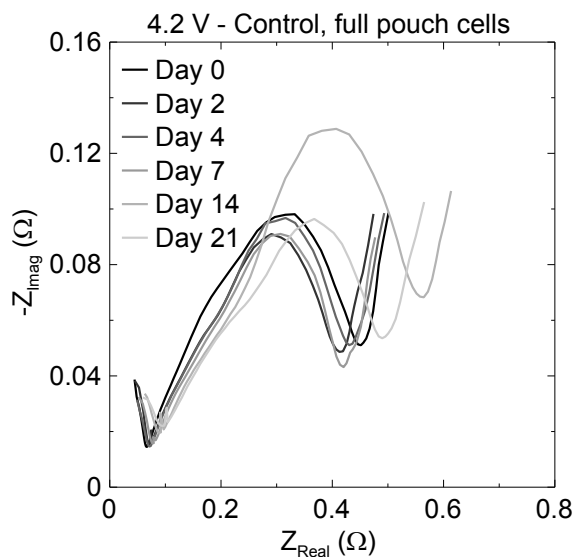


Figure 9.3 The impedance spectra measured at 4.2 V and 20°C for the control pouch cells after storage at 60°C and 4.2 V. The electrode area for all cells was 84.7 cm².

Table 9.2 summarizes the drop in voltage from 4.2 V for the 2% VC pouch cells stored at open circuit voltage and 60°C. The empty cells indicate the voltage drop data was not available. The voltage of the 2% VC pouch cells decreased with increasing storage time. Each entry in the table is the voltage drop measured of a single cell. The change in voltage of the 2% VC cells was significantly smaller than that for the control cells. After 21 days of storage, the control changed in voltage by 0.4587 V and the 2% VC cell changed in voltage by only 0.1267 V. This agrees with previous findings that showed that VC-containing cells had lower rates of electrolyte oxidation at the positive electrode and lower voltage drop during storage compared to cells containing control electrolyte.^{51,174}

Table 9.2 The drop in voltage during open circuit voltage storage at 60°C for the 2% VC cells with initial voltage of 4.2 V.

Days in Storage	2	4	7	14	21	28
Voltage Drop (V)	-	0.077	0.0915	0.1067	0.1267	-

Figure 9.4 shows the measured impedance spectra of the positive and negative symmetric cells assembled from the 2% VC cells stored at 60°C and 4.2 V for up to 28 days. The top panels of Figure 9.4 show the impedance spectra in a Nyquist representation. The middle and bottom panels of Figure 9.4 show the impedance spectra in an imaginary and real Bode plot, respectively. Unlike for the control cells shown in Figure 9.2, Figure 9.4 shows that the impedance for the positive and negative symmetric cells assembled from the 2% VC pouch cells were similar in magnitude, although different in shape. Unlike the control cells, there was minimal overall growth in the impedance spectra of the positive and negative symmetric cells over time. However, both the positive and negative symmetric cell impedance oscillated over time. This random oscillation is likely due to dynamic changes of the SEI layers in addition to gas evolution.

In Figure 9.4, the predominant feature for the positive symmetric cells occurred at a lower frequency than the predominant feature for the negative symmetric cell. The predominant feature for the negative symmetric cell began to split into two features after 21 days in storage. At high frequency (> 10 kHz), the positive and negative symmetric cell data were nearly identical.

Compared to the control cells, the impedance of the negative symmetric cells were larger for the 2% VC cells, and the impedance of the positive symmetric cells were smaller for the 2% VC cells. This agrees with previous findings that show that cells containing VC have less electrolyte oxidation at the positive electrode compared to cells containing control electrolyte, leading to smaller impedance of the positive symmetric cell.¹⁷⁴

Petibon et al. showed that while the impedance of positive symmetric cells was smaller for cells containing VC compared to cells containing control electrolyte, the negative symmetric cell impedance was larger for VC-containing cells.^{122,123} This is confirmed by the larger negative symmetric cell impedance shown in Figure 9.4 for VC cells compared to the smaller negative symmetric cell impedance shown in Figure 9.2 for control cells.

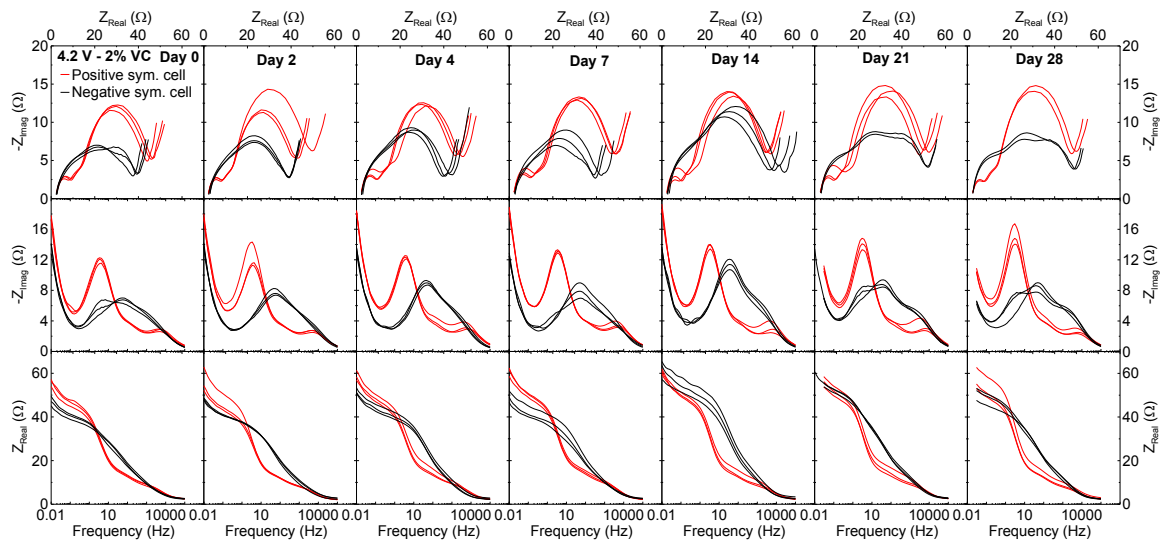


Figure 9.4 The Nyquist representation (top panels), imaginary Bode representation (middle panels), and real Bode representation (bottom panels) for the impedance of positive and negative symmetric cells made from the 2% VC pouch cells at 4.2 V, after storage at 60°C. Each panel has three datasets for positive symmetric cells and for negative symmetric cells. EIS was measured at 20°C from 10-30 mHz to 100 kHz. The electrode area for all cells was 1.00 cm².

Figure 9.5 shows the impedance spectra of the full 2% VC pouch cells measured just prior to disassembly for symmetric cells. As the storage time increased, the cell impedance grew. Unlike the control cells, there was no clear change in the shape of the spectra with increasing storage time for the 2% VC cells.

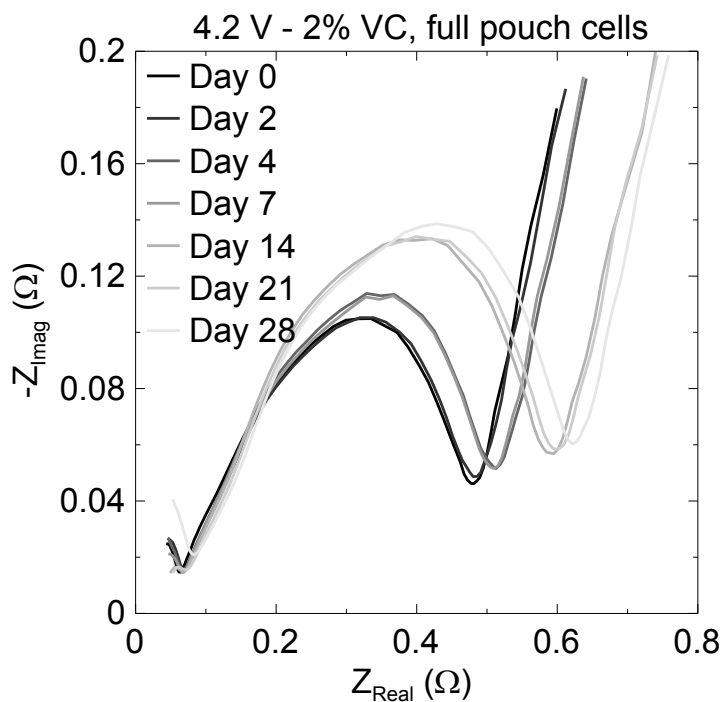


Figure 9.5 The impedance spectra measured at 4.2 V and 20°C for the 2% VC pouch cells after storage at 60°C and 4.2 V. The electrode area for all cells was 84.7 cm².

Figure 9.6 shows selected impedance spectra and the corresponding fitting results from the equivalent circuit model (Figure 9.1) for the control cells after 0 days and after 21 days of storage at 60°C and 4.2 V. Figure 9.6 shows spectra for both the positive and negative symmetric coin cells. Figure 9.6a shows Nyquist representations of the selected spectra. Figure 9.6b shows imaginary Bode representations and Figure 9.6c shows real Bode representations. There is good agreement between the measured spectra and the spectra obtained from fitting in all cases.

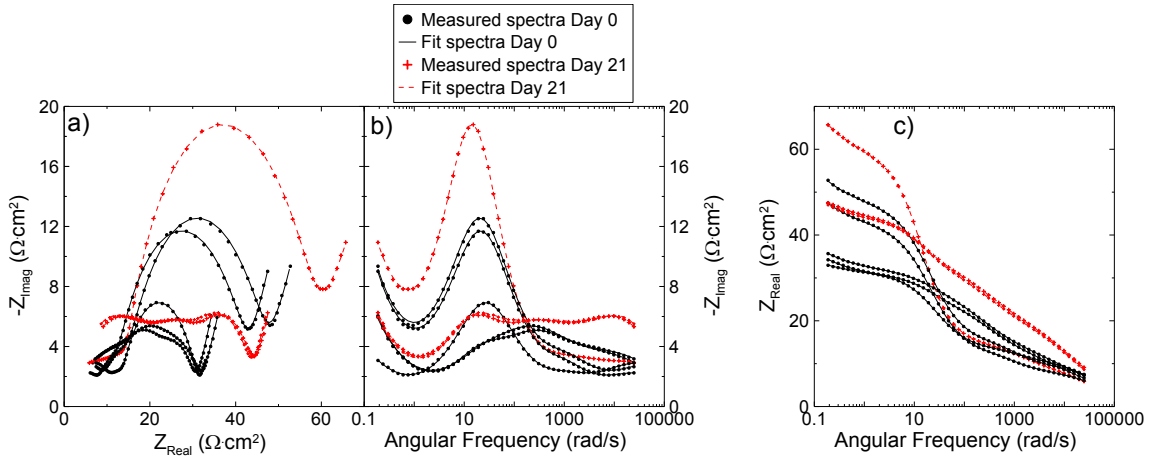


Figure 9.6 Selected impedance spectra and the corresponding fit for the control cells measured after 0 and 21 days in storage at 60°C and 4.2 V shown in a) Nyquist representation, b) imaginary Bode representation, and c) real Bode representation.

Figure 9.7 shows the fitting results as a function of storage time for the resistors in the equivalent circuit model (Figure 9.1) for the control cells (bottom panels) and the 2% VC cells (top panels) stored at 60°C and 4.2 V. Each panel shows the fitting parameters for the positive and negative symmetric cells assembled from the full pouch cells. Figure 9.7a and Figure 9.7d show the results for parameter R_1 , Figure 9.7b and Figure 9.7e show the results for parameter R_2 , and Figure 9.7c and Figure 9.7f show the results for parameter R_3 . For the positive symmetric cells, R_1 is associated with the positive electrode SEI. For the negative symmetric cells, both R_1 and R_2 are likely associated with the negative electrode SEI. For both the positive and negative symmetric cells, R_3 is associated with the contact impedances. It is unclear which process R_2 is associated with for the positive symmetric cells. More work is required to understand the complexities of symmetric cell impedance spectra.

Figure 9.7 shows that for control and 2% VC cells, R_1 was larger for the positive symmetric cells and R_2 was larger for the negative symmetric cells. R_3 was nearly identical for the positive and negative symmetric cells. The oscillatory behaviour of both the positive and negative symmetric cells for the 2% VC cells can be seen in the fluctuation of R_1 and R_2 shown in Figure 9.7a and Figure 9.7b. The oscillatory behaviour, but overall increase in impedance, of the positive symmetric cells for the control cells can be seen in the fluctuation of R_1 shown in Figure 9.7d. The difference between the three pair cells is most likely due to misalignment of the electrodes in the coin cells, resulting in an unknown effective electrode area. The symmetric coin cell assembly process may need modification in order to improve the accuracy of the electrode placement, and the accuracy of the electrode area used in normalization of the impedance spectra.

Figure 9.8a and Figure 9.8b shows the fitting results as a function of storage time for the sum of the resistances R_1 , R_2 , and R_3 , obtained using the equivalent circuit model for the 2% VC cells and the control cells, respectively, stored at 60°C and 4.2 V. Both panels show the fitting parameters for the positive and negative symmetric cells assembled from the full pouch cells. Figure 9.8b shows that for the control cells, the total resistance of the negative symmetric cells increased with storage time, and the total resistance of the positive symmetric cells oscillated with storage time but increased overall. Figure 9.8a shows that for the 2% VC cells, the total resistance of both the positive and negative symmetric cells oscillated slightly with time, but stayed relatively constant over the 28 days of storage.

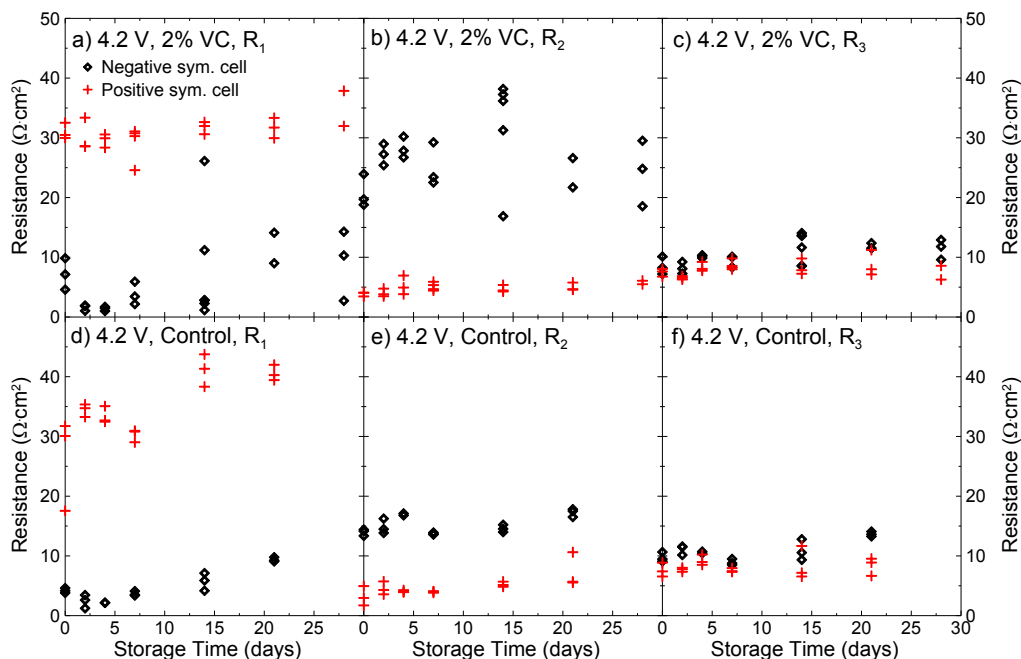


Figure 9.7 Parameters for the resistances a) R_1 , b) R_2 , and c) R_3 obtained from fitting, using an equivalent circuit model, the positive and negative symmetric cell impedance spectra from the control cells as a function of storage time at 60°C . Similarly, parameters for the resistances d) R_1 , e) R_2 , and f) R_3 from the 2% VC cells. The error bars, from fitting, for each measurement are equal in size to the symbols, and there are typically three pair cells shown for each measurement.

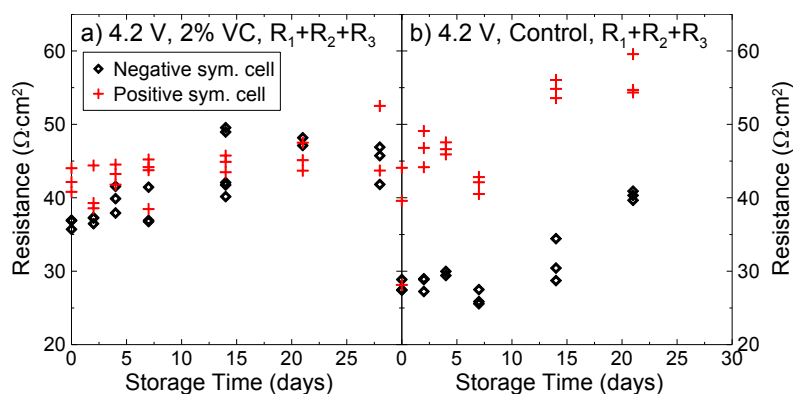


Figure 9.8 The sum of the resistances R_1 , R_2 , and R_3 , obtained from fitting using an equivalent circuit model, for the positive and negative symmetric cell impedance spectra from the a) 2% VC cells and b) control cells as a function of storage time at 60°C . The error bars, from fitting, for each measurement are equal in size to the symbols, and there are typically three pair cells shown for each measurement.

9.3 RESULTS: PES222 CELLS

Figure 9.9 shows the measured impedance spectra of the positive and negative symmetric cells assembled from the PES222 cells stored at 60°C and 4.2 V for up to 21 days. The top panels of Figure 9.9 show the impedance spectra in a Nyquist representation. The middle and bottom panels of Figure 9.9 show the impedance spectra in an imaginary and real Bode plot, respectively. The impedance of the negative symmetric cell grew significantly with storage time. While there was no overall growth in the impedance spectra of the positive symmetric cell, it oscillated with storage time. This oscillation is likely due to dynamic changes in the SEI layer. For example, it is possible that the impedance of the SEI layer changes as electrolyte oxidation or gas evolution occurs.

In Figure 9.9, the predominant feature for the positive and negative symmetric cells initially occurred at similar frequencies, but the predominant feature of the negative symmetric cell shifted to lower frequencies, and the predominant feature of the positive symmetric cell shifted to higher frequencies as the storage time increased. At high frequency (> 10 kHz), the positive and negative symmetric cell data were nearly identical.

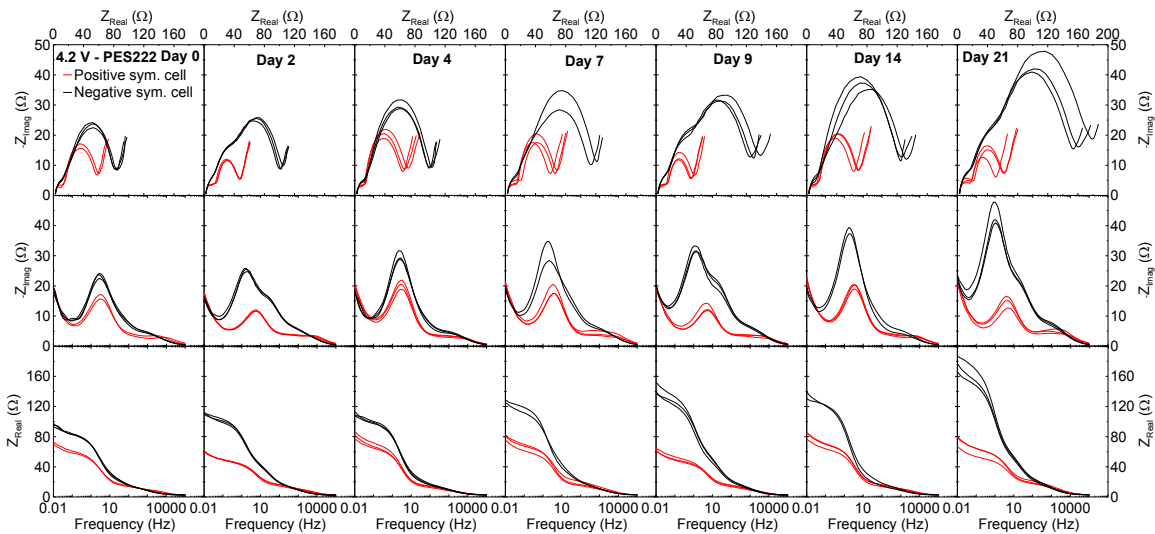


Figure 9.9 The Nyquist representation (top panels), imaginary Bode representation (middle panels), and real Bode representation (bottom panels) for the impedance of positive and negative symmetric cells made from the PES222 pouch cells at 4.2 V, after storage at 60°C. Each panel has three datasets for positive symmetric cells and for negative symmetric cells. EIS was measured at 20°C from 10-30 mHz to 100 kHz. The electrode area for all cells was 1.00 cm².

Wang et al.⁵¹ and Nelson et al.¹⁰ showed that cells containing PES, DTD, and TTSPi had lower rates of electrolyte oxidation at the positive electrode, less gas evolution, smaller charge slippage during cycling, and smaller voltage drop during open circuit voltage storage compared to cells containing VC or control electrolyte. This suggests that the positive electrode impedance of cells containing PES, DTD, and TTSPi would be smaller than that of cells containing VC or control electrolyte. This is confirmed in Figure 9.9, as the positive symmetric cell impedance was significantly smaller than the positive symmetric cell impedances shown in Figure 9.2 and Figure 9.4.

Table 9.3 summarizes the drop in voltage from 4.2 V and 4.4 V for the PES222 pouch cells stored at open circuit voltage and 60°C. Each entry in the table is the voltage drop

measured of a single cell. The empty cells indicate the voltage drop data was not available. The voltage of the PES222 pouch cells decreased with increasing storage time. The change in voltage of the PES222 cells stored at 4.4 V was significantly larger than that for the PES222 cells stored at 4.2 V, due to a higher rate of electrolyte oxidation at higher potential. After 21 days of storage, the 4.2 V PES222 cell changed in voltage by 0.139 V and the 4.4 V PES222 cell changed in voltage by 0.271 V.

Table 9.3 The drop in voltage during open circuit voltage storage at 60°C for the PES222 cells with initial voltage of 4.2 and 4.4 V.

Days in Storage	2	4	7	9	14	21
Voltage Drop from 4.2 V (V)	0.077	0.103	0.091	-	0.123	0.139
Voltage Drop from 4.4 V (V)	0.109	0.157	0.191	-	0.247	0.271

Figure 9.10 shows the measured impedance spectra of the positive and negative symmetric cells assembled from the first batch of PES222 cells stored at 60°C and 4.4 V for up to 21 days. The top panels of Figure 9.10 show the impedance spectra in a Nyquist representation. The middle and bottom panels of Figure 9.10 show the impedance spectra in an imaginary and real Bode plot, respectively. To ensure repeatability of the behaviour observed in Figure 9.10, a second batch of PES222 cells were studied. Figure 9.11 shows the measured impedance spectra of the positive and negative symmetric cells assembled from the second batch of PES222 cells stored at 60°C and 4.4 V for up to 28 days. The top panels of Figure 9.11 show the impedance spectra in a Nyquist representation. The middle and bottom panels of Figure 9.11 show the impedance spectra in an imaginary and real Bode plot, respectively.

Similarly to the data shown in Figure 9.2, Figure 9.4, and Figure 9.9, the positive and negative symmetric cell data were nearly identical at high frequency (> 10 kHz).

In Figure 9.10 and Figure 9.11, both the positive and negative symmetric cell impedance oscillated with increasing storage time. The size of the spectra and the frequencies of the predominant features oscillated with time. This is dramatically different than the spectra shown in Figure 9.9 for PES222 cells stored at 4.2 V. This suggests there is dynamic behaviour of both the positive and negative electrode SEI layers during 60°C storage at 4.4 V. Oscillatory behaviour of the impedance spectra of either the positive or negative symmetric cells (or both) may indicate dynamic changes to the SEI layers, gas evolution and consumption, and interaction between the positive and negative electrodes.

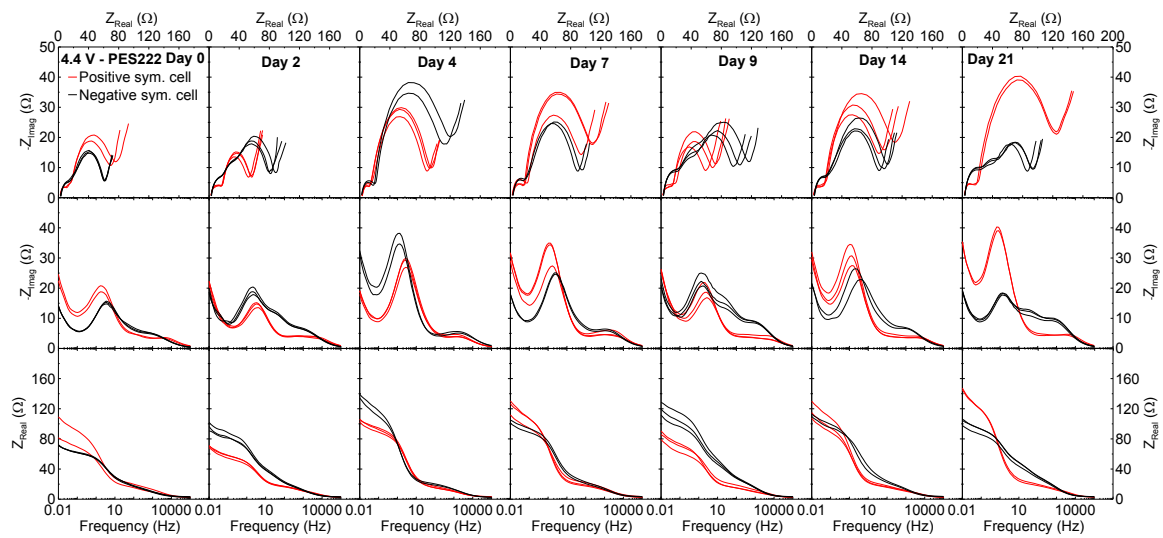


Figure 9.10 The Nyquist (top panels), imaginary Bode (middle panels), and real Bode (bottom panels) representation for the impedance of positive and negative symmetric cells made from the first batch of PES222 pouch cells at 4.4 V, after storage at 60°C . Each panel has three datasets for positive and negative symmetric cells. EIS was measured at 20°C from 10-30 mHz to 100 kHz. The electrode area for all cells was 1.00 cm^2 .

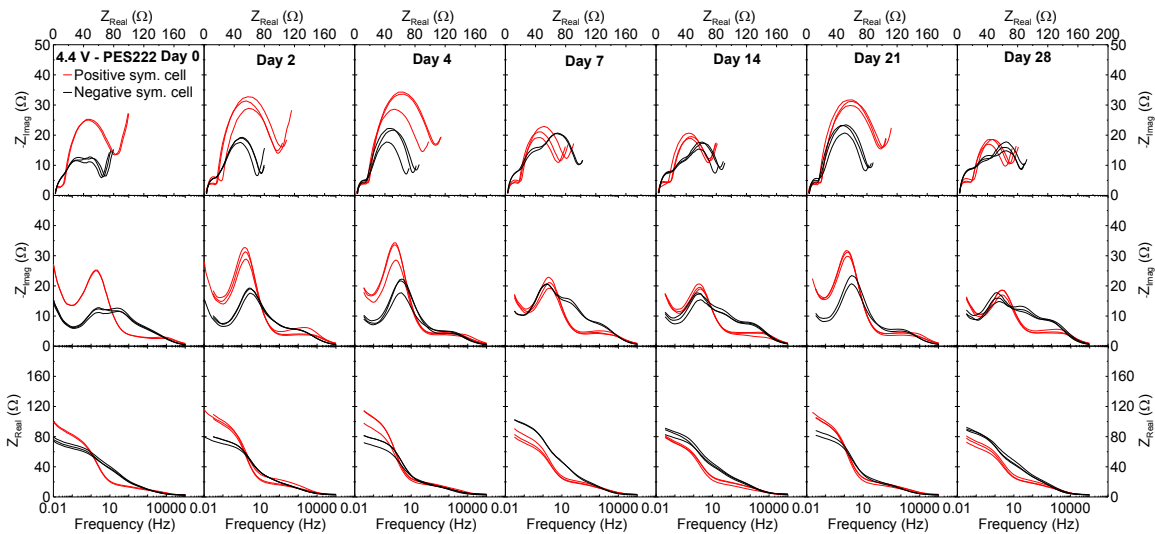


Figure 9.11 The Nyquist (top panels), imaginary Bode (middle panels), and real Bode (bottom panels) representation for the impedance of positive and negative symmetric cells made from the second batch of PES222 pouch cells at 4.4 V, after storage at 60°C. Each panel has three datasets for positive and negative symmetric cells. EIS was measured at 20°C from 10-30 mHz to 100 kHz. The electrode area for all cells was 1.00 cm².

Xiong et al. showed that the positive and negative electrode interact.^{87,91} For example, CO₂ that was produced at the positive electrode was subsequently consumed by the negative electrode in a charged full pouch cell, but was not consumed when the charged positive electrode was isolated. Xiong et al. determined that the interactions between the positive and negative electrodes in a full cell limited gas evolution and reduced impedance growth.^{87,91} It is possible that by monitoring the impedance of the positive and negative symmetric cells over storage time, that the interactions between the two electrodes was being observed. This interaction may not be observed in full pouch cells. For example, the magnitude of the impedance of the positive and negative symmetric cells shown in the bottom panels of Figure 9.11 oscillated with storage time. However, the sum of the impedances of the positive and negative symmetric cells does not appear

to change with storage time. This indicates that oscillatory behaviour can not be observed in the impedance of the full pouch cells, but was illustrated by the separate positive and negative symmetric cell impedance. This follows from the work presented in Chapters 4, 5, 6, and 7 which do not show oscillatory behaviour in full cell impedance spectra.

Furthermore, it is notable that the size of the positive and negative symmetric cell impedance were similar for PES222 cells at 4.4 V and 2% VC cells at 4.2 V. Nelson et al. found that the positive symmetric cell impedance was dramatically larger than the negative symmetric cell impedance after aggressive charge-hold-discharge cycling to 4.4 V and above.⁸² It is likely that the impedance of the positive electrode SEI only grows significantly when subjected to aggressive cycling tests or exposed to high potentials (> 4.4 V) for extended periods of time.

Figure 9.12 shows the fitting results as a function of storage time for the sum of the resistances R_1 , R_2 , and R_3 , obtained using the equivalent circuit model for the PES222 cells stored at 60°C and 4.2 V and 4.4 V. All panels show the fitting parameters for the positive and negative symmetric cells assembled from the full pouch cells and lines drawn as a guide to the eye. Figure 9.12a shows that for the PES222 cells stored at 4.2 V, the total resistance of the negative symmetric cells increased dramatically with storage time, and the total resistance of the positive symmetric cells oscillated with storage time. Figure 9.12b and Figure 9.12c show that for the PES222 cells stored at 4.4 V, the total resistance of both the positive and negative symmetric cells oscillated with time. The behaviour of the impedance of the negative symmetric cells was very different for the

cells stored at 4.2 V compared to the cells stored at 4.4 V. The impedance of the positive symmetric cells was larger in cells stored at 4.4 V compared to cells stored at 4.2 V. It is possible that the interactions between the positive and negative electrodes are more pronounced at 4.4 V compared to 4.2 V, resulting in oscillatory behaviour of both the positive and negative symmetric cells, and lower impedance of the negative symmetric cell. Since the impedance of the positive symmetric cell was larger at 4.4 V, compared to 4.2 V, it is possible that this inhibits the growth of the negative symmetric cell impedance due to interactions.

Figure 9.13 shows the sum of the positive and negative symmetric cell total resistances of the PES222 cells stored at 4.4 V and 60°C, from Figure 9.12b and Figure 9.12c, as a function of storage time. Figure 9.13 shows that, for the first batch of PES222 cells stored at 4.4 V, the sum of the total resistances of the positive and negative symmetric cells tended to increase with storage time, whereas the second batch was relatively constant with storage time. In Chapters 4, 5, 6, and 7, oscillatory behaviour of full pouch cell impedance was not observed. In some cases, the full pouch cell impedance decreased with cycle number, such as the impedance of NMC442/graphite pouch cells containing a polyethylene terephthalate separator and PES222 cycled to 4.4 V and 20°C in Chapter 6. In some cases, the full pouch cell impedance remained approximately constant with cycle number, such as the impedance of uncoated NMC442/graphite pouch cells containing PES222 cycled to 4.4 V and 4.425 V at 40°C in Chapters 4 and 5 and the impedance of NMC622/graphite cells cycled to 4.1 and 4.2 V at 40°C in Chapter 7. In several cases, the full pouch cell impedance increased with cycle number, dramatically so at high

potentials, such as the impedance of all NMC442/graphite pouch cells cycled to 4.45 V and above at 40°C in Chapter 4, the impedance of all NMC442/graphite pouch cells containing PES222 cycled to 4.45 and 4.5 V at 20°C in Chapter 6, and the impedance of single crystal NMC532 cycled to 4.1 V and above at 40°C in Chapter 7.

In all cases, the full pouch cell impedance did not oscillate with time or cycle number. It is possible that the individual impedance from the positive and negative electrode oscillated in the above mentioned cells, but this is not observable in the full pouch cell impedance. Furthermore, there are several factors, including temperature, upper cutoff potential, and cell chemistry, that impact the impedance growth of Li-ion cells.

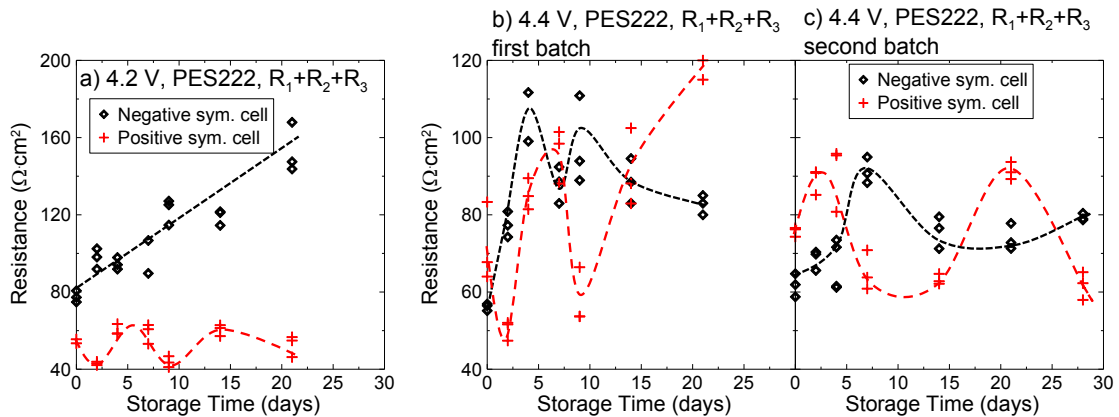


Figure 9.12 The sum of the resistances R_1 , R_2 , and R_3 , obtained from fitting using an equivalent circuit model, for the positive and negative symmetric cell impedance spectra from the PES222 cells stored at a) 4.2 V, b) 4.4 V (first batch), and c) 4.4 V (second batch) as a function of storage time at 60°C. The error bars, from fitting, for each measurement are equal in size to the symbols, and there are typically three pair cells shown for each measurement. Lines have been drawn as a guide to the eye.

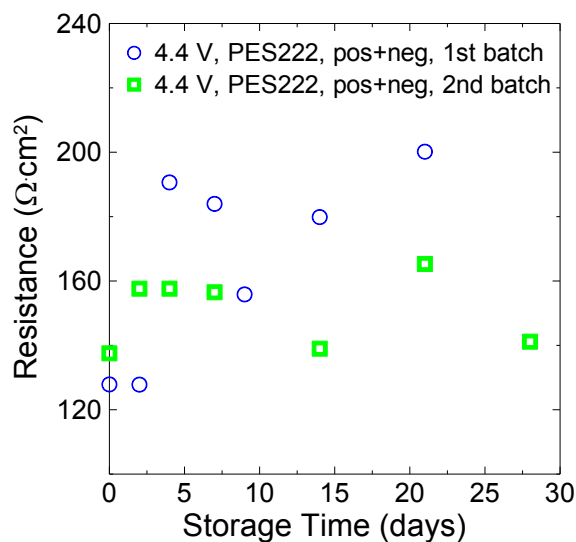


Figure 9.13 The sum of the total resistances (shown in Figure 9.12b and Figure 9.12c) of the positive and negative symmetric cells as a function of storage time at 60°C for the first and second batch of PES222 cells stored at 4.4 V.

9.4 CONCLUSION

The work presented here demonstrated the dynamic behaviour of the impedance related to the positive and negative electrode during high temperature storage. For control electrolyte, the positive electrode impedance grew significantly with storage time. For electrolyte containing VC, the positive and negative electrode impedance did not grow with storage time, but exhibited an oscillatory behaviour, likely due to dynamic changes of the SEI layers. For PES222 cells, the negative electrode impedance grew significantly in cells stored at 4.2 V, but exhibited oscillatory behaviour in cells stored at 4.4 V. For PES222 cells, the positive electrode exhibited small oscillatory behaviour in cells stored at 4.2 V, and large oscillatory behaviour in cells stored at 4.4 V. This oscillatory behaviour is likely due to dynamic changes of the positive and negative electrode SEI

layers, which are influenced by the interactions that occur between the negative and positive electrode. More work is required to confirm and then understand this oscillatory behaviour.

Furthermore, the fitting of symmetric cell impedance spectra using an equivalent circuit model was shown to be useful to learn about the specific changes occurring in the impedance spectra.

CHAPTER 10. CONCLUSIONS

10.1 CONCLUSIONS

Lithium-ion batteries play an important role in the transition away from non-renewable sources of energy. Technologies such as electric vehicles and grid energy storage require longer-lasting batteries with higher energy density and lower cost. Although increasing the upper cutoff potential of lithium-ion batteries would lead to higher capacity and higher energy density, achieving long-lasting high potential operation in lithium-ion cells is difficult.

The work presented in this thesis showed that impedance growth is one obstacle to high potential lithium-ion cells and is a large contributor to capacity fade and cell failure at high potential. Electrochemical impedance spectroscopy (EIS) measurements are quick and non-destructive to the cell and can illuminate the processes occurring in Li-ion cells as a function of time, cycle number, and potential. EIS measurements are particularly valuable when performed during cycling experiments.

This work aimed to characterize the problems associated with Li-ion cell operation at high potential. In particular, impedance growth and its relation to the SEI layers on both the positive and negative electrodes remain key factors in the failure of Li-ion cells operated to high potential. In order to make an impact on the Li-ion battery community, a vast number of systems need to be characterized and understood under a variety of testing conditions. The work presented in this thesis characterized a small selection of these systems.

Chapter 4 introduced EIS measurements coupled with cycling experiments. Chapter 4 demonstrated the importance of monitoring impedance growth as a function of time, cycle number, and potential. The impacts of electrode coatings and upper cutoff potential on the impedance and cycling performance of Li-ion cells were significant. While cells with appropriate electrolyte additives had little to no impedance growth and capacity fade when undergoing charge-hold-discharge cycling to 4.4 V, all cells had significant impedance growth and severe capacity fade when cycled to 4.5 V. It was also shown that the high frequency intercept was large when measured at 3.4 V, and decreased during charge to 4.4 V.

Chapter 5 compared the performance and impedance of NMC/graphite pouch cells to commercially available LiCoO₂/graphite cells under aggressive charge-hold-discharge cycling. Through differential voltage analysis, it was proposed that the growth of the negative electrode SEI was the cause for the small capacity fade and impedance growth observed for the LiCoO₂ cell cycled to 4.2 V. It was proposed that major damage to the positive electrode was the cause for the large capacity fade and impedance growth observed for the LiCoO₂ cells cycled to 4.35 and 4.4 V. Furthermore, the importance of using aggressive cycling conditions to test Li-ion cells was demonstrated.

Chapter 6 compared the performance and impedance of NMC/graphite cells containing different separator materials, current collectors, and positive electrode conducting diluents undergoing a variety of cycling tests. While some components improved the performance of cells when cycled to 4.4 and 4.45 V, all cells exhibited capacity fade and

impedance growth during 4.5 V cycling. Furthermore, Chapter 6 demonstrated that fitting impedance spectra using an equivalent circuit model was valuable to characterize the changes of separate processes and monitor how individual impedance components changed over time. The parameter R_1 , associated with the positive electrode solid electrolyte interphase (SEI) layer, in the equivalent circuit model was the largest and accounted for the large impedance growth observed in all cells studied.

Chapter 7 compared the performance and impedance of various types of NMC/graphite pouch cells containing different electrolyte systems. Chapter 7 demonstrated the usefulness of using a 4-wire system to monitor impedance growth as a function of time, cycle number, and potential and using an equivalent circuit model to fit the impedance spectra. In general for all cells studied, the capacity fade, impedance growth, and difference between the average charge and discharge voltage, ΔV , increased when the upper cutoff potential was increased. For many cells, the change in ΔV was significantly larger than the expected change in ΔV calculated from the corresponding cell impedance growth. This means that there was another process contributing to ΔV growth that was not captured in the measured impedance spectra, such as the impedance growth related to diffusion, and requires more work to understand. The resistances of the SEI layers as well as the high frequency intercept oscillated with measurement potential. The resistances of the SEI layers increased with increasing measurement potential and decreased with decreasing measurement potential. Alternatively, the high frequency intercept decreased with increasing measurement potential. This oscillation was found to be reversible over one cycle and irreversible over several cycles.

Chapter 8 presented three main types of impedance growth, including reversible growth, irreversible growth, and growth exhibiting hysteresis between the charge and discharge segments. The work presented in this thesis monitored how impedance growth changed with time, cycle number, and potential, in order to learn about the complex changes occurring within Li-ion cells. Chapter 8 discussed some literature that may be helpful in explaining these phenomena, and presented many that are unable to explain the phenomena observed in this work. Chapter 8 highlighted the lack of helpful, logical experiments in the literature related to reversible and irreversible impedance growth.

Chapter 9 compared the impedance growth of full pouch cells and symmetric coin cells containing various electrolyte systems during storage at 60°C and 4.2 or 4.4 V. Chapter 9 demonstrated the dynamic behaviour of the impedance related to the positive and negative electrode during high temperature storage. For cells containing control electrolyte, the positive electrode impedance grew significantly with storage time and for cells containing vinylene carbonate, the positive and negative electrode impedance did not grow with storage time. For cells containing PES222, the negative electrode impedance grew significantly in cells stored at 4.2 V, but exhibited oscillatory behaviour in cells stored at 4.4 V and the positive electrode exhibited small oscillatory behaviour in cells stored at 4.2 V, and large oscillatory behaviour in cells stored at 4.4 V. This oscillatory behaviour was likely due to dynamic changes of the positive and negative electrode SEI layers, which may have been influenced by the interactions that occur between the negative and positive electrode. More work is required to confirm and then

understand this oscillatory behaviour and the interactions between the positive and negative electrodes.

The work presented in this thesis motivates additional work to be done to characterize and understand impedance growth, particularly at high potentials. Some suggested future work will be discussed.

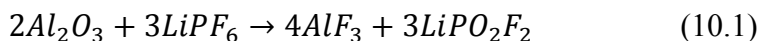
10.2 FUTURE WORK

The work presented in this thesis lays a foundation for future impedance studies. It is clear that impedance spectra and impedance growth are incredibly complex and impacted by a variety of factors. Furthermore, the appropriate choice of equivalent circuit model used to fit impedance spectra is important, and needs careful thought.

As Chapter 6 showed, the effective capacitance calculated from the fitting parameters obtained from the equivalent circuit model used did not yield correct values for the positive electrode SEI thickness, when a relative dielectric constant of unity was assumed. It is necessary to determine the approximate dielectric constant of both the positive and negative electrode SEI layers. Doing so will help to extract useful information about SEI layer thickness from the equivalent circuit model fitting parameters, and how the thickness changes as a function of time, cycle number, and potential. It would be useful to measure the dielectric constant of a variety of electrolytes and electrolyte components, including 1M LiPF₆ in ethylene carbonate (EC), 1M LiPF₆ in EC:ethyl methyl carbonate (EMC), 1M LiPF₆ in EC:EMC:dimethyl carbonate (DMC), in

addition to other salt concentrations. Dielectric measurements can be made using a capacitance cell and a frequency response analyzer.¹⁵⁷ Some of these values have been presented in the literature.¹⁵⁷ Characterizing how electrolyte additives change the dielectric constant of these electrolyte systems will be useful. It would be most useful to determine the dielectric constant of the positive and negative electrode SEI layers under the influence of a variety of electrolyte systems. It may be possible to determine approximate values of the dielectric constant of the SEI layers through careful EIS measurements and SEI thickness measurements. It would be necessary to have a system that produced an impedance spectrum that resembled that of an RC circuit, so that the capacitance value could be obtained directly from the spectrum. Furthermore, XPS or ellipsometry experiments to determine the SEI thickness would be necessary.

Chapter 6 showed that, in general, cells containing a polyethylene terephthalate (PET) separator had superior performance to cells containing a polypropylene (PP) separator. The PET separator had a higher content of Al₂O₃ in the separator, at 67% by weight compared to 11% by weight for the PP separator. It is possible that the Al₂O₃ reacts with LiPF₆ in the electrolyte, as shown in equation 10.1, to form LiPO₂F₂.



As discussed in Chapter 1, LiPO₂F₂ has been used as a salt and as an additive in Li-ion cells. Using LiPO₂F₂ in the electrolyte resulted in better capacity retention, a more stable SEI layer that had smaller impedance, and better ability to protect both the positive and negative electrode surface, compared to cells without LiPO₂F₂^{32,33}. It is possible that by

having a higher content of Al_2O_3 in the PET separator, that the LiPO_2F_2 formed through the reaction with LiPF_6 helped to improve the capacity retention and formation of stable SEI layers. Therefore, it would be interesting to study the performance and impedance of cells cycled to high potentials containing PES222 electrolyte in addition to LiPO_2F_2 . Studying a series of Li-ion cells containing different concentrations of LiPO_2F_2 added to the electrolyte would provide a comprehensive study of the effect of LiPO_2F_2 .

As Chapter 7 showed, cells containing natural graphite negative electrodes undergoing charge-hold-discharge cycling to 4.4 V had severe capacity fade and impedance growth. However, cells containing the same electrolyte and artificial graphite, in Chapter 4, had excellent performance when undergoing the same cycling conditions, and had little to no impedance growth. It is possible that particle cracking occurs in natural graphite, which is accelerated with increasing cycle number.¹⁶³ More work is required to observe and understand this particle cracking and how it may affect impedance growth in NMC/graphite cells.

Furthermore, Chapter 7 showed that the change in the average charge and discharge voltage, ΔV , did not agree with the expected ΔV , calculated from the corresponding cell impedance. However, the calculated change in ΔV did not include the Warburg diffusion impedance. If the Warburg diffusion impedance increased with cycle number, this may be causing the actual change ΔV to increase with cycle number, and may explain the discrepancy between the actual change and the calculated change in ΔV . It is therefore necessary to measure low frequency impedance of selected cells. Due to the large amount

of time required to perform low frequency measurements, it is important to carefully design experiments to characterize how the diffusion impedance changes with cycle number and with potential.

As discussed in Chapter 8, most researchers focus on how impedance changes or how the SEI layers change during a single cycle or only during the initial formation of the SEI layers. However, Chapter 8 highlighted the different types of impedance growth observed for different Li-ion cells undergoing long-term cycling tests. It is therefore necessary to characterize the components of the SEI layers during several cycles and several potentials, particularly near the end of life after severe impedance growth has been observed, in order to understand how and why impedance can change so dramatically with potential. Cycling experiments combined with EIS measurements can be performed alongside techniques such as X-ray photoelectron spectroscopy measurements to determine how the positive and negative SEI layers may depend on potential. Furthermore, the dynamic behaviour of the SEI layers can be studied through careful ellipsometry experiments,^{175,176} in-situ transmission electron microscopy (TEM),¹⁷⁷⁻¹⁸⁰ in-situ atomic force microscopy (AFM),^{181,182} and infrared near-field scanning optical microscopy.^{183,184}

McArthur et al. used ellipsometry to study the growth of SEI layers in Li/Si cells containing 0.1 M LiPF₆ in EC:DEC 1:2.¹⁷⁶ They found that there were reversible changes in the ellipsometric parameters that were related to state of charge. Ellis et al. used ellipsometry to study the growth of the SEI layer on an NMC positive electrode.¹⁷⁵ They

found that the SEI layer became thicker during charge and thinner during discharge. However, the thickness measured was significantly larger than that observed by XPS. Therefore, more work is required to understand the thickness results from ellipsometry experiments.

Zeng et al. used in-situ TEM to study the SEI layer on Au negative electrodes in 1M LiPF₆ EC:diethyl carbonate (DEC) 1:1 during lithiation and delithiation.¹⁸⁰ They were able to observe the formation of gaseous products, electrolyte oxidation, and the formation of the SEI layer. They found that the SEI layer grew quickly initially, and then maintained a constant thickness of approximately 200 nm. However, a thickness of 200 nm is approximately 10 times larger than the thickness of the negative electrode SEI layer commonly reported in literature.^{99,185} This indicates that using Au negative electrodes to study the SEI layers is not representative of the SEI layers formed in real full Li-ion cells.

Sacci et al. used in-situ TEM to study the SEI layer on Au negative electrodes in 1.2M LiPF₆ EC:DMC.¹⁷⁸ They found that the formation of the SEI was followed by lithium deposition, during which crystalline particles formed on the surface. They found that the formation and dissolution of these particles depended on potential. In-situ TEM will likely be very useful in understanding reversible and irreversible impedance growth in addition to observing the dynamic changes of the SEI layers.

Ramdon et al. used in-situ AFM to study LiFePO₄ positive electrodes in 1M LiPF₆ EC:DMC 1:1 during cycling.¹⁸² After a typical formation cycle, AFM was used before and after cycling the cell. They observed a change in shape of the electrode particles

before and after cycling, in which the particles became more rounded. Furthermore, they found that the positive electrode particles were larger after discharging compared to after charging. They claimed this was due to a phase change of the particles from the FePO_4 phase to the LiFePO_4 phase. In-situ AFM may be useful in understanding reversible and irreversible impedance growth.

Ayache et al. used infrared apertureless near-field scanning optical microscopy to study the SEI layers on negative electrodes.^{183,184} Ayache et al. studied a Sn negative electrode in 1M LiPF_6 EC:DEC 1:2.¹⁸⁴ They found that the SEI layer, which was rough, nonuniform, and porous, continued to grow during cycling, and that the Sn surface was never completely passivated. Ayache et al. studied a graphite negative electrode in 1M LiPF_6 EC:DEC 1:2.¹⁸³ They found that the SEI layer had significant growth in the outer layer, such that the inner layer was only visible in a few locations. This technique may be useful for understanding the dynamic nature of the SEI layers.

More work is also required to understand the reversible and irreversible changes to the high frequency intercept, representing the ionic and electronic path resistances, as a function of measurement potential. It is interesting that while R_{ct} increased at high potential, the electronic and ionic path resistances decreased. These changes may be due to the changes in the electrolyte as species are oxidized on the positive electrode at high potentials. XPS experiments combined with cycling and EIS measurements may be useful for understanding these dynamic changes.

As Chapter 9 showed, the positive and negative electrode SEI layers and the positive and negative symmetric cell impedance are incredibly complex, and influenced significantly by electrolyte additives and upper cutoff potential. The dynamic behaviour observed for some cells requires more investigation.

Chapter 3 presented several different equivalent circuit models used to fit impedance spectra of Li-ion cells. It is necessary to determine which equivalent circuit model is appropriate for the system under study. An experiment with a large matrix of cells can be designed to illustrate the contributions from the positive and negative electrodes to cell impedance. For example, several identical cells can be cycled using equipment capable of cycling experiments coupled with EIS measurements taken at regular intervals at several potentials. In addition to the full pouch cell impedance measurements, pouch cells can be removed from testing at regular intervals. These full pouch cells can be disassembled and assembled into symmetric coin cell and full coin cells, so that EIS measurements can be taken of each type of cell. This would be repeated, such that the full pouch cell impedance, positive symmetric cell impedance, negative symmetric cell impedance, and full coin cell impedance is monitored as a function of time, cycle number and potential. An equivalent circuit model can be used to fit the measured impedance spectra. Ideally, this would help to characterize impedance growth at several potentials, and would help to illustrate the corresponding process(es) responsible for changes to the cell impedance.

It may also be possible for three electrode cells, in which a reference electrode is placed between the two working electrodes, to be used to distinguish the contribution to

impedance from the positive and negative electrodes. Solchenbach et al. used a thin insulated gold wire as a reference electrode in a $\text{LiFePO}_4/\text{graphite}$ cell.¹⁸⁶ While they claimed that the gold wire reference electrode was stable for 500 hours at 20°C , they found that the potential of the gold wire began to drift after only 10 hours at 40°C . It is not clear if three electrode cells are reliable enough. It is necessary to compare impedance results from symmetric cells and from three electrode cells.

Lastly, it is not just necessary to fit impedance spectra using an equivalent circuit model to learn about the complex changes with a Li-ion cell, but to better understand the circuit models and fitting methods used. Using appropriate equivalent circuit models is imperative for the proper analysis of impedance spectra. An in-depth investigation into different equivalent circuit models and their physical relevance to the processes occurring in Li-ion cells is necessary.

The goal of studies on reversible and irreversible impedance growth in Li-ion cells is to have a complete atomic understanding of the structure and composition of the positive and negative electrode SEI layers as a function of time, cycle number, potential, temperature, cell chemistry, electrolyte system, experimental protocol and cell history. The results in this thesis suggest that reaching this goal is at least several decades away.

REFERENCES

1. June 26, 2017 <http://nissannews.com/en-CA/nissan/canada/channels/Sales-Reports-Canada/releases/nissan-group-reports-record-december-and-2016-calendar-year-canadian-sales>.
2. June 26, 2017 <http://gmauthority.com/blog/gm/chevrolet/chevrolet-sales-numbers/>.
3. J. Axsen, S. Goldberg, J. Bailey, G. Kamiya, B. Langman, J. Cairns, M. Wolinetz, and A. Miele, *Electrifying Vehicles: Insights from the Canadian Plug-in Electric Vehicle Study, Sustainable Transportation Research Team, Simon Fraser University, Vancouver, Canada*, (2015).
4. Tesla, June 26, 2017 https://www.tesla.com/en_CA/blog/the-week-electric-vehicles-went-mainstream.
5. C. P. Aiken, J. Self, R. Petibon, X. Xia, J. M. Paulsen, and J. R. Dahn, *J. Electrochem. Soc.*, **162**, A760–A767 (2015).
6. J. Xia, J. Self, L. Ma, and J. R. Dahn, *J. Electrochem. Soc.*, **162**, A1424–A1431 (2015).
7. L. E. Downie and J. R. Dahn, *J. Electrochem. Soc.*, **161**, A1782–A1787 (2014).
8. J. C. Burns, N. N. Sinha, G. Jain, H. Ye, C. M. VanElzen, W. M. Lamanna, A. Xiao, E. Scott, J. Choi, and J. R. Dahn, *J. Electrochem. Soc.*, **159**, A1095–A1104 (2012).
9. N. P. W. Pieczonka, Z. Liu, P. Lu, K. L. Olson, J. Moote, B. R. Powell, and J. Kim, *J. Phys. Chem. C*, **117**, 15947–15957 (2013).
10. K. J. Nelson, G. L. D'Eon, A. T. B. Wright, L. Ma, J. Xia, and J. R. Dahn, *J. Electrochem. Soc.*, **162**, A1046–A1054 (2015).
11. L. Ma, J. Xia, and J. R. Dahn, *J. Electrochem. Soc.*, **161**, A2250–A2254 (2014).
12. *Linden's Handbook of Batteries, 4th Edition*, p. 1200, McGraw-Hill Professional; 4th edition, (2010).
13. K. Nelson, thesis, Dalhousie University (2014).
14. June 26, 2017 <http://www.infomine.com/investment/metal-prices/cobalt/>.

15. June 26, 2017 <http://www.infomine.com/investment/metal-prices/nickel/>.
16. June 26, 2017 <http://www.infomine.com/investment/metal-prices/manganese/>.
17. 3M, June 26, 2017 [http://multimedia.3m.com/mws/media/7734580/3mtm-battery-electrolyte-presentation.pdf?fn=3M Battery Electrolyte Pres.pdf](http://multimedia.3m.com/mws/media/7734580/3mtm-battery-electrolyte-presentation.pdf?fn=3M%20Battery%20Electrolyte%20Pres.pdf).
18. Z. Lu, D. D. MacNeil, and J. R. Dahn, *Electrochem. Solid-State Lett.*, **4**, A200–A203 (2001).
19. C. H. Chen, J. Liu, and K. Amine, *J. Power Sources*, **96**, 321–328 (2000).
20. K. Amine, C. H. Chen, J. Liu, M. Hammond, A. Jansen, D. Dees, I. Bloom, D. Visser, and G. Henriksen, *J. Power Sources*, **97–98**, 684–687 (2001).
21. J. R. Dahn, T. Zheng, Y. Liu, and J. S. Xue, *Science (80-.)*, **270**, 590–593 (1995).
22. M. N. Obrovac and L. Christensen, *Electrochem. Solid-State Lett.*, **7**, A93–A96 (2004).
23. M. N. Obrovac and L. J. Krause, *J. Electrochem. Soc.*, **154**, A103–A108 (2007).
24. M. N. Obrovac and V. L. Chevrier, *Chem. Rev.*, **114**, 11444–11502 (2014).
25. M. N. Obrovac, L. Christensen, D. B. Le, and J. R. Dahn, *J. Electrochem. Soc.*, **154**, A849 (2007).
26. H. Wu and Y. Cui, *Nano Today*, **7**, 414–429 (2012).
27. C.-M. Park, J.-H. Kim, H. Kim, and H.-J. Sohn, *Chem. Soc. Rev.*, **39**, 3115 (2010).
28. W. J. Weydanz, M. Wohlfahrt-Mehrens, and R. A. Huggins, *J. Power Sources*, **8182**, 237–242 (1999).
29. V. L. Chevrier, L. Liu, D. B. Le, J. Lund, B. Molla, K. Reimer, L. J. Krause, L. D. Jensen, E. Figgemeier, and K. W. Eberman, *J. Electrochem. Soc.*, **161**, A783–A791 (2014).
30. J.-A. Choi, S. H. Kim, and D.-W. Kim, *J. Power Sources*, **195**, 6192–6196 (2010).

31. J. Hao, G. Lei, Z. Li, L. Wu, Q. Xiao, and L. Wang, *J. Memb. Sci.*, **428**, 11–16 (2012).
32. B. Yang, H. Zhang, L. Yu, W. Z. Fan, and D. Huang, *Electrochim. Acta*, **221**, 107–114 (2016).
33. G. Yang, J. Shi, C. Shen, S. Wang, L. Xia, H. Hu, H. Luo, Y. Xia, and Z. Liu, *RSC Adv.*, **7**, 26052–26059 (2017).
34. T. R. Jow, K. Xu, O. Borodin, and M. Ue, Eds., *Electrolytes for Lithium and Lithium-Ion Batteries*, Springer New York, (2014).
35. M. S. Ding, A. von Cresce, and K. Xu, *J. Phys. Chem. C*, **121**, 2149–2153 (2017).
36. L. Suo, O. Borodin, W. Sun, X. Fan, C. Yang, F. Wang, T. Gao, Z. Ma, M. Schroeder, A. von Cresce, S. M. Russell, M. Armand, A. Angell, K. Xu, and C. Wang, *Angew. Chemie - Int. Ed.*, **55**, 7136–7141 (2016).
37. K. Xu, *Chem. Rev.*, **104**, 4303–4417 (2004).
38. L. D. Ellis, J. Xia, A. J. Louli, and J. R. Dahn, *J. Electrochem. Soc.*, **163**, A1686–A1692 (2016).
39. R. Fong, U. von Sacken, and J. R. Dahn, *J. Electrochem. Soc.*, **137**, 2009 (1990).
40. Z. Zhang, L. Hu, H. Wu, W. Weng, M. Koh, P. C. Redfern, L. A. Curtiss, and K. Amine, *Energy Environ. Sci.*, **6**, 1806 (2013).
41. J. Xia, M. Nie, J. C. Burns, A. Xiao, W. M. Lamanna, and J. R. Dahn, *J. Electrochem. Soc.* (2015).
42. J. C. Burns, A. Kassam, N. N. Sinha, L. E. Downie, L. Solnickova, B. M. Way, and J. R. Dahn, *J. Electrochem. Soc.*, **160**, A1451–A1456 (2013).
43. L. Ma, D. Y. Wang, L. E. Downie, J. Xia, K. J. Nelson, N. N. Sinha, and J. R. Dahn, *J. Electrochem. Soc.*, **161**, A1261–A1265 (2014).
44. K. J. Nelson, J. Xia, and J. R. Dahn, *J. Electrochem. Soc.*, **161**, A1884–A1889 (2014).
45. L. Xia, D. Wang, H. Yang, Y. Cao, and X. Ai, *Electrochem. commun.*, **25**, 98–100

(2012).

46. X. L. Yao, S. Xie, C. H. Chen, Q. S. Wang, J. H. Sun, Y. L. Li, and S. X. Lu, *J. Power Sources*, **144**, 170–175 (2005).

47. H. F. Xiang, H. Y. Xu, Z. Z. Wang, and C. H. Chen, *J. Power Sources*, **173**, 562–564 (2007).

48. D. Aurbach, Y. Talyosef, B. Markovsky, E. Markevich, E. Zinigrad, L. Asraf, J. S. Gnanaraj, and H.-J. Kim, *Electrochim. Acta*, **50**, 247–254 (2004).

49. X. Zuo, C. Fan, X. Xiao, J. Liu, and J. Nan, *J. Power Sources*, **219**, 94–99 (2012).

50. M. Hu, X. Pang, and Z. Zhou, *J. Power Sources*, **237**, 229–242 (2013).

51. D. Y. Wang, J. Xia, L. Ma, K. J. Nelson, J. E. Harlow, D. Xiong, L. E. Downie, R. Petibon, J. C. Burns, A. Xiao, W. M. Lamanna, and J. R. Dahn, *J. Electrochem. Soc.*, **161**, A1818–A1827 (2014).

52. D. Y. Wang, N. N. Sinha, R. Petibon, J. C. Burns, and J. R. Dahn, *J. Power Sources*, **251**, 311–318 (2014).

53. J. Jeon, S. Yoon, T. Park, J.-J. Cho, S. Kang, Y.-K. Han, and H. Lee, *J. Mater. Chem.*, **22**, 21003–21008 (2012).

54. J. Xia, L. Ma, C. P. Aiken, K. J. Nelson, L. P. Chen, and J. R. Dahn, *J. Electrochem. Soc.*, **161**, A1634–A1641 (2014).

55. J. Xia, N. N. Sinha, L. P. Chen, G. Y. Kim, D. J. Xiong, and J. R. Dahn, *J. Electrochem. Soc.*, **161**, A84–A88 (2013).

56. X. X. Li, Z. Yin, and C. Wang, *Ionics (Kiel)*, **20**, 795–801 (2014).

57. J. Xia, N. N. Sinha, L. P. Chen, and J. R. Dahn, *J. Electrochem. Soc.*, **161**, A264–A274 (2013).

58. N. N. Sinha, J. C. Burns, and J. R. Dahn, *J. Electrochem. Soc.*, **161**, A1084–A1089 (2014).

59. E. Peled, *J. Electrochem. Soc.*, **126**, 2047–2051 (1979).

60. M. Nie, D. Chalasani, D. P. Abraham, Y. Chen, A. Bose, and B. L. Lucht, *J. Phys. Chem. C*, **117**, 1257–1267 (2013).
61. M. Nie and B. L. Lucht, *J. Electrochem. Soc.*, **161**, A1001–A1006 (2014).
62. E. Peled, D. Golodnitsky, and G. Ardel, *J. Electrochem. Soc.*, **144**, 208–210 (1997).
63. P. Ganesh, P. R. C. Kent, and D. Jiang, *J. Phys. Chem. C*, **116**, 24476–24481 (2012).
64. D. Aurbach, *J. Power Sources*, **89**, 206–218 (2000).
65. K. Edström, M. Herstedt, and D. P. Abraham, *J. Power Sources*, **153**, 380–384 (2006).
66. A. J. Smith, J. C. Burns, X. Zhao, D. Xiong, and J. R. Dahn, *J. Electrochem. Soc.*, **158**, A447–A452 (2011).
67. Q. Zhang and R. E. White, *J. Power Sources*, **179**, 793–798 (2008).
68. M. Nie, D. P. Abraham, D. M. Seo, Y. Chen, A. Bose, and B. L. Lucht, *J. Phys. Chem. C*, **117**, 25381–25389 (2013).
69. J. T. Lee, N. Nitta, J. Benson, A. Magasinski, T. F. Fuller, and G. Yushin, *Carbon N. Y.*, **52**, 388–397 (2013).
70. R. Dedryvère, L. Gireaud, S. Grugeon, S. Laruelle, J.-M. Tarascon, and D. Gonbeau, *J. Phys. Chem. B*, **109**, 15868–75 (2005).
71. K. Xu, *Chem. Rev.*, **114**, 11503–11618 (2014).
72. S. Shi, Y. Qi, H. Li, and L. G. Hector, *J. Phys. Chem.*, **117**, 8579–8593 (2013).
73. L. Zhao, I. Watanabe, T. Doi, S. Okada, and J. Yamaki, *J. Power Sources*, **161**, 1275–1280 (2006).
74. D. Aurbach, E. Zinigrad, Y. Cohen, and H. Teller, *Solid State Ionics*, **148**, 405–416 (2002).
75. S. S. Harilal, J. P. Allain, A. Hassanein, M. R. Hendricks, and M. Nieto-Perez, *Appl. Surf. Sci.*, **255**, 8539–8543 (2009).

76. D. Lu, J. Tao, P. Yan, W. A. Henderson, Q. Li, Y. Shao, M. L. Helm, O. Borodin, G. L. Graff, B. Polzin, C.-M. Wang, M. Engelhard, J.-G. Zhang, J. J. De Yoreo, J. Liu, and J. Xiao, *Nano Lett.*, **17**, 1602–1609 (2017).
77. M. G. S. R. Thomas, P. G. Bruce, and J. B. Goodenough, *J. Electrochem. Soc.*, **132**, 1521–1528 (1985).
78. D. Guyomard and J. M. Tarascon, *J. Electrochem. Soc.*, **139**, 937–948 (1992).
79. D. Aurbach, K. Gamolsky, B. Markovsky, G. Salitra, Y. Gofer, U. Heider, R. Oesten, and M. Schmidt, *J. Electrochem. Soc.*, **147**, 1322–1331 (2000).
80. M. Moshkovich, M. Cojocaru, H. E. Gottlieb, and D. Aurbach, *J. Electroanal. Chem.*, **497**, 84–96 (2001).
81. D. Y. Wang, N. N. Sinha, J. C. Burns, C. P. Aiken, R. Petibon, and J. R. Dahn, *J. Electrochem. Soc.*, **161**, 467–472 (2014).
82. K. J. Nelson, D. W. Abarbanel, J. Xia, Z. Lu, and J. R. Dahn, *J. Electrochem. Soc.*, **163**, A272–A280 (2016).
83. L. Yang and B. L. Lucht, *Electrochem. Solid-State Lett.*, **12**, A229 (2009).
84. W. Choi and A. Manthiram, *J. Electrochem. Soc.*, **153**, A1760 (2006).
85. A. J. Smith, S. R. Smith, T. Byrne, J. C. Burns, and J. R. Dahn, *J. Electrochem. Soc.*, **159**, A1696–A1701 (2012).
86. Y.-M. Song et al., *J. Mater. Chem. A*, **2**, 9506–9513 (2014).
87. D. J. Xiong, L. D. Ellis, K. J. Nelson, T. Hynes, R. Petibon, and J. R. Dahn, *J. Electrochem. Soc.*, **163**, A3069–A3077 (2016).
88. S. E. Sloop, J. B. Kerr, and K. Kinoshita, *J. Power Sources*, **119–121**, 330–337 (2003).
89. M. Broussely, P. Biensan, F. Bonhomme, P. Blanchard, S. Herreyre, K. Nechev, and R. J. Staniewicz, *J. Power Sources*, **146**, 90–96 (2005).
90. R. Dedryvère, D. Foix, S. Franger, S. Patoux, L. Daniel, and D. Gonbeau, *J. Phys.*

Chem. C, **114**, 10999–11008 (2010).

91. D. J. Xiong, R. Petibon, M. Nie, L. Ma, J. Xia, and J. R. Dahn, *J. Electrochem. Soc.*, **163**, A546–A551 (2016).

92. Z. Chen, Y. Qin, K. Amine, and Y.-K. Sun, *J. Mater. Chem.*, **20**, 7606–7612 (2010).

93. Y.-K. Sun, S.-W. Cho, S.-W. Lee, C. S. Yoon, and K. Amine, *J. Electrochem. Soc.*, **154**, A168 (2007).

94. H. G. Song, K.-S. Park, and Y. J. Park, *Solid State Ionics*, **225**, 532–537 (2012).

95. P. Mohan and G. Paruthimal Kalaigan, *Ceram. Int.*, **40**, 1415–1421 (2014).

96. J. Xia, Z. Lu, J. Camardese, and J. R. Dahn, *J. Power Sources*, **306**, 516–525 (2016).

97. B. Li, M. Xu, T. Li, W. Li, and S. Hu, *Electrochem. commun.*, **17**, 92–95 (2012).

98. J. Self, D. S. Hall, L. Madec, and J. R. Dahn, *J. Power Sources*, **298**, 369–378 (2015).

99. L. Madec, R. Petibon, J. Xia, J.-P. Sun, I. G. Hill, and J. R. Dahn, *J. Electrochem. Soc.*, **162**, A2635–A2645 (2015).

100. R. Bernhard, M. Metzger, and H. A. Gasteiger, *J. Electrochem. Soc.*, **162**, A1984–A1989 (2015).

101. J. Xia, K. J. Nelson, Z. Lu, and J. R. Dahn, *J. Power Sources*, **329**, 387–397 (2016).

102. F. Lin, I. M. Markus, D. Nordlund, T.-C. Weng, M. D. Asta, H. L. Xin, and M. M. Doeff, *Nat. Commun.*, **5**, 3529 (2014).

103. S. Zheng, R. Huang, Y. Makimura, Y. Ukyo, C. A. J. Fisher, T. Hirayama, and Y. Ikuhara, *J. Electrochem. Soc.*, **158**, A357–A362 (2011).

104. Y. Makimura, S. Zheng, Y. Ikuhara, and Y. Ukyo, *J. Electrochem. Soc.*, **159**, A1070–A1073 (2012).

105. T. Hayashi, J. Okada, E. Toda, R. Kuzuo, N. Oshimura, N. Kuwata, and J. Kawamura, *J. Electrochem. Soc.*, **161**, A1007–A1011 (2014).

106. S. Muto, Y. Sasano, K. Tatsumi, T. Sasaki, K. Horibuchi, Y. Takeuchi, and Y. Ukyo, *J. Electrochem. Soc.*, **156**, A371 (2009).
107. D. P. Abraham, R. D. Twisten, M. Balasubramanian, I. Petrov, J. McBreen, and K. Amine, *Electrochem. commun.*, **4**, 620–625 (2002).
108. D. P. Abraham, R. D. Twisten, M. Balasubramanian, J. Kropf, D. Fischer, J. McBreen, I. Petrov, and K. Amine, *J. Electrochem. Soc.*, **150**, A1450 (2003).
109. J. Li, H. Liu, J. Xia, A. R. Cameron, M. Nie, G. A. Botton, and J. R. Dahn, *J. Electrochem. Soc.*, **164**, A655–A665 (2017).
110. J. C. Burns, G. Jain, A. J. Smith, K. W. Eberman, E. Scott, J. P. Gardner, and J. R. Dahn, *J. Electrochem. Soc.*, **158**, A255 (2011).
111. D. A. Stevens, R. Y. Ying, R. Fathi, J. N. Reimers, J. E. Harlow, and J. R. Dahn, *J. Electrochem. Soc.*, **161**, A1364–A1370 (2014).
112. R. Fathi, J. C. Burns, D. A. Stevens, H. Ye, C. Hu, G. Jain, E. Scott, C. Schmidt, and J. R. Dahn, *J. Electrochem. Soc.*, **161**, A1572–A1579 (2014).
113. T. M. Bond, J. C. Burns, D. A. Stevens, H. M. Dahn, and J. R. Dahn, *J. Electrochem. Soc.*, **160**, A521–A527 (2013).
114. J. Xia, L. Ma, and J. R. Dahn, *J. Power Sources*, **287** (2015).
115. J. Self, C. P. Aiken, R. Petibon, and J. R. Dahn, *J. Electrochem. Soc.*, **162**, A796–A802 (2015).
116. C. P. Aiken, J. Xia, D. Y. Wang, D. A. Stevens, S. Trussler, and J. R. Dahn, *J. Electrochem. Soc.*, **161**, A1548–A1554 (2014).
117. R. de Levie, *Electrochim. Acta*, **8**, 751–780 (1963).
118. N. Ogihara, S. Kawauchi, C. Okuda, Y. Itou, Y. Takeuchi, and Y. Ukyo, *J. Electrochem. Soc.*, **159**, A1034–A1039 (2012).
119. D. W. Abarbanel, K. J. Nelson, and J. R. Dahn, *J. Electrochem. Soc.*, **163**, A522–A529 (2016).

120. J. Li, L. E. Downie, L. Ma, W. Qiu, and J. R. Dahn, *J. Electrochem. Soc.*, **162**, A1401–A1408 (2015).
121. B. Gyenes, D. A. Stevens, V. L. Chevrier, and J. R. Dahn, *J. Electrochem. Soc.*, **162**, A278–A283 (2014).
122. R. Petibon, C. P. Aiken, N. N. Sinha, J. C. Burns, H. Ye, C. M. VanElzen, G. Jain, S. Trussler, and J. R. Dahn, *J. Electrochem. Soc.*, **160**, A117–A124 (2012).
123. R. Petibon, N. N. Sinha, J. C. Burns, C. P. Aiken, H. Ye, C. M. VanElzen, G. Jain, S. Trussler, and J. R. Dahn, *J. Power Sources*, **251**, 187–194 (2014).
124. J. E. B. Randles, *Discuss. Faraday Soc.*, **1**, 11–19 (1947).
125. J.-M. Atebamba, J. Moskon, S. Pejovnik, and M. Gaberscek, *J. Electrochem. Soc.*, **157**, A1218 (2010).
126. B. Yann Liaw, G. Nagasubramanian, R. G. Jungst, and D. H. Doughty, *Solid State Ionics*, **175**, 835–839 (2004).
127. T. Osaka, T. Momma, D. Mukoyama, and H. Nara, *J. Power Sources*, **205**, 483–486 (2012).
128. D. Mukoyama, T. Momma, H. Nara, and T. Osaka, *Chem. Lett.*, **41**, 444–446 (2012).
129. T. Osaka, S. Nakade, M. Rajamäki, and T. Momma, *J. Power Sources*, **119**, 929–933 (2003).
130. P. Suresh, A. K. Shukla, and N. Munichandraiah, *J. Appl. Electrochem.*, **32**, 267–273.
131. S. Zhang, M. S. Ding, K. Xu, J. Allen, and T. R. Jow, *Electrochem. Solid-State Lett.*, **4**, A206 (2001).
132. M. Itagaki, K. Honda, Y. Hoshi, and I. Shitanda, *J. Electroanal. Chem.*, **737**, 78–84 (2015).
133. H. Nara, D. Mukoyama, T. Yokoshima, T. Momma, and T. Osaka, *J. Electrochem. Soc.*, **163**, A434–A441 (2016).

134. T. K. Dong, A. Kirchev, F. Mattera, J. Kowal, and Y. Bultel, *J. Electrochem. Soc.*, **158**, A326 (2011).
135. S. Buller, M. Thele, R. W. A. A. De Doncker, and E. Karden, *IEEE Trans. Ind. Appl.*, **41** (2005).
136. J. Huang, Z. Li, B. Y. Liaw, and J. Zhang, *J. Power Sources*, **309**, 82–98 (2016).
137. P. Agarwal, M. E. Orazem, and L. H. Garcia-Rubio, *J. Electrochem. Soc.*, **139**, 1917–1927 (1992).
138. L. Ma, J. Xia, and J. R. Dahn, *J. Electrochem. Soc.*, **162**, A1170–A1174 (2015).
139. Linear Technology, June 26, 2017 <http://www.linear.com/designtools/software/#LTspice>.
140. M. Metzger, C. Marino, J. Sicklinger, D. Haering, and H. A. Gasteiger, *J. Electrochem. Soc.*, **162**, A1123–A1134 (2015).
141. J. C. Burns, X. Xia, and J. R. Dahn, *J. Electrochem. Soc.*, **160**, A383–A386 (2012).
142. LG Chem, May 23, 2017 <http://www.meircell.co.il/files/LG ICR18650C1.pdf>.
143. Samsung SDI, May 23, 2017 <http://gamma.spb.ru/media/pdf/liion-lipolymer-lifepo4-akkumulyatory/ICR18650-30B.pdf>.
144. LG Chem, May 23, 2017 <http://meircell.co.il/files/LG ICR18650B1.pdf>.
145. J. H. Shim, J. M. Han, J. H. Lee, and S. Lee, *ACS Appl. Mater. Interfaces*, **8**, 12205–12210 (2016).
146. J. Li, A. R. Cameron, H. Li, S. Glazier, D. Xiong, M. Chatzidakis, J. Allen, G. A. Botton, and J. R. Dahn, *J. Electrochem. Soc.*, **164**, 1534–1544 (2017).
147. J. R. Dahn, J. Xia, Y. Wang, R. Petibon, L. Ma, K. Nelson, and L. E. Downie, *US Pat. Appl. Publ.*, **2017002570** (2017).
148. I. Bloom, L. K. Walker, J. K. Basco, D. P. Abraham, J. P. Christophersen, and C. D. Ho, *J. Power Sources*, **195**, 877–882 (2010).

149. I. Bloom, A. N. Jansen, D. P. Abraham, J. Knuth, S. A. Jones, V. S. Battaglia, and G. L. Henriksen, *J. Power Sources*, **139**, 295–303 (2005).
150. K. Honkura, K. Takahashi, and T. Horiba, *ECS Trans.*, **13**, 61–73 (2008).
151. H. M. Dahn, A. J. Smith, J. C. Burns, D. A. Stevens, and J. R. Dahn, *J. Electrochem. Soc.*, **159**, A1405–A1409 (2012).
152. H. C. Wu, H. C. Wu, E. Lee, and N. L. Wu, *Electrochem. commun.*, **12**, 488–491 (2010).
153. R. Petibon, J. Xia, L. Ma, M. K. G. Bauer, K. J. Nelson, and J. R. Dahn, *J. Electrochem. Soc.*, **163**, A2571–A2578 (2016).
154. N. N. Sinha, A. J. Smith, J. C. Burns, G. Jain, K. W. Eberman, E. Scott, J. P. Gardner, and J. R. Dahn, *J. Electrochem. Soc.*, **158**, A1194 (2011).
155. J. Xia, R. Petibon, D. Xiong, L. Ma, and J. R. Dahn, *J. Power Sources*, **328**, 124–135 (2016).
156. L. Madec, J. Xia, R. Petibon, K. J. Nelson, J.-P. Sun, I. G. Hill, and J. R. Dahn, *J. Phys. Chem. C*, **118**, 29608–29622 (2014).
157. D. S. Hall, J. Self, and J. R. Dahn, *J. Phys. Chem. C*, **119**, 22322–22330 (2015).
158. M. S. Ding, K. Xu, and T. R. Jow, *J. Electrochem. Soc.*, **147**, 1688 (2000).
159. R. S. Arumugam, L. Ma, J. Li, X. Xia, J. M. Paulsen, and J. R. Dahn, *J. Electrochem. Soc.*, **163**, A2531–A2538 (2016).
160. C. Li, H. P. Zhang, L. J. Fu, H. Liu, Y. P. Wu, E. Rahm, R. Holze, and H. Q. Wu, *Electrochim. Acta*, **51**, 3872–3883 (2006).
161. S. C. Jung and Y. Han, *J. Phys. Chem. Lett.*, **4**, 2681–2685 (2013).
162. S. L. Glazier, K. J. Nelson, J. P. Allen, J. Li, and J. R. Dahn, *J. Electrochem. Soc.*, **164**, A1203–A1212 (2017).
163. Y.-S. Park, T.-W. Lee, M.-S. Shin, S.-H. Lim, and S.-M. Lee, *J. Electrochem. Soc.*, **163**, A3078–A3086 (2016).

164. D. J. Xiong, L. D. Ellis, R. Petibon, T. Hynes, Q. Q. Liu, and J. R. Dahn, *J. Electrochem. Soc.*, **164**, A340–A347 (2016).
165. L. Feng, X. Xu, M. Shui, W. Zheng, J. Shu, L. Hui, L. Xu, L. Chen, and Y. Ren, *Solid State Ionics*, **265**, 49–54 (2014).
166. S. S. Zhang, K. Xu, and T. R. Jow, *Electrochim. Acta*, **49**, 1057–1061 (2004).
167. K. Ciosek Högström, S. Malmgren, M. Hahlin, M. Gorgoi, L. Nyholm, H. Rensmo, and K. Edström, *Electrochim. Acta*, **138**, 430–436 (2014).
168. L. Madec, R. Petibon, K. Tasaki, J. Xia, J.-P. Sun, I. G. Hill, and J. R. Dahn, *Phys. Chem. Chem. Phys.*, **17**, 27062–27076 (2015).
169. W. Li, A. Dolocan, P. Oh, H. Celio, S. Park, J. Cho, and A. Manthiram, *Nat. Commun.*, **8**, 1–10 (2017).
170. J. Cannarella and C. B. Arnold, *J. Power Sources*, **245**, 745–751 (2014).
171. R. Jung, M. Metzger, F. Maglia, C. Stinner, and H. A. Gasteiger, *J. Electrochem. Soc.*, **164**, A1361–A1377 (2017).
172. S. Erol and M. E. Orazem, *J. Power Sources*, **293**, 57–64 (2015).
173. S. Erol, M. E. Orazem, and R. P. Muller, *J. Power Sources*, **270**, 92–100 (2014).
174. J. C. Burns, N. N. Sinha, D. J. Coyle, G. Jain, C. M. VanElzen, W. M. Lamanna, A. Xiao, E. Scott, J. P. Gardner, and J. R. Dahn, *J. Electrochem. Soc.*, **159**, A85 (2012).
175. L. D. Ellis, R. J. Sanderson, and J. R. Dahn, in *100th Canadian Chemistry Conference and Exhibition*, Toronto, ON (2017).
176. M. A. McArthur, S. Trussler, and J. R. Dahn, *J. Electrochem. Soc.*, **159**, A198–A207 (2012).
177. A. Kushima, K. P. So, C. Su, P. Bai, N. Kuriyama, T. Maebashi, Y. Fujiwara, M. Z. Bazant, and J. Li, *Nano Energy*, **32**, 271–279 (2017).
178. R. L. Sacci, N. J. Dudney, K. L. More, L. R. Parent, I. Arslan, N. D. Browning, and R. R. Unocic, *Chem. Commun.*, **50**, 2104 (2014).

179. R. R. Unocic, X.-G. Sun, R. L. Sacci, L. A. Adamczyk, D. H. Alsem, S. Dai, N. J. Dudley, and K. L. More, *Microsc. Microanal.*, 1–9 (2014).
180. Z. Zeng, W.-I. Liang, H. Liao, H. L. Xin, Y.-H. Chu, and H. Zheng, *Nano Lett.*, **14**, 1745–1750 (2014).
181. A. Tokranov, B. W. Sheldon, C. Li, S. Minne, and X. Xiao, *ACS Appl Mater Interfaces*, **6**, 6672–6686 (2014).
182. S. Ramdon, B. Bhushan, and S. C. Nagpure, *J. Power Sources*, **249**, 373–384 (2014).
183. M. Ayache, D. Jang, J. Syzdek, and R. Kostecki, *J. Electrochem. Soc.*, **162**, A7078–A7082 (2015).
184. M. Ayache, S. F. Lux, and R. Kostecki, *J. Phys. Chem. Lett.*, **6**, 1126–1129 (2015).
185. H. Bryngelsson, M. Stjerndahl, T. Gustafsson, and K. Edström, *J. Power Sources*, **174**, 970–975 (2007).
186. S. Solchenbach, D. Pritzl, E. J. Y. Kong, J. Landesfeind, and H. A. Gasteiger, *J. Electrochem. Soc.*, **163**, A2265–A2272 (2016).

APPENDIX A

Table 0.1 Cell details for some of the lithium-ion pouch cells presented in this thesis.

LiFUN Technology: Li[Ni_{0.4}Mn_{0.4}Co_{0.2}]O₂ (NMC442)/graphite pouch cells Pouch cell dimensions: 40 mm x 20 mm x 3.5 mm Capacity ~ 240 mAh, Electrode Area ~ 100 cm²		
	Positive Electrode	Negative Electrode
Composition	96.2:1.8:2.0 active material:CB:PVDF	95.4:1.3:1.1:2.2 active material:CB:CMC:SBR
Thickness of two coatings on current collector	105 μm	110 μm
Density of coating	3.55 g/cm ³	1.55 g/cm ³
Areal density of single coating	16 mg/cm ³	9.5 mg/cm ³
LiFUN Technology: NMC442/graphite pouch cells with CB Pouch cell dimensions: 40 mm x 20 mm x 3.0 mm Capacity ~ 160 mAh, Electrode Area ~ 86 cm²		
	Positive Electrode	Negative Electrode
Composition	96.4:1.6:2.0 active material:CB:PVDF	95.4:1.3:1.1:2.2 active material:CB:CMC:SBR
Thickness of two coatings on current collector	81 μm	142 μm
Density of coating	3.1 g/cm ³	1.4 g/cm ³
Areal density of single coating	10.7 mg/cm ³	10.0 mg/cm ³
LiFUN Technology: NMC442/graphite pouch cells with CNT Pouch cell dimensions: 40 mm x 20 mm x 3.0 mm Capacity ~ 180 mAh, Electrode Area ~ 86 cm²		
	Positive Electrode	Negative Electrode
Composition	98.1:0.4:1.5 active material:CNT:PVDF	95.4:1.3:1.1:2.2 active material:CB:CMC:SBR
Thickness of two coatings on current collector	80 μm	142 μm
Density of coating	3.15 g/cm ³	1.4 g/cm ³
Areal density of single coating	10.7 mg/cm ³	10.0 mg/cm ³

LiFUN Technology: NMC622/natural graphite pouch cells Pouch cell dimensions: 40 mm x 20 mm x 3.5 mm Capacity ~ 260 mAh, Electrode Area ~ 100 cm²		
	Positive Electrode	Negative Electrode
Composition	96:2:2 active material:CB:PVDF	95:2:1:2 active material:CB:CMC:SBR
Thickness of two coatings on current collector	136 μm	200 μm
Density of coating	3.2 g/cm ³	1.55 g/cm ³
Areal density of single coating	19.3 mg/cm ³	13.6 mg/cm ³
LiFUN Technology: Single crystal NMC532/natural graphite pouch cells Pouch cell dimensions: 40 mm x 20 mm x 3.5 mm Capacity ~ 200 mAh, Electrode Area ~ 100 cm²		
	Positive Electrode	Negative Electrode
Composition	96:2:2 active material:CB:PVDF	95.4:1.3:1.1:2.2 active material:CB:CMC:SBR
Thickness of two coatings on current collector	148 μm	182 μm
Density of coating	3.5 g/cm ³	1.55 g/cm ³
Areal density of single coating	21.1 mg/cm ³	13.6 mg/cm ³
LiFUN Technology: Single crystal NMC532/artificial graphite pouch cells Pouch cell dimensions: 40 mm x 20 mm x 3.5 mm Capacity ~ 220 mAh, Electrode Area ~ 100 cm²		
	Positive Electrode	Negative Electrode
Composition	96:2:2 active material:CB:PVDF	95.4:1.3:1.1:2.2 active material:CB:CMC:SBR
Thickness of two coatings on current collector	148 μm	182 μm
Density of coating	3.5 g/cm ³	1.55 g/cm ³
Areal density of single coating	21.1 mg/cm ³	13.6 mg/cm ³